

Turbulent Mixing in Explosions

Approved for public release; distribution is unlimited.

January 2000



Prepared for:
Defense Threat Reduction Agency
45045 Aviation Drive
Dulles, VA 20166-7517

DNA001-94-C-0015

Heinz Reichenbach
Peter Neuwald

Prepared by: Ernst-Mach Institut
Fraunhofer Institut für Kurzzeitdynamik
Eckerstraße 4
79104 Freiburg i. Br.
Federal Republic of Germany

DTIC QUALITY INSPECTED

20000825 033

DESTRUCTION NOTICE:

Destroy this report when it is no longer needed. Do not return to sender.

PLEASE NOTIFY THE DEFENSE THREAT REDUCTION AGENCY, ATTN: ADM, 45045 AVIATION DRIVE, DULLES, VA 20166-7517, IF YOUR ADDRESS IS INCORRECT, IF YOU WISH IT DELETED FROM THE DISTRIBUTION LIST, OR IF THE ADDRESSEE IS NO LONGER EMPLOYED BY YOUR ORGANIZATION.

DISTRIBUTION LIST UPDATE

This mailer is provided to enable DTRA to maintain current distribution lists for reports. (We would appreciate you providing the requested information.)

- Add the individual listed to your distribution list.
- Delete the cited organization/individual.
- Change of address.

Note:

Please return the mailing label from the document so that any additions, changes, corrections or deletions can be made easily. For distribution cancellation or more information call DTRA/ADM (703) 325-1036.

NAME: _____

ORGANIZATION: _____

OLD ADDRESS

NEW ADDRESS

TELEPHONE NUMBER: () _____

DTRA PUBLICATION NUMBER/TITLE

CHANGES/DELETIONS/ADDITIONS, etc.)

(Attach Sheet if more Space is Required)

DTRA or other GOVERNMENT CONTRACT NUMBER: _____

CERTIFICATION of NEED-TO-KNOW BY GOVERNMENT SPONSOR (if other than DTRA): _____

SPONSORING ORGANIZATION: _____

CONTRACTING OFFICER or REPRESENTATIVE: _____

SIGNATURE: _____

CUT HERE AND RETURN

**DEFENSE THREAT REDUCTION AGENCY
ATTN: ADM
45045 AVIATION DRIVE
DULLES, VA 20166-7517**

**DEFENSE THREAT REDUCTION AGENCY
ATTN: ADM
6801 TELEGRAPH ROAD
ALEXANDRIA, VA 22310-3398**

REPORT DOCUMENTATION PAGE			Form Approved OMB No. 0704-0188
<p>Public reporting burden for this collection of information is estimated to average 1 hour per response, including the time for reviewing instructions, searching existing data sources, gathering and maintaining the data needed, and completing and reviewing the collection of information. Send comments regarding this burden estimate or any other aspect of this collection of information, including suggestions for reducing this burden, to Washington Headquarters Services, Directorate for Information Operations and Reports, 1215 Jefferson Davis Highway, Suite 1204, Arlington, VA 22202-4302, and to the Office of Management and Budget, Paperwork Reduction Project (0704-0188), Washington, DC 20503.</p>			
1. AGENCY USE ONLY (Leave Blank)	2. REPORT DATE	3. REPORT TYPE AND DATES COVERED	
	January 2000	Technical 07/94 – 03/98	
4. TITLE AND SUBTITLE		5. FUNDING NUMBERS	
Turbulent Mixing in Explosions		C - DNA 001-94-C-0015 PE - 62715H PR - AG TA - BE WU - DH00012	
6. AUTHORS			
Heinz Reichenbach and Peter Neuwald			
7. PERFORMING ORGANIZATION NAME(S) AND ADDRESS(ES)		8. PERFORMING ORGANIZATION REPORT NUMBER	
Ernst-Mach Institut — Fraunhofer Institut für Kurzzeitdynamik Eckerstr. 4 79104 Freiburg i. Br. Federal Republic of Germany			
9. SPONSORING / MONITORING AGENCY NAME(S) AND ADDRESS(ES)		10. SPONSORING / MONITORING AGENCY REPORT NUMBER	
Defense Threat Reduction Agency 45045 Aviation Drive Dulles, VA 20166-7517 SWET/Giltfrud		DSWA-TR-98-53	
11. SUPPLEMENTARY NOTES This work is sponsored by the Defense Threat Reduction Agency under RDT&E RMC code B 4662 D AG BE 00012 8010 A 25904D.			
12a. DISTRIBUTION / AVAILABILITY STATEMENT		12b. DISTRIBUTION CODE	
Approved for public release; distribution is unlimited.			
13. ABSTRACT (Maximum 200 words) The report focuses on an experimental investigation of the dynamics of turbulent flow-field features that arise from the detonation of a charge. The three main features covered are <ul style="list-style-type: none">▪ the detonation products cloud due to a freefield or 1-D confined, 2-D freefield detonation,▪ the (inert) products jet ejected from a detonation inside a chamber with an outlet opening and▪ an explosive-driven turbulent jet of combustible gas ejected from a small chamber into a wider one. The experiments were carried out at laboratory scale, employing Nitropenta (PETN) —charges of about 0.5 g. The main diagnostics were cinematographic high-speed shadow photography and pressure measurements. The main findings are that in the long-wavelength regime the spatial characteristics of the turbulent products cloud depend on the geometry (3-D freefield detonation ≠ 1-D-confined detonation). Experiments in the two-chamber system with a combustible jet showed that the turbulent mixing in an explosive-driven jet facilitates combustion, which results in an additional pressure increase. An estimate of the burning rate which is essentially governed by the amount of turbulent mixing can be inferred from the time-history of the average pressure in the system.			
14. SUBJECT TERMS			15. NUMBER OF PAGES
Freefield Detonation Confined Detonation	Turbulent Mixing Detonation Products Unsteady Jet	Combustion Burning Rate	Small-Scale Experiments Shadow Photography Pressure Measurements
			16. PRICE CODE
17. SECURITY CLASSIFICATION OF REPORT UNCLASSIFIED	18. SECURITY CLASSIFICATION OF THIS PAGE UNCLASSIFIED	19. SECURITY CLASSIFICATION OF ABSTRACT UNCLASSIFIED	20. LIMITATION OF ABSTRACT SAR

Summary

This report describes the essential part of investigations performed within the DSWA contract DNA 001-94-C-0015 "Turbulent mixing in explosions". The project has its base in small-scale laboratory experiments and high-speed photographic techniques were applied to give insight into a variety of flow phenomena. Three main aspects were explored, namely

The dynamics of the turbulent products cloud from an explosion of a spherical HE-charge. Small-scale Nitropenta charges in the weight range of approximately 0.5 g were used to simulate the spherical freefield detonation of a HE charge. Three different geometries were used: spherical charges in free air, hemispherical charges mounted on a rigid plate and hemicylindrical charges in narrow chamber facilitating 2-D expansion only.

The dynamics of unsteady jets. Main object of this study was the product jet that is ejected from a small chamber after a small-scale charge is detonated inside the room. Different geometrical configurations were investigated with respect to the question how the jet which is prone to instabilities develops. In addition, the influence of shock waves impinging on the jet was a part of the study, which was accompanied by shock tube test.

Laboratory simulation of afterburning effects. Considered here is combustion of an explosion-driven turbulent jet of combustible gas in the expansion chamber of a two-chamber system. The process is initiated in a small pre-chamber, filled with a combustible gas/air mixture, and provided with an explosive ignitor charge. The pre-chamber is connected to the main enclosure by a sealed orifice. Upon ignition of the explosive charge the seal is broken and a blast wave created that injects the fuel jet into the main enclosure which combust with air. The effects of turbulent mixing are monitored by high-speed photography and by the means of the pressure gain in the expansion chamber, which can be compared to corresponding numerical simulations.

Table of Contents

Section	Page
Summary	ii
Figures	v
Tables	xiii
1 Introduction	1
2 Basic Measurement Techniques	3
2.1 Time-Resolved Shadow-Photography	3
2.2 Single-Shot Shadow-Photography	4
2.3 Pressure Measurements	4
2.4 Charges	4
3 Simulation of a Spherical Detonation	6
3.1 Phenomenology of a Spherical Detonation	6
3.2 Laboratory Simulation	6
4 2-D Detonation Simulated by Means of Hemicylindrical Charges	11
4.1 Experimental Setup	11
4.2 Experimental Results	11
5 Unsteady Jets Created by a Detonation Inside a Chamber	15
5.1 Experimental Setup	15
5.2 Flow Visualization	15

Table of Contents (Continued)

Section		Page
6	Simulation of Afterburning in Turbulent Jets	20
6.1	Experimental Setup	20
6.2	Flow Visualization	21
6.3	Initial Data Analysis	22
6.4	Revised Strategy of Data Evaluation for the Combustion Experiments	24
7	Development Of A Small Bomb-Calorimeter	27
7.1	Design and Diagnostics	27
7.2	Experimental Results	28
8	Tables and Figures	32
9	References	148
	Distribution List	149

Figures

Figure		Page
1	Schematic sketch of the 24-spark Cranz-Schardin camera.	32
2	Schematic sketch of the single shot setup for shadow photography.	32
3	Manufacturing process of hemicylindrical charges.	33
4	Schematic wave diagram for the detonation of a spherical high-explosives (HE) charge (specifically for an unbalanced explosive like TNT).	34
5	Shadow photograph showing the detonation of a hemispherical NP-charge mounted on a transparent Makrolon pane. Charge weight $W = 0.45$ g, time after ignition $t = 0.2$ ms (Test 0822.MM).	35
6	Pseudo-color version of the shadowgraph from Figure 5. Grey values are mapped to a palette of colors in order to enhance flow features.	36
7	The shadowgraph from Figure 5 after some postprocessing including spatial low pass filtering, contrast stretching.	37
8	Pseudo-color version of Figure 7.	38
9	Shadow photograph (pseudo-color version) showing another experiment with a hemispherical NP-charge mounted on a transparent Makrolon pane. Charge weight $W = 0.64$ g, time after ignition $t = 0.2$ ms (Test 0826.MM).	39
10	Third example of an experiment with a hemispherical NP-charge mounted on a transparent Makrolon pane. Charge weight $W = 0.47$ g, time after ignition $t = 0.25$ ms (Test 0825.MM).	40
11	Sequence of shadowgraphs from Test 14756. Hemispherical charge on Makrolon plate. ($W = 0.64$ g).	41
12	Sequence of shadowgraphs from Test 14757. Hemispherical charge on Makrolon plate. ($W = 0.63$ g).	45
13	Sequence of shadowgraphs from Test 15086. Spherical charge in free air ($W = 0.49$ g).	49

Figures (Continued)

Figure		Page
14	Sequence of shadowgraphs from Test 15087. Spherical charge in free air ($W = 0.53$ g).	53
15	Scaled wave diagram for the detonation of a TNT-charge according to a 2-D AMR calculation [1].	57
16	Comparison of the experimental results for the primary blast front to the data from AIRBLAST.	57
17	Comparison of the experimental results for the secondary blast front to the results of the 2-D AMR calculation.	58
18	Fit based on the experimental data replacing the result of 2-D AMR calculation in the wave diagram.	58
19	Experimental data from Tests 15086 and 15087 compared to the wave diagram. Tests were performed with spherical charges in free air. Charge weight: 0.49 g (Test 15086) and 0.53 g (Test 15087).	59
20	Experimental data from single-shot tests compared to the wave-diagram. The shadowgraphs were analyzed for the apparent maximum and minimum radial extent of the products cloud visible within the field of view.	60
21	Polynomial fit of the data ensemble derived from the evaluation of single -shot experiments.	61
22	The average radial extent of the products cloud as derived from single-shot experiments compared to the results of the 2-D AMR calculation.	62
23	Example for the color-contour plots of the 3-D AMR calculation (courtesy A. L. Kuhl) used in the comparison to shadow photographs	63
24	Setup for the experiments with hemicylindrical charges.	64
25	Constructive details for mounting the hemicylindrical charges.	65
26	Sequence of shadow photographs from Test 14667. Hemicylindrical charge, length 10 mm.	66

Figures (Continued)

Figure		Page
27	Sequence of shadow photographs from Test 14937. Hemicylindrical charge, length 20-mm length.	67
28	Sequence of shadow photographs from Test 14991. Hemicylindrical charge, length 40-mm length.	68
29	Comparison of shadow photographs from 2-D experiments to a 3-D test	69
30	Wave diagram for the tests with hemicylindrical charges. Data are scaled with $(2W/l)^{1/2}$	70
31	Wave diagram 4-7 rescaled to match the wave diagram for 3-D experiments (for rescaling see Chapter 4.2.2).	70
32	Schematic sketch of the detonation chamber (versions C and D for free-field expansion).	71
33	Schematic sketch of the detonation chamber in the modified setup with Makrolon windows (versions A and B).	71
34	Shadow photograph of a detonating HX2-ignitor 0.25 ms after ignition.	72
35	Products cloud of HX2 2.45 ms after ignition. Detonator aligned with line of sight.	72
36	Products cloud 2.71 ms after ignition. Different test with the detonator aligned perpendicular to the line of sight.	73
37	Blast and products cloud from a detonation chamber. Cinematographic sequence of shadowgraphs. Charge: HX2, outlet from chamber 20 mm wide, expansion confined by Makrolon windows (Configuration A).	74
38	Comparison of two further tests for Configuration A approximately 1.1 ms after ignition.	78
39	Shadow photographs for a test in Configuration A (outlet width 20 mm, Makrolon windows).	79
40	Shadow photographs for a test in Configuration B (outlet width 10 mm, Makrolon windows).	80

Figures (Continued)

Figure		Page
41	Shadow photographs for a test in Configuration C (outlet width 20 mm, free expansion).	81
42	Shadow photographs for a test in Configuration D (outlet width 10 mm, free expansion).	82
43	Modification of the detonation chamber setup version A .	83
44	Pressure-time history at the reflector.	84
45	Shadow photograph of the products cloud in the closed expansion chamber (Test 15261/11) at $t = 1.07$ ms.	85
46	Interaction of the first reflected blast front with the products cloud at $t = 1.15$ ms. (Test 15261/12).	86
47	Further development of the products cloud at $t = 1.23$ ms. (Test 15261/13).	87
48	Schematic sketch of a setup for shock tube experiments on a shock impinging onto a turbulent flow field.	88
49	Shock tube experiment Test 15283/6. Reflected shock shortly before impinging on artificially generated turbulent flow ($t = -20$ μ s).	89
50	Postprocessed version of Figure 49. The brightness of the area to the right hand of the turbulent border was increased to give more contrast to the borderline.	89
51	Influence of the reflected shock on the turbulent flowfield at $t = 50$ μ s (Test 15283/7).	90
52	Influence of the reflected shock on the turbulent flowfield at $t = 120$ μ s (Test 15283/8).	90
53	Influence of the reflected shock on the turbulent flowfield at $t = 300$ μ s (Test 15283/11).	91
54	Influence of the reflected shock on the turbulent flowfield at $t = 600$ μ s (Test 15283/7).	91
55	Influence of the reflected shock on the turbulent flowfield at $t = 800$ μ s (Test 15283/18).	92

Figures (Continued)

Figure		Page
56	Unprocessed version of Figure 55 in comparison.	92
57	Schematic of the test chamber for experiments on combustion in turbulent jets.	93
58	Photograph of the test setup. Front cover of detonation chamber removed.	94
59	Shadow photograph from the reference Test 006/15336 at t = 0.515 ms.	95
60	Shadow photograph from Test 0020/15350 at t = 0.32 ms	96
61	Shadow photograph from Test 0020/15350 at t = 2ms.	96
62	Output of the photodiode monitoring the expansion chamber. Charge detonates at t= 0.	97
63	Output of the photodiode for a test with retarded reaction (Test 016).	97
64	Test 7: 900 mbar C ₂ H ₂	100
65	Test 11: 900 mbar C ₂ H ₂	101
66	Test 13: 900 mbar C ₂ H ₂	102
67	Test 14: 840 mbar C ₂ H ₂	103
68	Test 16: 800 mbar C ₂ H ₂	104
69	Test 17: 815 mbar C ₂ H ₂	105
70	Test 20: 500 mbar C ₂ H ₂	106
71	Test 21: 500 mbar C ₂ H ₂	107
72	Test 26: 500 mbar C ₂ H ₂	108
73	Test 27: 500 mbar C ₂ H ₂	109
74	Test 28: 500 mbar C ₂ H ₂	110

Figures (Continued)

Figure		Page
75	Test 29: 500 mbar C ₂ H ₂	112
76	Test 33: 400 mbar C ₂ H ₂	113
77	Test 34: 400 mbar C ₂ H ₂	114
78	Test 35: 400 mbar C ₂ H ₂	115
79	Test 36: 400 mbar C ₂ H ₂	116
80	Test 37: 600 mbar C ₂ H ₂ + (1O ₂ + 2N ₂)	117
81	Test 38: 600 mbar C ₂ H ₂ + (1O ₂ + 2N ₂)	118
82	Test 40: 700 mbar C ₂ H ₂ + (1O ₂ + 2N ₂)	119
83	Test 41: 700 mbar C ₂ H ₂ + (1O ₂ + 2N ₂)	120
84	Test 43: 700 mbar C ₂ H ₂ + (1O ₂ + 1N ₂)	121
85	Test 44: 700 mbar C ₂ H ₂ + (1O ₂ + 1N ₂)	122
86	Test 45: 700 mbar C ₂ H ₂ + (1O ₂ + 1N ₂)	123
87	Test 46: 700 mbar C ₂ H ₂ + (1O ₂ + 1N ₂)	124
88	Test 47: 700 mbar C ₂ H ₂ + (1O ₂ + 1N ₂)	125
89	Test 48: 700 mbar C ₂ H ₂ + (1O ₂ + 1N ₂)	126
90	Test 72: 150 mbar CH ₄	128
91	Test 73: 250 mbar CH ₄	129
92	Test 74: 375 mbar CH ₄	130
93	Test 80: 380 mbar CH ₄	131
94	Test 85: 250 mbar CH ₄	132
95	Test 86: 250 mbar CH ₄	133

Figures (Continued)

Figure		Page
96	Test 87: 250 mbar CH ₄	134
97	Experimentally obtained excess pressure values for the aceytelene experiments.	135
98	Fit parameters [a log t/t ₀] for the acetylene experiments.	135
99	Result of a preliminary Cartesian-Grid AMR simulation of XY combustion jet; visualization of the oxidizer region at t=1.5 ms (courtesy Allen Kuhl).	136
100	Original pressure-time history of the reference test and sliding average	137
101	Reference signal used for the modified evaluation modus.	137
102	Test 11 (900 mbar acetylene in 32 cm ³ prechamber): pressure difference and fit curve.	138
103	Test 11: grey: original pressure difference, blue: result of sliding average, red: result of power series fit.	138
104	Summary of the results for the experiments acetylene in the 32 cm ³ prechamber.	139
105	Time derivative of the above tests.	139
106	Comparison to an approximation with Vibe-functions.	140
107	Corresponding comparison for the time derivatives.	140
108	Summarizing the result for the acetylene tests.	141
109	Summarizing the results for the methane tests.	141
110	Definition of the parameters t ₀ , t ₁ , and Δp _{max} .	142
111	Non-dimensional plots of the pressurization for all tests.	142
112	Summary of parameters t ₀ , t ₁ , and Δp _{max} .	143
113	Schematic of the custom-designed small bomb calorimeter.	144

Figures (Continued)

Figure		Page
114	Decrease of overtemperature in the calorimeter for Test 06 (0.25 g NP in air)	145
115	Overttemperature at the outside of the calorimeter jacket Test 06 (0.25 g NP in air).	145
116	Semilogarithmic plot of the difference of the jacket temperature to the ambient temperature.	146
117	Semilogarithmic plot of the difference of the jacket temperature to the final temperature.	146
118	Energy released by the detonation of Nitropenta charges in air (test setup: single chamber, Tests 04.KM – 17.KM).	147

Tables

Table	Page
1 Results for the HX2-detonator (at $T \approx 26^\circ\text{C}$, $p_0 \approx 990$ mbar).	29
2 Summary of setup variations.	94
3 Data of acetylene, C_2H_2 .	98
4 Data of methane, CH_4 .	98
5 Summary of the measurements with acetylene in the 32 cm^3 detonation chamber.	99
6 Summary of the experiments with acetylene in the 72 cm^3 detonation chamber.	111
7 Summary of the experiments with methane in the 72 cm^3 detonation chamber.	127

Section 1

Introduction

The main objective of this research program was to study the fluid-dynamic aspects of turbulent mixing in a limited number of common explosion geometries by means of laboratory experiments. The focus on the mixing processes is motivated by their fundamental role in relevant topics connected to chemical explosions, such as *turbulent combustion and afterburning* induced by explosions, especially by unbalanced or fuel-air explosives, *the formation and transport of hazardous plumes* (collateral effects in explosion events, distribution of biological or chemical material) and the *turbulent combustion in guns*.

The statement of work included four tasks:

- Task 1
The study of explosion dynamics in the case of unconfined 3-D propagation with spherical or hemispherical small-scale Nitropenta charges,
- Task 2
an analogous study in the case of hemicylindrical charges where the propagation is confined to the narrow space between two parallel plates, which was expected to be a kind of a 2-D version of Task 1,
- Task 3
the study of non-steady turbulent jets, which are one of the fundamental phenomena in the studies mentioned above,
- Task 4
application experiments, which were to be determined during the contracting period according to the needs of DSWA.

The work for all tasks focussed on the use of flow visualization to give insight into the dynamics relevant to turbulent mixing and to provide a data base for the validation of numerical models. Both the experimental and the numerical approach to unsteady turbulence have inherent limitations. For hydrocode calculations it is doubtful to what extent existing turbulence models apply to the highly unsteady dynamics of explosion fields. Thus it is difficult to rate the reliability of results when a combustion model is implemented into these codes. Discrepancies to experimental results might be due to an inadequate turbulence model, an inadequate combustion model, and/or an inadequate coupling of both turbulent mixing and combustion. Therefore simulations alone cannot reveal the fundamental mechanisms that control the exothermic process of combustion. The experimental approach though facilitates the measurement of a rather narrow set of flow variables only. Further limitations exist: the measurable flow variables do not necessarily coincide with those in which turbulent dynamics is preferably discussed, e.g., vorticity or kinetic turbulent energy. And the number of samples is limited in space (e.g., single point measurements) and/or in time (e.g., due to limits to framing rates of high-speed camera systems). An additional complexity is due to the random nature of

turbulence, which causes large statistical ensembles to be necessary to derive conclusive information. This is a fallback especially for full-scale tests, since the expense in time and money prohibits a sufficiently large number of test repetitions to give statistically meaningful results. Whereas these can be gathered by means of long-time monitoring of the flow in the case of steady or quasi-steady turbulence, test repetition (and accurate reproducibility) is essential in the unsteady case. Multiple tests are more easily done on a small-scale base as in our laboratory experiments, though the number of experiments feasible here might still be small in terms of statistical confidence.

Thus neither the numerical simulation nor the experiment alone can give new insights into the problem of turbulent mixing. A joint effort is necessary with a strong feedback from both sides to find a common basis (i.e., comparable output from both the experiment and the calculation) for comparison and to design experiments which allow to validate numerical calculations. This process causes a need for revising experimental strategies as well as the reformulation of numerical test runs, which is reflected in the exploratory research program described here.

Section 2

Basic Measurement Techniques

Based on the line of thought described in the introduction the optimum experiment would yield quantitative data at a high time-resolution simultaneously everywhere in the interesting regions of the flow field. This optimum is nearly not feasible at the current state of measurement techniques (in some sense it might be at a very high expense for very setup-specific experimental equipment). Thus we decided that the second best is to exploit flow visualization which at least presents the whole flow field with good spatial resolution and in the case of a quasi-cinematographic study also yields some time-resolved information on the development of flow features. Though less quantitative than for example a pressure record, flow visualization can generate valuable material for the comparison to numerical results.

2.1 Time-Resolved Shadow-Photography.

The basic setup of the Cranz-Schardin camera is shown in Figure 1. The camera attained a cinematographic sequence of shadow photographs by the means of 24 sparks which are triggered individually in a pre-determined time sequence. In correspondence to the array of 6×4 the imaging part of the camera consists of an array of 6×4 lenses. The divergent light from each spark is focussed onto the corresponding lens by the means of a spherical mirror. Mirror size and the divergence of the light bundle restrict the maximum field of view to a diameter of approximately 22.5 cm. Since the mirror folds back the light path we have an upper, divergent light path above a lower convergent light path. Test objects are normally placed in the lower path but if they are large it can happen that they extend into the upper path, especially in the region where both paths overlap. This can cause spurious effects on the shadow photographs, the object creates a shadow effect in the upper path which is depicted as if it was located in the lower path. The same holds true when the test objects are open and shock waves enter the region of the upper path.

Another effect that should be noted is that of the light path convergence. It is not relevant for objects with a narrow depth. If the object depth gets large, the magnification with which the rear side is projected onto the reference plane (and depicted on the negative) is different from the magnification of its front side. For an object depth of 50 cm this difference is about 9 % and has to be taken into consideration.

This shadowgraphy setup was originally developed for phenomena without any self-luminosity. Since the focus was put on very short exposure times – which cannot be attained with mechanical shutter systems – the camera is operated in an open shutter technique with the lab darkened during the experiment. The exposure time for the background illumination is thus decided by the spark duration. If there is some self-luminous region within the field of view it exposes the negative for some seconds in the worst case or typically for those few milliseconds that the luminosity exists. This part of the exposure reveals no time-resolved information. The contribution to exposure due to self-luminescence is kept small, since the luminous field radiates into the complete

sphere and the lenses of camera receive light only from a small solid angle. The receipt efficiency for the deliberate background is much larger, but nevertheless sometimes overexposure due to the luminescence can occur.

2.2 Single-Shot Shadow-Photography.

The setup for single-shot shadow photographs uses two spherical mirrors in a z-type arrangement (see Figure 2). The field of view has a diameter of approximately 60 cm and the background illumination is by a parallel light bundle. Effects like the spurious pictures of objects due to the backfolding of the light path are avoided. Since the mode of operation is the same, the effects of self-luminous areas within the field of view are essentially the same as in the Cranz-Schardin camera.

2.3 Pressure Measurements.

In addition to high-speed photography we always perform pressure measurements when feasible. Our choice for pressure gages are piezo-electric ones from Kistler, type 603B connected to Kistler charge amplifiers type 5001. The amplifier output is fed into a transient recorder system (up to now LeCroy type T.R. 8837 F) which operates a maximum of 16 channels simultaneously. The data are sampled at rates up to 20 MHz per channel into on-board memory with 8k words per channel and is copied to disk after the experiment. The signal rise-time is limited by the low-pass filter in the charge amplifiers which has a cut-off frequency of 380 kHz. The maximum rise-time for the signals is thus about 2 μ s.

During the current study we have also applied piezo-resistive pressure transducer to monitor quasi-steady pressures and thermocouples as well as thermo-resistors (e.g. PT100) to measure the temperature of gases and model walls.

2.4 Charges.

In order to resume some facts about our spherical small-scale HE-charges: they essentially consist of very fine grained Nitropenta powder (pentaerythritol tetranitrate $C_5H_8N_4O_{12}$, PETN). The powder is dissolved in acetone with a small volume percentage of gun-cotton admixed so that it forms a highly viscous paste. Two electrodes connected by a fine wire are fixed in a centered holder that is repeatedly dipped into the paste. By the repetitive dipping and drying a droplet of the explosive is grown around the central wire. When the droplet size is sufficient, an ideal spherical charge can be turned on a lathe before the holder is removed. The finished charge has a diameter of 10 mm. From previous tests the TNT equivalent value of these spherical charges was determined to be approximately 1.2. The charges can be quite reliably ignited by applying a high voltage discharge (in the order of 8 to 10 kV) to the electrodes which vaporizes the central ignition wire thus driving the detonation of the Nitropenta charge.

For the current study new type of small-scale charges had to be developed: hemispherical charges and hemicylindrical charges. These were assembled on special holders from Makrolon. The hemicylindrical charges with 10 mm length, for example, were manufactured as outlined in the following paragraph (refer also to Figure 3).

An axial hole is bored into a cylinder of Makrolon ($r = 5$ mm, $l = 20$ mm). Then a hemicylindrical part ($r = 5$ mm, $l = 10$ mm) is cut out in the middle of the cylinder and the bore hole in this region is notched. An ignition wire is inserted through the bore hole and connected to supply wires. The notch around the ignition wire is filled with about 10 mg pure, fine-grained Nitropenta powder. Then a hemicylindrical Nitropenta charge, casted in a mould, is glued into the cut-out.

Both the hemispherical and the hemicylindrical charges are not as reliable as the corresponding full-body charges, since the ignition wire is not embedded in Nitropenta. For some samples the contact between the ignition wire and the surrounding Nitropenta seemed insufficient and the wire explosion did not initiate the detonation of the charge, only caused its fragmentation. This problem increased with decreasing radius and increasing length of the hemicylindrical charges.

For part of the experiments we also used a commercially available charge with a weight in the order of 40 mg. This charge which comes under the tradename HX2 is described in Section 5 and Section 6.

Section 3

Simulation of a Spherical Detonation

3.1 Phenomenology of a Spherical Detonation.

At the set-off of the study the problem under consideration was the turbulent mixing in the fireball, created by the detonation of a spherical high-explosives (HE) charge. The fireball gases expand at a high velocity, which drives a strong blast wave in the surrounding atmosphere. The detonation products of solid explosives charge are typically quite dense compared to the shock-compressed air, hence the density ratio across the interface is rather large. Such density interfaces are unstable against a variety of instability mechanisms, which cause small initial perturbations to grow rapidly into a turbulent mixing region. Figure 4 shows a typical schematic wave diagram for this type of detonation. Salient features are the primary blast wave that separates after some time from the detonation products which decelerate much faster. It is followed by a secondary shock. This front originally propagates outwards, after some time though it reverses its propagation direction towards the detonation center, thus initiating an implosion phase. Having reached the center the secondary front is again reflected outwards, thus interacting with the fireball interface and reshocking it. The secondary shock is presumably in part again reflected at the interface, thus setting up another, but weaker cycle of the same wave processes until their influence on the mixing decreases and an asymptotic mixing phase is reached.

3.2 Laboratory simulation.

3.2.1 Flow Visualization.

The most direct way to simulate this type of detonation in laboratory scale is to ignite a spherical small-scale charge in free air, fixed in position by its ignition wires only. In the beginning of the study we refrained from this kind of test due to safety aspects, since any hazard for lab personnel and equipment was to be excluded. The first experiments thus were carried out in the blast wave tank of our lab, a steel chamber of 120 cm x 120 cm and 60 cm in height. Optical access is gained by means of two optical windows 20 cm x 69 cm in size. This blast chamber was positioned in the optical path of the single-shot shadow-photography setup, due to its large dimensions 24-spark cinematography was impossible. During the initial phase our confidence grew that tests outside this chamber were feasible, provided that a number of (less strict) safety precautions were taken. The first concept was to assemble a steel holder with a hemispherical charge into a 10-mm thick transparent Makrolon pane which could be put upright into the optical path of the 24-spark camera. This setup narrowed the dimension of the detonation product cloud by a factor of two with respect to the visualization direction. Since the shadowgraph technique integrates over all density effects along the optical path-length through the 3-dimensional cloud, such setup can help to get a better view into the inside of the fireball. Shielding the most vulnerable part of the optics, the mirror, by means of a glass pane of sufficient quality finally made it also feasible to perform free-

field test with spherical charges of up to 0.5 g in weight in the 24-spark camera setup . Figures 5 to 14 show a few examples from the three different types of experiments

In Figure 5 we see the detonation of a hemispherical charge mounted on a Makrolon pane. The charge weight for this test was $W = 0.45 \text{ g}$ and the test was performed in the blast tank. In the center of the picture the core region around the detonating charge is overexposed. The hot detonation products are self-luminous and a certain amount of the light is radiated into the aperture of the visualization optics. This light is time-integrated over the whole experimental time frame. Thus no specific instance can be attributed to this structure since we apply an open shutter technique. This effect can not be totally suppressed, but is at least an order of magnitude less than in conventional photography used in freefield tests where about the complete area shown in the shadowgraph would be opaque.

The other visible structures are due to the shadowgraph technique and caused by density variations afflicting the background illumination. This illumination is generated by means of a 300-ns spark fired 0.2 ms after the detonation. The first blast front which is has just reached the roof of the blast tank is quite prominent in the picture. It is essentially spherical, but we can see a number of precursing jets which are probably due to small grains of Nitropenta ejected from the charge. These jets are not necessarily propagating in the plane of the picture; since the shadow effects are integrated through the whole 3-D volume afflicted by the detonation they might as well have an out-of-plane component of propagation directed towards the observer. The area behind this first blast front is not free from disturbances, the jets can create their own turbulent wakes. In addition, the optical quality of the Makrolon pane adds some noise to the photograph. Nevertheless we find some cauliflower-like cloud within the sphere covered by the blast front. This cloud is signified by stronger differences in the grey values and an overall darker appearance. We tend to identify this cloud as a representation of the detonation products cloud.

Half way between the first blast front and the center of detonation we find another spherical structure, the secondary blast wave, here accompanied by a third pressure wave.

Since the most interesting part is the detonation products cloud we tried a few concepts to enhance the contrast of its features. Figure 6 to 8 show a few examples for the test shown in Figure 5. The first one, Figure 6, just converts the grey values of the original pixels into a color scheme. Though both Figures are essentially identical, subjectively a better contrast of the turbulent plumes can be gained. The second one, Figure 7, is based on a more complex sequence of procedures. These include low pass filtering of the original pictures (blurring), stretching of the grey value range in the picture, arithmetic addition of the processed picture to the original, a technique which can give additional contrast to the borderline of the products cloud, but obscures the smallest scales of disturbances visible in the original. Figure 8 finally is again a pseudo-color version of Figure 7. The major fallback of these post-processing techniques is that it is difficult to apply them automatically, since each photograph of a test series has different characteristics. Figure 8, the shadowgraph from another detonation experiment in pseudo-color representation is comparable to Figure 6 in contrast, whereas one gains less contrast by this method in Figure 10.

Figure 9 shows again the instance 0.2 ms after the detonation, but the charge weight in this case was 0.64 g. Thus the blast front has proceeded a bit further. At the same time it has not separated as much from the products cloud as in Figure 6. The higher charge weight is also reflected in the larger area of overexposure around the detonating charge.

Figure 10 is again a test with a smaller charge weight of 0.47 g, but at a later time of 0.25 ms. Here the secondary blast front is not as pronounced as in Figure 9, it appears to be more afflicted by the turbulent field in the products cloud.

The three examples already show the kind of scatter to be found in the comparison of different tests. It is due to the random nature of initial perturbations which for example arise from the unburned grains of Nitropenta ejected during the detonation. The main advantage of these single-shot photographs is the comparatively large field of view which allows to look at the whole products cloud and rate the non-uniformity of its boundary.

Figures 11 and 12 originate from tests outside the blast tank. Again the test were performed with hemispherical charges mounted on a Makrolon pane. For these tests the experiments were set up in the optical path of the 24-spark camera. Thus the field of view is more limited for the sake of time-resolved information of the blast propagation and the growth of the products cloud. In addition, the reference plane for shadowgraphy was set to quite large distances from the plane of detonations, which gives more sensitivity for the density effects. Thus blast fronts appear broader than in the previous photographs, but we have a gain in the contrast with which the features of the products cloud are depicted. Again we find a number of precursing bow waves from small particles and for short times it is quite obvious that part of them are directed out of the plane of the photographs.

Figures 13 and 14 show tests with spherical Nitropenta charge in free air. The first blast front in both cases is clearly visible as well as the secondary shock which appears at $t = 0.341$ ms in Figure 13 and at $t = 0.220$ ms in Figure 14. The products cloud is also depicted with good contrast. Care has to be taken with a third strong shock line that shows up at $t = 0.941$ ms at the bottom of the picture in Figure 13. This is an artifact due to the fact that the primary shock front has entered the upper part of the folded light path of the 24-spark arrangement. The same effect leads to a spurious shock line in Figure 14 first showing up at $t = 0.901$ ms. In Figure 14 this line appears to be much thicker since different reference planes were chosen for the both tests.

3.2.2 Analysis.

The concept to analyze our experimental data was to derive data material for the comparison to the wave diagram shown qualitatively in Figure 4. This wave diagram is again shown in Figure 15, but more quantitatively based on a 2-D AMR calculation[1]. The diagram presents the radial location of a flow feature versus the time after detonation. Both time and radius are scaled with the cube root of the charge weight.

From our photographs the location of the primary blast front at different time instances is most easily derived. Figure 16 summarizes a number of results for both hemispherical

and spherical charges. The data scatter is comparatively small and the resulting curve is in good agreement with a data set derived from the Airblast code [2].

The next salient feature is that of the secondary blast front. The experimental result are shown in Figure 17. They are in agreement with the curve derived from the 2-D AMR calculation, even a number of data points during the implosion phase could be found. A fit function through the experimental data points (see Figure 18) will replace the result of the calculation in the following.

The crucial part of the comparison is the boundary of the products cloud. The numerical results are given in form of the radius where a given average concentration of fuel can be found. Figure 19 displays two such iso-contour lines. There is no experimental equivalence that represent the fuel concentration since the photographs only display density effects. In the previous section it was outlined which features – in our interpretation – define the product cloud. We can pick out features on our cinematographic photographs and derive scaled time-distance curves for these. An example is shown in Figure 19, which relates to Figures 13 and 14. The analyzed structures were the central plume in test 15086 and the central plume and the one left to it in test 15087 and, in addition the pocket in-between them. It appears that the plumes (i.e., the heads of the cauliflower structures) are initially immediately behind the primary blast front. At a certain radius they start to separate and decelerate which is in general agreement with the phenomenology seen in the 2-D AMR calculation. The location where this happens differs quite a lot from plume to plume and no direct correspondence to the averaged values of the fuel concentration is obvious. The comparison of the central plume and the pocket of test 15087 shows that there can be large variations in the local radius of the product cloud, here ranging from $1.9 \text{ m/kg}^{1/3}$ to $3.2 \text{ m/kg}^{1/3}$ in the final state.

Another plot of essentially the same kind is shown in Figure 20. Here the results of a number of single-shot experiments are summarized. Green symbols denote the values for the apparent minimum radius of the cloud found in the photographs, red symbols those for the maximum extension of the cloud. Considerable scatter can be found for these data points but they are not extending to such large values of the radius as in Figure 19. The reason for this can probably be seen in the two different optical setups. Both setups differ with respect to the sensitivity and detectability. In the tests with the 24-spark setup we increased the sensitivity considerably, thus already smaller density effects (or thinner layers of comparable density effects) can give contrast in the photographs.

In order to analyze a self-consistent data ensemble we thus evaluated the single-shot experiments separately, since these photographs are obtained at a more or less constant sensitivity. By means of a fit function we derived some kind of average value for the boundary location of the products cloud. The fit function is shown in Figure 21 together with the bandwidth (in grey) which contains essentially all the data points measured. The value of this bandwidth is about $\pm 0.5 \text{ m/kg}^{1/3}$.

In Figure 22 this average "cloud radius" – along with the bandwidth – is inserted into the wave diagram. Here it shows some degree of correspondence to the contour line $c = 0.1$ of the fuel concentration in the numerical calculations. Though encouraging, this correspondence should not be over-interpreted, since a smaller threshold of de-

tectability can shift the actual values for the "cloud radius" to the right, as indicated in Figure 19.

Included into Figure 22 is an attempt to analyze colored contour plots from a 3-D AMR calculation (an example is shown in Figure 23) analogous to our shadow photographs, i.e., to find the minimum and maximum value of the cloud extent. Three points have to be taken into account in rating the comparison. The plots again depicted the fuel concentration, not density changes. The concentration was depicted in a specific color scheme. It is thus rather subjective which concentration level generates the largest color contrast, i.e., which features are most salient to the eye. (This problem is quite similar to that of different sensitivities in our photographs). In addition, the numerical results present a real 2-D plane cut from the 3-D field. Thus it is possible to find deep pockets. In contrast, in our photographs the whole 3-D field is projected onto a plane, which can easily obscure the real depth of pockets. In effect, such a direct comparison of numerical to experimental results is only feasible and conclusive when it is based on artificial shadowgraphs which are generated from the numerical results and mimic the experimental situation sufficiently well.

In summary, the experimental results are in good agreement to the numerical simulation with respect to the blast front propagation and at least in qualitative agreement with respect to the average growth of the products cloud. The variety of cloud formations is rather widespread and even a data ensemble derived from more than 40 tests shows a considerable scatter due to the turbulence and its sensitivity to the initial perturbations. Thus only a larger statistical ensemble can yield improved accuracy. Complete analysis of the photographic material then requires a computerized, at least semi-automatical detection of the cloud boundary which might prove to be a demanding problem for even highly specialized image processing systems. In addition, a numerical equivalent to the photographic material is necessary for comparison.

Section 4

2-D Detonation Simulated by Means of Hemicylindrical Charges

Parallel to those experiments with hemispherical and spherical charges outlined in Section 3 we performed a study on the detonation of hemicylindrical charges confined in the narrow gap between two parallel walls. The study was motivated by the expectation that such a model could serve as a 2-D representation of the detonation dynamics seen in the previous section.

4.1 Experimental Setup.

During the planning phase of the research program we already expected a certain ambiguity of the photographs from 3-D experiments due to the large optical depth of the turbulent clouds. The concept arose that the anticipated problems might be resolved when the detonation field only propagates within one plane and is confined in the depth. In order to yield a valid 2-D equivalent the hemispherical charges of the 3-D tests had to be replaced by hemicylindrical charges and the length of the cylinder had to correspond to the width of the confinement. Thus a narrow test chamber was developed – and more than once modified during the study – which is depicted in Figure 24. It essentially consists of two 10-mm thick Makrolon panes to facilitate optical access. A number of fixtures keep them parallel and adjust the gap between them to the length of the cylindrical charge. Three sides of the model remain open, thus the blast wave can escape the test chamber. This keeps the load on the windows smaller than for a completely closed chamber. A steel rail forms the bottom of the model. The charge is inserted by means of a holder (constructive details shown in Figure 25) which guarantees the correct position of the charge and maximum air-tightness around the ignition wire and provides electrical and mechanical decoupling of the charge assembly from the rest of the model. The bottom of the model was equipped with piezo-electric pressure transducers, their connection plugs show up in the photograph of Figure 24 and give an idea of their locations.

Three different versions of the test chamber were assembled, the main difference being the depth of the air gap. Starting with 1 cm we changed to 2 cm and finally 4 cm, and for every setup hemicylindrical charges of the corresponding length were developed. The variation was necessary to enlarge the parameter range of scaled distances that could be covered by the setup.

4.2 Experimental Results.

4.2.1 Flow Visualization.

Figures 26, 27 and 28 show representative sequences of shadowgraphs from the tests in the 1-cm wide, the 2-cm wide and the 4 cm-wide setup. The sequences show that the tests did not exactly fulfil our expectations of easier interpretation. Though a strong front appears which we can identify as the primary blast front it is accompanied by a set

of further circular fronts in its immediate vicinity. A possible reason is that the model is not completely non-responding to the detonation of the charge. It may cause waves inside the Makrolon windows which also will be visualized and can easily be misinterpreted as shock waves in the gas phase. The distinction between both is not a simple task since the speed of sound in the Makrolon (≈ 1450 m/s) is in the same order of magnitude as the propagation speed of the blast fronts in the observed region. In addition, any tilt or stress in the windows can alter the visual appearance of the blast fronts from dark to bright and this – in conjunction with the different parallaxes of each light path – can occur from frame to frame of a shadowgraph series. After the initial tests with the setup we thus splitted the windows horizontally and tried to decouple the upper part within the field of view of the Cranz-Schardin camera from the bottom part by means of a shock-insulating fixture. This insulation proved to be only partially helpful; it could not reduce the waves in the Makrolon completely.

The identification of the products cloud posed a more difficult problem. In the 3-D experiments we found some quite distinct difference in the appearance of the cloud and the region between it and the primary shock. From test to test the shape of the cloud showed large differences, but not the criteria by which to identify it. In the shadowgraphs of the 2-D experiments the border of the products cloud was less obvious, the primary blast front is – often, but not always – very soon followed by a narrow band with fine-grained turbulent structures. Then a band with little granulation (see for example Figure 28) can be found, again followed by a more turbulent area. In Figure 28 there is even another area marked out where there is a texture change in the turbulent area. Whereas it appears to have no predominant directivity in the latter region, the texture in the first two turbulent bands is a sort of striation in mostly radial direction. The reason for these bands is probably due to boundary layer effects which can play some important role in the narrow 2-D setups. But these effects do not reproduce themselves from test to test; in Figure 27 for example only a single homogeneous area of turbulent structures can be found. It is thus not easy to differentiate between boundary layer effects and the actual turbulence in the products cloud. Furthermore, instabilities on the border of the products cloud do not show the phenomenology we have encountered in the 3-D experiments. All turbulent structures appear to be nearly spherical with rather short-scale disturbances of small amplitude, whereas we can find deep pockets and large extending plumes in the 3-D case. We thus have to suspect that the 2-D setup has at least a strong influence on the preferred wavelengths in the turbulence or that even boundary layer turbulence might be more dominant than other instability mechanisms. Nevertheless we tried to analyze the data material obtained in the 2-D tests. Before the results are shown a few remarks on scaling are necessary.

4.2.2 Some Considerations on Scaling.

The comparison between different experiments in the case of 3-D spherical explosions is quite straightforward and attained by means of applying a scaling of length and time with the cube root of the charge weight W . Essentially – though somewhat obscured – this scaling is based on a similarity analysis. The rigid application would be to normalize all lengths with a characteristic length, here the charge diameter, and the time with a characteristic time, derived as the quotient of a characteristic velocity (e. g., the sound speed in the ambient air) and the chosen characteristic length. This way one would end

up with dimensionless quantities. But customarily the characteristic length is replaced by the cube root of the charge weight, which is proportional to the charge radius and the characteristic velocity, the sound speed, is left out of the scaling since the ambient atmosphere is assumed to be near to standard conditions.

This scaling cannot be applied to the 2-D detonations quite that straightforward, but it can be easily modified to cope with them. Instead of a rigid analysis we will use the following plausibility argument.

In the case of a spherical explosions the detonation energy of the charge is contained in a volume $V_0 = 4/3 \pi R_0^3$ previous to the ignition. After the ignition this volume rapidly increases to $V_{3D}(t) = 4/3 \pi r_{3D}^3$. In different experiments we have equivalent situations when the instantaneous volumes are equivalent. The same holds true for the situation of a hemispherical charge at zero height of burst, but the actual charge weight has to be doubled to take into account the mirror source due to the completely reflecting surface.

In the case of our 2-D setup the initial volume of the charge is $V_0 = \pi R_0^2 l$, where l denotes the length of the hemicylinder and the width of the setup. Expansion is restricted to two dimension, thus the volume increases with the square of the radius to values $V_{2D}(t) = \pi r_{2D}^2 l$. An equivalent to the $W^{1/3}$ -scaling in the 3-D case is thus a scale factor of $(W/l)^{1/2}$ for cylindrical charges, respectively $(2W/l)^{1/2}$ for the hemicylindrical charges on the completely reflective bottom of the setup. This scaling is applied to both time and length since the sound velocity is not changed by the geometry of the setup. The dimension of the scaling factor in the 2-D case thus comes out as $[kg/m]^{1/2}$ and differs from that of the 3-D case which is $[kg]^{1/3}$.

A comparison of the instantaneous volumes $V_{3D}(t)$ and $V_{2D}(t')$ shows how scaled data from 3-D experiments can be transferred to the 2-D scale and vice versa. The situations are equivalent when

$$V_{3D}(t) = V_{2D}(t') \quad (1)$$

or

$$4/3 \pi r_{3D}^3 = \pi r_{2D}^2 l \quad (2)$$

Inserting the scaled radii

$$z_{3D} = r_{3D} / W^{1/3} \text{ and } z_{2D} = r_{2D} / (W/l)^{1/2} \quad (3)$$

yields

$$z_{3D} = (3/4)^{1/3} z_{2D}^{2/3} \quad (4)$$

or

$$z_{3D} / z_{2D} = (3/4)^{1/3} z_{2D}^{-1/3} \quad (5)$$

the factor that maps 2-D results to the 3-D representation. Since the scales for lengths and times are identical, the same factor has to be applied for the rescaling of the corresponding time. Conversion from 3-D results to the 2-D representation yields a rescaling factor of

$$z_{2D} / z_{3D} = (4/3)^{1/2} z_{3D}^{1/2} \quad (6)$$

This compares a test with a spherical charge to one with a cylindrical charge confined between two parallel planes. The same factors hold true for hemicylindrical charges with semi-infinite expansion (or hemispherical charges), if the data are scaled with the doubled actual charge weight $(2W/l)^{1/2}$ (or $(2W)^{1/3}$ in case of the hemispheres) to take into account the effect of the mirror source.

4.2.3 Data Analysis.

In correspondence to the 3-D experiments Figure 30 shows a wave diagram for the 2-D experiments with hemicylindrical charges. Included are data points from all three setup widths, obtained from the photo material as well as from the pressure records of the gages at the bottom of the model. The data are scaled with the doubled actual charge weight. The general phenomenology follows that seen in the 3-D tests though we were not able to gather data of the secondary shock during the implosion phase. Considerable scatter for small values of r is found for the secondary shock. These data originate from the pressure records at the bottom of the model and thus might be afflicted by a turbulent boundary layer through which the secondary shock has to propagate. The data for the products cloud are derived from test 14937, the only test where just one turbulent border line can be found. For the other tests the identification was too ambiguous as pointed out in Chapter 4.2.1. In order to compare these data to the data from the 3-D tests Section 3 we applied the rescaling outlined in the previous chapter. The result is shown in Figure 31. It appears that the primary blast front propagates more slowly than expected. The data for the secondary shock and the limited data for the products cloud are in qualitative, but not decisive agreement with our results from the 3-D experiments. The experimental evidence from the shadow photographs indicates that the detonation couples into the walls of the model, i.e., that we do not have the situation of non-responding walls. Thus one can assume that there is some amount of energy not transferred to the gaseous phase. In consequence a smaller factor than 2 might be appropriate for taking into account the effect of the mirror source.

4.2.4 Critical Assessment.

The 2-D experiments posed more problems than expected, both technically and phenomenologically. The percentage of hemicylindrical charges that could be successfully ignited was much poorer than what we are used to from spherical charges. The results indicate strong, partly not reproducible boundary layer effects in the narrow setup and a lack of control over the energy released into the gaseous phase. And last, but most relevant, the instabilities on the border of the products cloud seem to develop at a different wavelength spectrum and might even be dominated by different mechanisms compared to the phenomena in a corresponding 3-D situation. Since the 2-D experiments were quite time-consuming and did not promise immediate answer to the questions arisen we thus decided to continue with a different set of experiments outlined in the following section.

Section 5

Unsteady Jets Created by a Detonation Inside a Chamber

In this set of experiments the focus was not put on the simulation of a spherical detonation in the free-field, but on the turbulent product cloud that is ejected from a chamber where a detonation occurs. Nevertheless there is some close relationship to the experiments outlined in Section 4 and in addition to experiments done in a further DSWA project [3] concerned with the fluid-dynamics of detonations in multi-chamber systems.

5.1 Experimental Setup

The new setup basically consists of a closed detonation chamber that is connected to the ambient air by means of a narrow outlet slot. The inner dimension of the metal chamber were $117 \times 130 \times 40 \text{ mm}^3$ and two outlet widths were realized, 10 mm and 20 mm. A sketch of this chamber is shown in Figure 32. In a modified version Makrolon plates of approximately $400 \times 500 \text{ mm}^2$ are attached to the front and back wall of the chamber, thus confining the propagation of the blast wave and the expansion of the products cloud in spanwise direction to the 40-mm depth of the model. A sketch is shown in Figure 33.

In the center of the detonation chamber a small charge was installed. In this case we used an ignitor system that is commercially available under the tradename HX2. It is a non-spherical charge of a multi-layer structure: in its core a thin ignition wire is attached to a basic, inert body of 10 mm height and 2 mm width. Around it there is a first explosive layer containing silveracide and other substances like cellulose. This is covered again by a layer of Nitropenta and cellulose. Finally a thin layer of lacquer is applied to the complete charge. The total charge weight is not too well defined but an equivalent of 40 mg Nitropenta or 50 mg TNT is about the right order of magnitude. Since the charge is non-spherical Figures 34 to 36 characterize the form of the blast fronts and the products cloud. Figure 34 shows that the first blast front is soon not too far from being spherical and even the disturbances on the secondary blast are acceptable. Besides we see a lot of wakes of small particles preceding the primary blast front which are due to the lacquer layer. A stronger influence of the charge geometry can be seen in Figure 35 and 36 that show the non-uniformity of the products cloud at later times after the ignition.

5.2 Flow Visualization.

We have performed 12 visualization experiments with the four possible setups of the detonation chamber which will be denoted as follows:

	outlet 20 mm wide	outlet 10 mm wide
with Makrolon windows	A	B
free field propagation	C	D

The main features that show up in the shadowgraph series are comparable for all test.

Figure 37 presents the complete cinematographic sequence of 24 frames (setup: configuration **A**), covering the time range from $t = 0.15$ ms to $t = 2.45$ ms after the ignition in steps of 0.1 ms. It has to be noted that the upper edges of the Makrolon windows appear a second time in the lower part of the field of view due to the fact that they are located in the area of overlap between incoming and reflected light path. In frame 1 the primary shock front has just left the outlet. At the outlet's edges the afterflow rolls up into two vortices. In frame 2 the vortices are somewhat obscured by the ghost picture of the Makrolon window's borders, but seem to have already separated from the outlet' edges. This becomes more obvious in frame 3. Besides, we see the formation of a second pair of vortices. The primary shock front is about to reach the ends of the model and has obtained a nearly semi-circular shape. In the meantime also a second shock front (one of the multifold reflections within the detonation chamber) has left the outlet. In frame 4 both shocks have propagated outwards, the primary one is diffracted at the corners of the model causing the emanation of rarefaction waves. The two vortices in both the left and right vortex pair show a distinct interaction: the vortex formed later in time overtakes the first one. The outflow from the detonation chamber gets contracted between the vortex pairs and its front area begins to form a flat mushroom-like cap whose ends are rolled up in the outer vortices of the vortex pairs. A 100 μ s later, in frame 5 the vortex interaction has continued: the vortices of each pair rotate around each other, deforming the border lines of the jet-like outflow. Besides we find the first mark of a third shock wave having left the outlet of the detonation chamber, which becomes more prominent in frame 6. The vortices in the original vortex pairs have in the meantime begun to smear out, becoming less distinct as individual structures. This continues in frame 7, where also a fourth shock appears. In the following frames the outflow develops to a turbulent jet ending in a mushroom-shaped region with an inner core of seemingly unstructured turbulence and an outer region with small but to some amount regularly spaced turbulent cells. The outer region grows with time and loses some of its regularity.

Concerning the shock wave pattern we find that from frame 9 on fronts with a large radius of curvature show up in the shadowgraphs. This again are ghost pictures: the first shock fronts have propagated into the region of the incoming light beam.

Figure 38 shows a comparison of two tests with the same setup at an intermediate time. The salient features are the same, but we find variations in the shape of the mushroom-like structure and the disturbances on its outer surface layer.

Figure 40 shows a test for the configuration **B** with a 10 mm outlet and Makrolon windows. The outflow is thus more concentrated. At an intermediate time (test a) we find mainly the same structure as for the tests with the 20-mm outlet (see Figure 39), but the mushroom is smaller and its structure less distinct in contrast. For the late times the appearance is quite comparable, the plume above the 10 mm outlet being more longish and narrower than the one above the 20 mm outlet.

Figure 41 and 42 show shadowgraphs from test without the Makrolon windows (with 3D-propagation into the ambient air), Figure 41 for a 20 mm outlet, Figure 42 for a 10 mm one. Here the outflow appears again as jet-like stems under a broadened turbulent cap. But the disturbances on the surface seem to be less orderly than in the case of the

2D-confinement. For the outlet width of 10 mm the final state is an oblong plume that lacks some of the features we find for the 20-mm wide outlet. Here the cap of the plumes show a small number of protrusions with a comparatively large characteristic length, giving it a cauliflower-like appearance.

In summary, the tests give further indication, that the large wavelengths of the turbulent spectrum which cause the typical shape of the products cloud in the case of free expansion are suppressed when the expansion is restricted in one dimension to a narrow gap between two plates.

5.2.1 Interaction of the Products Jet with an Impinging Blast Front.

5.2.1.1 Modifications of the Setup. A further point of interest was the question whether a shock that impinges onto the turbulent products cloud will amplify the disturbances on its borderline. Some modifications of the configuration were necessary, they are shown in Figure 43. The new setup is essentially a modification of configuration **A** from the previous test series; i.e. the detonation chamber has an outlet width of 20 mm and the complete setup is closed on the front and back by Makrolon windows. In contrast to the previous tests the blast no longer expands beyond the borders of the setup; the model is now closed by a hemicylindrical reflector with a diameter of 225 mm. Six pressure gages were installed, two at the bottom of the expansion chamber, four along the circumference.

In addition the chamber in which the HX2 ignitor is brought to detonation was fitted out with a foam lining on the four 40 mm wide walls. This helps to damp the multiple reflections within the chamber and to get rid of most of a number of spurious waves leaving the chamber through the 20 mm wide outlet. Our preliminary tests showed that only two shocks of significant strength follow the primary one.

5.2.1.2 Experimental Results. Figure 44 shows an excerpt from the pressure-time histories at the four gages along the reflector. All four records are quite comparable, those at symmetrically positioned gages nearly identical. Both the first and the second shock arrive earlier under 67.5° than under 22.5° , since the fronts are not perfectly hemicylindrical, but the deviation in shape is nearly neglectable.

Figure 45 shows a frame from a 24-spark series of shadow-photographs. This photograph at $t=1.07$ ms captured a situation where the three dominant shocks have already all been reflected at the hemicylindrical wall of the expansion chamber and propagate in reversed direction onto the outlet of the explosion chamber. The third shock front that is largest in diameter is comparatively near to the reflector. It thus allows to rate the slight mismatch between the curvatures of the reflector and the shock front. The primary shock (the one with the smallest diameter) is about to impinge on the turbulent outflow plume.

Figures 46 and 47 show the next frames of this shadowgraph series 80 μ s and 160 μ s later. The primary shock has hit the turbulent plume which seems to contract a bit. The overall appearance of the turbulent structures in the border of the plume does not change significantly from Figure 45 to Figure 47. The effect of the interaction between the shock and disturbances on the border of the outflow plume is not as pronounced as we expected it to be. This result is consistent with findings made in accompanying shock tube experiments.

5.2.1.3 Shock Tube Tests. In normal shock tube experiments we find rather stable laminar flow behind the shock front. Thus the turn-over to turbulence has to be triggered off by comparatively large disturbances. In order to generate a flow field with a considerable amount of turbulence we introduced a set of obstacles into the flow. After a number of tests with different geometries we came up with the configuration shown in Figure 48. Behind the front row of rhombic pins large vortices are formed. These vortices are chopped up by a row of thin round pins and a wire mesh woven into it. This "turbulence generator" is located 100 mm upstream the 200 mm long test section.

The downstream end of the test section is closed by a rigid wall which can be equipped with three pressure gages. This wall reflects the shock wave running ahead of the turbulent flow.

The shock Mach number (and the percentage of flow blockage through the generator grid) determines the velocity of the flow and the strength and speed of the reflected wave. The location where the reflected shock impinges on the generated turbulence should be fixed to a point within the field of view. Thus the position of the reflector has to be optimized for a certain parameter set.

Figures 49 - 56 show some frames from a series of shadow photographs for a test with this configuration. The reflector is located immediately at the end of the test section. The incident shock has a Mach number M_s of 2.3.

Figure 49 shows the situation some 10 μ s before the reflected shock — moving from right to left — impinges on the front of the turbulent flow moving from the right to the left. Though the turbulent flow is characterized by a fine scale granulation its leading edge is marked out by a band-like structure (approximately 4 to 5 cm wide) with higher contrast. The front of this turbulent region is inclined and shows some large scale disturbance: one can see four indentations with an almost regular spacing between 16 to 20 mm and a depth around 6 to 10 mm.

In Figure 51, taken 67 μ s later, the reflected shock has hit upon the turbulent front and nearly propagated through the band at the leading edge which is thus compressed. The undulation of the front is squeezed flat; though the large scale disturbances are still recognizable in parts, the depth of the indentations has become smaller than 4 mm. The front becomes even smoother another 67 μ s later in Figure 52. In addition one can see that the previously smooth and narrow front of the reflected shock is disintegrating into a few frayed lines: the inhomogeneity of the turbulent flow field generates locally differences in the properties of the shock propagation.

It takes some time until large disturbances on the leading edge of the turbulent flow become prominent again. Figure 52 shows the situation approximately 300 μ s after the

reflected shock has hit the turbulent front, Figure 54 the situation after 600 μ s and Figure 55 after 800 μ s. In Figure 53 the indentations are still smaller than at the beginning (Figure 49), but it already seems as if a larger wavelength is dominating them. This can be most clearly seen in Figure 55, where we find two major indentations with a depth of 10 mm and 16 mm and a spacing around 33 mm.

To summarize the experiment: it shows that a shock wave impinging on a turbulent flow does not necessarily trigger off a faster growth of large scale disturbances on the boundary of the turbulent area, but can change its spatial characteristics. This is at least the case for the experimental situation where the shock creates a counterflow in the opposite direction to the turbulent flow. A shock impinging from behind, i.e., one that causes an additional flow component to the original mean propagation of the turbulent flow poses a different problem, the result should not be transferred to this situation.

Section 6

Simulation of Afterburning in Turbulent Jets

The study of the turbulent products jet in the closed expansion chamber led to a further set of experiments which can be termed as experiments on the combustion of turbulent fuel jets. These experiments were initiated by the question what destructive potential the detonation of an unbalanced explosive provides by the way of afterburning which distributes an additional energy release in space and time.

The typical experiments in our laboratory are small-scale simulations at scales that range from approximately 1:50 to 1:200. Safety considerations and regulations restrict us essentially to one type of explosive; custom-made Nitropenta charges of a weight between 0.1 and 1.0 g. It is rather difficult to modify these charges in a way that causes their detonation to produce a reliable amount of fuel that facilitates experiments on afterburning. Thus we decided to follow a different concept which is to detonate a charge in an atmosphere that supplies the fuel by the way of an inflammable gaseous mixture.

6.1 Experimental Setup

6.1.1 Two-Chamber System.

The setup for the experiments, which is essentially the two-chamber system seen in Figure 43 with some modifications, is shown in schematically in Figure 57, Figure 58 depicts a photograph of the final version of the setup. The volume of the detonation chamber was decreased by the means of steel inserts to 32 cm³ or 72 cm³. It contains the charge and is filled with the inflammable gas mixed to air. A rectangular outlet connects this chamber to the larger hemicylindrical expansion chamber. Before the detonation is initiated, a thin foil diaphragm closes the outlet. The blast wave of the detonation can rupture it and releases a jet-like flow of fuel (the inflammable gas mixture) from the detonation chamber into the air atmosphere of the expansion chamber. The mixing of fuel and oxidizer necessary for a reaction to occur is mainly caused by the turbulence of the jet flow. This is in contrast to the combustion of premixed systems, but essentially what we expect for afterburning in explosions.

The diameter of the expansion chamber is 225 mm and its depth 40 mm. To facilitate optical investigations front and rear of the model are closed by 10 mm windows of Makrolon, a transparent polycarbonate. The inner dimensions of the detonation chamber and the geometry of the outlet opening can be changed by inserts. Table 2 summarizes the dimensions of different versions used in the experiments up to now.

6.1.2 Diagnostics.

The side walls of the expansion chamber were equipped with a number of piezo-electric pressure gages (Kistler 603b) and one piezo-resistive pressure gage. Additional diagnos-

tics were a photo diode monitoring the luminescence caused by the hot reaction products in the expansion chamber and cinematographic shadow photography visualizing the flow field in the expansion chamber.

6.1.3 Charge.

In most of the experiments the reaction was initiated by the detonation a HX2-ignitor located in the center of the detonation chamber. The HX2-ignitor was already described in the previous section. The essential part of the explosive is PETN; according to the manufacturer the total amount of explosive may vary between 27 and 42 mg. From our experience with this detonator a smaller variation seems realistic and we consider a TNT-equivalent of about 50 mg appropriate.

6.1.4 Fuel Simulants.

Up to now two different gases were used to serve as fuel: acetylene and for a number of exploratory experiments methane. Table 3 and Table 4 summarize the characteristics of these gases. The amount of fuel added to the air in the detonation chamber was varied; in some of the tests with a 72 cm³ detonation chamber additional oxygen was mixed to the atmosphere. The partial pressures of the components specific to the individual tests are listed in Tables 5 to 7.

6.2 Flow Visualization.

Figure 59 shows one shadowgraph from a cinematographic sequence for a reference test with the 32 cm² detonation chamber, test 006. In this reference case the detonation chamber is filled with air only, thus the jet expelled through the outlet is inert. In this respect the test is essentially identical to the tests described in Section 5.2.1, but the smaller volume of the detonation chamber changes the outflow rate and the form of the turbulent products jet. Directly above the cloud we find some spots in deep black, which are parts of the disrupted diaphragm. Figures 60 and 61 shows shadowgraphs from a test where the detonation chamber was filled with a mixture of 500 mbar acetylene and 500 mbar air. Most salient is the core region which is very bright due to overexposure. Since the jet is reactive and combusts with the ambient air it gains higher temperatures which cause it to be luminous. The light flux from the luminous areas is time-integrated on the shadowgraphs since we apply an open shutter technique. Thus the overexposed areas give no time-resolved information on development of the luminous cloud. Though the optical setup diminishes the effect of the self-luminosity it can not be completely suppressed since mechanical shuttering is not feasible for the short exposure times needed for the shadowgraphs. In consequence the products cloud is depicted with very little contrast in the early stages as in Figure 60. In Figure 61 the same overexposed area is visible, but the visibility of the products cloud is better because its extent is larger than the overexposed area. An interesting aspect is the width of the products cloud near the floor of the expansion chamber. Whereas in the inert cloud forms a kind of balloon attached to the outlet opening, the reactive cloud has a comparatively wide stem between the floor and the balloon shape. The reactive cloud

seems to entrain more air from the bottom layer of the expansion chamber than the inert jet.

Since we could not get time-resolved pictures of the luminous area in the products cloud we installed a photodiode which monitored the light flux from the window of the expansion chamber. Figure 62 shows a comparison of typical signals for a test without any reaction and a test with combustion. The photodiode signal in the reactive case is a factor 10 larger in magnitude. The signal rises immediately after the ignition of the HX2 and decays quite slowly after having attained a maximum at approximately 2 ms.

The inflammable jet was not brought to reaction in every test. Especially to high partial pressures of acetylene in the prechamber seemed to suppress the initiation of the combustion. But there were also tests where the experimental evidence indicated some retardation for the start of combustion. Figure 63 shows an example. It is the photodiode output for test 016 with 800 mbar acetylene admixed to 200 mbar air. Directly after ignition the luminosity rises to a first maximum and starts to decay. After about 1.8 ms the combustion appears to be re-initiated and a maximum comparable to that of Figure 62 is attained at $t = 3.5$ ms.

This effect of retarded reaction is also reflected in the pressure-time histories. Pressure gages are our preferred diagnostic tool for the analysis of this set of experiments which will be outlined in the following.

6.3 Initial Data Analysis.

The results presented here are obtained from the pressure recordings of gage 2. This gage monitors the side-on pressures of the blast wave and the multiple reverberations in the expansion chamber whereas the other gages are exposed to head-on reflections. For all tests where a reaction occurred and a pressure-rise effect was noticeable the pressure records at this gage are compared to a reference test (HX2-detonation only, detonation chamber and jet contain no fuel). The records have a length of approximately 16 ms. After about 10 ms a more or less stable plateau value is obtained. Thus we did an average of the overpressure values in the interval from 10 to 16 ms, which we term p_{end} . In case a reaction occurred this value is larger than the corresponding one for the reference test, the difference being termed p_{excess} . A theoretical value for this excess pressure can be derived from the amount of fuel and its heat of combustion, assuming that the combustion of the fuel and the air in the expansion chamber is complete, stoichiometrical and adiabatic.

For a further analysis of the pressure records it is advisable to separate the slower pressure increase due to the combustion of the fuel from the pressure spikes due to shock wave reverberation (period approximately 0.5 ms). Thus we applied a moving average:

$$\overline{p(t)} = \frac{1}{\tau} \int_{t-\tau/2}^{t+\tau/2} p(t) dt \quad (7)$$

with an averaging window of 1 ms. This average pressure should be due to the increase of the internal energy due to the explosion and the fuel combustion:

$$\overline{p(t)} = (\gamma - 1) \frac{E(t)}{V_2} \quad (8)$$

$$E(t) = E(t)_{\text{combustion}} + E_{\text{explosion}} = \mu(t)m_C Q_0 + E_{\text{explosion}} \quad (9)$$

where V_2 denotes the volume of the expansion chamber, m_C the total mass of fuel, $\mu(t)$ the mass fraction of fuel already burned at instant t and Q_0 the heat of combustion of the fuel. Thus taking the difference of the average pressure records for a test with combustion to the reference test without fuel can be used to evaluate the time history of the mass fraction burned:

$$\mu(t) = \frac{\overline{p(t)}_{\text{combustion}} - \overline{p(t)}_{\text{inert}}}{\pi_C}; \quad \text{where : } \pi_C = (\gamma - 1) \frac{m_C Q_0}{V_2} \quad (10)$$

denotes the theoretical value for the maximum excess pressure.

During the combustion time which ends approximately after 4 ms the history of the mass fraction burned can be approximated by a logarithmic function of time:

$$\mu(t) = a \log_{10}(t/t_0) \quad (11)$$

which allows to evaluate a corresponding burning rate:

$$-\dot{\mu}(t) = \frac{-a}{\ln(10)t} \quad (12)$$

The experimental values for the end pressure p_{end} , the fit curve and the burning rate are given in Tables 5 to 7 along with the theoretical value for the excess pressure π_C . The actual pressure-time histories and the corresponding scaled sliding averages are shown in Figures 64 to 96.

The scaling of the pressure difference curves is still preliminary. When applied to the experimental data it states that the combustion ends while leaving about 30 to 50 % of the fuel uncombusted (see also Figure 97). This might be a misinterpretation due to a wrong assumption about the heat of combustion. Taking into account that the fuel might already be decomposed by the explosion in the detonation chamber one gets a smaller value for the energy release via combustion, i.e., a smaller scaling factor. This would mean that a larger amount of the fuel is burned at the end of the combustion regime. A thermodynamical analysis of the system is done by A. K. Oppenheim [4].

In addition Allen Kuhl, Lawrence Livermore National Laboratory, performs direct numerical simulations of the EMI experiments by means of the AMR code. A preliminary example is shown in Figure 99. The sliding time-averages of the pressure-time histories form the main data body for a comparison between simulation and experiment which appears rather promising [5-7].

6.4 Revised Strategy of Data Evaluation for the Combustion Experiments.

The last chapter compiled the data of all combustion experiments carried out up to now. The salient result of the initial evaluation was that in the majority of experiments we find a combustion regime where the pressurization essentially follows a log-t behavior. Based on this fact we revised the evaluation procedure in order to obtain a simpler and more uniform representation of the complete data set.

The major disadvantage of the sliding-average method is that the averaging length of 1 ms does not completely smooth out the oscillations due to shock wave reverberations. This introduces a certain arbitrariness into the further evaluation steps. But a larger averaging length is not advisable since as soon as it is of the same order of magnitude as the combustion period it will artificially reduce the slope of the pressure-rise curves.

Nevertheless the data indicated some intermediate time range ($1\text{ms} < t < 4\text{ ms}$), where the pressure rise can be approximated by a simple logarithmic fit:

$$\Delta p(t) \approx a \log_{10}(t/t_0) \quad (13)$$

This is only a zero order approximation that necessarily does not describe the start-off and decay phase of combustion properly.

Thus the main objective of refining the evaluation method is to expand the validity range of the fit function. For the time being this is accomplished by expanding the fit function to a power series in terms of $\log(t)$. In addition, we tried to overcome the fall-backs of the sliding average method as outlined in the following.

6.4.1 Characterization of the Reference Test 06.

Figure 100 shows the original pressure-time history of the explosion-only case, test 06, and the corresponding sliding time-average. The averaged history still shows a rippled structure due to the "acoustic" noise. Thus a fair enough approximation of this time-average would be a step-function rising at the time-of-arrival ToA from zero to a value of 0.148 bar. Under this condition it virtually makes no difference whether one time-averages the pressure records in case of combustion and subtracts this reference value afterwards or performs it the other way round.

Closer inspection of the combustion experiments shows that their pressure signature is well correlated to that of the reference test for the first two pressure peaks ($t < 1\text{ ms}$), then the peak structure gets decorrelated. Taking the difference of the original pressure histories rather than that of the averaged ones in this time regime thus reveals more accurate information on the initial phase of pressurization. In consequence we decided upon the following strategy:

- We idealize the reference test 06 by the signal shown in Figure 101
- and subtract this signal from the original pressure histories of the combustion tests.

- By means of a least mean square fit the resulting pressure difference history is then expanded into a power series:

$$\Delta p(t) \approx \sum_{n=0}^6 A_n \cdot (\log_{10}(t))^n \quad (14)$$

Figure 102 shows the actual pressure difference curve and the resulting fit for test 11 with a logarithmic, Figure 103 with a linear time axis. For comparison the previous result from the sliding average technique is also incorporated. The fit function and the sliding average compare quite well, but the fit has the merit of being smoother and allowing to establish a well defined maximum value of the pressure gain.

Concerning the start of the combustion process: the initial pressure differences for $t < 1$ ms are rather small, their order of magnitude compares to the limits of test reproducibility. Thus the original and the fit curves can tell only little about this initial phase.

6.4.2 Further Proceeding

In our initial analysis we pointed out that the pressure gain curves should be normalized by

$$\pi_c = (\gamma - 1) \frac{m_c Q_0}{V_2} \quad (15)$$

to relate it to the mass fraction burned. Since we have to take into account that the detonation decomposes the fuel and dissociate the oxygen and nitrogen in the pre-chamber, the initial choice of values for the heat of combustion Q_0 was too simplistic. The thermodynamic analysis of all our experimental cases is not yet accomplished. Thus we decided for the meantime to inspect the resulting fit functions of the experiments for the maximum value Δp_{\max} and to use this value to normalize the pressure difference curves:

$$\pi(t) = \frac{\Delta p(t)}{\Delta p_{\max}} \quad (16)$$

Figure 104 summarizes the result for the acetylene experiments in the 32 cm³ chamber.

If we assume

- that no work is performed, which is justified since the volume of the combustion chamber is constant
- and that the heat transfer is zero (for small t it should be negligible though we find a pressure loss for large times)
- and that the combustion process consumes all fuel,

i.e., that Δp_{\max} reflects the complete energy release obtainable from the combustion of the fuel, then $\pi(t)$ is approximately equivalent to $\mu(t)$, the mass fraction burned.

From the smooth fit functions the time derivative of $\pi(t)$ can easily be obtained. With the above assumption it reflects the burning rate of the combustion process. Figure 105 again summarizes the experimental results. Included are the functions $f(t) = 0.3/t$ and $f(t) = 0.4/t$, which reflect the typical results of the initial evaluation (keeping in mind that scaling has changed by a factor from 1.5 to 2).

6.4.3 Comparison to Vibe-Functions.

Normally in combustion theory the preferred way to describe the time development of the mass fraction burned is by means of a Vibe-function:

$$f(\theta) = \frac{e^{-\alpha(1-\theta)^{\beta}} - e^{-\alpha}}{1 - e^{-\alpha}}, \text{ where } \theta = t/T_0 \quad (17)$$

Figure 106 shows two comparisons between the logarithmic power series fit and matched Vibe-functions (the match being made manually, not by a non-linear fitting algorithm), Figure 107 shows the corresponding time derivatives.

6.4.4 Summary for Complete Test Matrix.

Figure 108 is identical to Figure 104, but now also the tests with acetylene in the 72 cm³ are incorporated. In continuation the tests with methane are added in Figure 109.

The data for the additional tests were analyzed following essentially the same concept as outlined above. In order to present all data in one diagram we then evaluated in addition to Δp_{\max} the values of t_o , the time where the fit function attains the value zero (which in some way defines the start-off of the exothermic process, that in some experiments was significantly retarded) and t_i , the time where the maximum value of $\Delta p(t)$ is attained. Figure 110 demonstrates these definitions at the example of test 11.

Figure 111 shows a diagram of all experimental results obtained so far. The pressure gain is again normalized with Δp_{\max} , the time-axis is shifted to compensate the different start-off delays t_o and scaled with the "combustion period" $t_i - t_o$. Most of the experiments are given as grey lines, only a few are marked out in color and labeled in the legend. To complete the information Figure 112 gives three bar-plots for the parameters t_o , t_i and Δp_{\max} . The bars are labeled with the test number, the initial partial pressure of the fuel being appended to this label. In addition, the color of the bar indicates the test series: dark blue denotes the tests with the 32 cm³ pre-chamber and acetylene, light blue the test with the 72 cm³ pre-chamber and acetylene and green the tests with the 72 cm³ chamber and methane.

Section 7

Development of a Small Bomb-Calorimeter

The charge we use to initiate the combustion experiments is – as stated earlier in this report - the commercially available HX2-ignitor. The information from the manufacturer does not clearly define the energy release of this charge, a relevant parameter for both the thermodynamic analysis of our experiments and the comparison to numerical simulations. Thus we thought it useful to have an experimental possibility to characterize this energy release. In addition, the gain in excess pressure is lower than expected from theoretical analysis. A possible reason can be incomplete combustion. But furthermore, close inspection of the measured pressure-time histories reveals a slow overpressure decay in the combustion chamber after the maximum average pressure has been attained. Thus another effect to be taken into account might be heat transfer to the walls. In previous studies it was justified to neglect heat-transfer effects since the time-scales of the experiments were of the same order of magnitude as the arrival time of the first shock. In the more recent studies the focus has shifted away from the first few shocks to the development of the system at larger times. Here an increased influence of heat transfer has to be anticipated. So it is also worthwhile to investigate its influence on our experiments. The same holds true for the general characterization of our custom-made small-scale charges and the experiments in the project "Fluid-Dynamics of Explosions in Multi-Chamber Systems" where the monitored time periods also have significantly increased.

Based on these demands we have designed and manufactured a small cylindrical bomb calorimeter to facilitate simultaneous measurement of the overpressure and air and wall temperature for detonations of small charges and gaseous mixture.

7.1 Design and Diagnostics.

Figure 113 shows a schematic diagram of this calorimeter. The form is essentially cylindrical, but the inner edges between the both faces and the jacket are rounded off to avoid extreme overpressure in these edges due to the superposition of shock reflections. The inner volume of the calorimeter is 603 cm³, the inner surface approximately 400 cm². The plug at the left in Figure 113 holds two metal pins which can be connected to the high voltage supply, the charge wires can simply be soldered to these pins. Since the plug is screwed into the base of the calorimeter, an easy preparation of the tests is facilitated. All diagnostics are mounted into the cover assembly the opposite face consists of. Four bolts hold the base and the cover assembly together. The whole setup is designed to withstand a maximum static overpressure of approximately 100 bar.

The calorimeter has a mass of 4780 g, most of the material being steel (tradename Monix 20, 30CrNiMo8 steel) with the exception of the four bolts and the inner part of the plug.

The installed diagnostics are

- a piezo-resistive pressure transducer, gage 1 (Kistler 4075 A 100), to measure the long-term history of the chamber pressure,
- a piezo-electric transducer, gage 2 (Kistler 603 B), to measure the initial pressure history with high time-resolution,
- a thermocouple – its tip penetrating 4mm into the chamber – to measure the gas temperature, and
- two thermo-elements (PT100) to measure the temperature-time history at the outside of the calorimeter wall from the start up to the time of equilibrium. These thermo-elements were mounted opposite to each other at the middle of the calorimeter jacket

For the first exploratory experiments the calorimeter was placed on two wooden supports without any further insulation against the ambient air. Later on the calorimeter was placed in a Styrofoam housing.

The essential parameter of the bomb calorimeter is its heat capacity. A first estimate can be derived from the mass of the calorimeter and some value of the specific heat c_p of steel obtained from literature. The actual values differ for different sorts of steel, but a value of $c_p = 0.477 \text{ Jg}^{-1}\text{K}^{-1}$ is stated to be typical. This value yields a total heat capacity Γ of 2280 JK^{-1} or 545 cal K^{-1} . This value is in agreement with a calibration series done by means of controlled electrical heat supply.

7.2 Experimental Results.

7.2.1 Preliminary Testing.

To make sure that the assembled bomb calorimeter is air tight it has been pressurized to about 20 bars. Whereas the first version of the plug facilitating the easy mounting of the charge failed this test a redesigned version showed no pressure loss at all when monitored for periods in the order of 10 minutes. In addition, temperature read-outs from the thermo-elements and the thermocouple showed that the temperature changes due to sudden pressure changes could be detected.

A number of tests with electrical sparks were done, where a voltage of 8 kV was discharged through a small gap between two wires. The thermocouple inside the calorimeter registered a momentaneous temperature rise of about 1.4 K for a single spark, but the released energy was too small to have an observable effect on the jacket temperature.

7.2.2 Preliminary Results for the HX2-Ignitor.

In the development phase three test on the HX2-ignitor were performed. Table 1 summarizes the results.

The results show that the amount of energy released by the detonation of the HX2-ignitor verges on the sensitivity limit of our calorimeter, which is given by a reliable measurement of the equilibrium temperature by the thermo-elements. Nevertheless, the values for the heat of detonation are in the expected order of magnitude. A certain amount of scatter has to be expected since the manufacturer only guarantees the total charge weight to be between 27 and 42 mg.

Table 1 Results for the HX2-detonator (at $T \approx 26^\circ\text{C}$, $p_0 \approx 990 \text{ mbar}$).

test	p_1	p_2	p_{end}	ΔT_{in}	ΔT_1	ΔT_2	ΔH_{Det}
No	bar	bar	mbar	K	K	K	cal
03	2.5	?(> 8.4)	2	19.9	0.06	0.08	38.2
04	2.5	10.5	2	25.2	0.10	-	54.5
05	2.5	11.25	2	22.2	0.08	0.08	43.6

where:

- p_1 peak overpressure initial reflection
- p_2 peak overpressure second reflection
- p_{end} overpressure level after 10 - 80 seconds
- ΔT_{in} maximum overtemperature (from thermocouple)
- ΔT_1 equilibrium overtemperature of calorimeter (from 1st PT100)
- ΔT_2 equilibrium overtemperature of calorimeter (from 2nd PT100)
- ΔH_{Det} estimate for heat of detonation

7.2.3 Preliminary Results for Nitropenta Charges.

One test was performed with a custom-made Nitropenta charge of $m = 0.25\text{g}$. The charge was essentially spherical but not machined to perfect geometry. Due to the manufacturing of our charges the content is not absolutely pure PETN: Nitropenta powder is dissolved in acetone with 2%Vol of gun-cotton admixed to form a highly viscous paste from which the final charge is grown by repeated dipping and drying.

The charge was detonated in an atmosphere of 983 mbar air at a temperature of 27.3°C . The incident reflected overpressure at the piezo-electric gage p_1 was 34 bar, the second reflection was higher than 98 bar and caused an overload of the transducer sys-

tem, the third reflection had a peak overpressure of 60 bar. The final pressure p_{end} in the chamber between 5 and 80 sec was 186 mbar. The overtemperature inside the calorimeter rose to a value larger than 115 K, overloading the corresponding amplifier. Within about 5 min the overtemperature relaxed to a value of approximately 1 K (refer to Figure 114).

Figure 115 shows the read-out from one of the thermo-elements mounted on the calorimeter jacket.

The overtemperature peaks at a value of 1.59 K and then decreases – within a period of approximately 25 min – to a value of 1.1 K. Since the calorimeter was not insulated against the ambient air heat transfer from the calorimeter wall to the outside is possible. Thus we did a semi-logarithmic plot of the overtemperature versus time shown in Figure 116, expecting an essentially logarithmic decay of the overtemperature. If at all, we can find this for times larger than 15 min with a rather small decay rate of 0.0036 min^{-1} , which means a temperature loss of 0.35 % per minute. But we are not sure that this decay can be attributed to heat transfer to the environment. Figure 117 shows another logarithmic plot of the measured data, in this case the difference between the instantaneous temperature and the final temperature at $t = 25 \text{ min}$. Here we find a distinct range of exponential decay for the period between 5 and 20 min. Based on the rate of decay the value at $t = 25 \text{ min}$ should differ 0.01 K from the final temperature, a difference in the order of the read-out accuracy.

Thus we assume for the time being that the temperature decrease of Figure 115 is mainly due to the redistribution of heat in the calorimeter walls and that the overtemperature of 1.1 K at $t = 25 \text{ min}$ is equal to the equilibrium temperature of the calorimeter system. This assumption is in good agreement with an analytical estimate for the thermal relaxation (see Letter Report 13).

The value of 1.1 K for the final overtemperature yields a value of 600 cal for the energy released by the detonation of the 0.25-g NP charge. This amounts to a heat of detonation ΔH_{det} of 2400 cal / g, a value that is too high compared to the bomb calorimetry experiments performed at Lawrence Livermore National Laboratory [1]. With a series of experiments on confined and unconfined 25-g PETN-charges. LLNL derived a value of about 1500 cal/g for the heat of detonation in a vacuum atmosphere and a value of 1916 cal/g in an atmosphere of 0.38 bar oxygen. The latter value is close to the heat of combustion for PETN, which amounts to 1957 cal/g.

Prior to the design of our bomb calorimeter we exploited some experiments in a rectangular chamber with inner dimensions of 117 mm x 130 mm x 40 mm for a feasibility test. Charges of various weights were detonated and the temperature on the outer side of the aluminum walls was measured at two locations. The setup consist of 5291 g aluminum and 694 g steel in form of bolts. With the specific heat of aluminum ($c_p = 0.214 \text{ cal/gK}$) and steel ($c_p = 0.114 \text{ cal/g}$) the heat capacity of the setup amounts to 1211 cal/K. Figure 118 shows the released energy versus charge weight. From this data set we get a value of 580 cal for a 0.25-g charge which is in good agreement to the findings of our first bomb calorimeter experiment.

But more interestingly, a linear regression on the data from the feasibility tests yields a value of 1932 cal/g for the heat of detonation. This compares well to the data for a

PETN explosion in an oxygen atmosphere. The fact that we obtain too large values from single experiments is reflected in the regression by an unexpected and somewhat (at least for the time being) inexplicable offset of 97.5 cal. This offset is by far too large to be explained by the energy released via the exploding wire which initiates the detonation of our charges.

A few further experiments in our calorimeter with varied charge weights yielded – again by means of a linear regression – a result of 2190 cal/g.

Though there are still some open questions which can lead to further modifications of the bomb calorimeter and the modus of analysis it is a tool which facilitates at least the comparison of different tests. Our intention is to continue the experiments with series of Nitropenta charges in different atmospheres (air, oxygen or nitrogen for example) and then with charges in inflammable atmospheres corresponding to the combustion experiments of Section 6.

Section 8 Figures and Tables

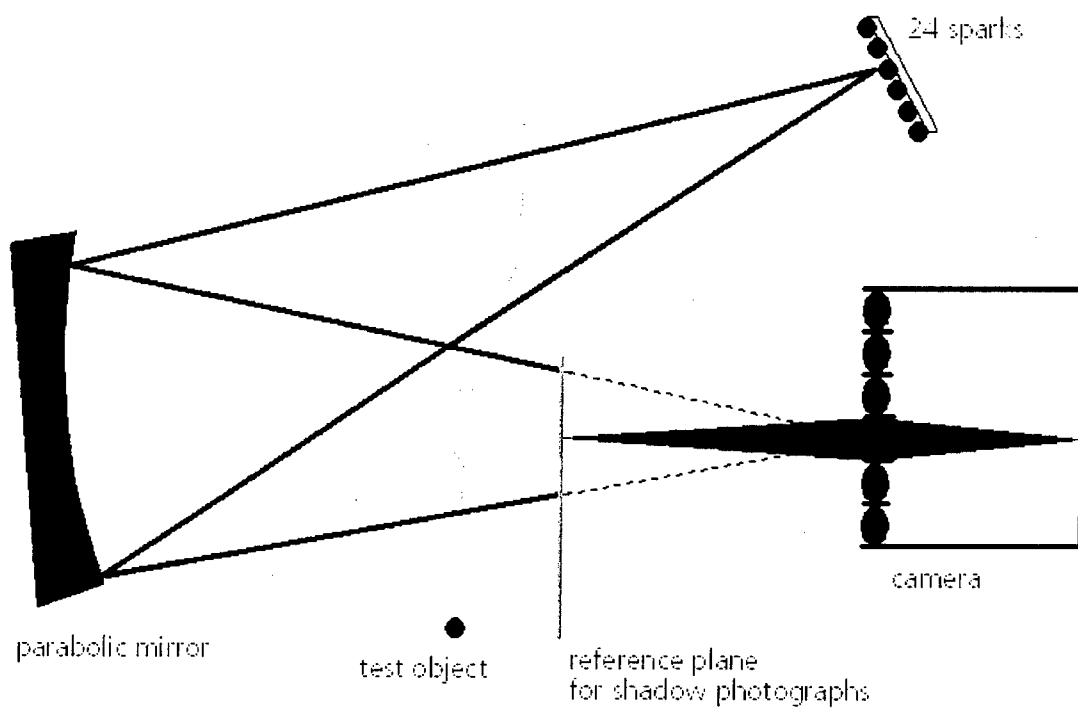


Figure 1 Schematic sketch of the 24-spark Cranz-Schardin camera.

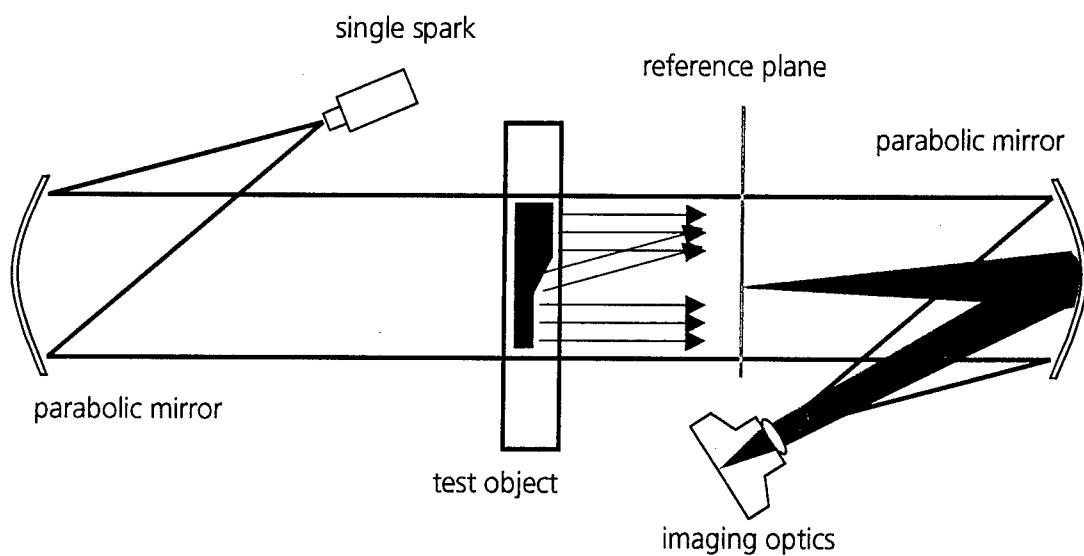
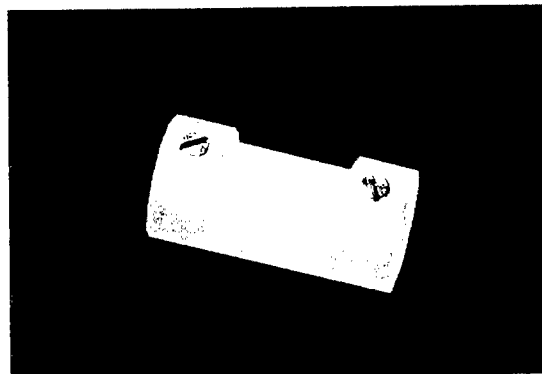
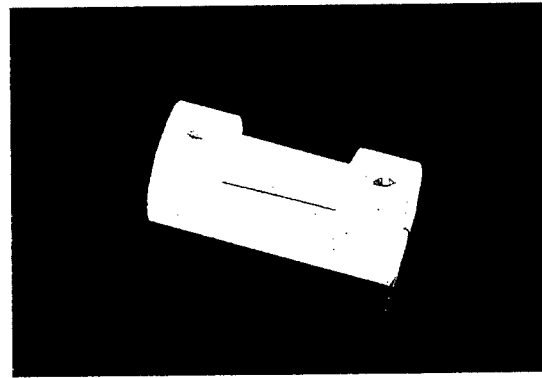


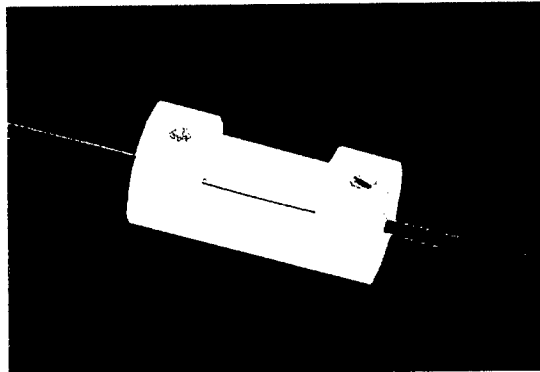
Figure 2 Schematic sketch of the single shot setup for shadow photography.



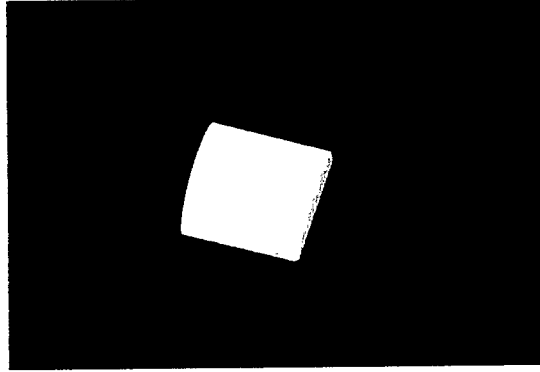
(a) Makrolon body



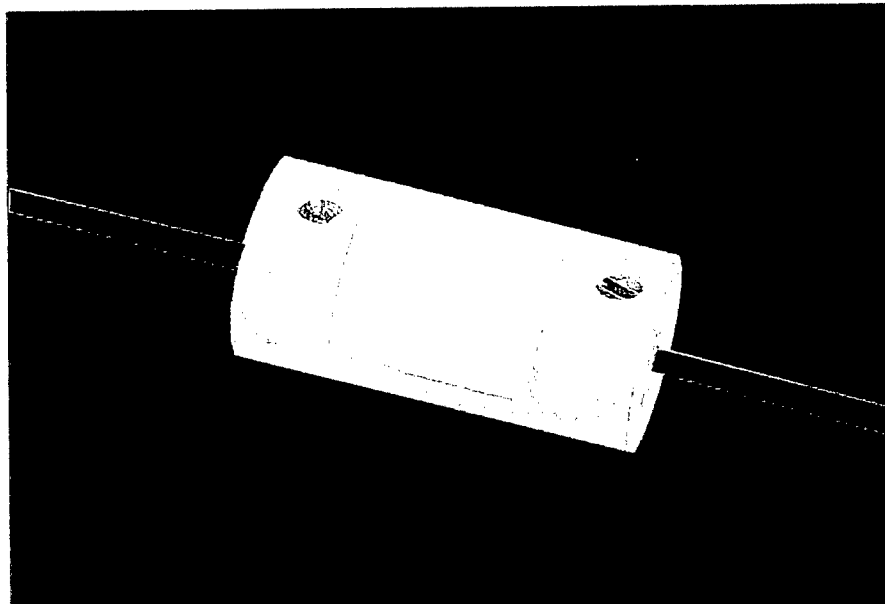
(b) Inserted ignition wire



(c) Connected supply wires



(d) Nitropenta body, casted in mould



(e) Assembled 1cm charge

Figure 3 Manufacturing process of hemicylindrical charges.

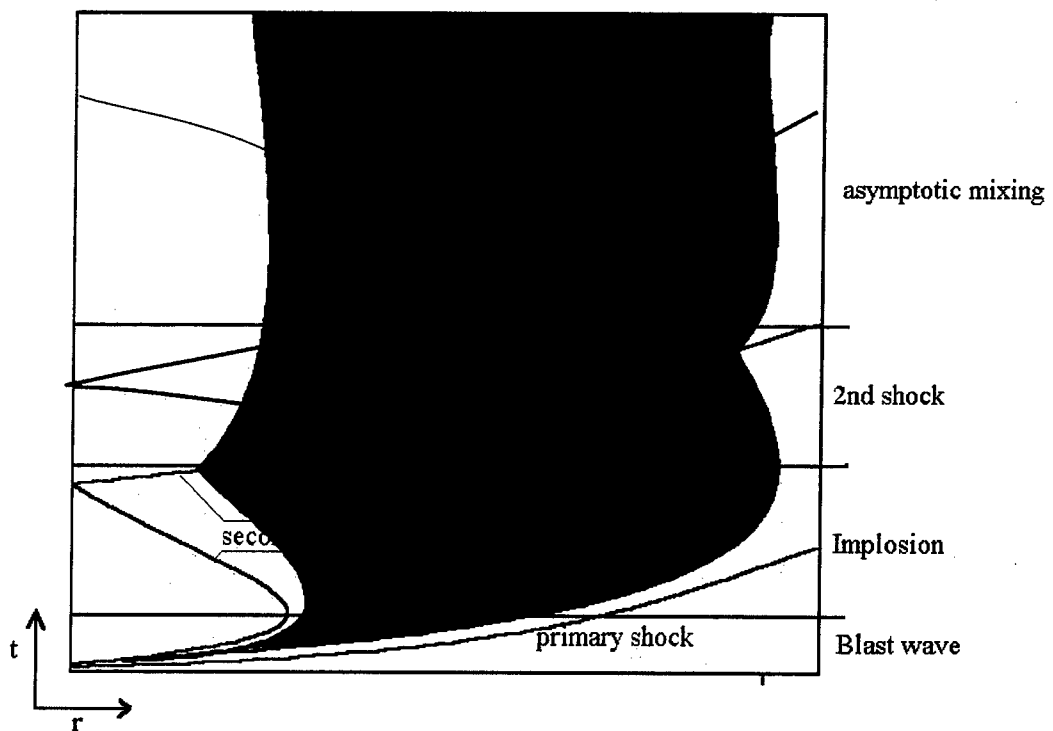


Figure 4 Schematic wave diagram for the detonation of a spherical high-explosives (HE) charge (specifically for an unbalanced explosive like TNT). Red curves identify blast fronts, blue curves give a qualitative picture of iso-contour lines for the normalized concentration of fuel (i. e., unburned detonation products). The annotations on the right hand characterize the four main phases relevant to turbulent mixing.



Figure 5 Shadow photograph showing the detonation of a hemispherical NP-charge mounted on a transparent Makrolon pane.
The test was performed in the EM blast tank. Charge weight $W = 0.45$ g, time after ignition $t = 0.2$ ms (test 0822.MM).



Figure 6 Pseudo-color version of the shadowgraph from Figure 5. Grey values are mapped to a palette of colors in order to enhance flow features.



Figure 7 The shadowgraph from Figure 5 after some postprocessing including spatial low pass filtering, contrast stretching.



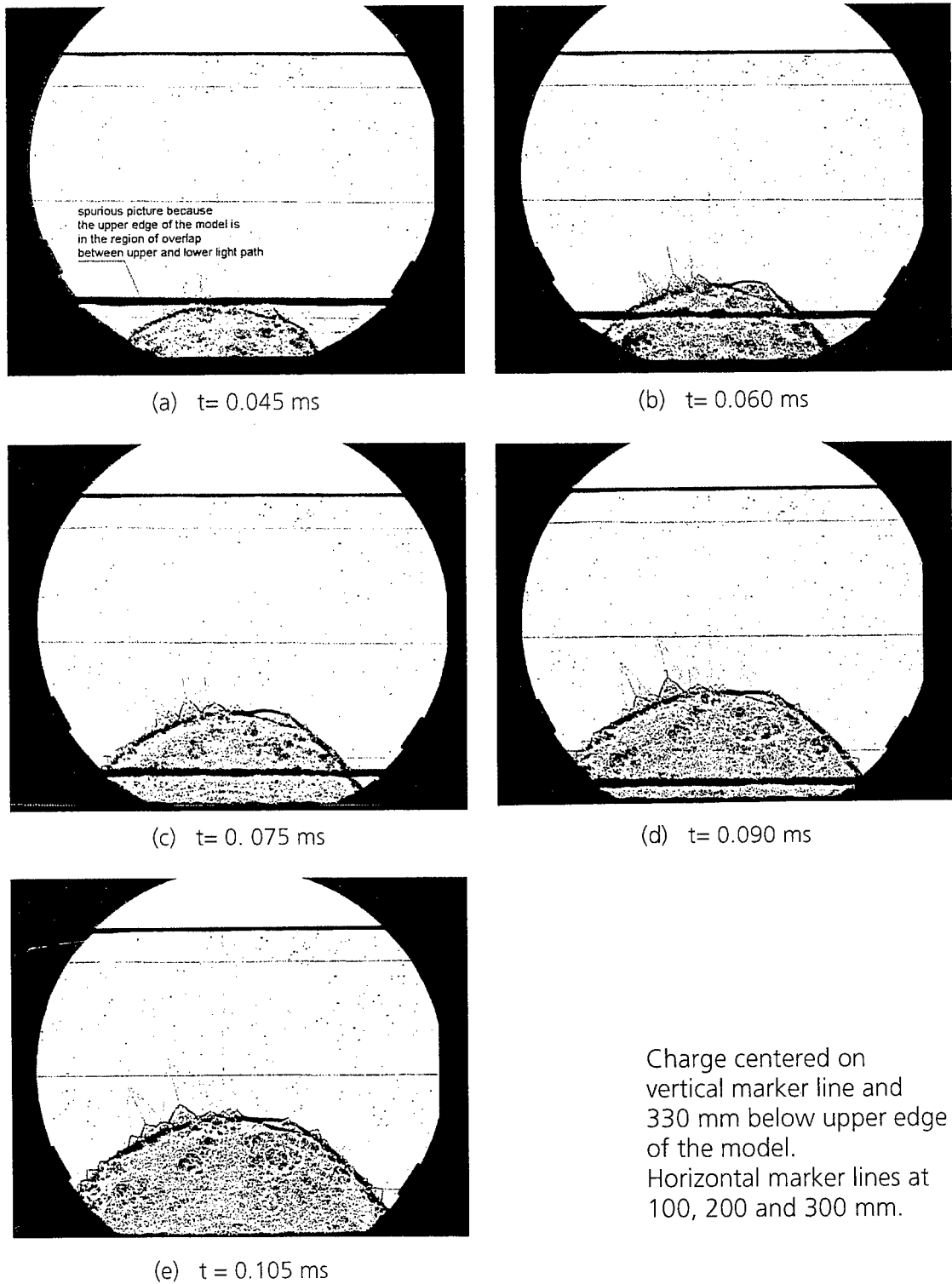
Figure 8 Pseudo-color version of Figure 7.



Figure 9 Shadow photograph (pseudo-color version) showing another experiment with a hemispherical NP-charge mounted on a transparent Makrolon pane. The test was also performed in the EMI blast tank. Charge weight $W = 0.64$ g, time after ignition $t = 0.2$ ms (test 0826.MM).



Figure 10 Third example of an experiment with a hemispherical NP-charge mounted on a transparent Makrolon pane. Charge weight $W = 0.47$ g, time after ignition $t = 0.25$ ms (test 0825.MW).



Charge centered on
vertical marker line and
330 mm below upper edge
of the model.
Horizontal marker lines at
100, 200 and 300 mm.

Figure 11 Sequence of shadowgraphs from Test 14756. Hemispherical charge on Makrolon plate. ($W = 0.64 \text{ g}$).

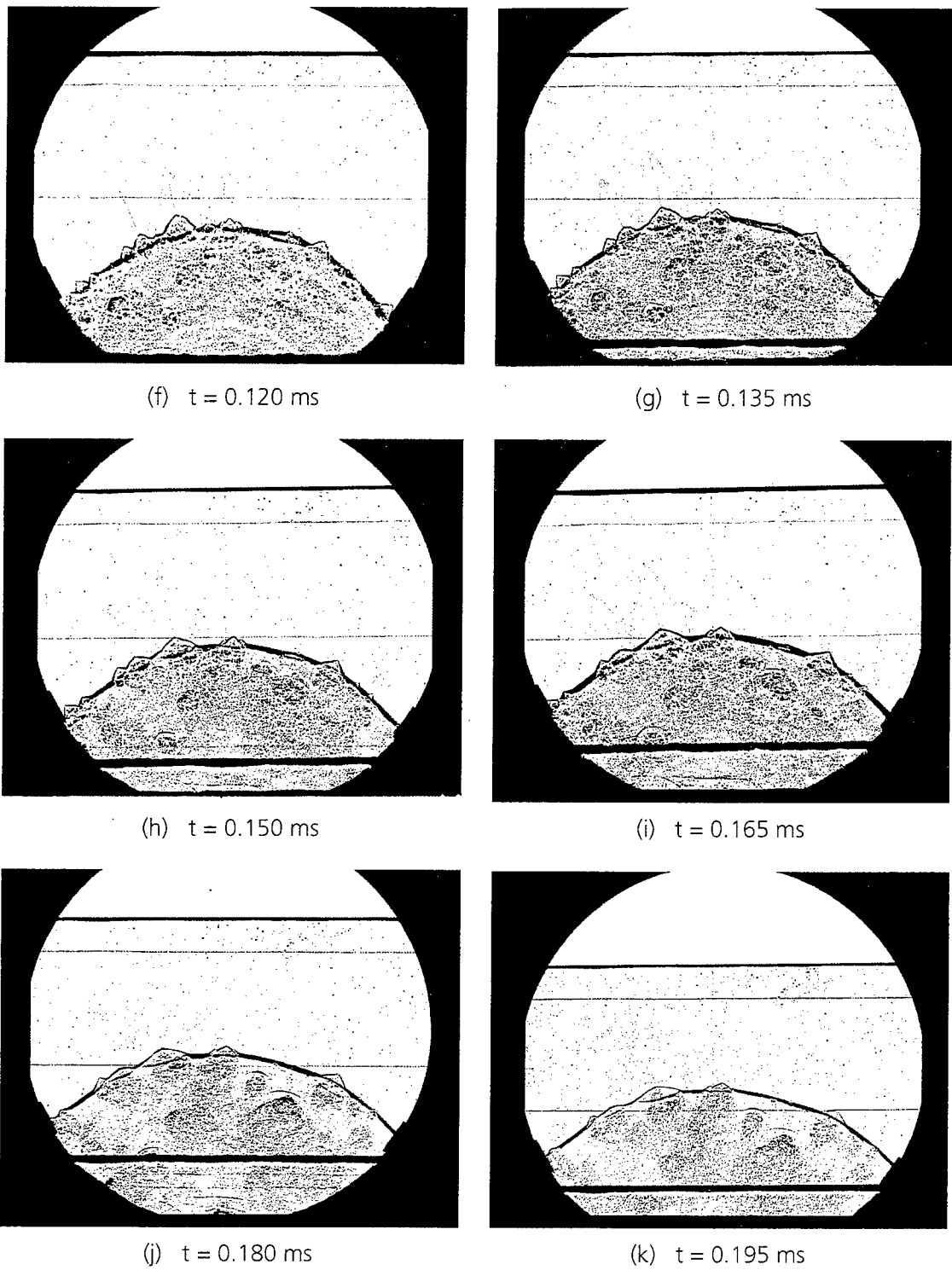
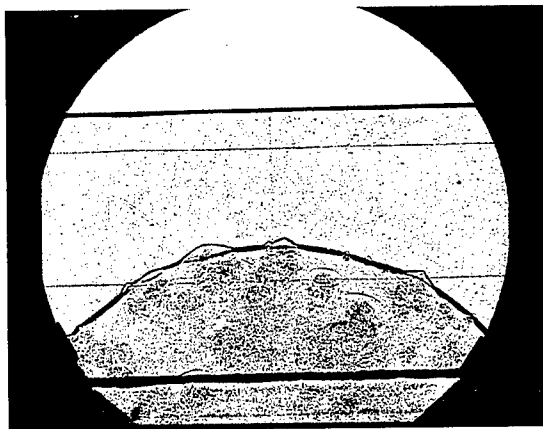


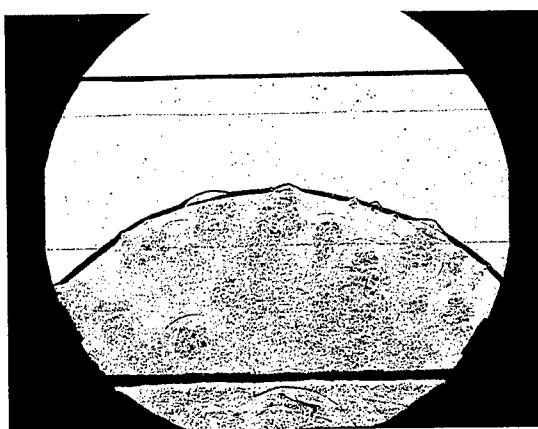
Figure 11 Sequence of shadowgraphs from Test 14756. Hemispherical charge on Makrolon plate. (Continued)



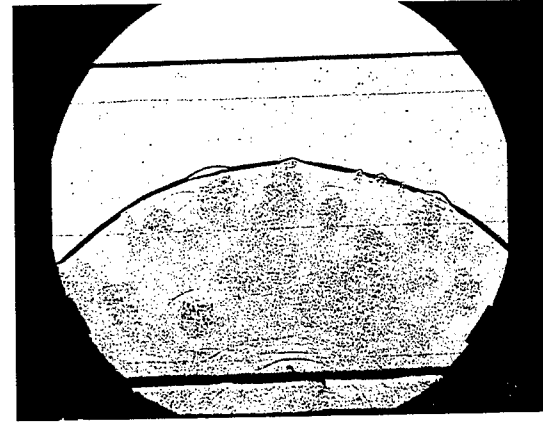
(l) $t = 0.210$ ms



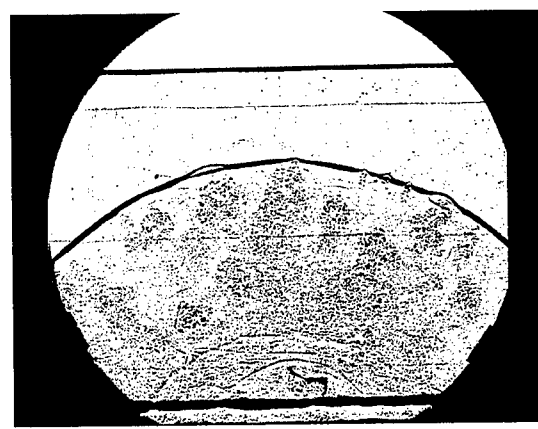
(m) $t = 0.225$ ms



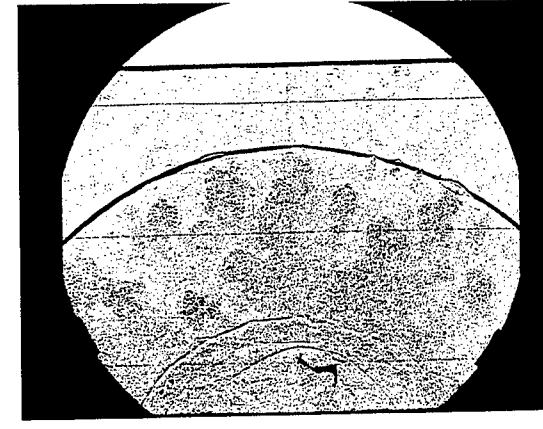
(n) $t = 0.240$ ms



(o) $t = 0.255$ ms



(p) $t = 0.270$ ms



(q) $t = 0.285$ ms

Figure 11 Sequence of shadowgraphs from Test 14756. Hemispherical charge on Makrolon plate. (Continued)

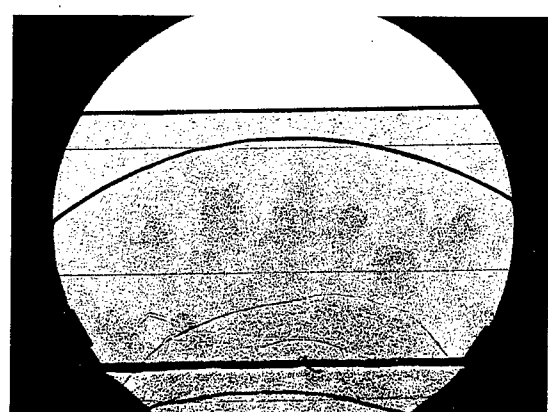
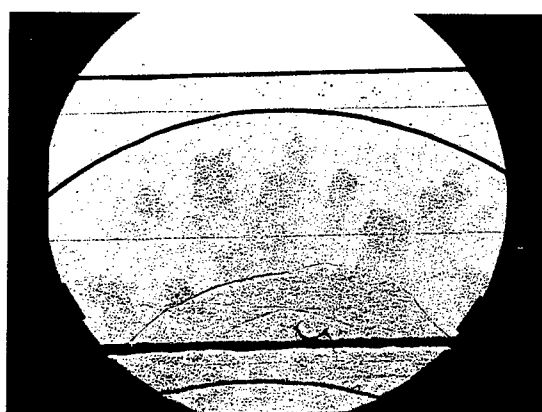
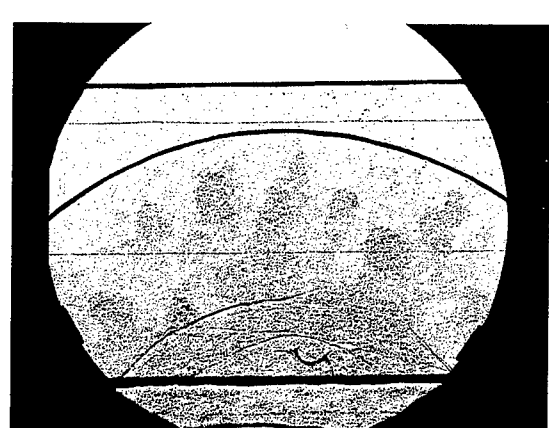
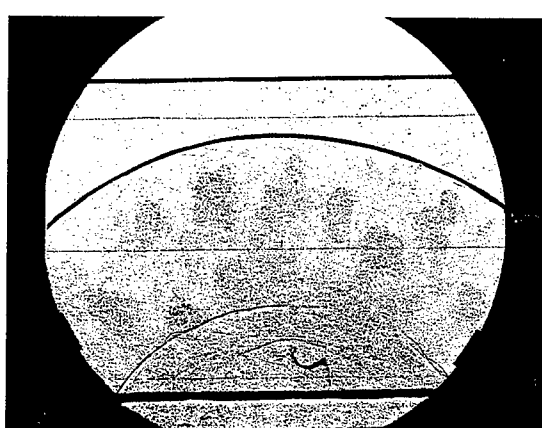
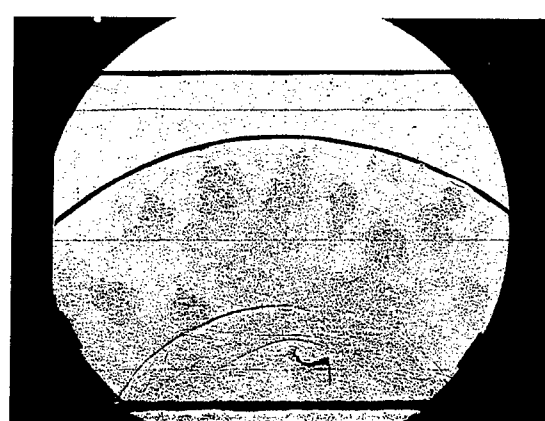
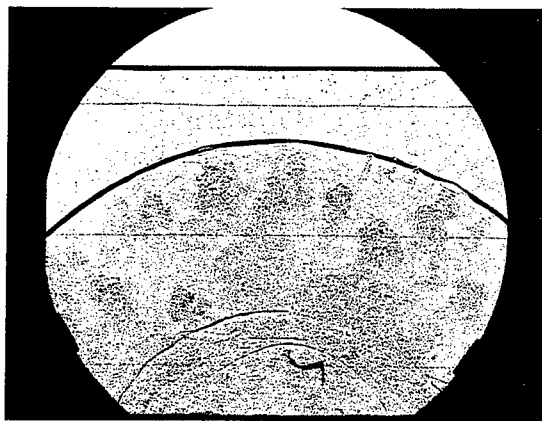


Figure 11 Sequence of shadowgraphs from Test 14756. Hemispherical charge on Makrolon plate. (Continued)

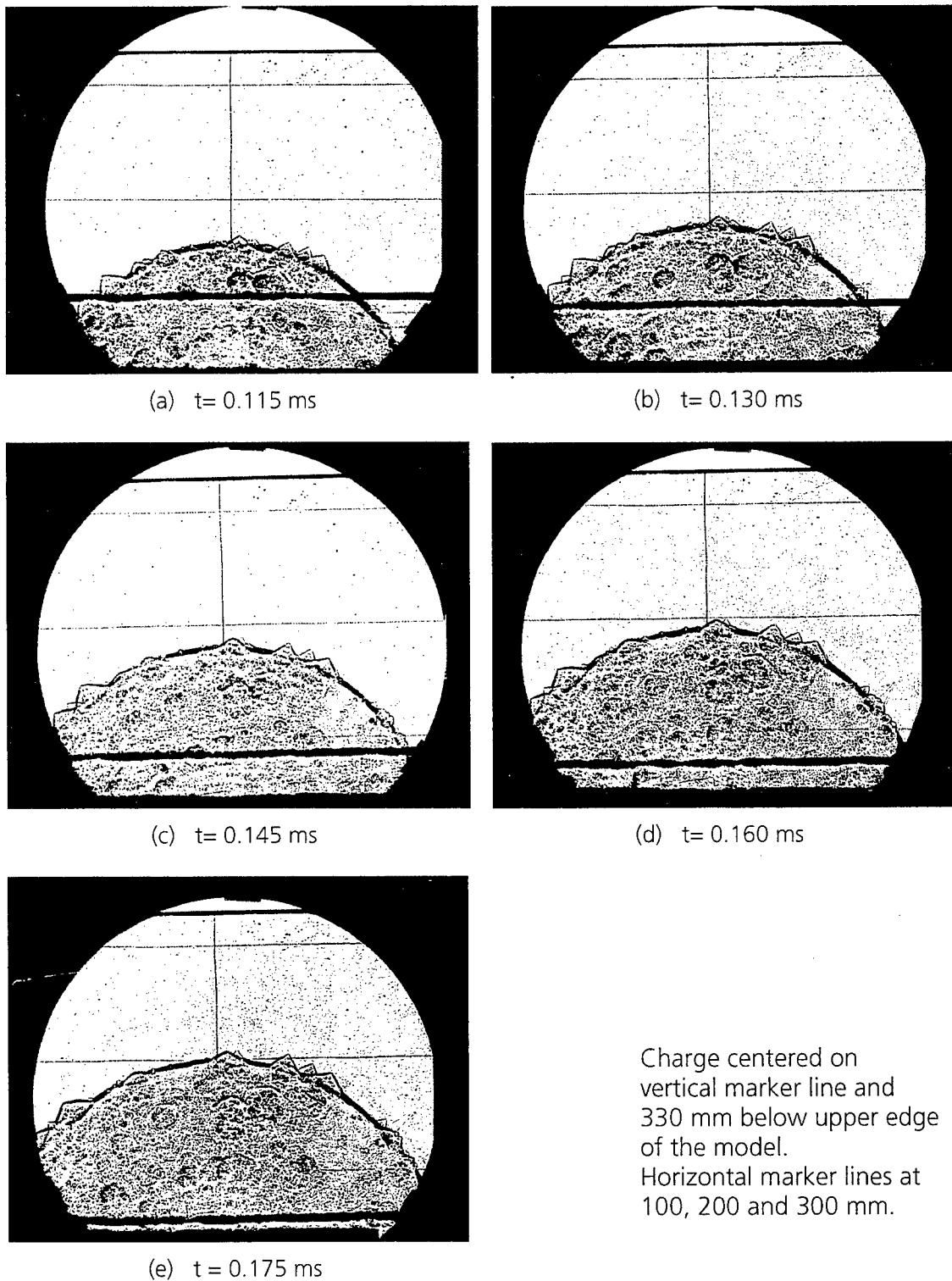


Figure 12 Sequence of shadowgraphs from Test 14757. Hemispherical charge on Makrolon plate. ($W = 0.63$ g)

Charge centered on
vertical marker line and
330 mm below upper edge
of the model.
Horizontal marker lines at
100, 200 and 300 mm.

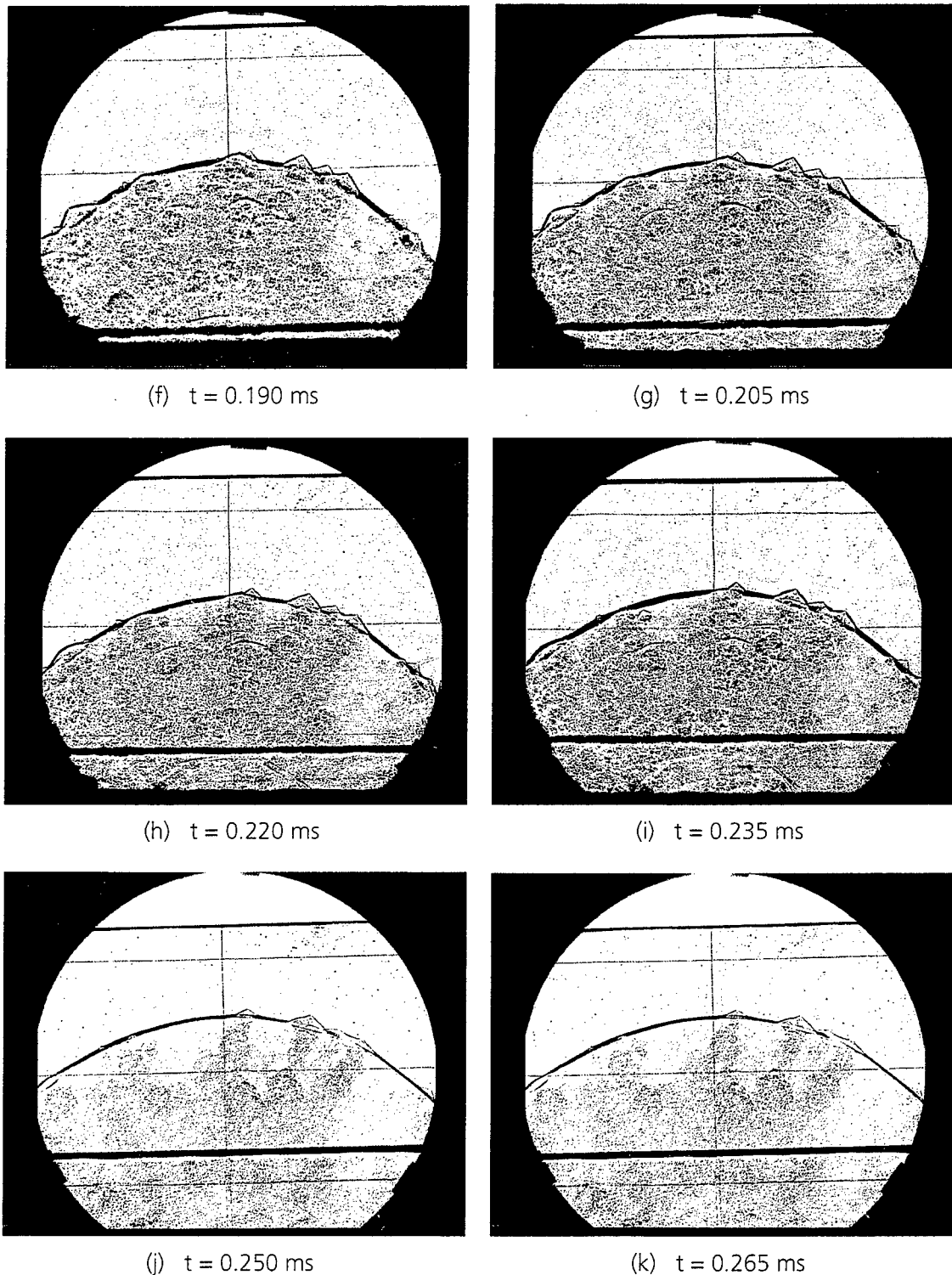
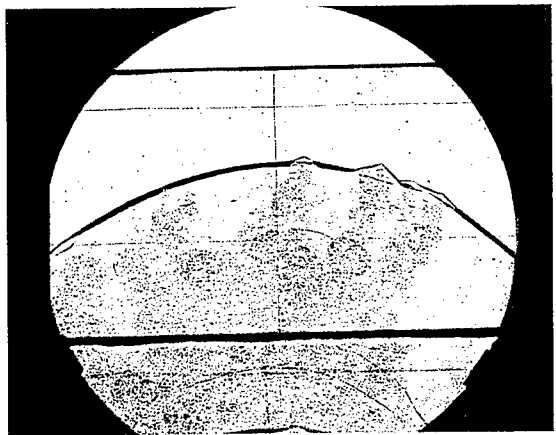
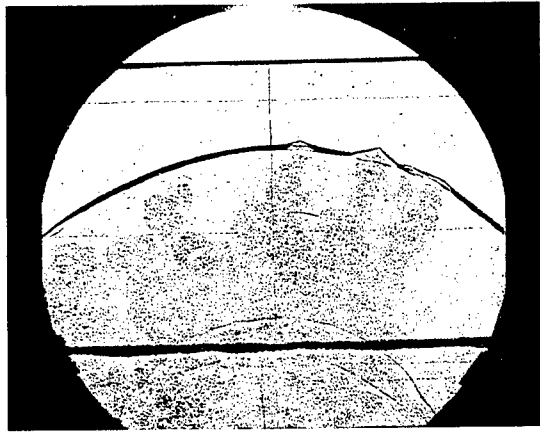


Figure 12 Sequence of shadowgraphs from Test 14757. Hemispherical charge on Makrolon plate. (Continued)



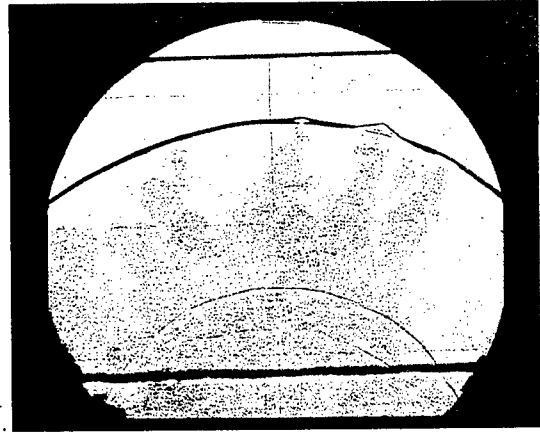
(l) $t = 0.280$ ms



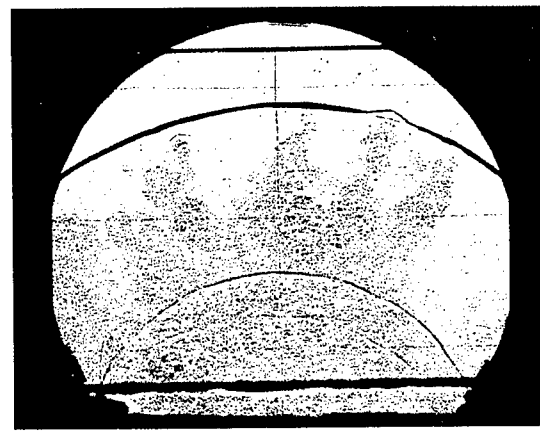
(m) $t = 0.295$ ms



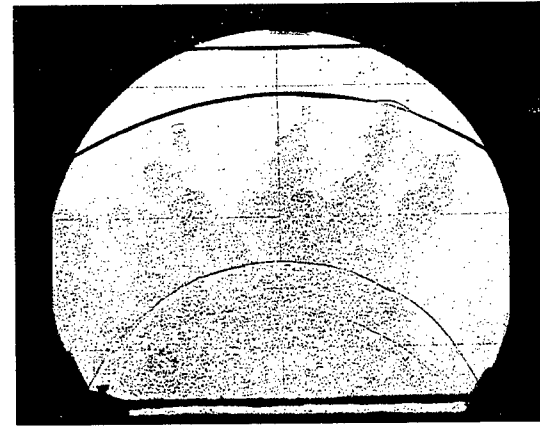
(n) $t = 0.310$ ms



(o) $t = 0.325$ ms

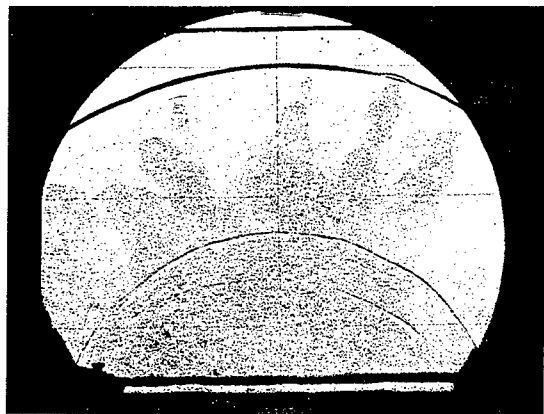


(p) $t = 0.340$ ms

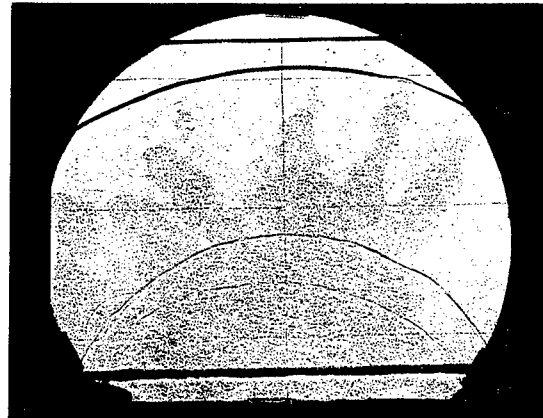


(q) $t = 0.355$ ms

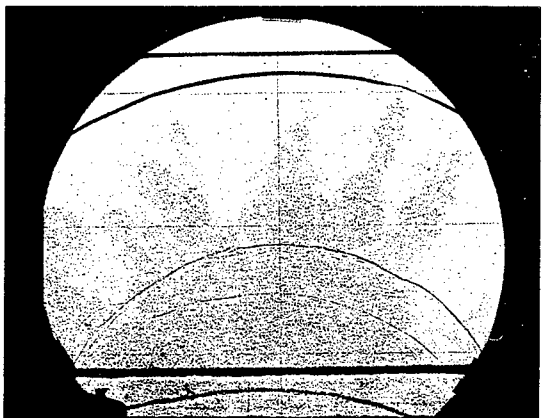
Figure 12 Sequence of shadowgraphs from Test 14757. Hemispherical charge on Makrolon plate. (Continued)



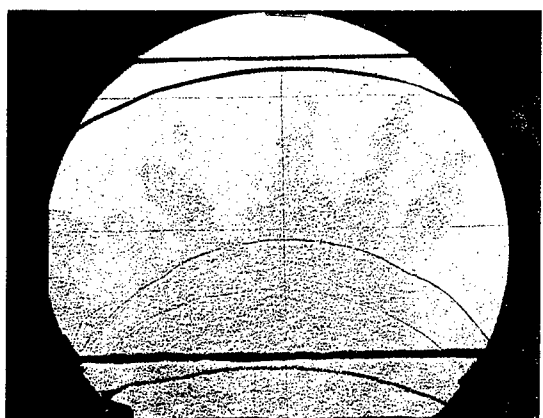
(r) $t = 0.370$ ms



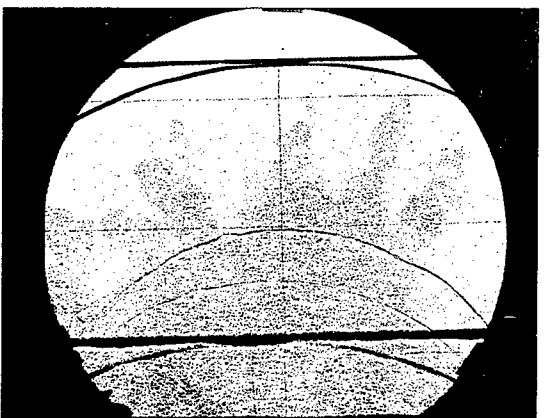
(s) $t = 0.385$ ms



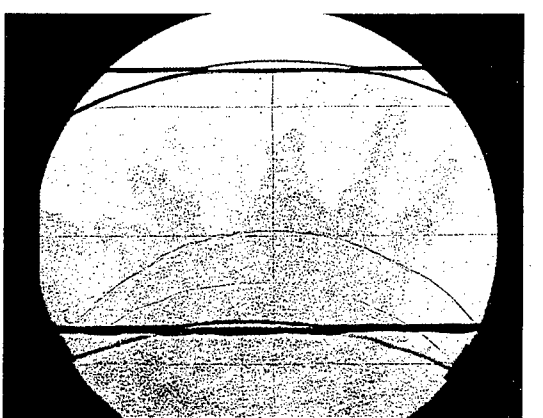
(t) $t = 0.400$ ms



(u) $t = 0.415$ ms

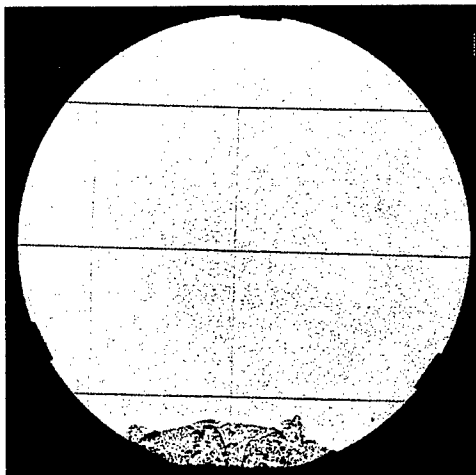


(v) $t = 0.430$ ms

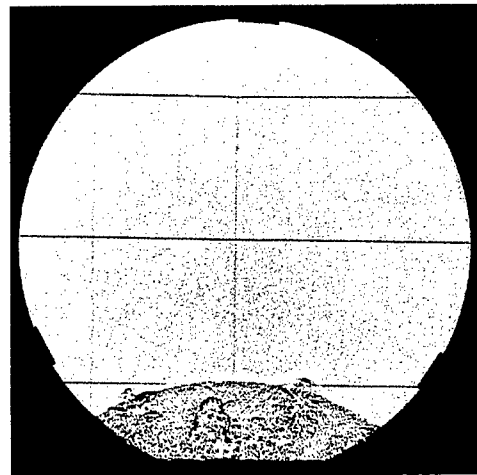


(w) $t = 0.445$ ms

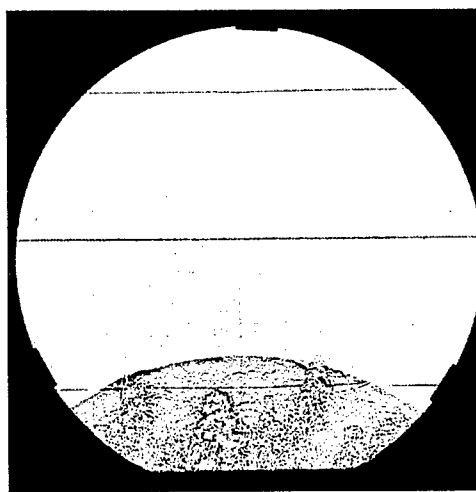
Figure 12 Sequence of shadowgraphs from Test 14757. Hemispherical charge on Makrolon plate. (Continued)



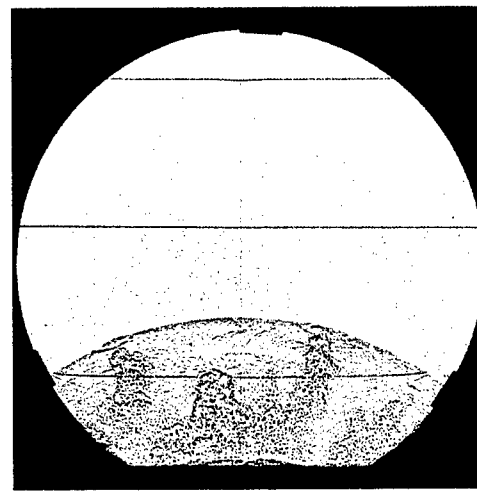
(a) $t = 0.181$ ms



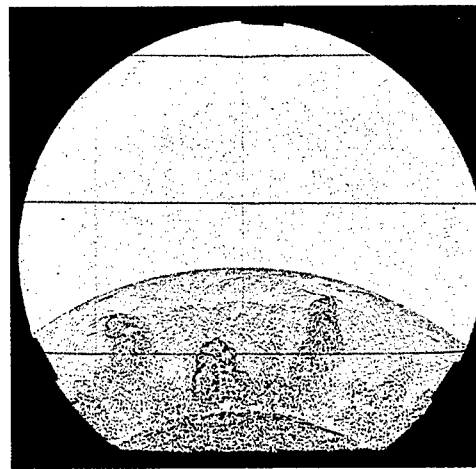
(b) $t = 0.221$ ms



(c) $t = 0.261$ ms



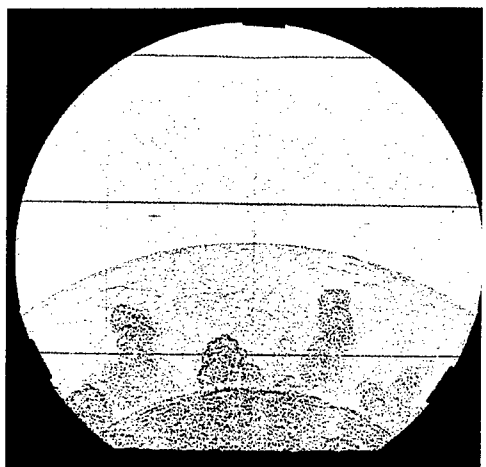
(d) $t = 0.301$ ms



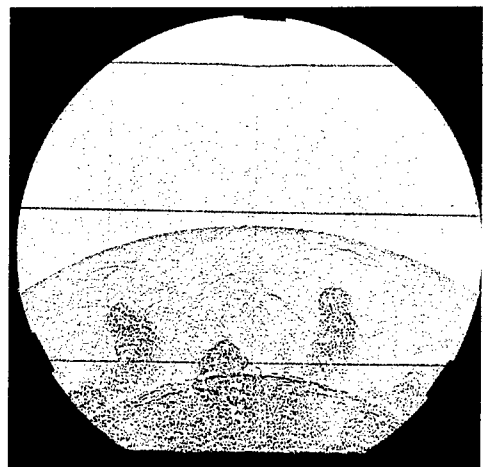
(e) $t = 0.341$ ms

Charge centered on right vertical marker line and 200 mm below lower horizontal marker line.
Grid width of marker lines:
100 mm x 100 mm.

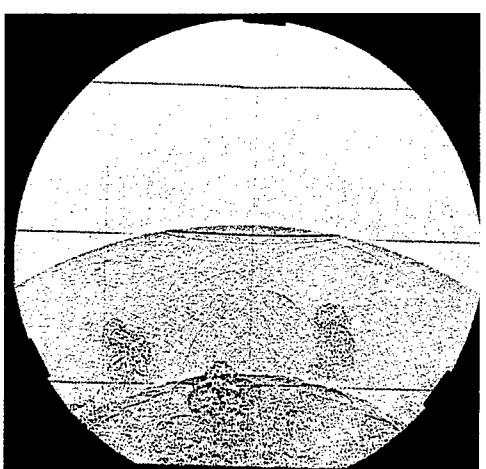
Figure 13 Sequence of shadowgraphs from Test 15086. Spherical charge in free air ($W = 0.49$ g).



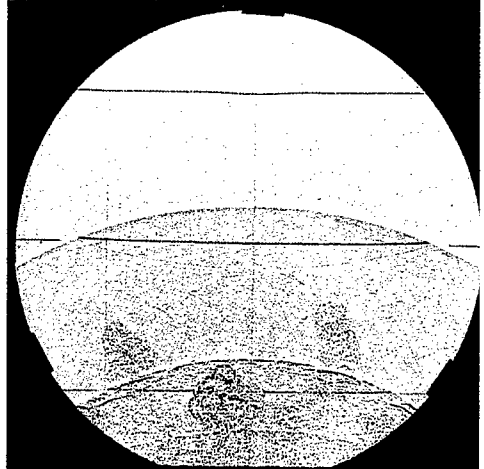
(f) $t = 0.381$ ms



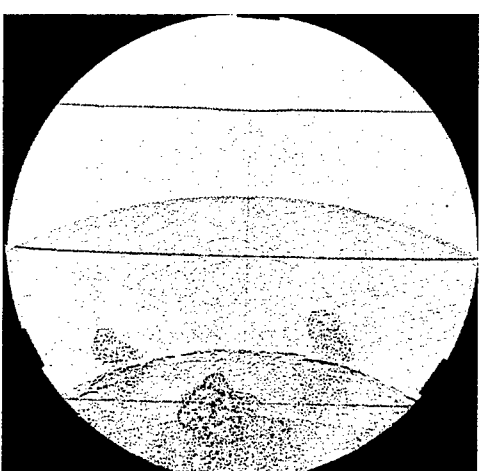
(g) $t = 0.421$ ms



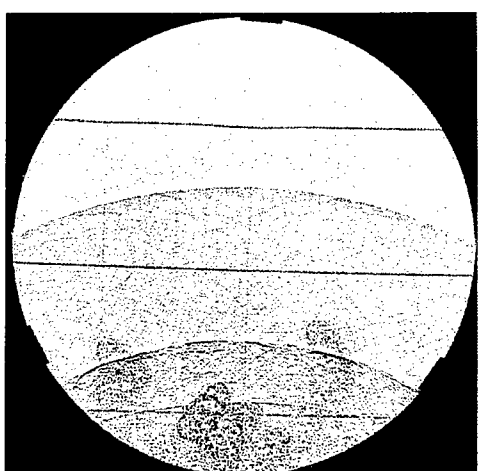
(h) $t = 0.461$ ms



(i) $t = 0.501$ ms

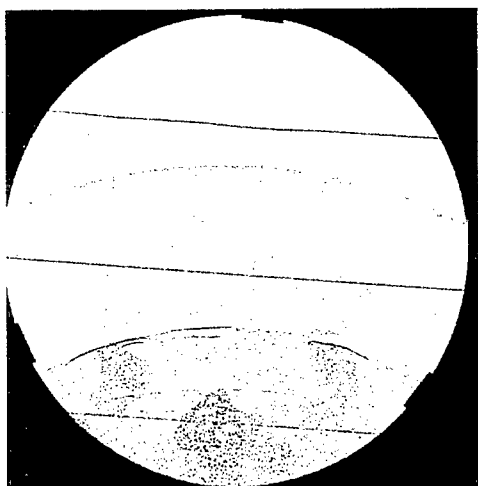


(j) $t = 0.541$ ms

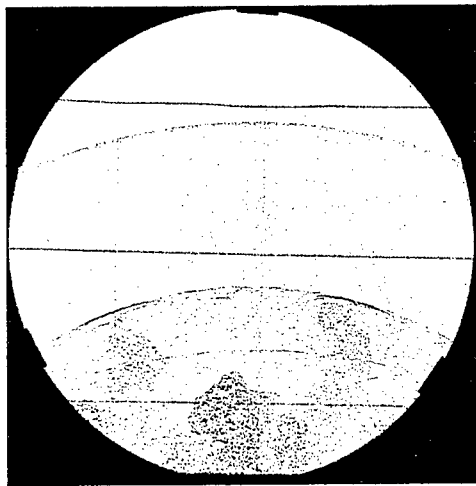


(k) $t = 0.581$ ms

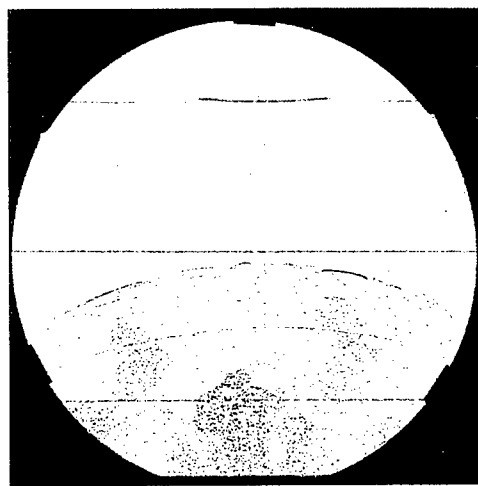
Figure 13 Sequence of shadowgraphs from Test 15086. Spherical charge in free air. (Continued)



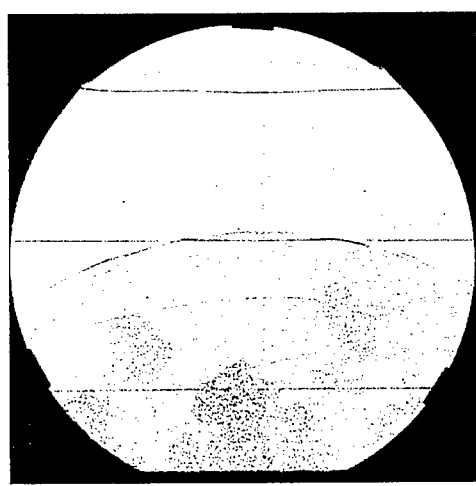
(l) $t = 0.621$ ms



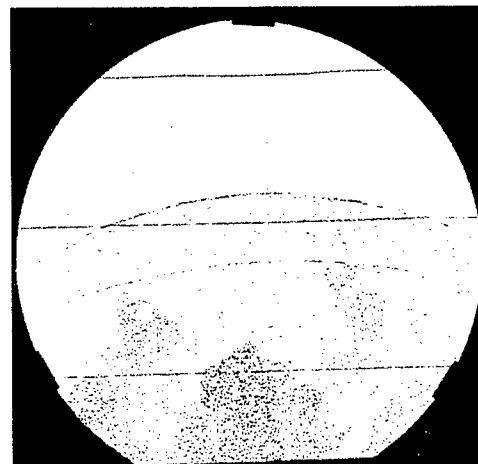
(m) $t = 0.661$ ms



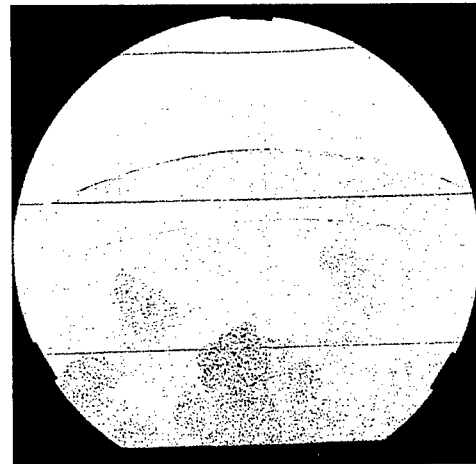
(n) $t = 0.701$ ms



(o) $t = 0.741$ ms



(p) $t = 0.781$ ms



(q) $t = 0.821$ ms

Figure 13 Sequence of shadowgraphs from Test 15086. Spherical charge in free air. (Continued)

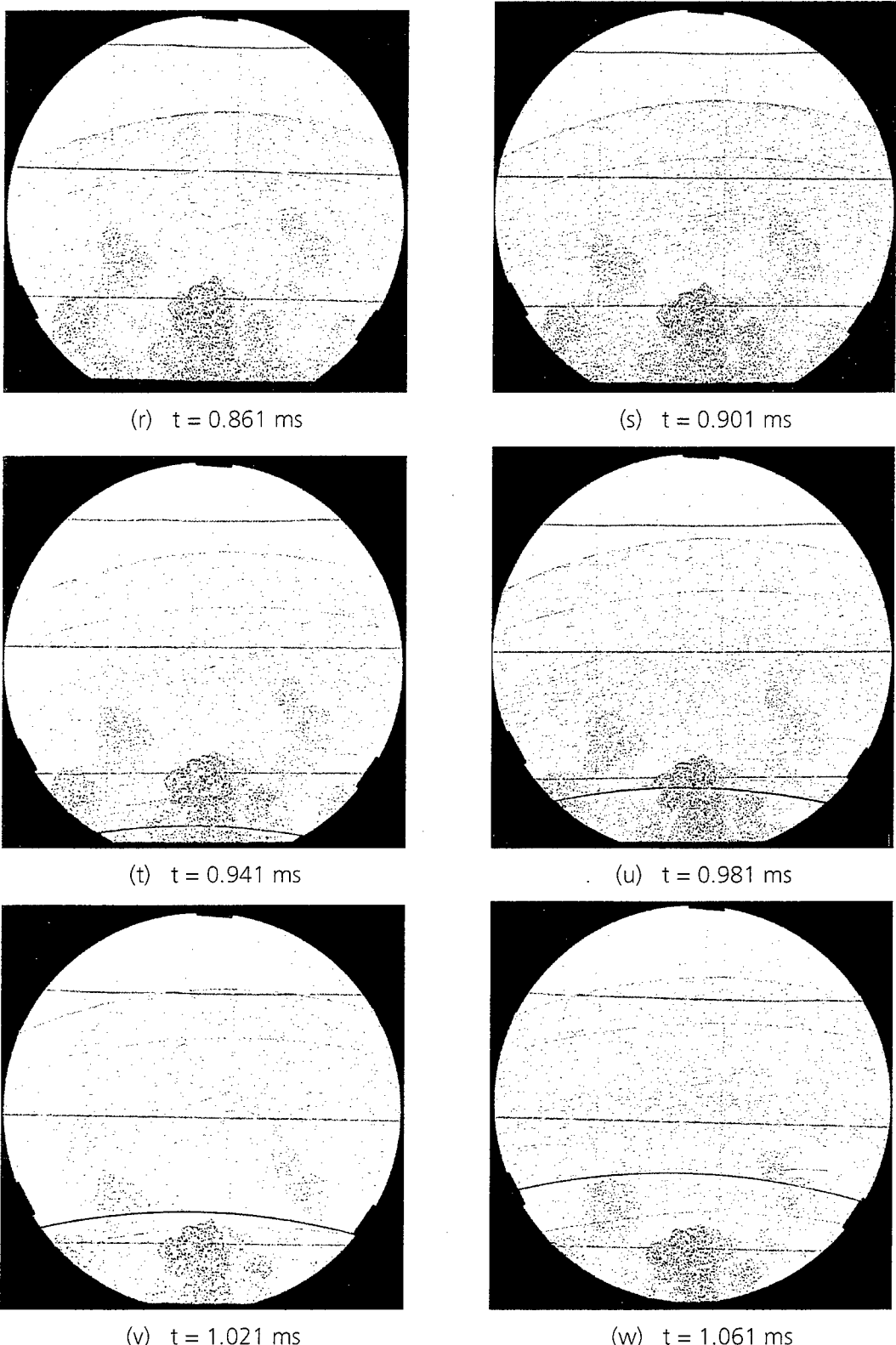
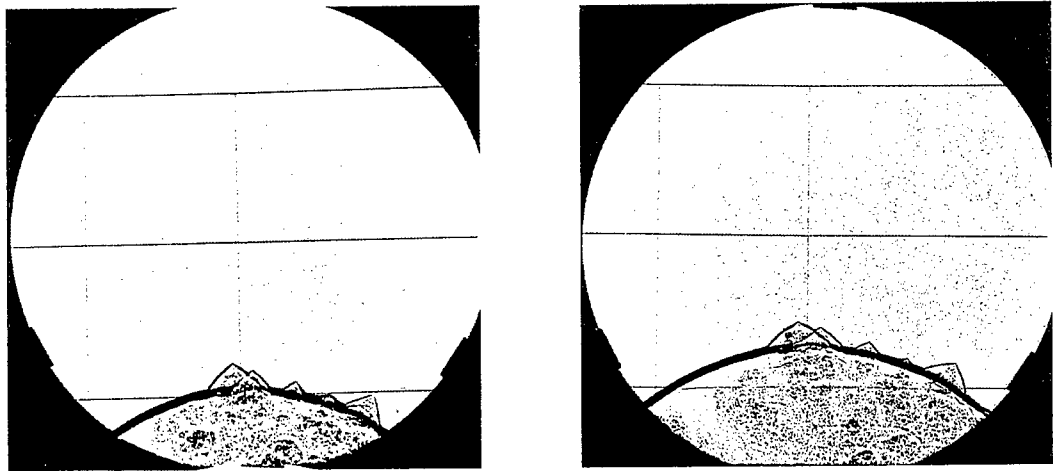
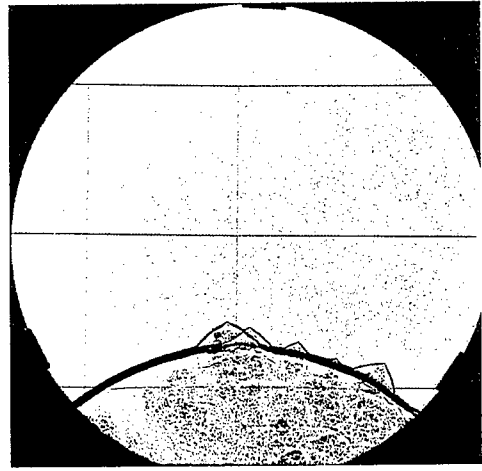


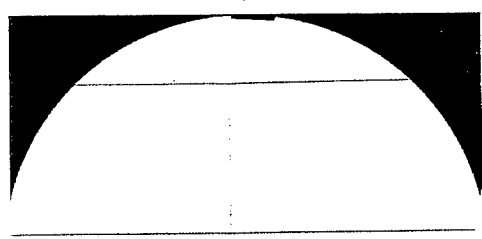
Figure 13 Sequence of shadowgraphs from Test 15086. Spherical charge in free air. (Continued)



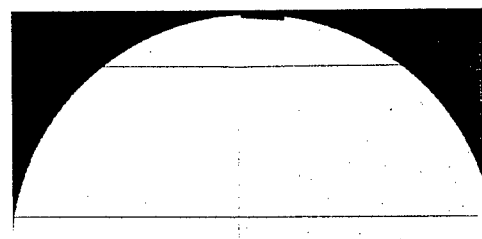
(a) $t = 0.140$ ms



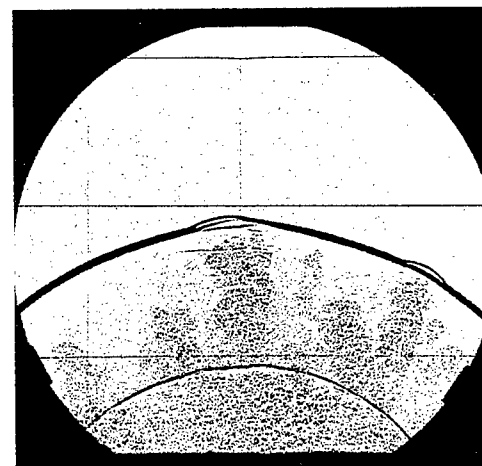
(b) $t = 0.180$ ms



(c) $t = 0.220$ ms



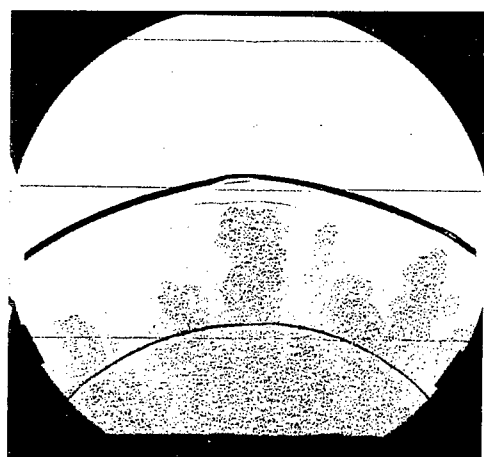
(d) $t = 0.260$ ms



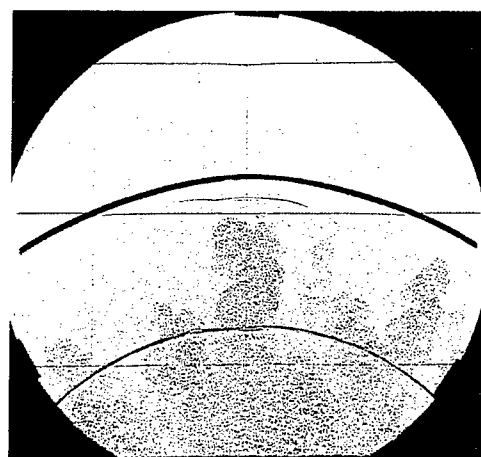
(e) $t = 0.300$ ms

Charge centered on right vertical marker line and 150 mm below lower horizontal marker line.
Grid width of marker lines: 100 mm x 100 mm.

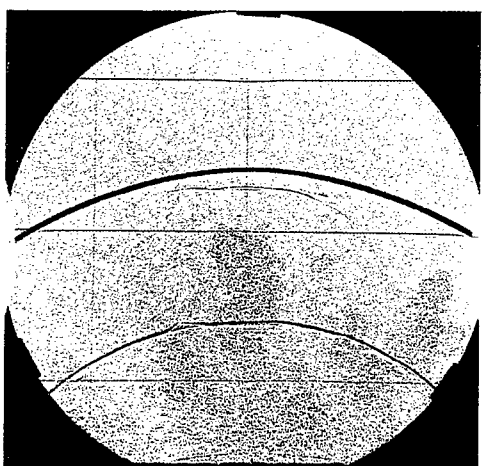
Figure 14 Sequence of shadowgraphs from Test 15087. Spherical charge in free air ($W = 0.53$ g).



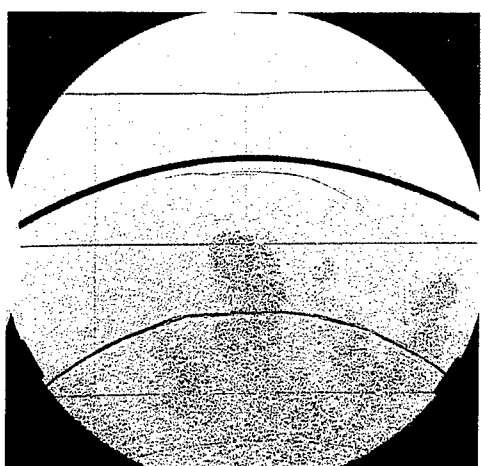
(f) $t = 0.340$ ms



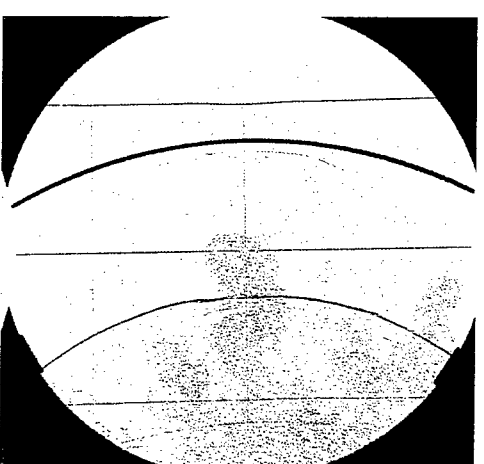
(g) $t = 0.380$ ms



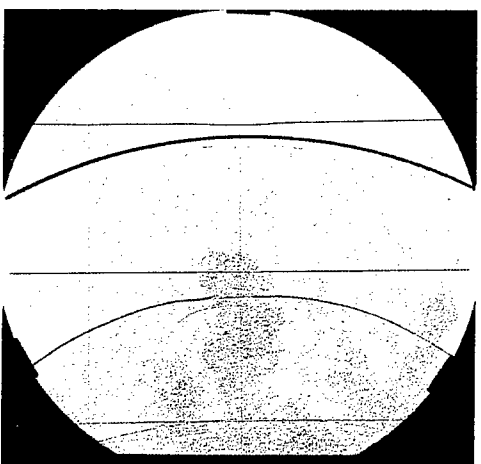
(h) $t = 0.420$ ms



(i) $t = 0.460$ ms



(j) $t = 0.500$ ms



(k) $t = 0.540$ ms

Figure 14 Sequence of shadowgraphs from Test 15087. Spherical charge in free air. (Continued)

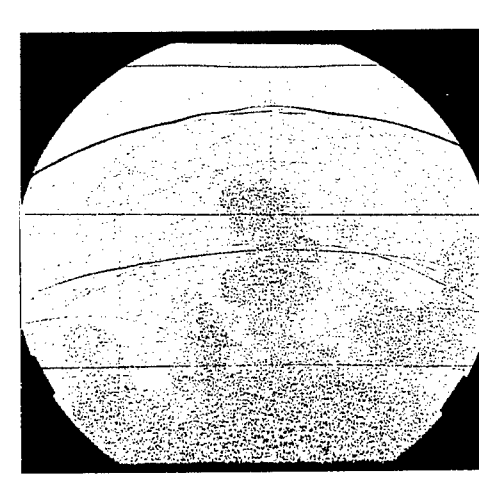
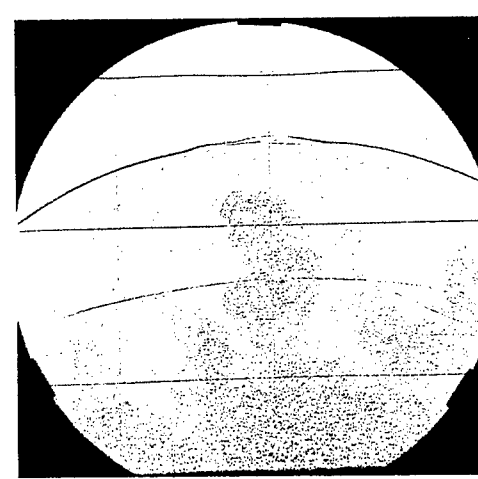
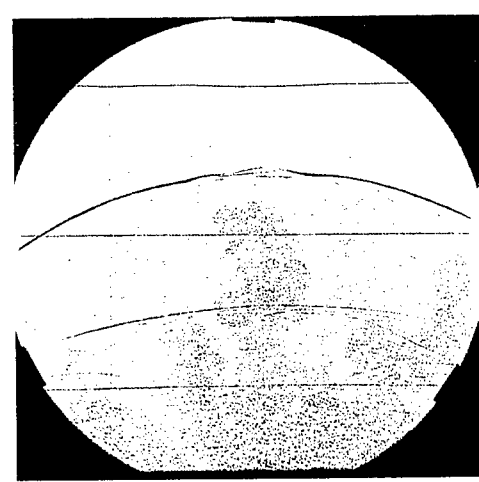
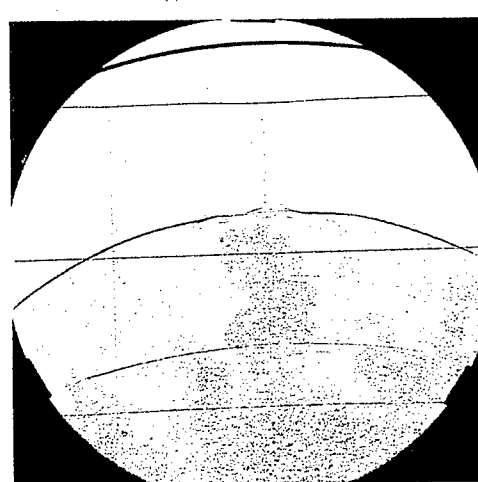
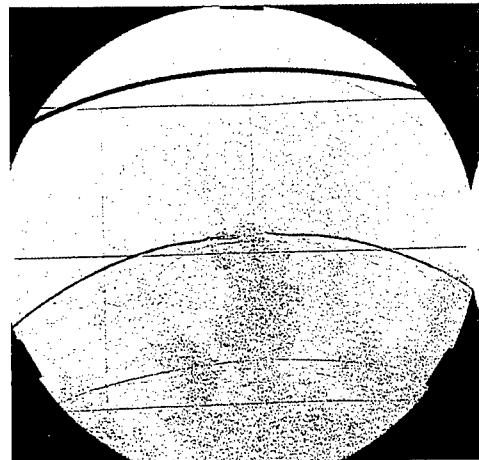
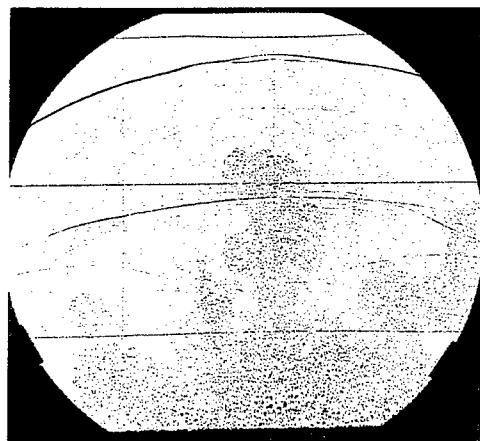
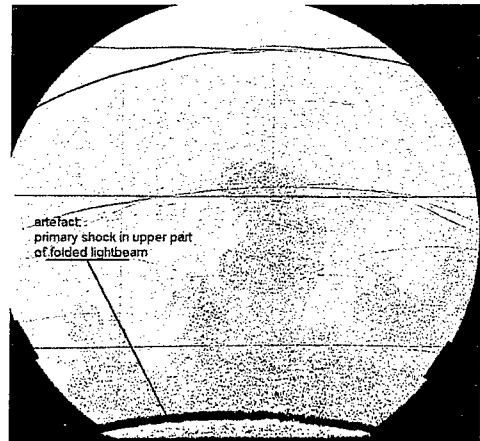


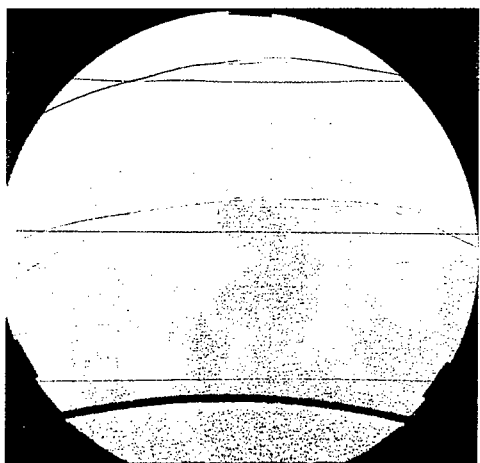
Figure 14 Sequence of shadowgraphs from Test 15087. Spherical charge in free air. (Continued)



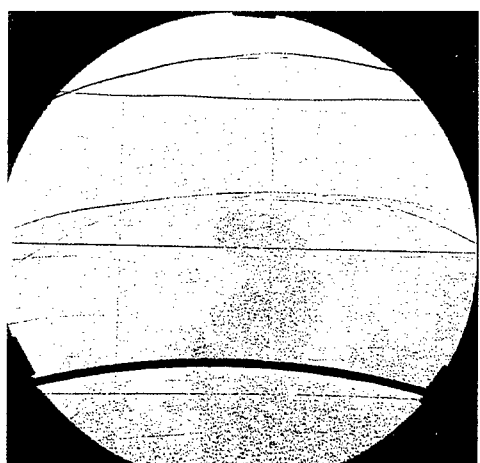
(r) $t = 0.861$ ms



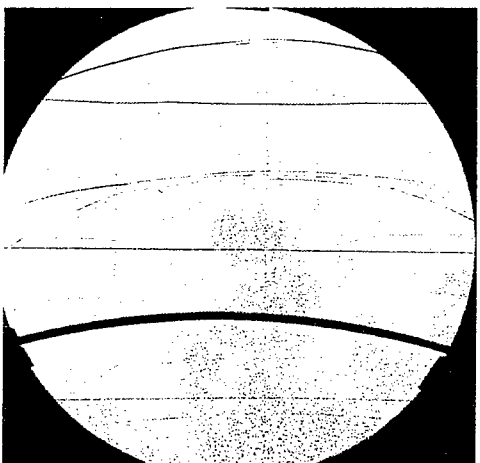
(s) $t = 0.901$ ms



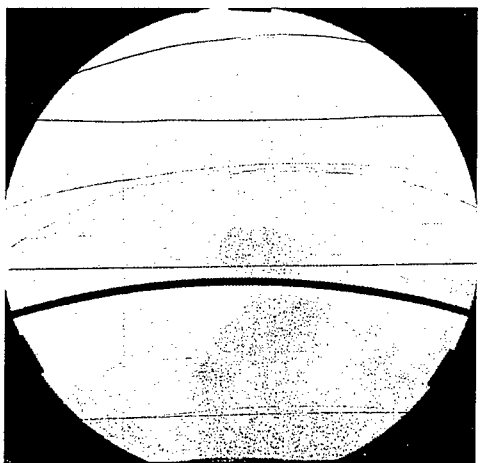
(t) $t = 0.941$ ms



(u) $t = 0.981$ ms



(v) $t = 1.021$ ms



(w) $t = 1.061$ ms

Figure 14 Sequence of shadowgraphs from Test 15087. Spherical charge in free air. (Continued)

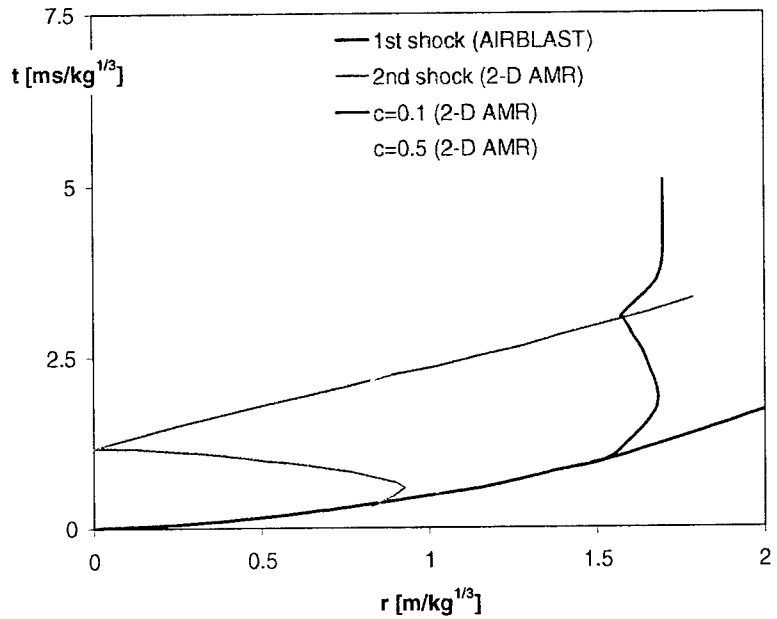


Figure 15 Scaled wave diagram for the detonation of a TNT-charge according to a 2-D AMR calculation [1]. Data for the primary blast front are derived from the code AIRBLAST [2]. The red and green line are iso-contour lines of the normalized, average concentration of fuel (unburned detonation products).

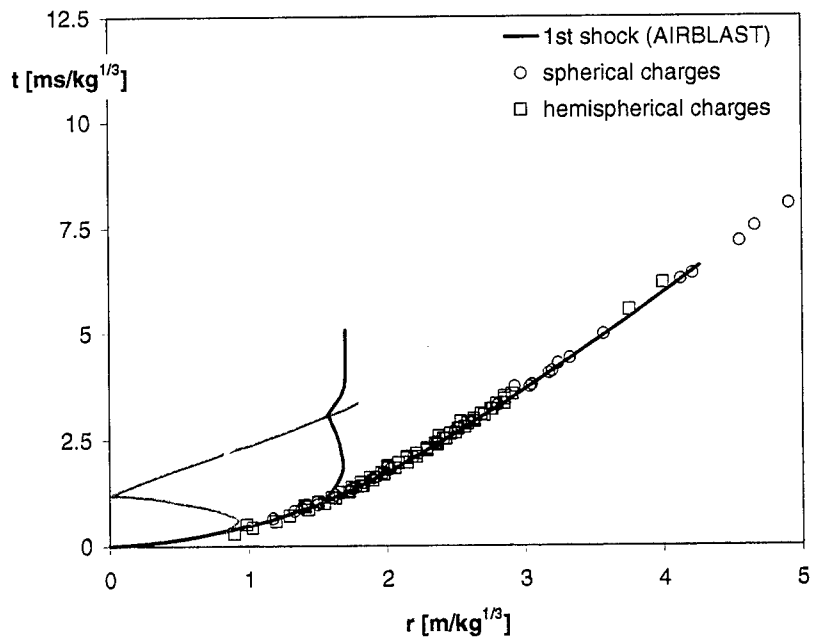


Figure 16 Comparison of the experimental results for the primary blast front to the data from AIRBLAST.

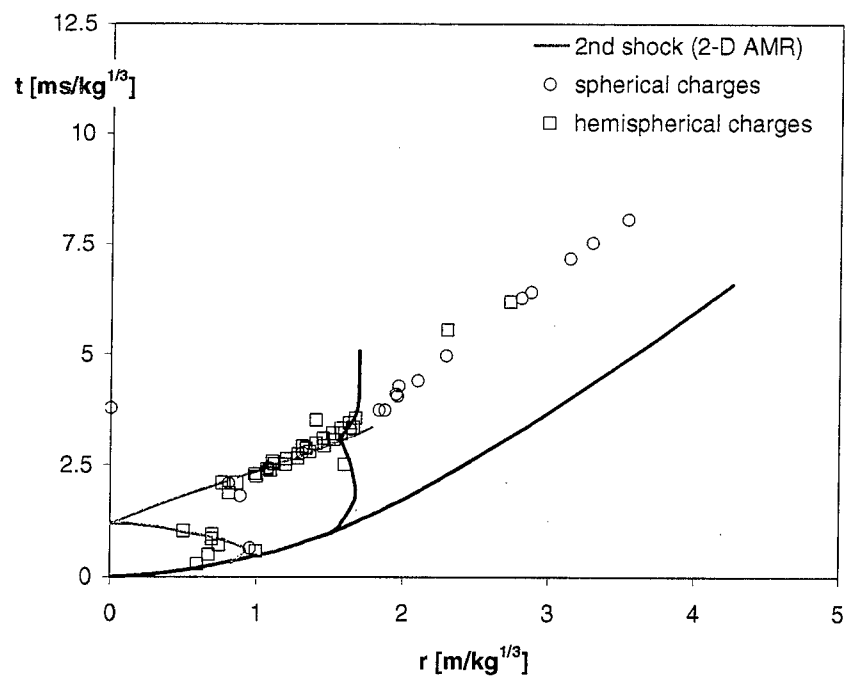


Figure 17 Comparison of the experimental results for the secondary blast front to the results of the 2-D AMR calculation.

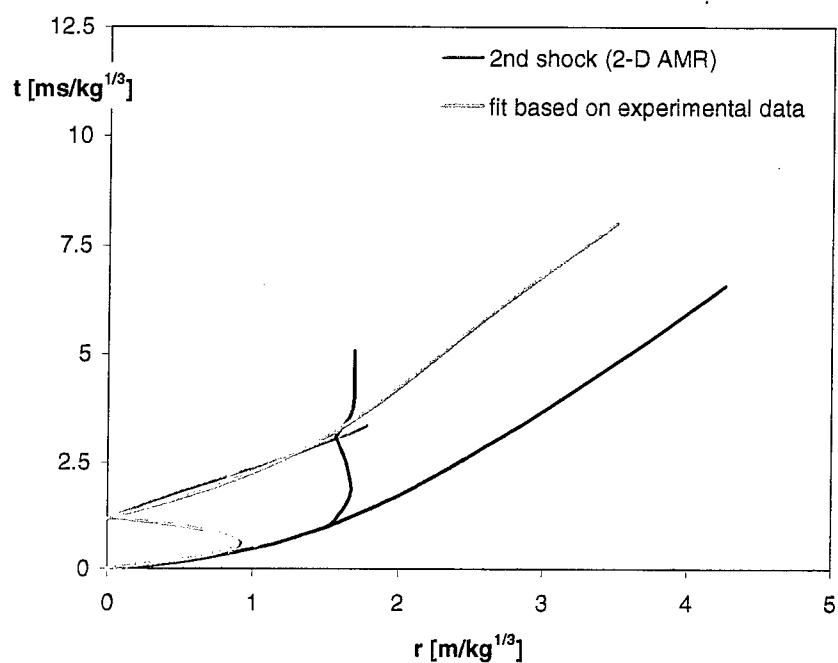


Figure 18 Fit based on the experimental data replacing the result of 2-D AMR calculation in the wave diagram.

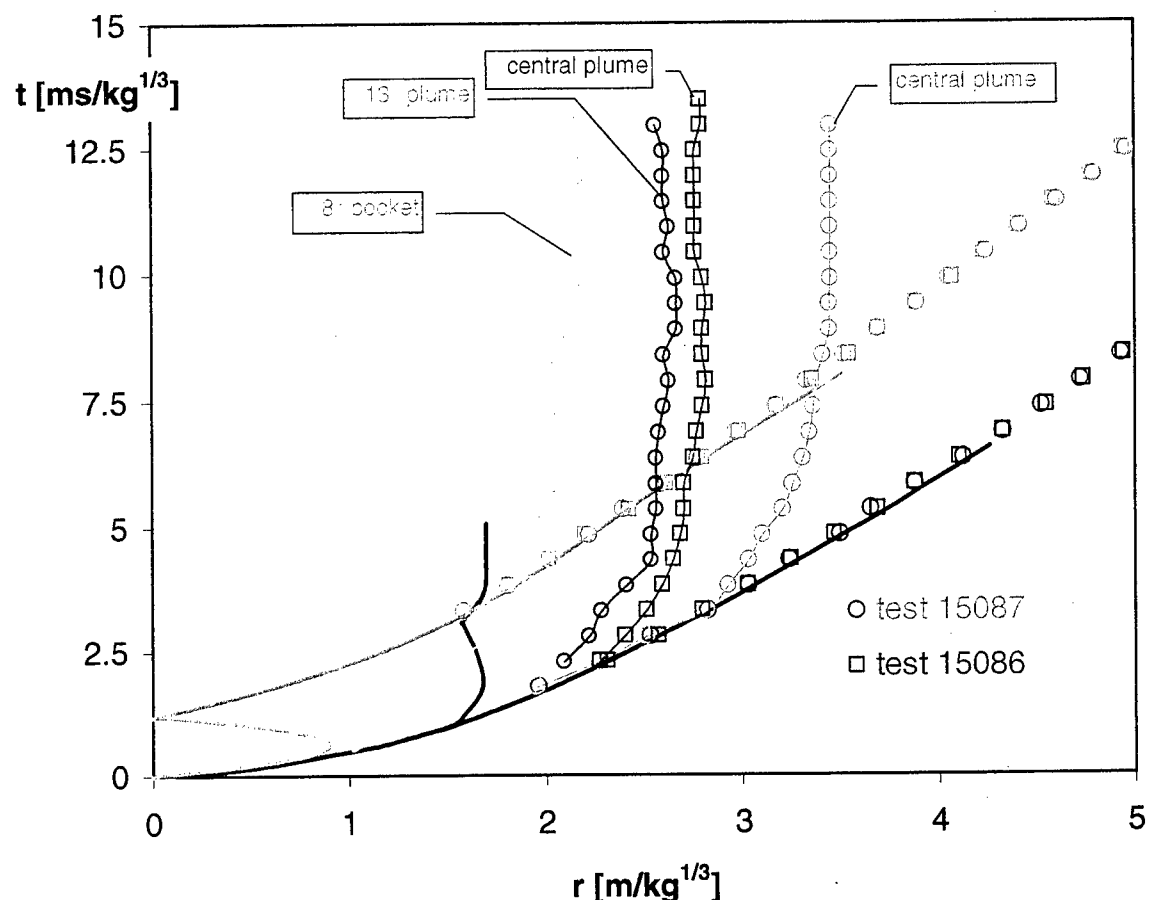


Figure 19 Experimental data from Tests 15086 and 15087 compared to the wave diagram. Tests were performed with spherical charges in free air. Charge weight: 0.49 g (test 15086) and 0.53 g (test 15087).

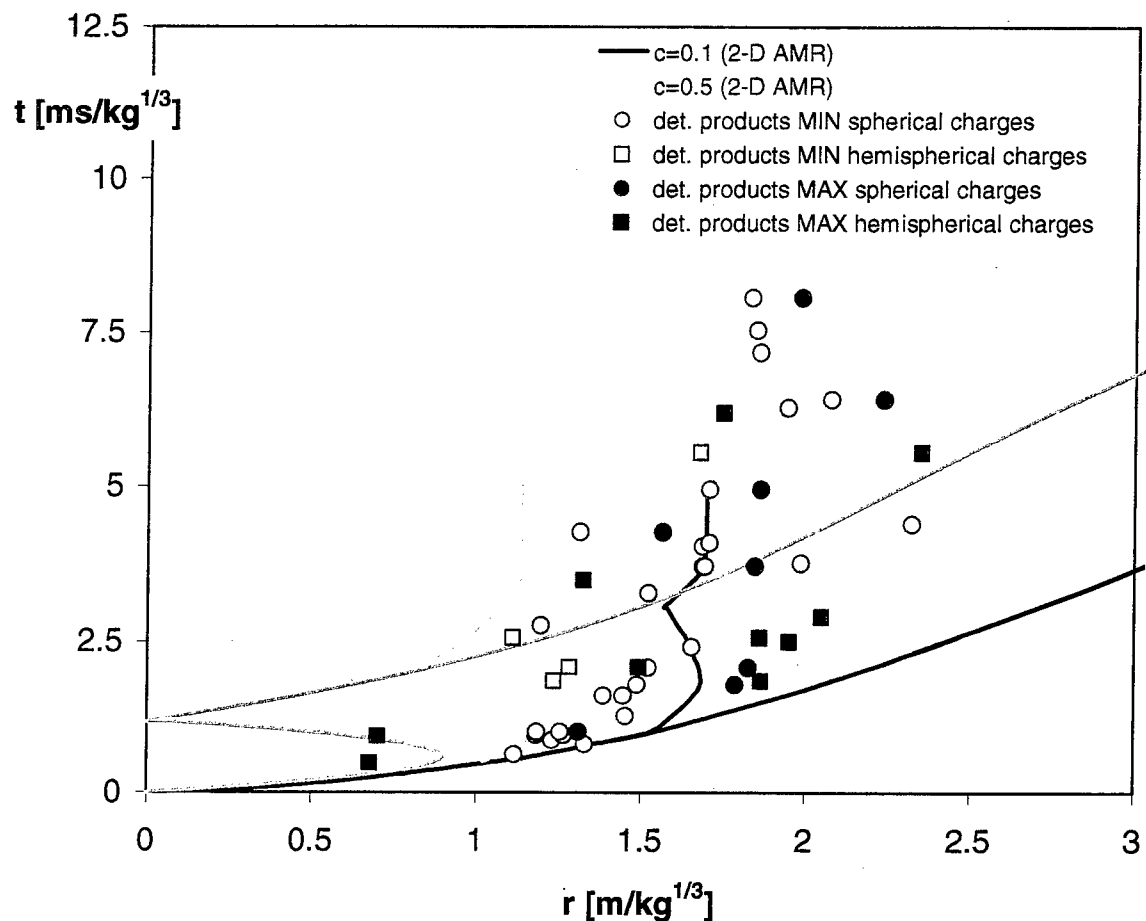


Figure 20 Experimental data from single-shot tests compared to the wavediagram. The shadowgraphs were analyzed for the apparent maximum and minimum radial extent of the products cloud visible within the field of view. Differences to Figure 19 can be explained by different detectability thresholds of the two optical setups.

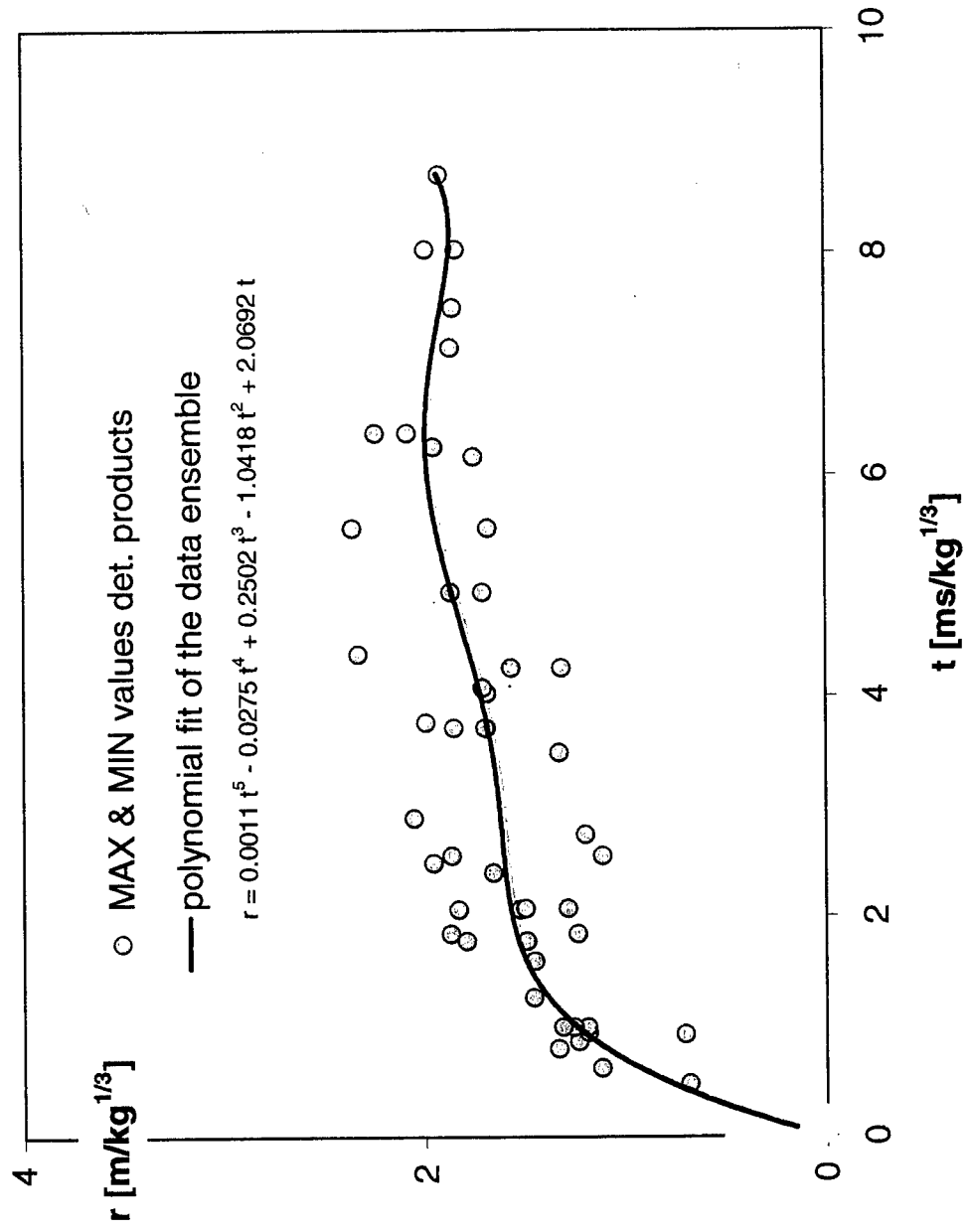


Figure 21 Polynomial fit of the data ensemble derived from the evaluation of single -shot experiments. In grey the bandwidth containing all data samples (approximately $\pm 0.4 \text{ m}/\text{kg}^{1/3}$)

Figure 21

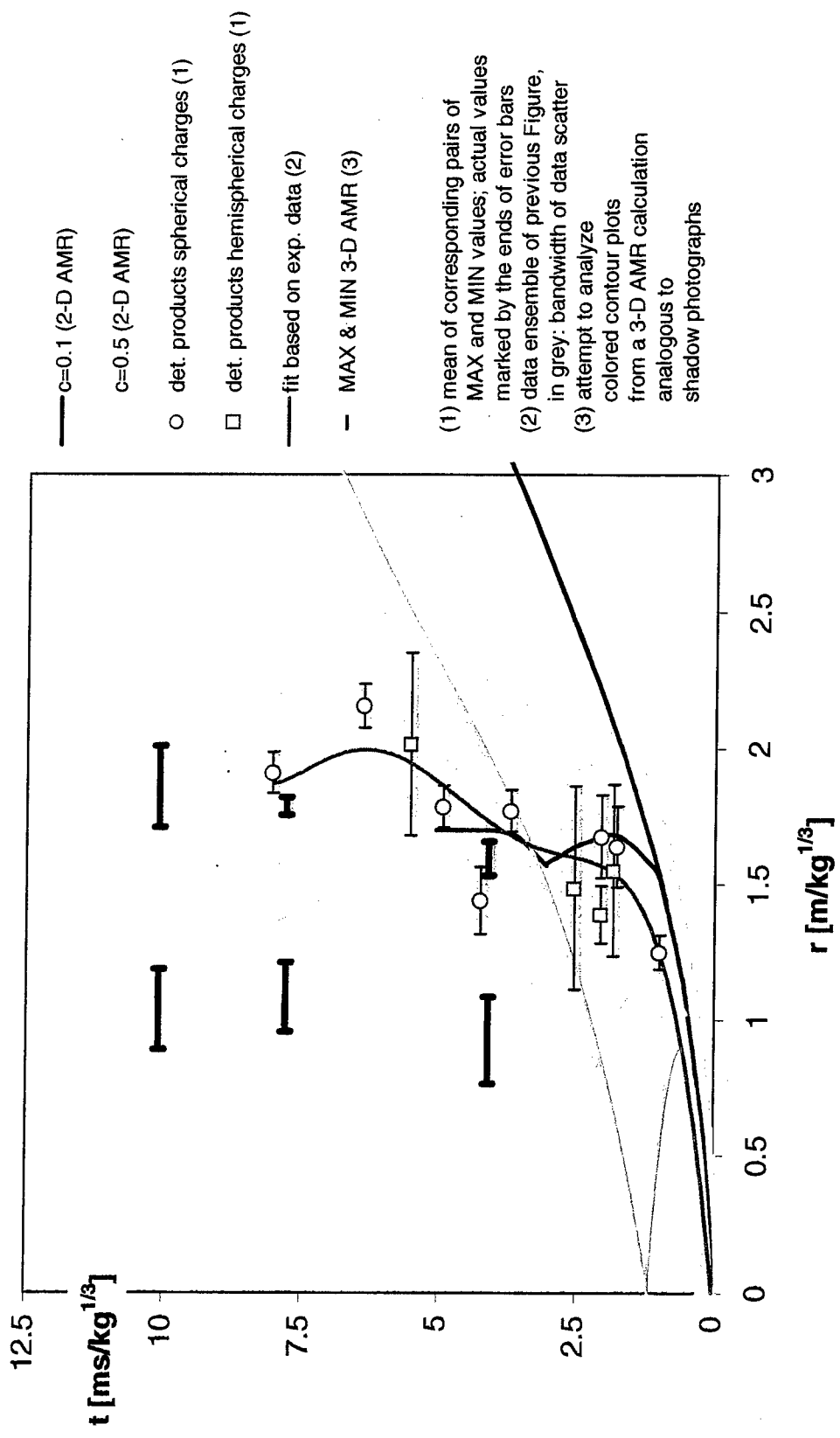


Figure 22

The average radial extent of the products cloud as derived from single-shot experiments compared to the results of the 2-D AMR calculation. Also included are some data from a 3-D AMR calculation.

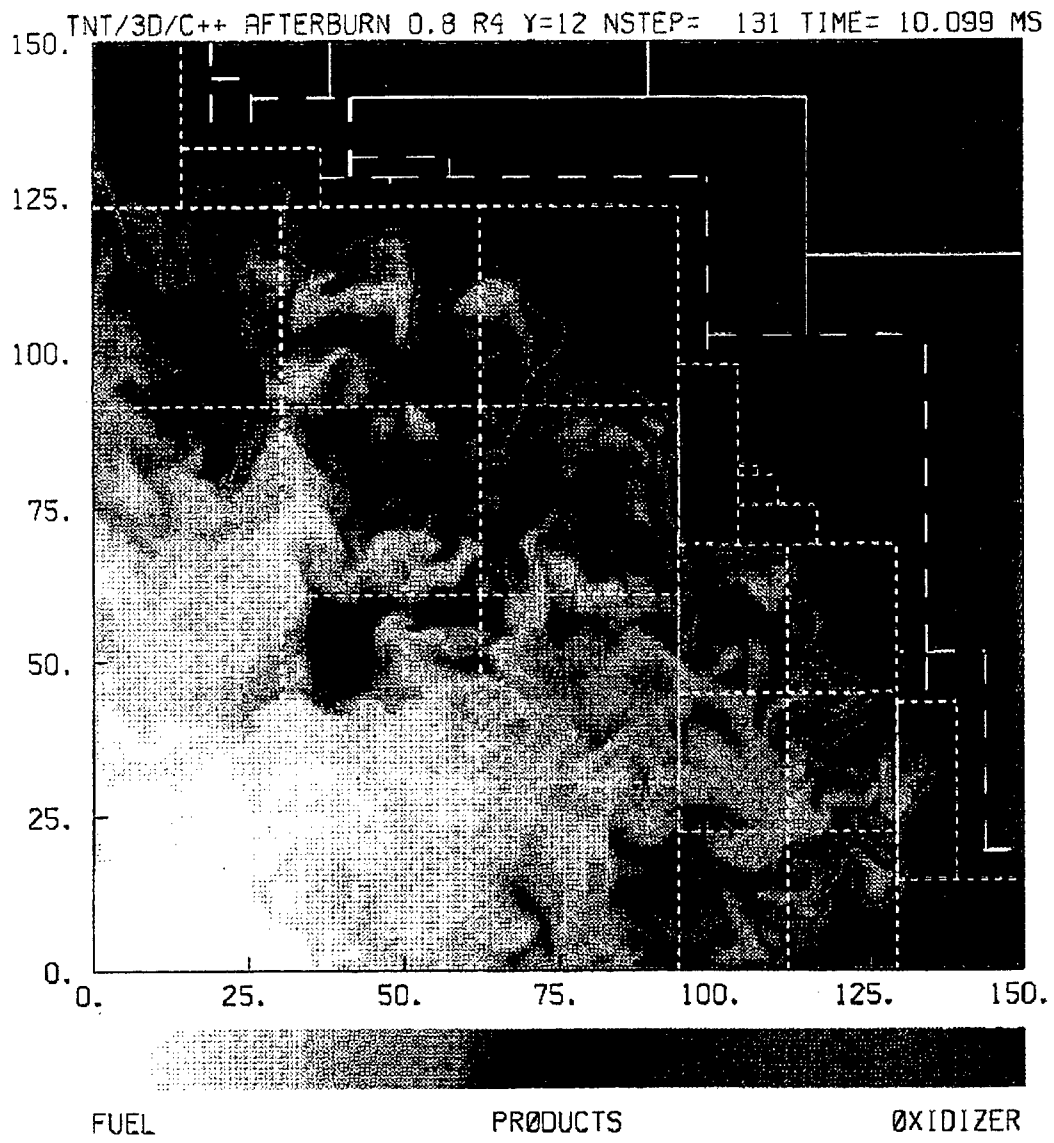


Figure 23 Example for the color-contour plots of the 3-D AMR calculation (courtesy A. L. Kuhl) used in the comparison to shadow photographs.

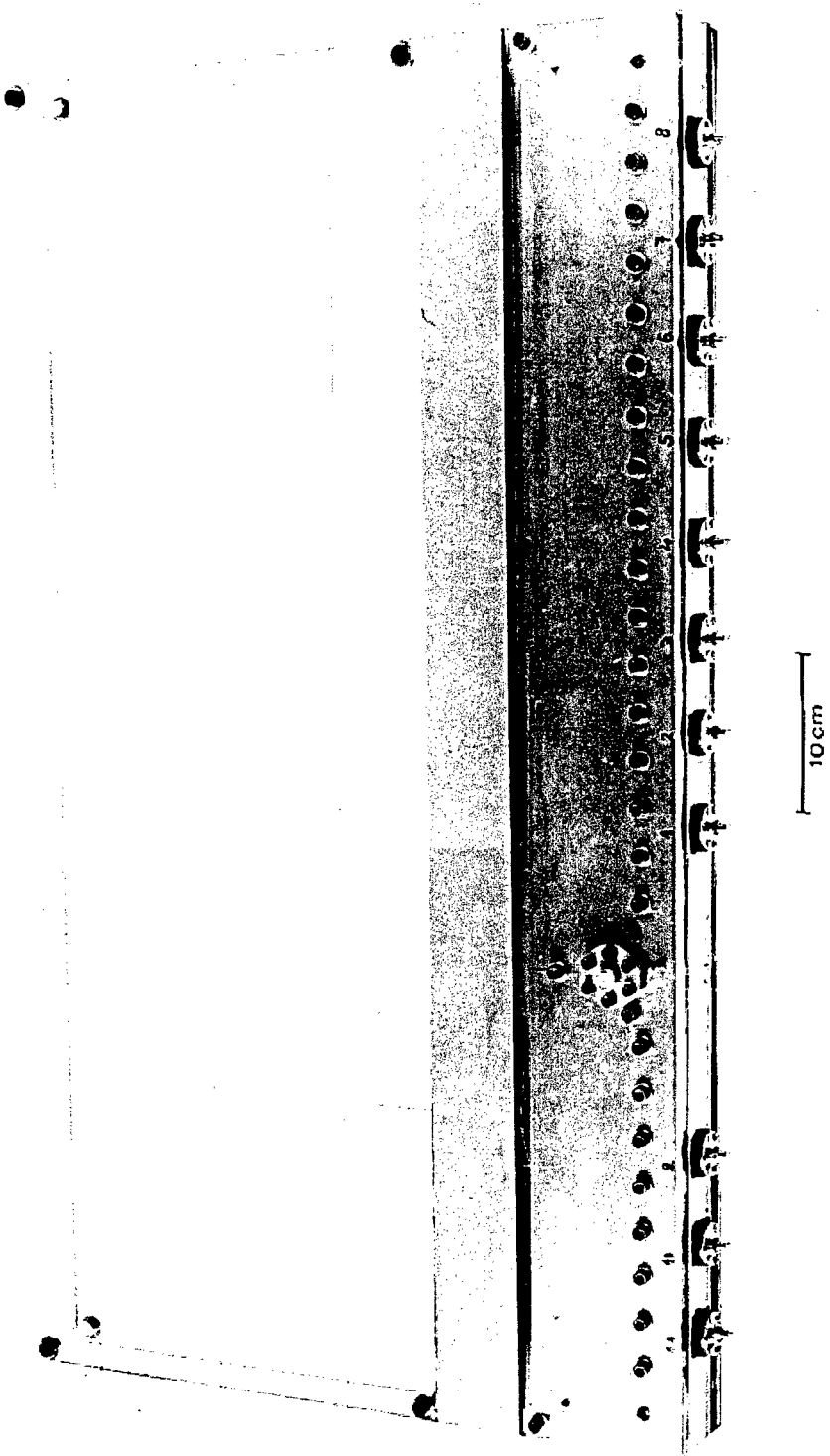


Figure 24

Setup for the experiments with hemicylindrical charges. The photograph shows the final version which is 40 mm in depth and has splitted Makrolon windows to suppress induced waves in visible area of the Makrolon windows. The circular steel plug approximately one third of the models width from the left edge is the fixture holding the charge, the plugs at the bottom of the model hold the pressure gages.

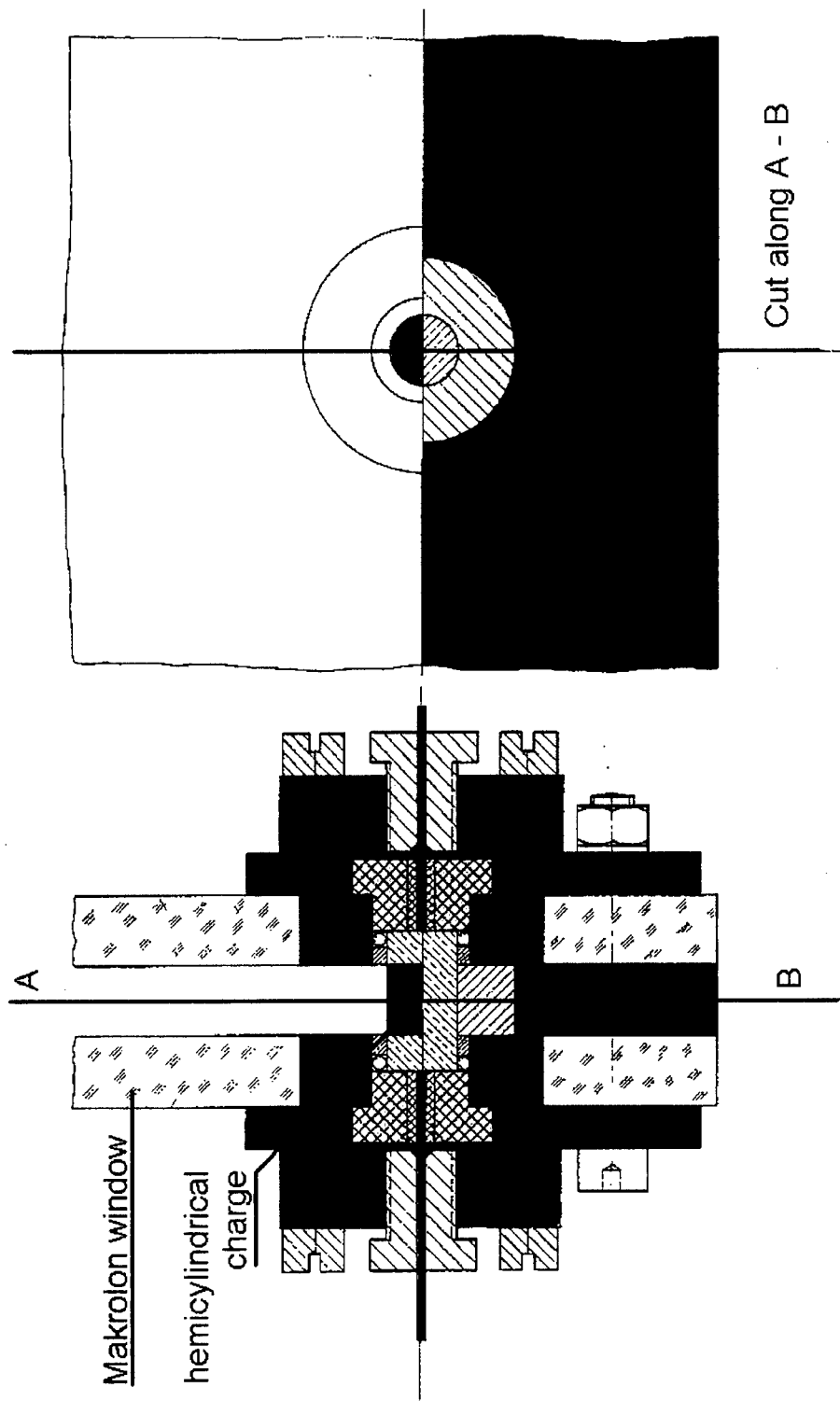
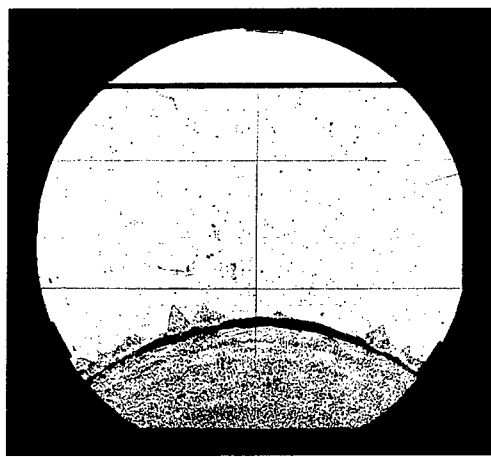
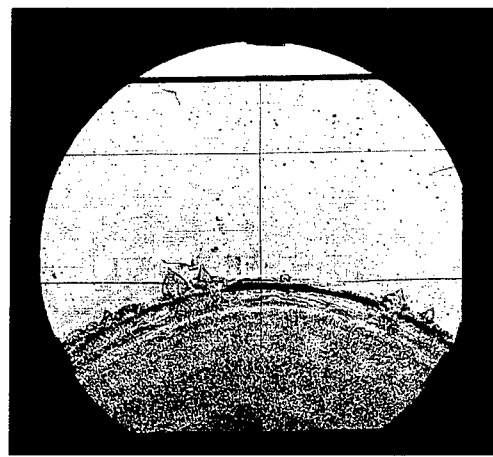


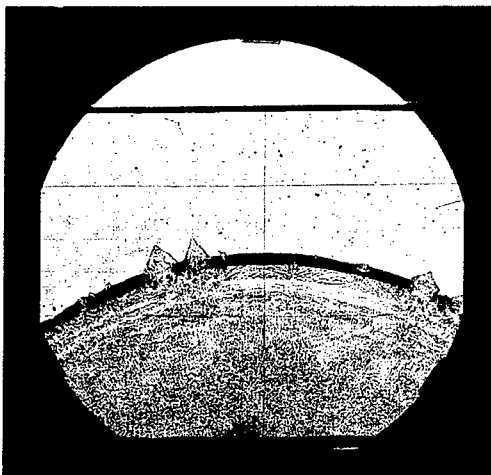
Figure 25 Constructive details for mounting the hemicylindrical charges. The charges assembled on a Makrolon holder (grey) are inserted into a steel fixture which assures right positioning. Special care has been taken to keep the arrangement airtight and to provide mechanical (shock damping) and electrical insulation between the charge assembly and the rest of the model.



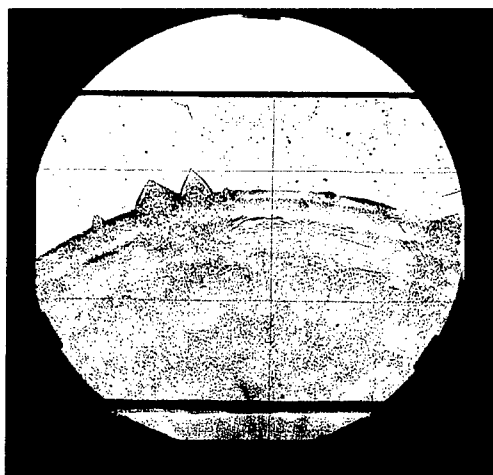
(a) frame 4: $t = 0.107$ ms



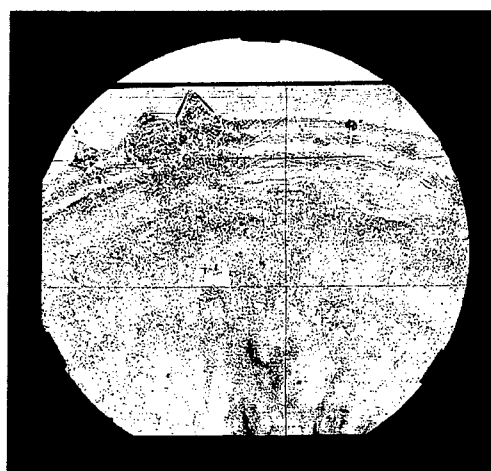
(b) frame 6: $t = 0.124$ ms



(c) frame 10: $t = 0.157$ ms

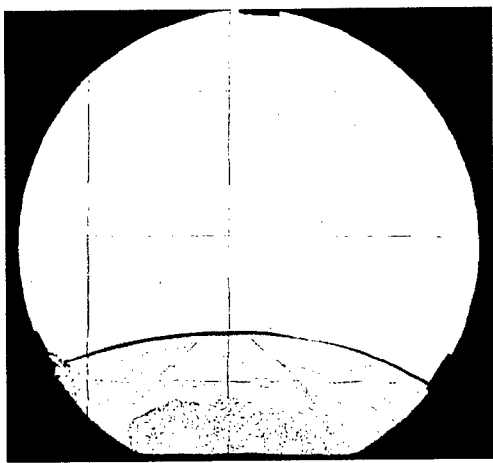


(d) frame 14: $t = 0.191$ ms

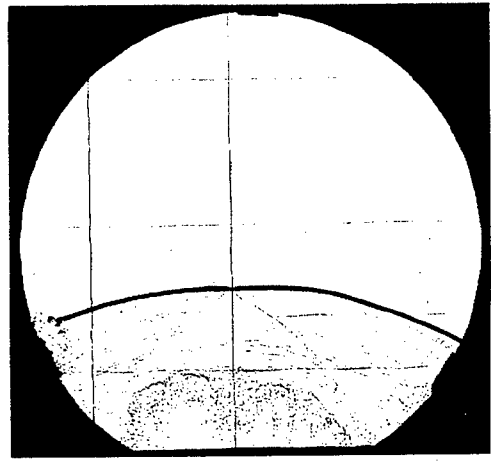


(e) frame 20: $t = 0.241$ ms

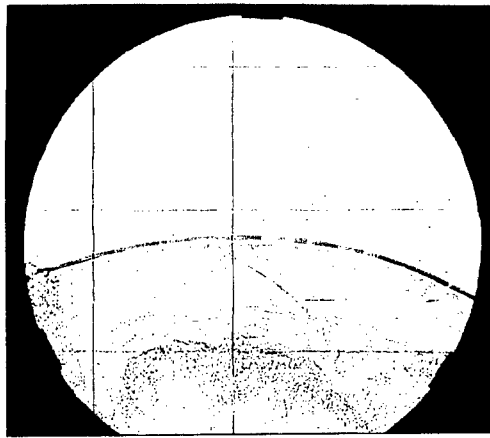
Figure 26 Sequence of shadow photographs from Test 14667. Hemicylindrical charge, length 10 mm.



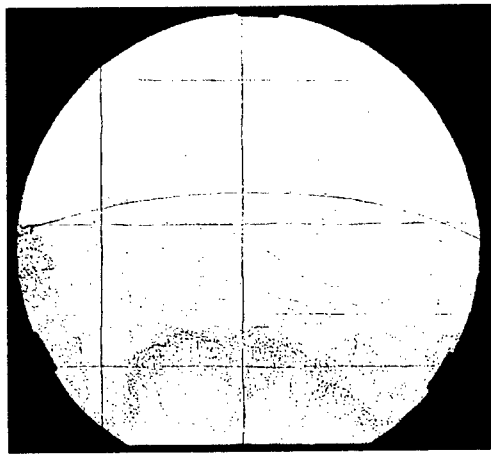
(a) frame 4: $t = 0.242$ ms



(b) frame 5: $t = 0.270$ ms

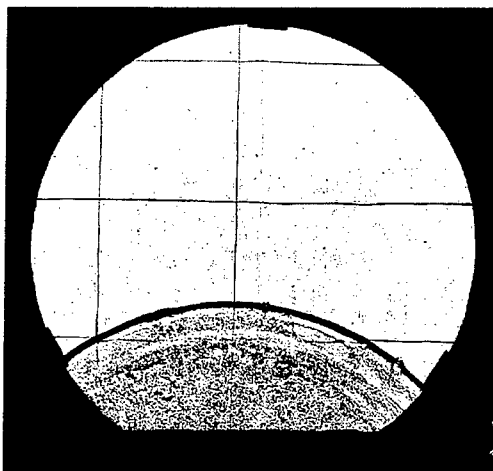


(c) frame 6: $t = 0.299$ ms

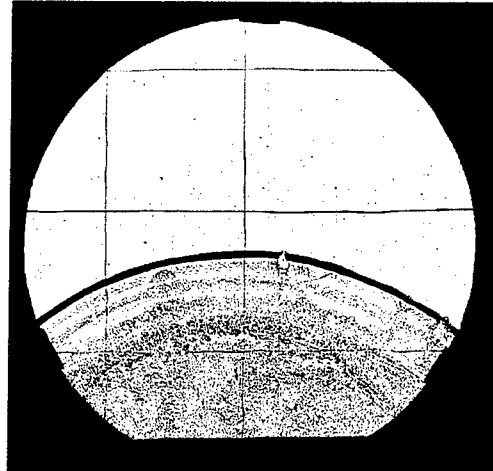


(d) frame 8: $t = 0.356$ ms

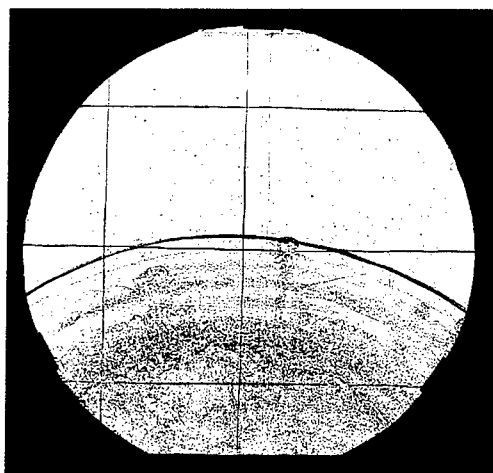
Figure 27 Sequence of shadow photographs from Test 14937. Hemicylindrical charge, length 20 mm.



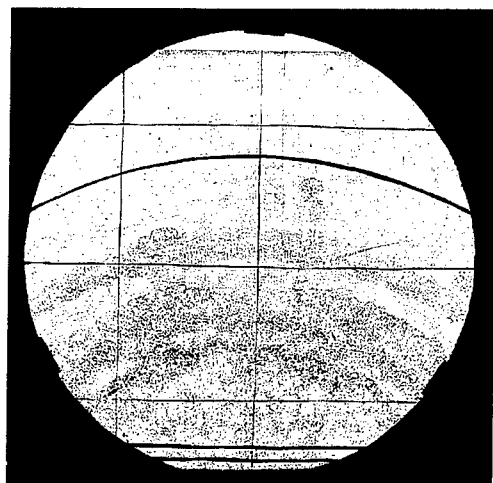
(a) frame 6: $t = 0.225$ ms



(b) frame 8: $t = 0.275$ ms

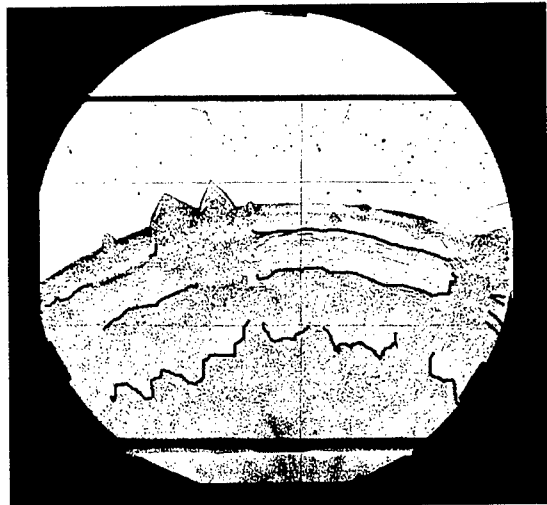


(c) frame 10: $t = 0.325$ ms

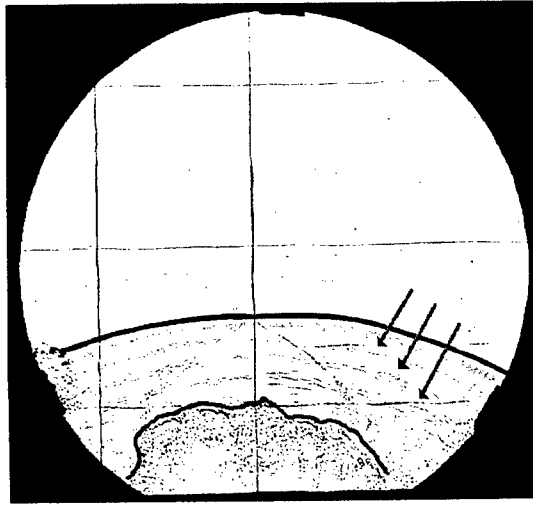


(d) frame 14: $t = 0.425$ ms

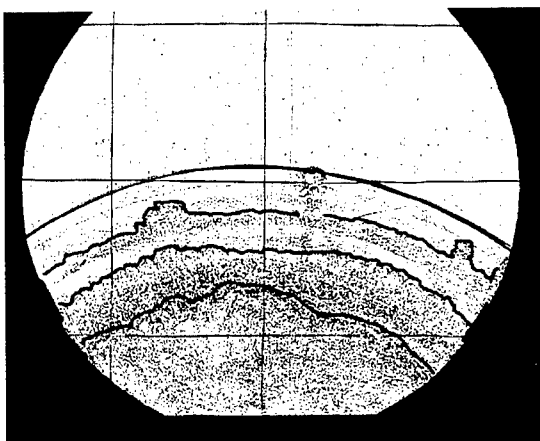
Figure 28 Sequence of shadow photographs from Test 14991. Hemicylindrical charge, length 40 mm.



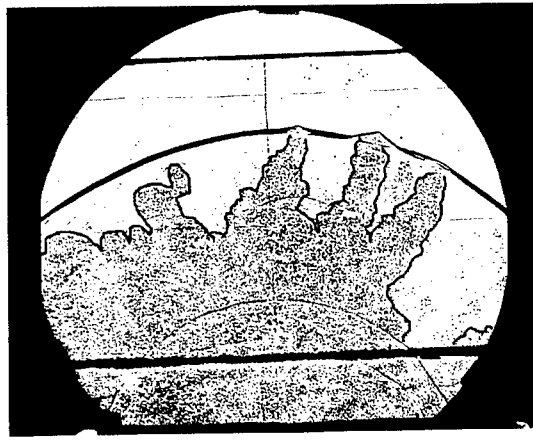
(a) hemicylindrical charge 10 mm
Test 14667, frame 14, $t = 0.191$ ms



(b) hemicylindrical charge 20 mm
Test 14937, frame 5, $t = 0.270$ ms



(c) hemicylindrical charge 40 mm
Test 14991, frame 10, $t = 0.325$ ms



(d) hemispherical charge
Test 14757, frame 15, $t = 0.310$ ms

Figure 29 Comparison of shadow photographs from 2-D experiments to a 3-D test .
Possible candidates for the border of the turbulent products cloud are marked in red. For the 2-D tests note the ambiguity of the borderline, the comparative lack of large disturbance with regard to amplitudes and wavelengths and additional shock-wave-like structures behind the primary blast front.

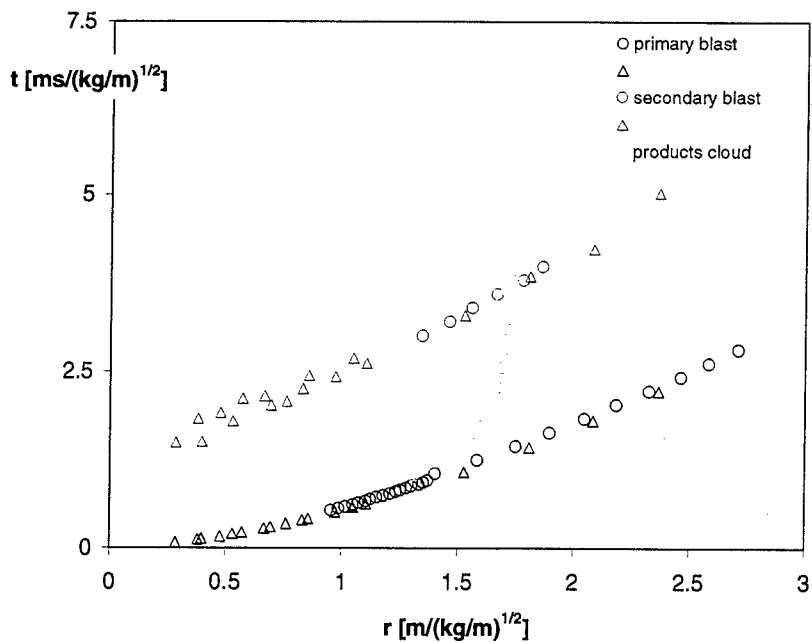


Figure 30 Wave diagram for the tests with hemicylindrical charges. Included are tests with 1-cm, 2-cm and 4-cm long charges, based on both shadow photographs (circles) and pressure measurements (triangles). Data are scaled with $(2W/l)^{1/2}$.

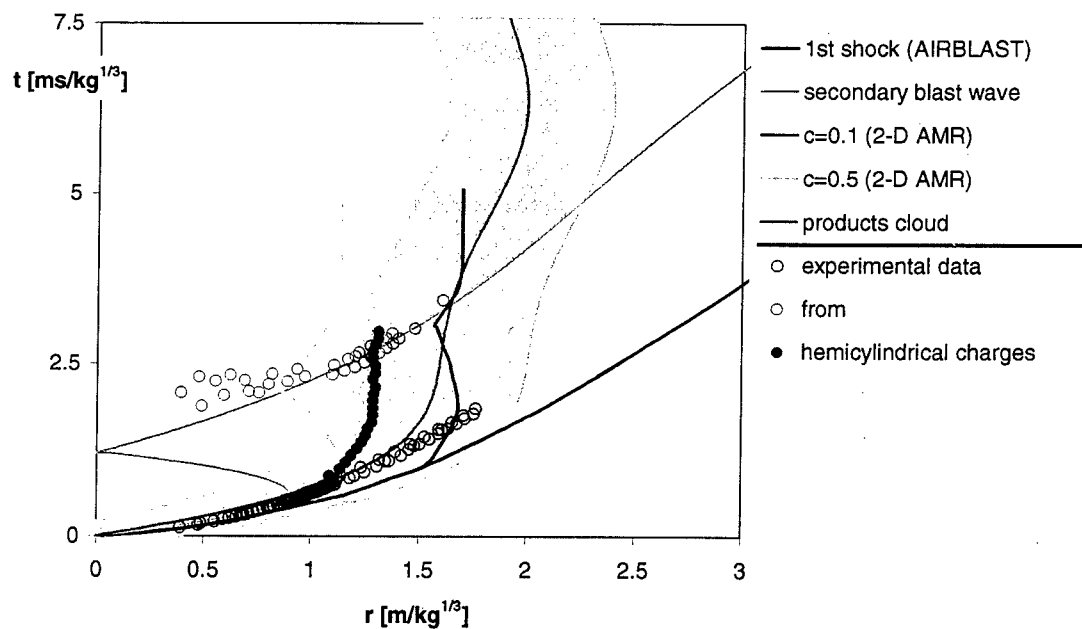


Figure 31 Wave diagram 30 rescaled to match the wave diagram for 3-D experiments (for rescaling see Chapter 4.2.2).

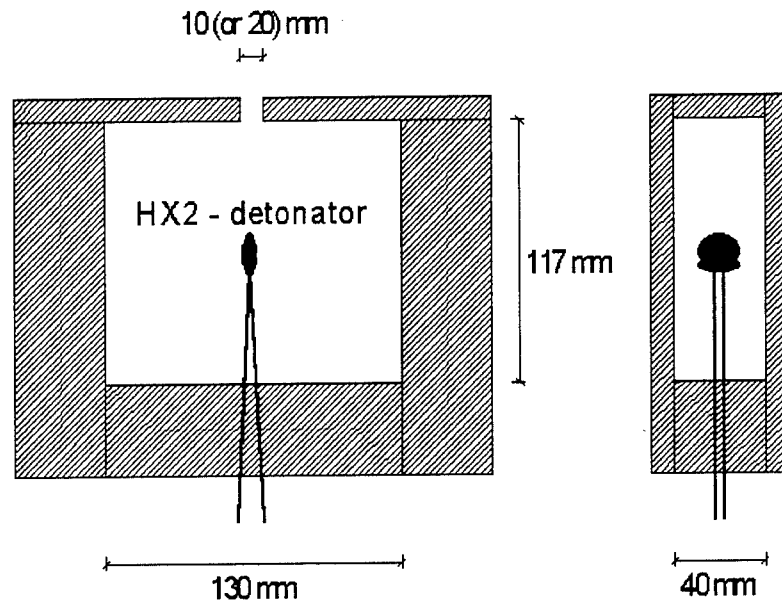


Figure 32 Schematic sketch of the detonation chamber (versions C and D for free-field expansion).

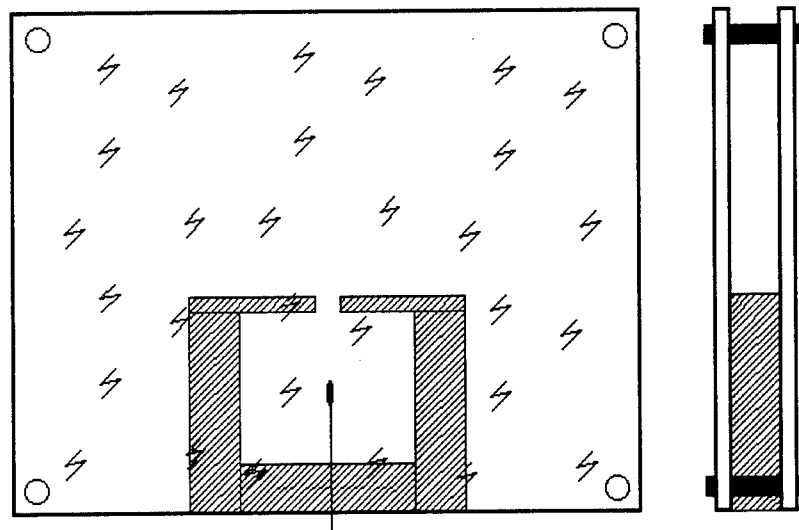


Figure 33 Schematic sketch of the detonation chamber in the modified setup with Makrolon windows (versions A and B).

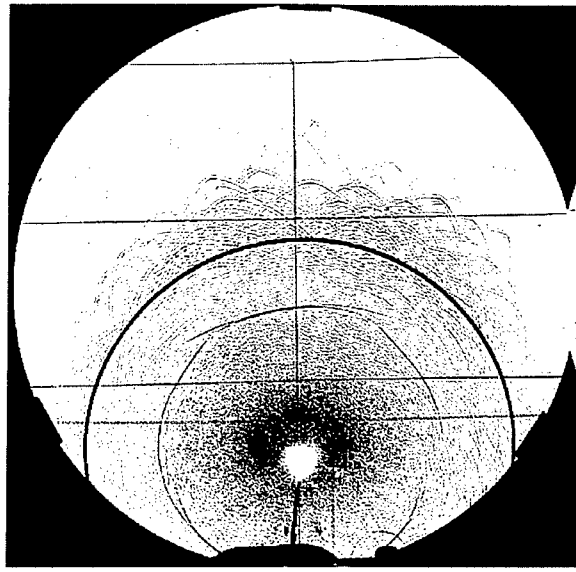


Figure 34 Shadow photograph of a detonating HX2-ignitor 0.25 ms after ignition.

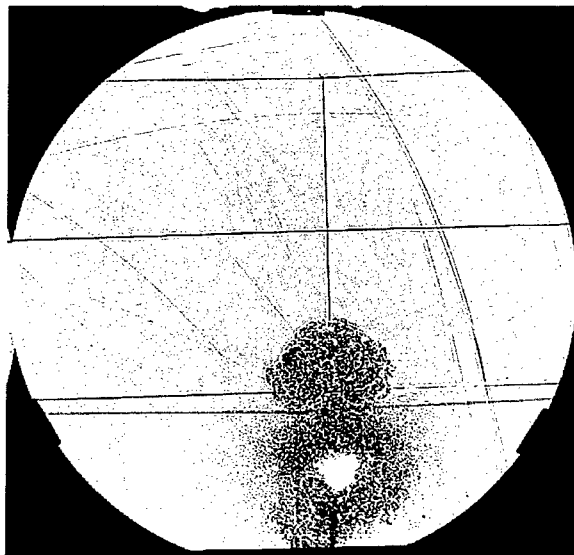


Figure 35 Products cloud of HX2 2.45 ms after ignition. Detonator aligned with line of sight.

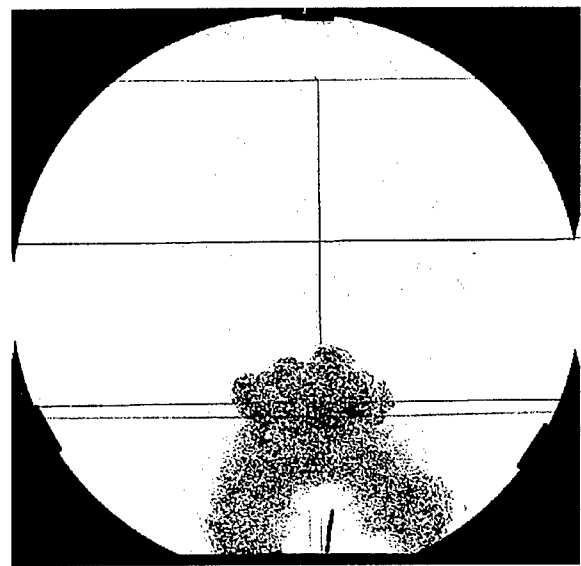
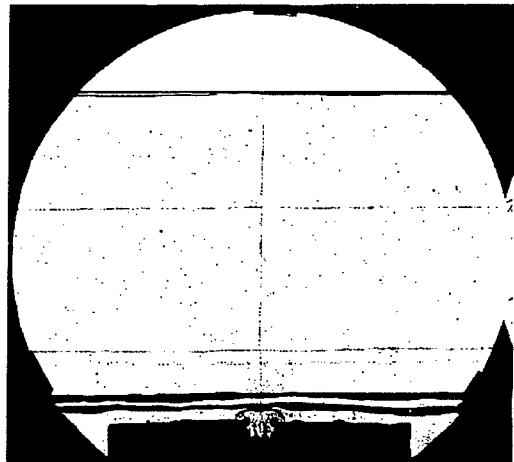
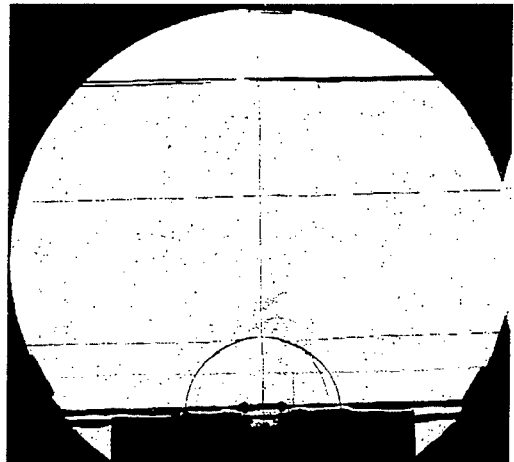


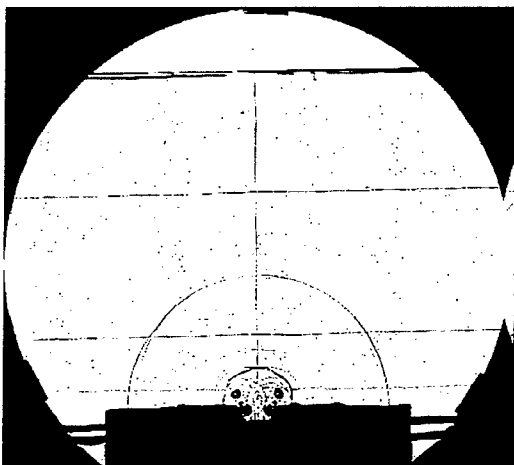
Figure 36 Products cloud 2.71 ms after ignition. Different test with the detonator aligned perpendicular to the line of sight.



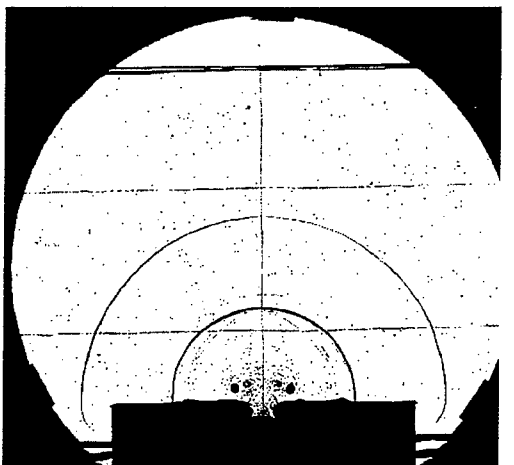
(a) frame 1: $t = 0.15$ ms



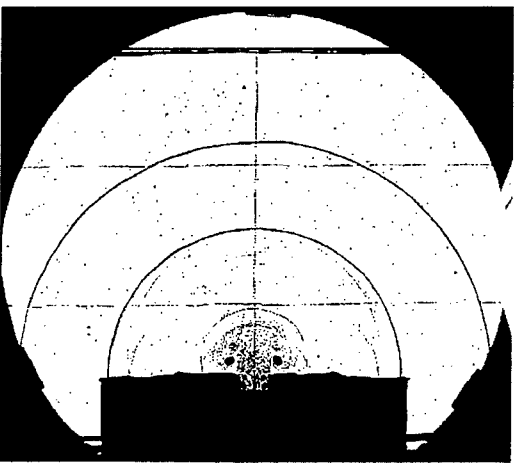
(b) frame 2: $t = 0.25$ ms



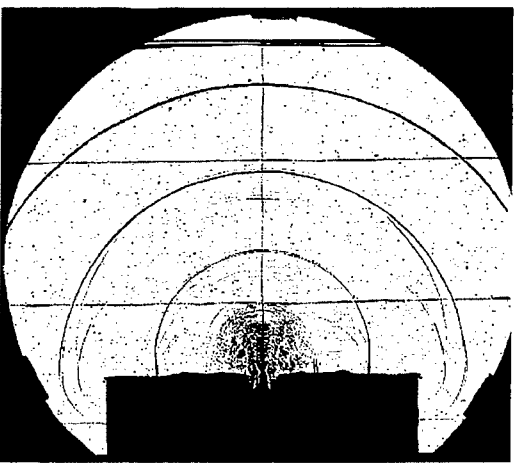
(c) frame 3: $t = 0.35$ ms



(d) frame 4: $t = 0.45$ ms

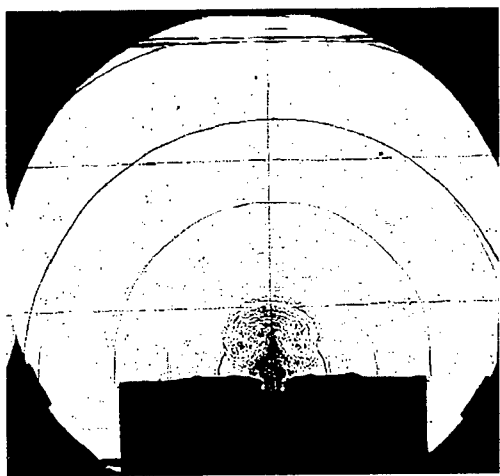


(e) frame 5: $t = 0.55$ ms

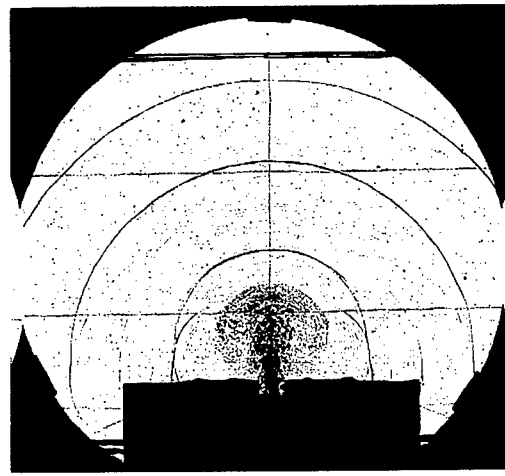


(f) frame 6: $t = 0.65$ ms

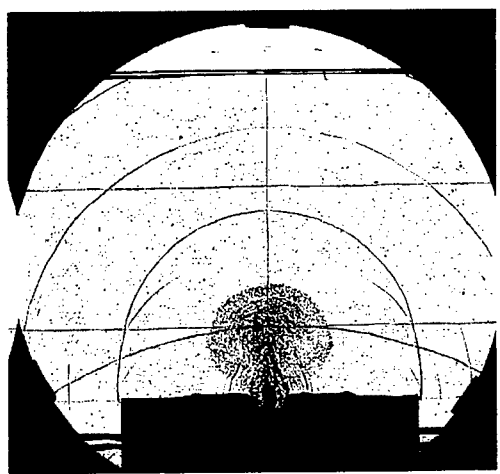
Figure 37 Blast and products cloud from a detonation chamber. Cinematographic sequence of shadowgraphs. Charge: HX2, outlet from chamber 20 mm wide, expansion confined by Makrolon windows (Configuration **A**).



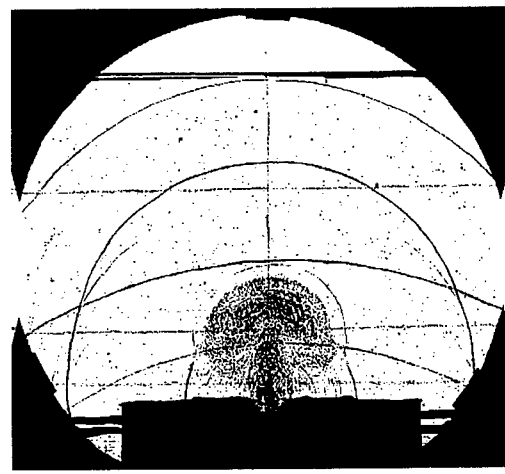
(g) frame 7: $t = 0.75$ ms



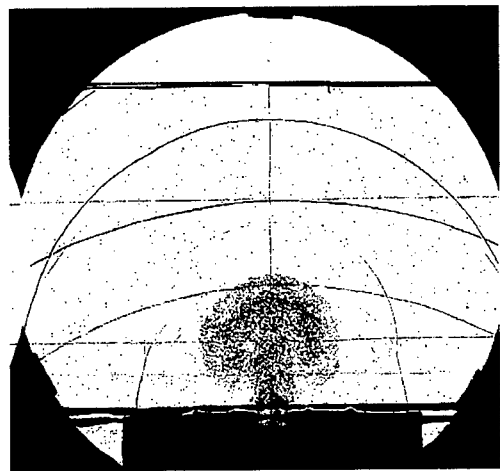
(h) frame 8: $t = 0.85$ ms



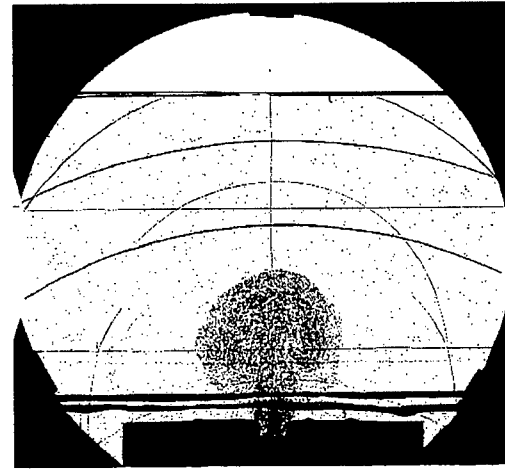
(i) frame 9: $t = 0.95$ ms



(j) frame 10: $t = 1.05$ ms

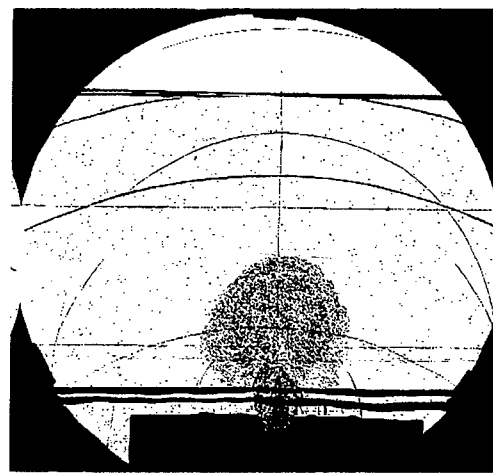


(k) frame 11: $t = 1.15$ ms

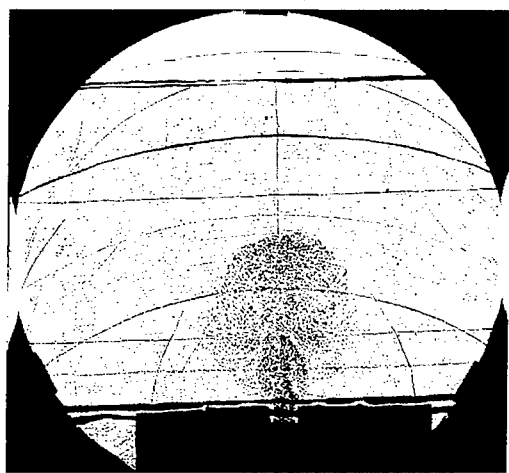


(l) frame 12: $t = 1.25$ ms

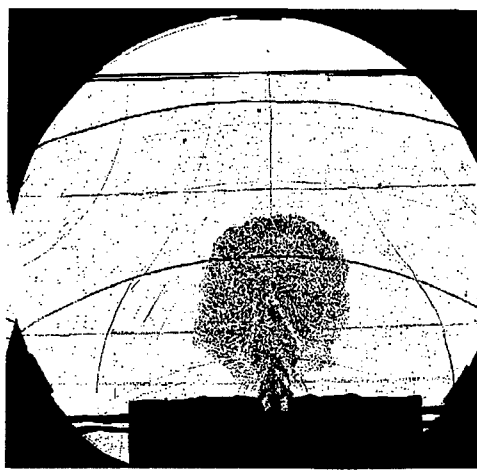
Figure 37 Blast and products cloud from a detonation chamber. Cinematographic sequence of shadowgraphs. Charge: HX2, outlet from chamber 20 mm wide, expansion confined by Makrolon windows (Configuration **A**). (Continued)



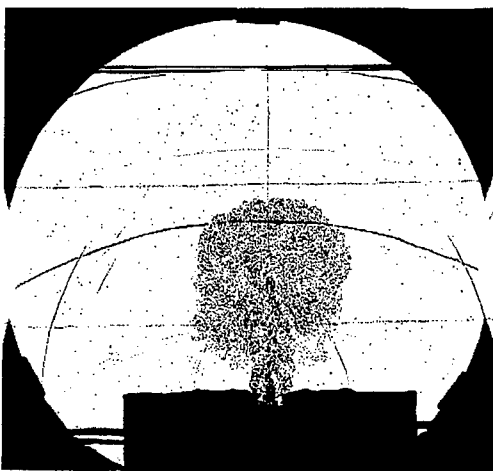
(m) frame 13: $t = 1.35$ ms



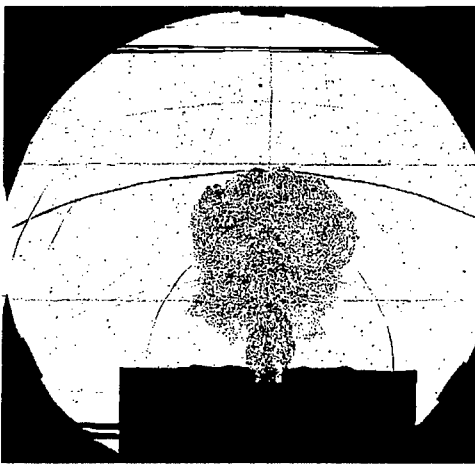
(n) frame 14: $t = 1.45$ ms



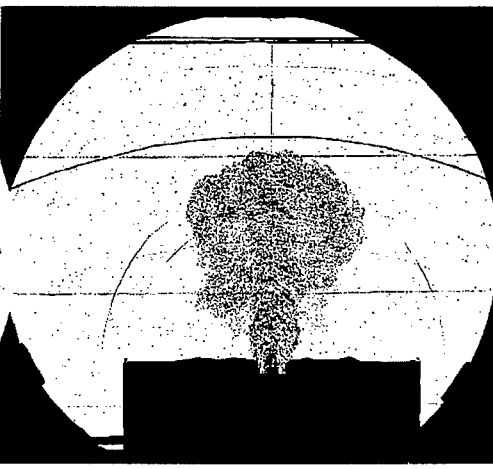
(o) frame 15: $t = 1.55$ ms



(p) frame 16: $t = 1.65$ ms

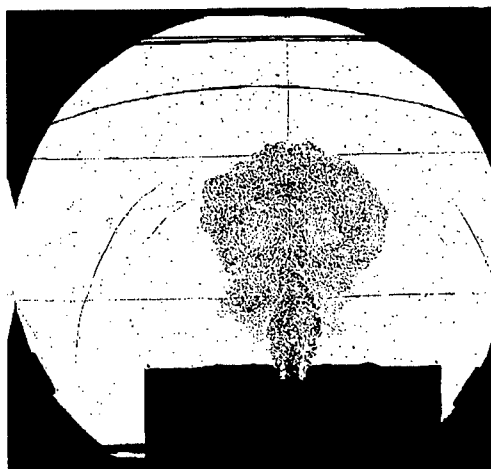


(q) frame 17: $t = 1.75$ ms

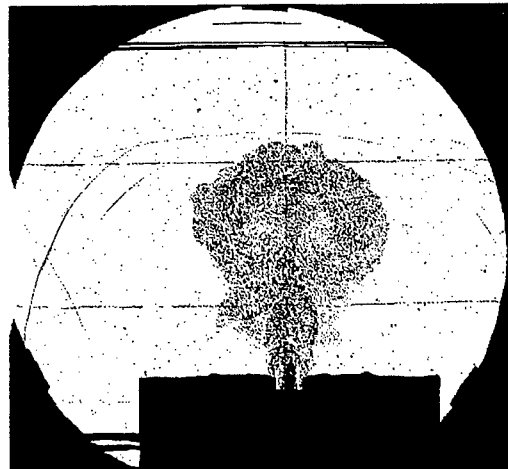


(r) frame 18: $t = 1.85$ ms

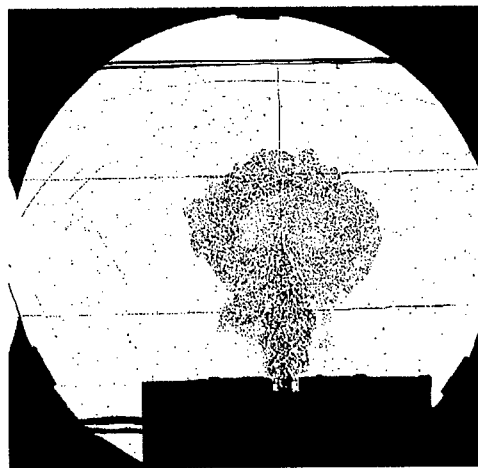
Figure 37 Blast and products cloud from a detonation chamber. Cinematographic sequence of shadowgraphs. Charge: HX2, outlet from chamber 20 mm wide, expansion confined by Makrolon windows (Configuration **A**). (Continued)



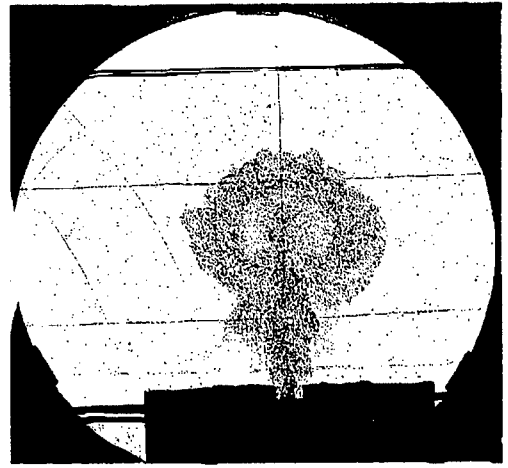
(s) frame 19: $t = 1.95$ ms



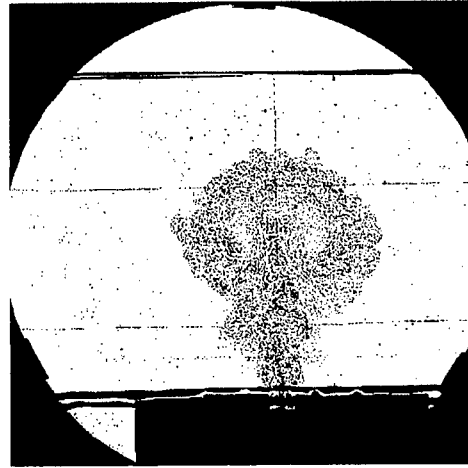
(t) frame 20: $t = 2.05$ ms



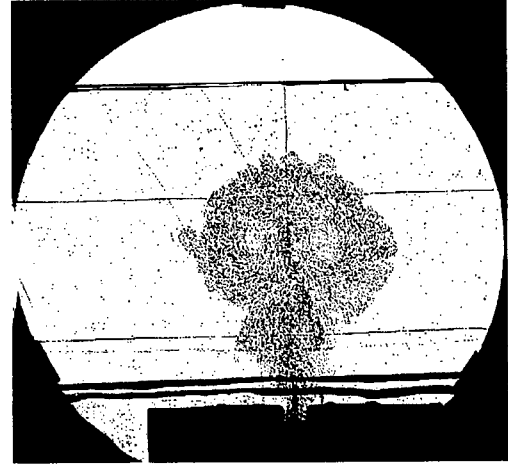
(u) frame 21: $t = 2.15$ ms



(v) frame 22: $t = 2.25$ ms



(w) frame 23: $t = 2.35$ ms



(x) frame 24: $t = 2.45$ ms

Figure 37 Blast and products cloud from a detonation chamber. Cinematographic sequence of shadowgraphs. Charge: HX2, outlet from chamber 20 mm wide, expansion confined by Makrolon windows (Configuration **A**). (Continued)

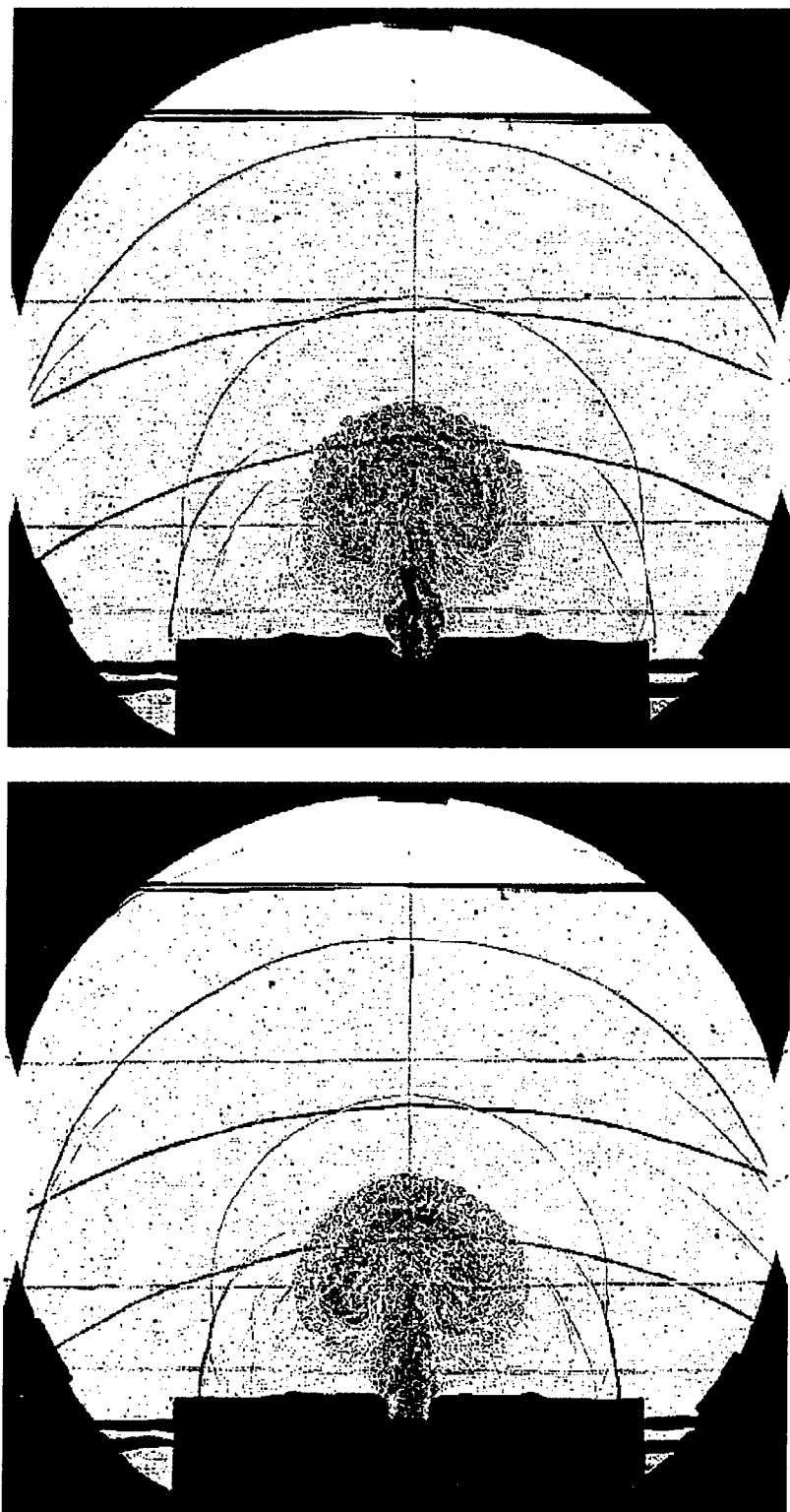
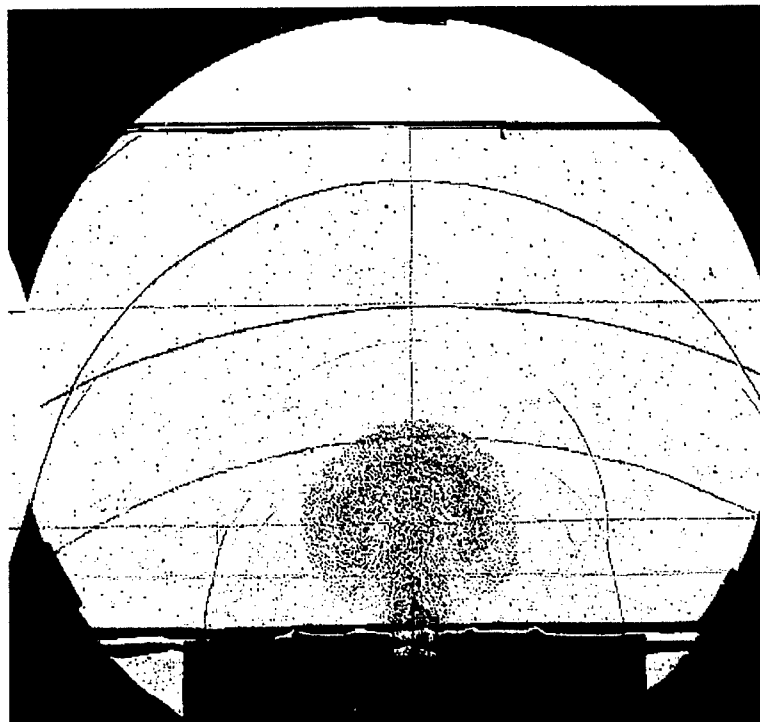
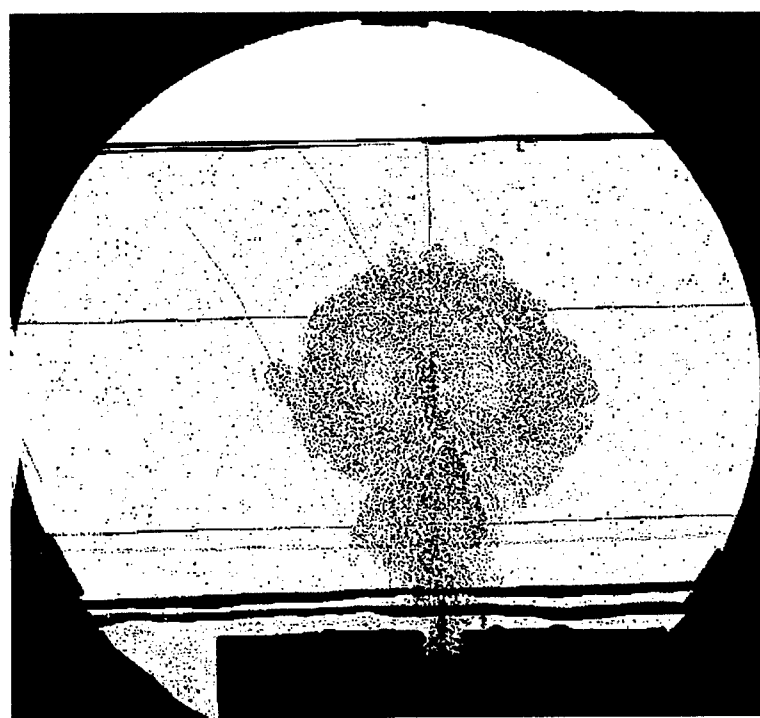


Figure 38 Comparison of two further tests for Configuration A approximately 1.1 ms after ignition.

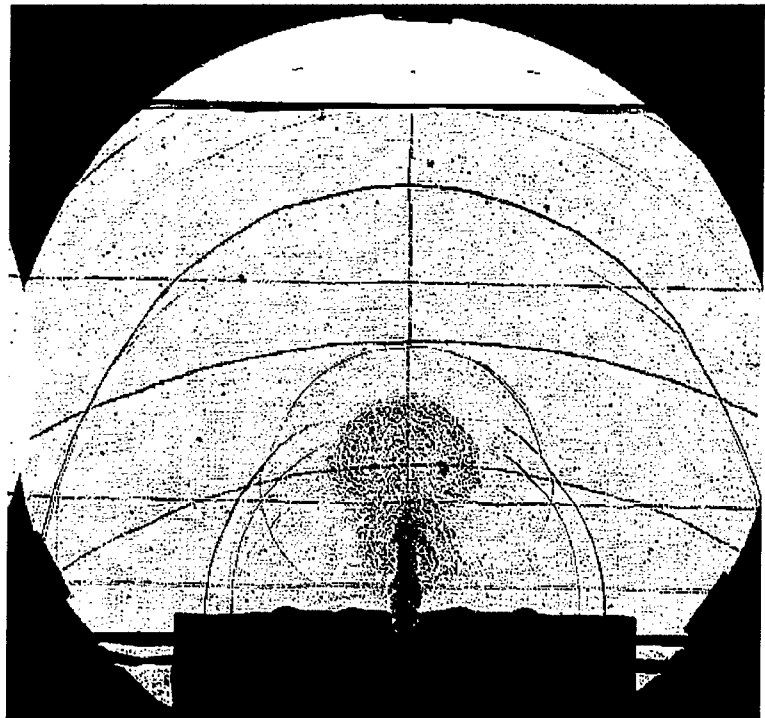


(a) frame 11, $t = 1.15$ ms

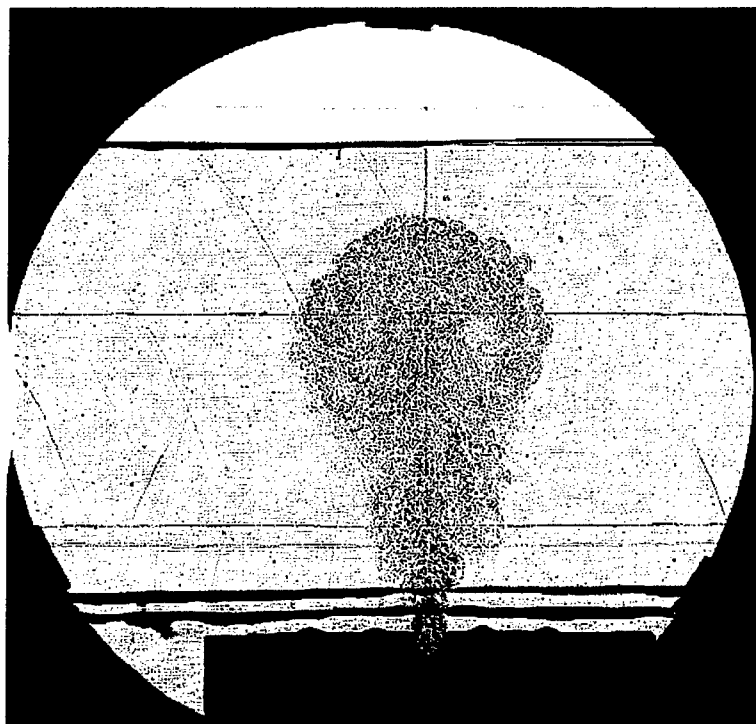


(b) frame 24, $t = 2.45$ ms

Figure 39 Shadow photographs for a test in Configuration A
(outlet width 20 mm, Makrolon windows).

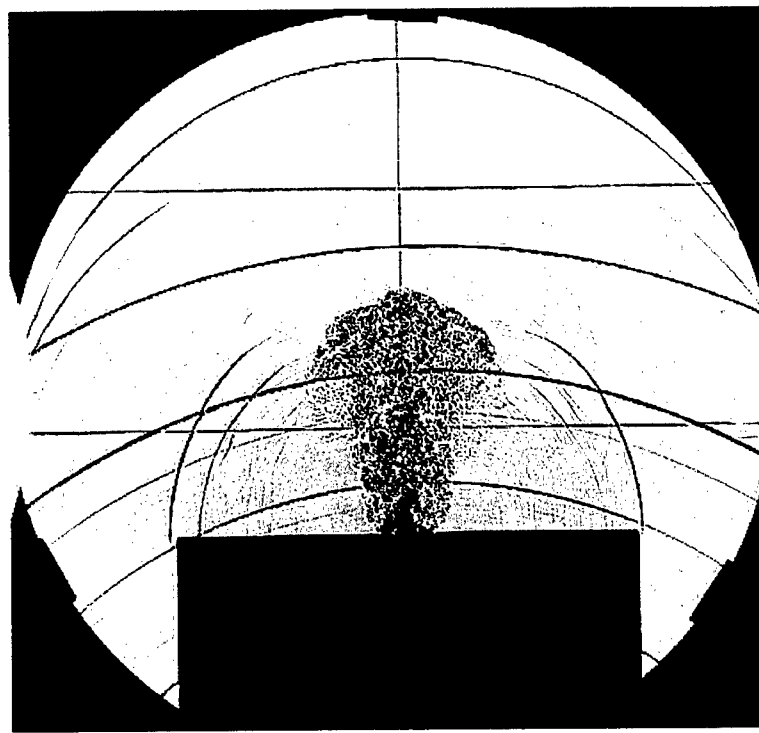


(a) frame 10, $t = 1.1$ ms

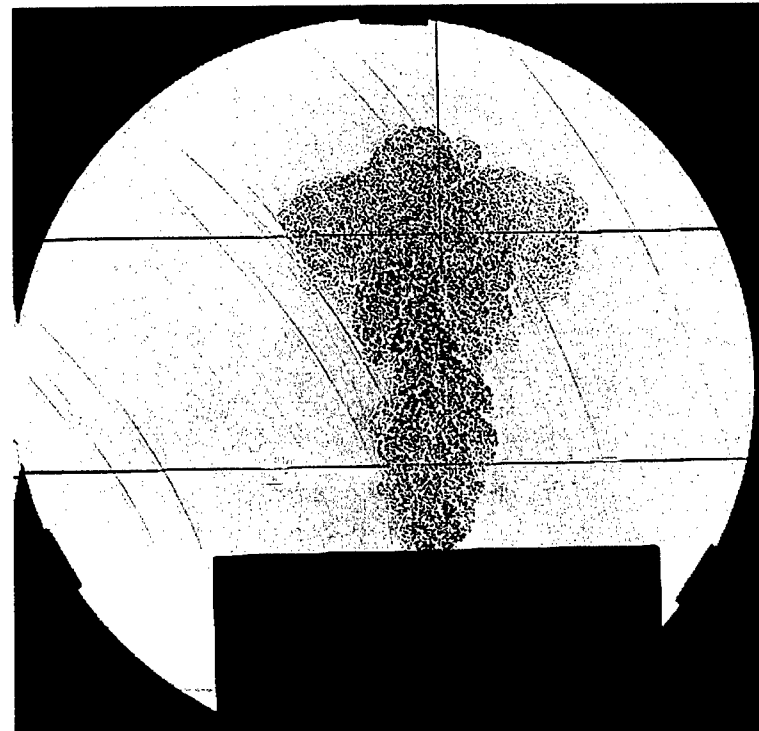


(b) frame 24, $t = 2.5$ ms

Figure 40 Shadow photographs for a test in Configuration **B**
(outlet width 10 mm, Makrolon windows).

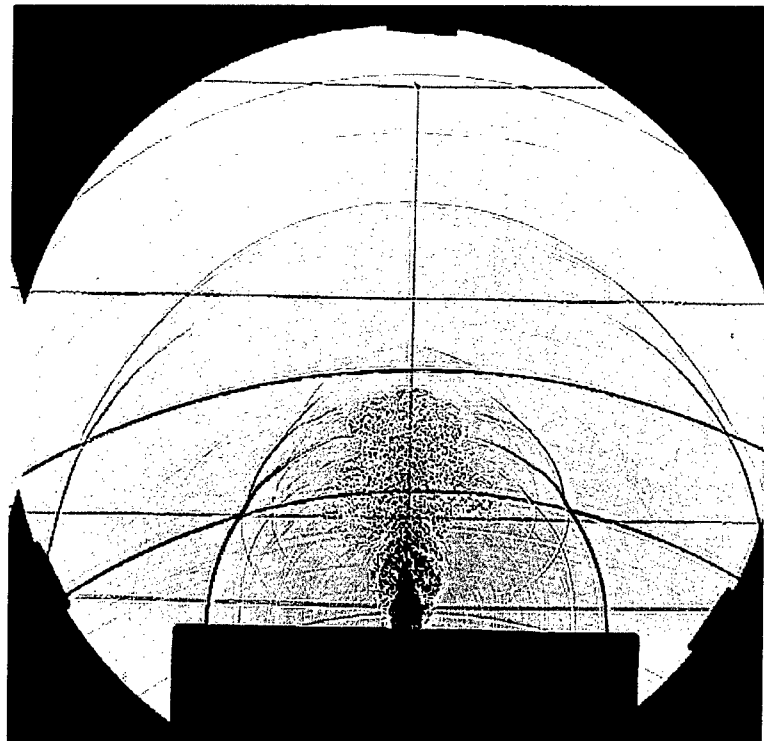


(a) frame 10, $t = 1.1$ ms



(b) frame 24, $t = 2.5$ ms

Figure 41 Shadow photographs for a test in Configuration C
(outlet width 20 mm, free expansion).



(a) frame 10, $t = 1.1$ ms



(b) frame 24, $t = 2.5$ ms

Figure 42 Shadow photographs for a test in Configuration **D** (outlet width 10 mm, free expansion).

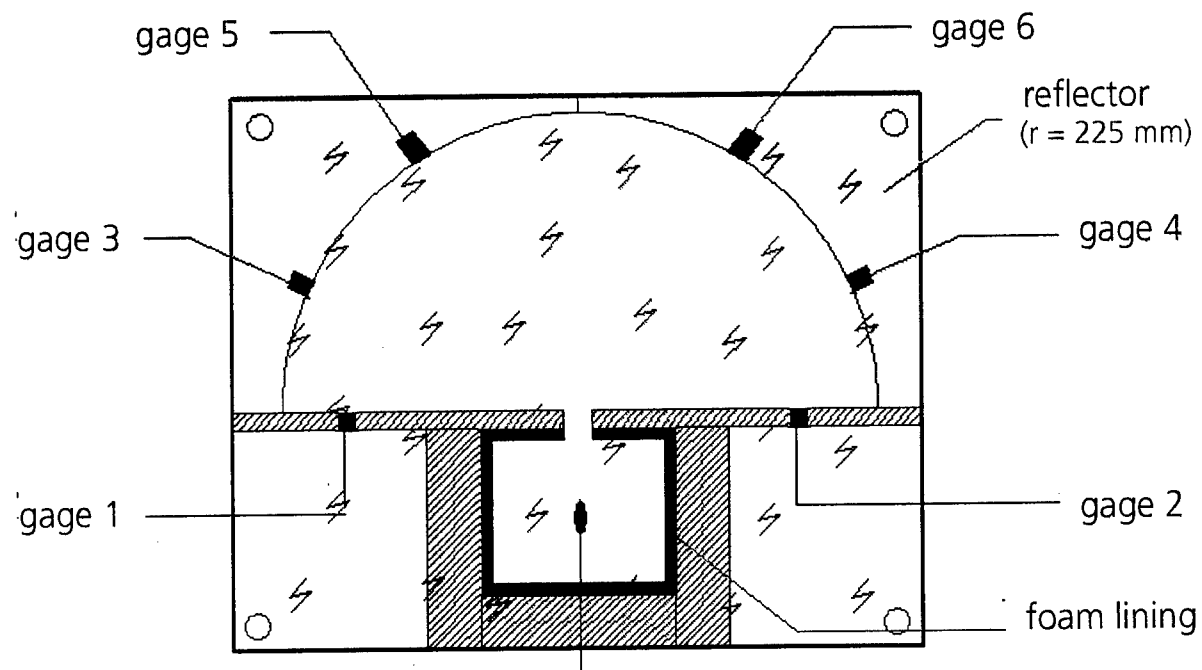


Figure 43 Modification of the detonation chamber setup version **A**. The space between the Makrolon windows is changed to a closed hemicylindrical expansion chamber and 6 pressure gages are installed. The outlet is again a 20-mm wide slot. The inner wall of the detonation chamber is fitted with a foam lining to reduce the multiple reflections within the chamber.

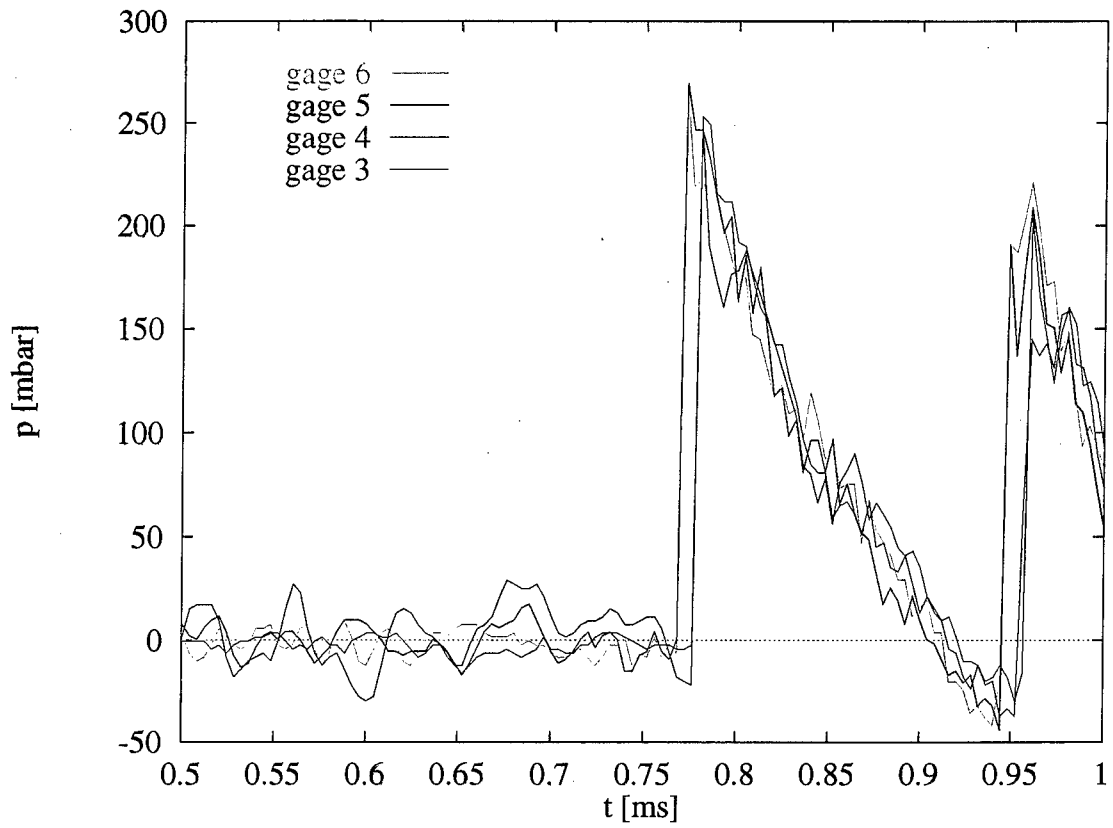


Figure 44 Pressure-time history at the reflector. The good agreement of arrival times at the gages shows that the blast fronts are nearly hemicylindrical.

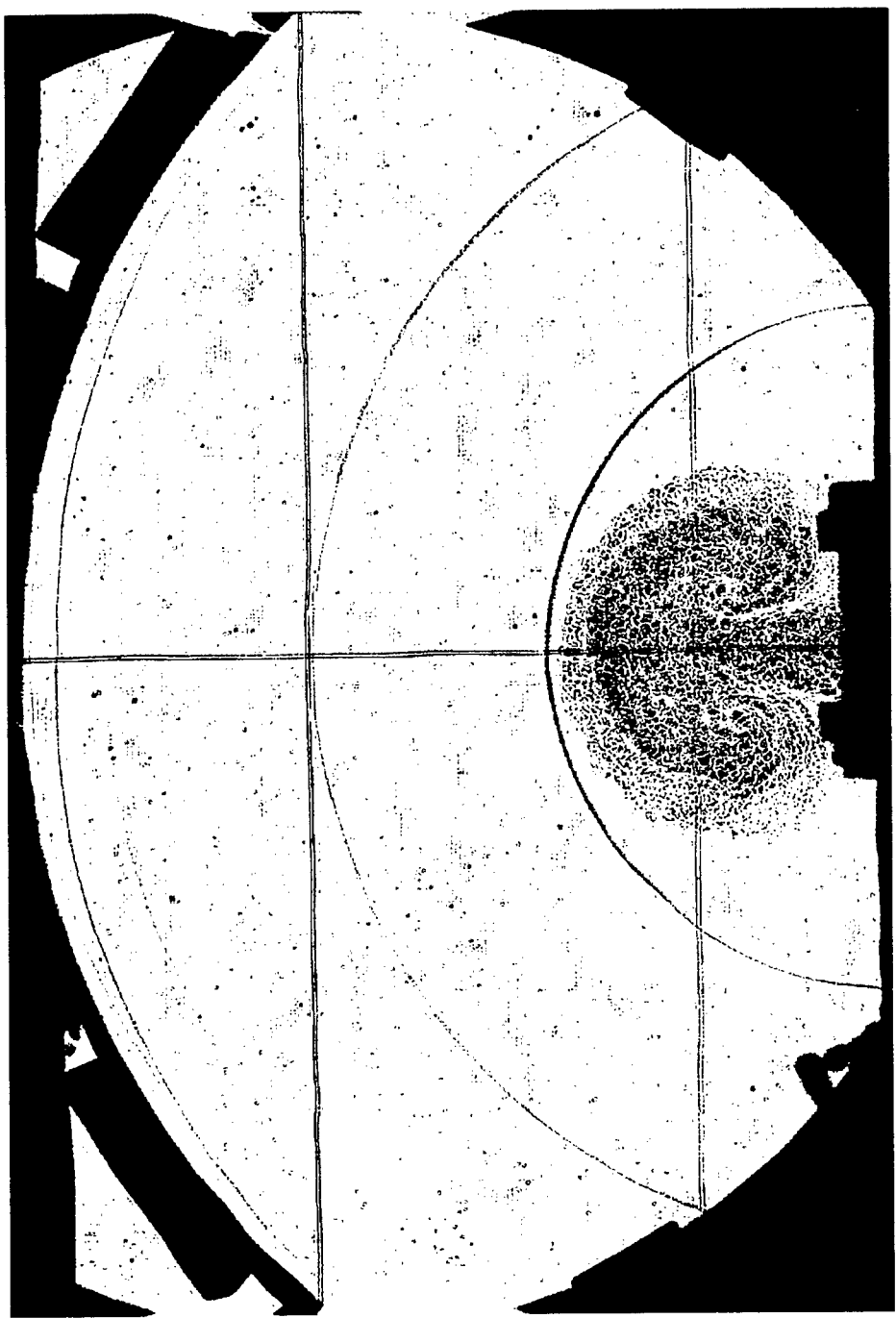


Figure 45
Shadow photograph of the products cloud in the closed expansion chamber (test 15261/11) at $t=1.07$ ms. All visible blast fronts have been reflected and are propagating towards the center. The reflected first blast is about to impinge on the products cloud.

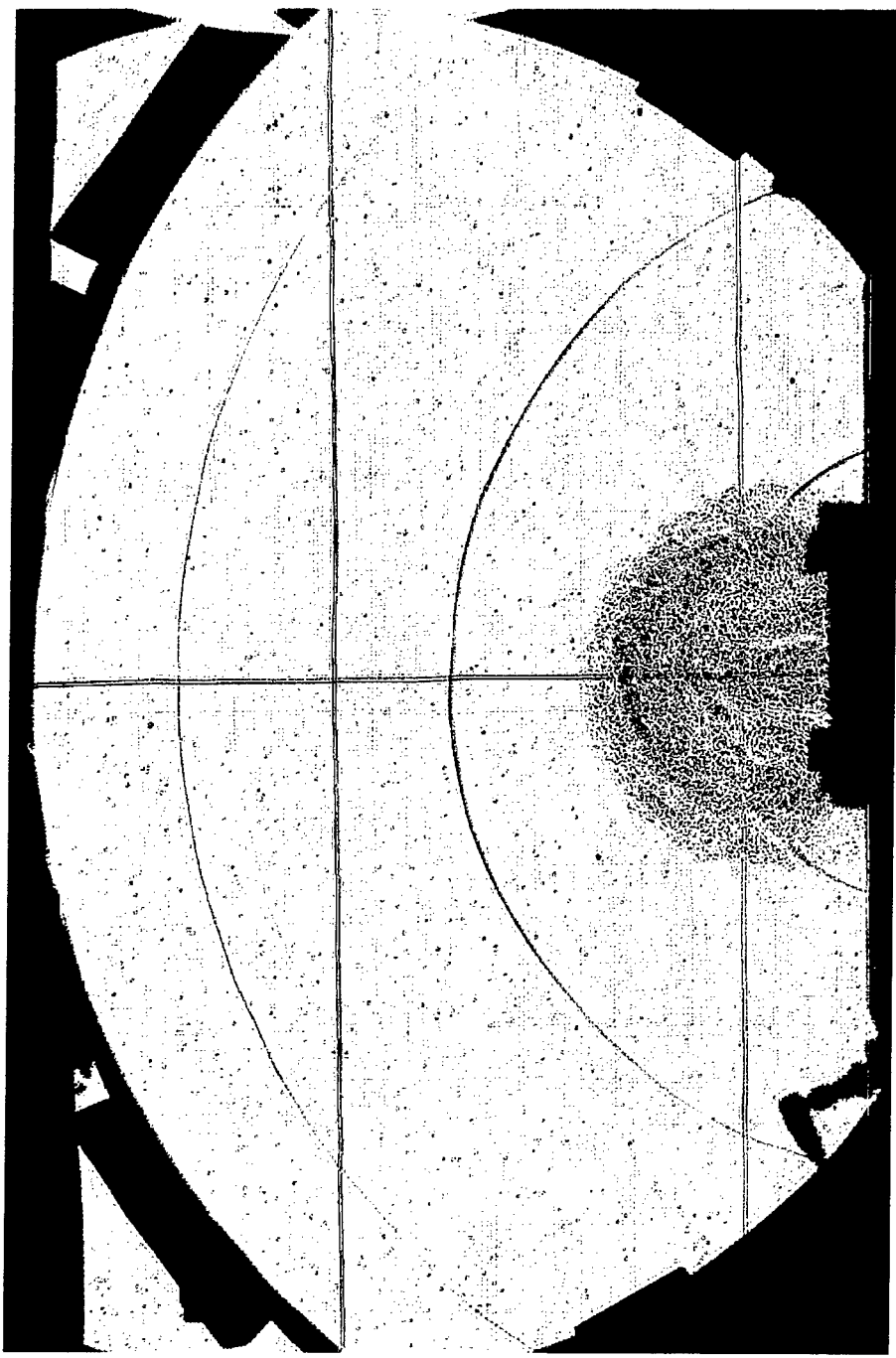


Figure 46 Interaction of the first reflected blast front with the products cloud at $t = 1.15$ ms. (test 15261/12).

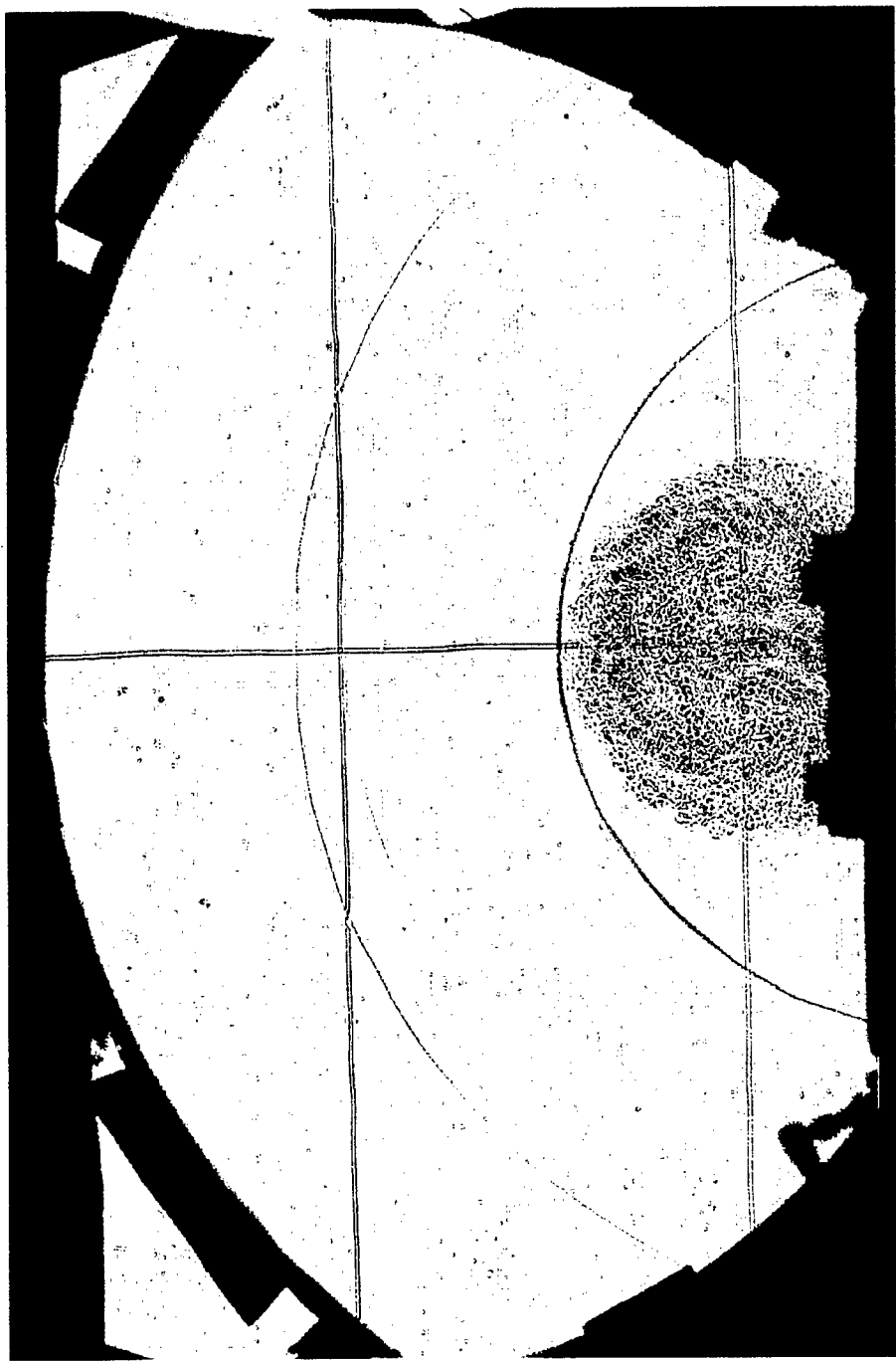


Figure 47 Further development of the products cloud at $t = 1.23$ ms. (Test 15261/13).

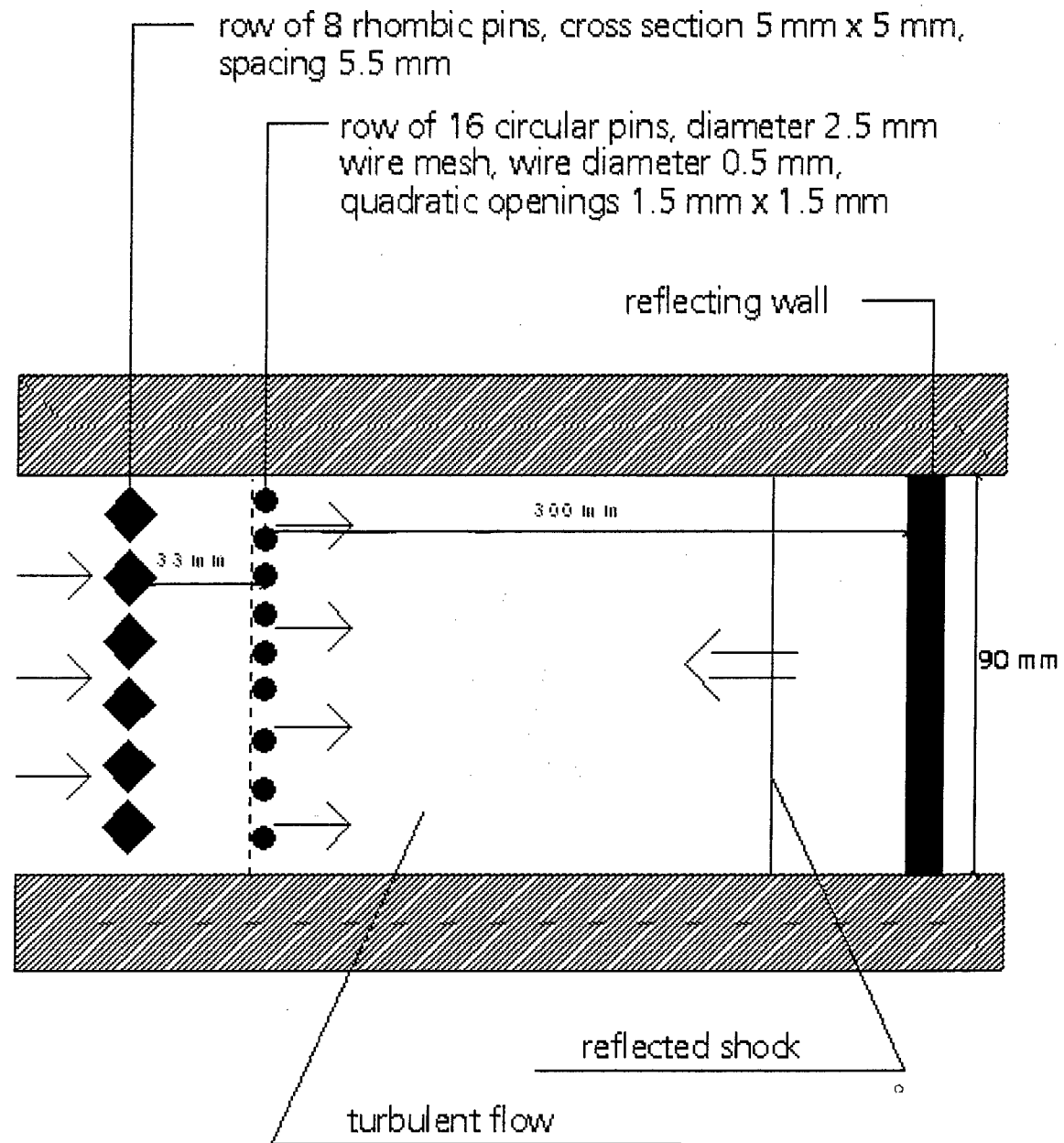


Figure 48 Schematic sketch of a setup for shock tube experiments on a shock impinging onto a turbulent flow field.

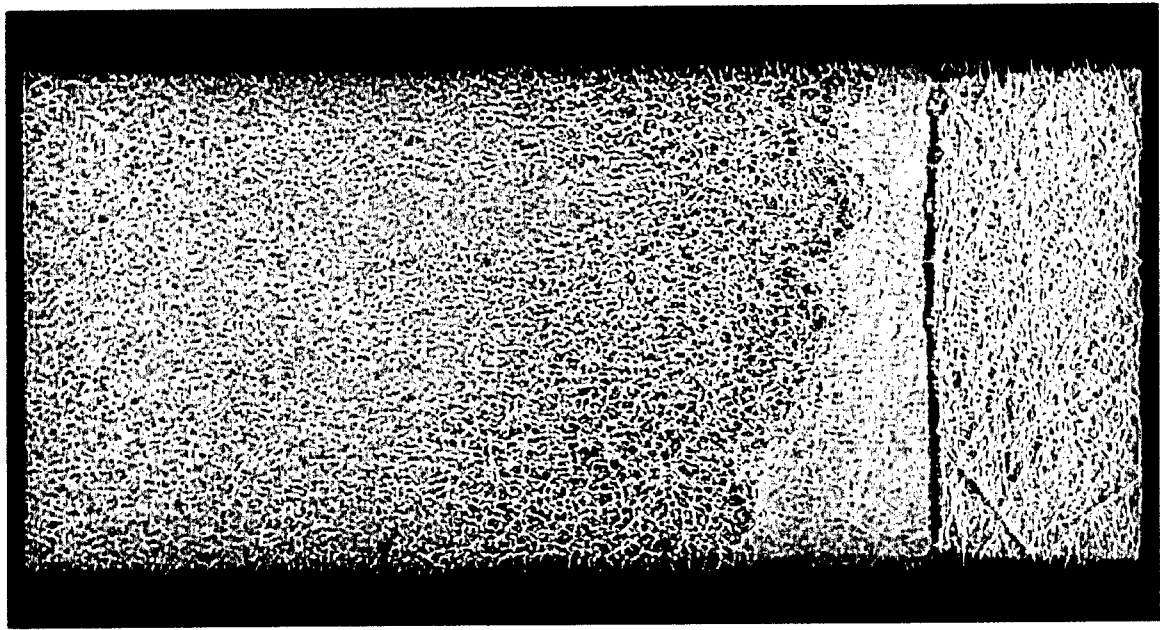


Figure 49 Shock tube experiment Test 15283/6. Reflected shock shortly before impinging on artificially generated turbulent flow ($t = -20 \mu s$).

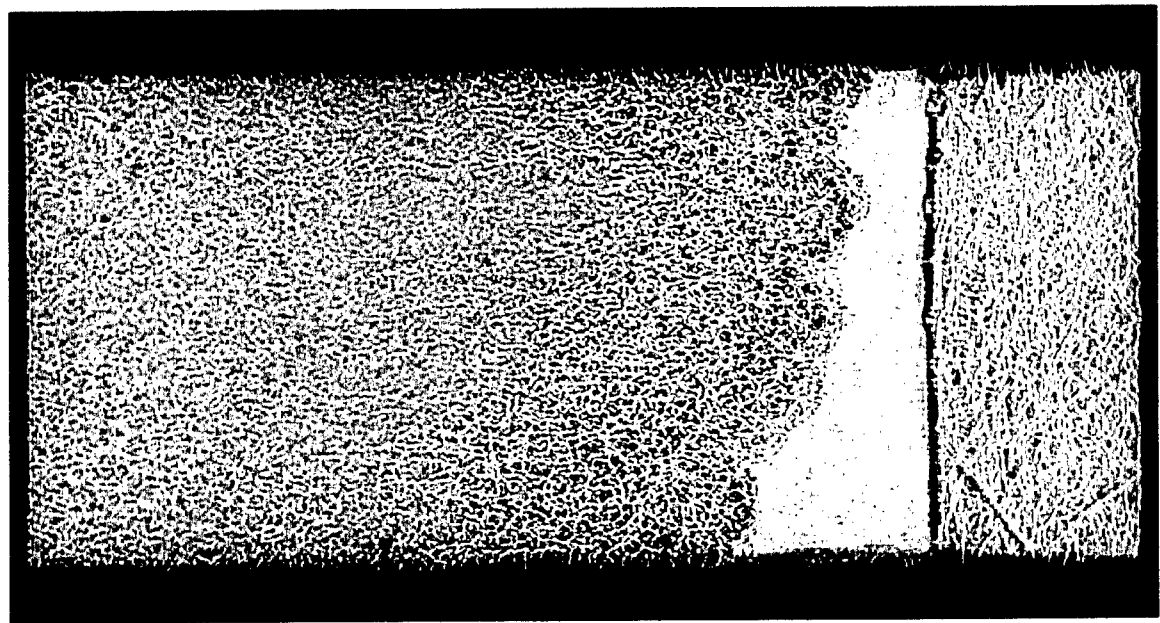


Figure 50 Postprocessed version of Figure 49. The brightness of the area to the right hand of the turbulent border was increased to give more contrast to the borderline.

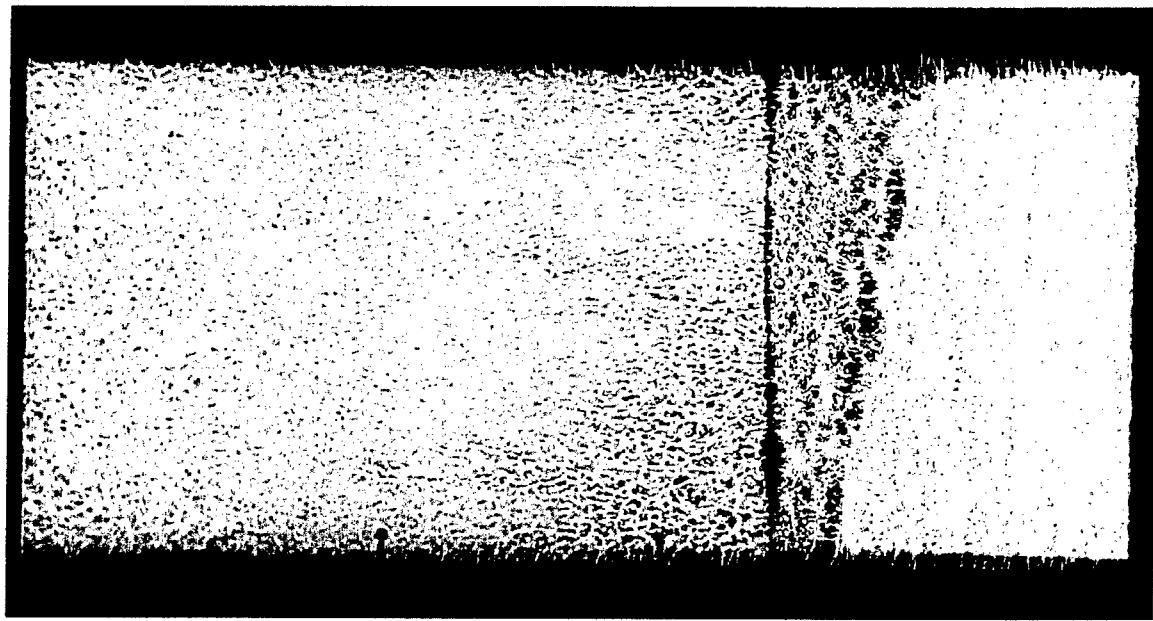


Figure 51 Influence of the reflected shock on the turbulent flowfield at $t = 50 \mu s$
(Test 15283/7).

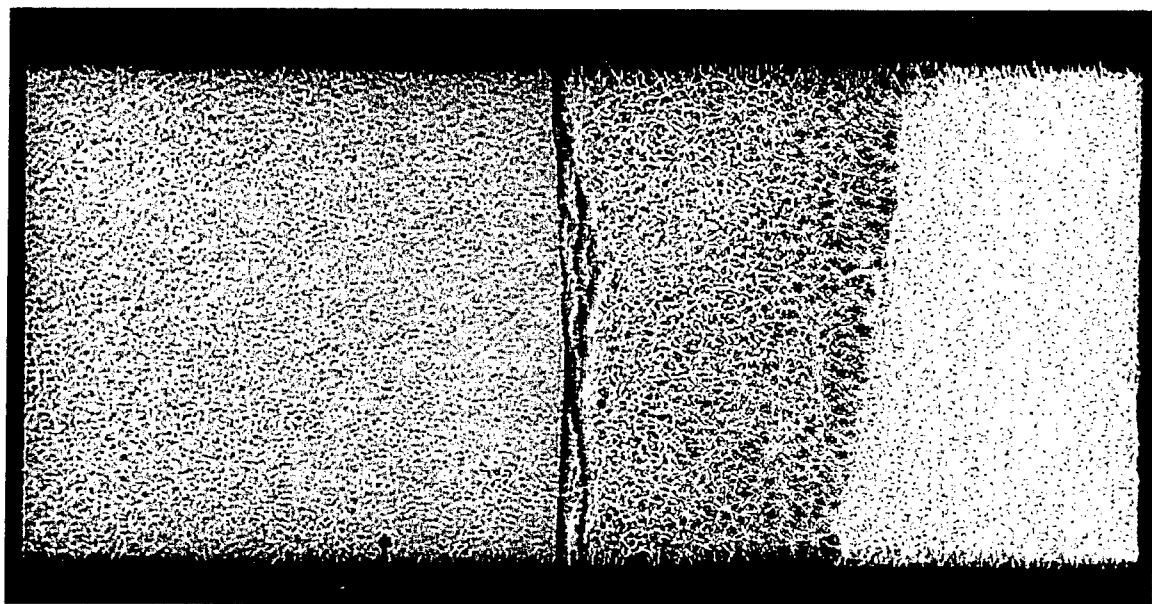


Figure 52 Influence of the reflected shock on the turbulent flowfield at $t = 120 \mu s$
(Test 15283/8).

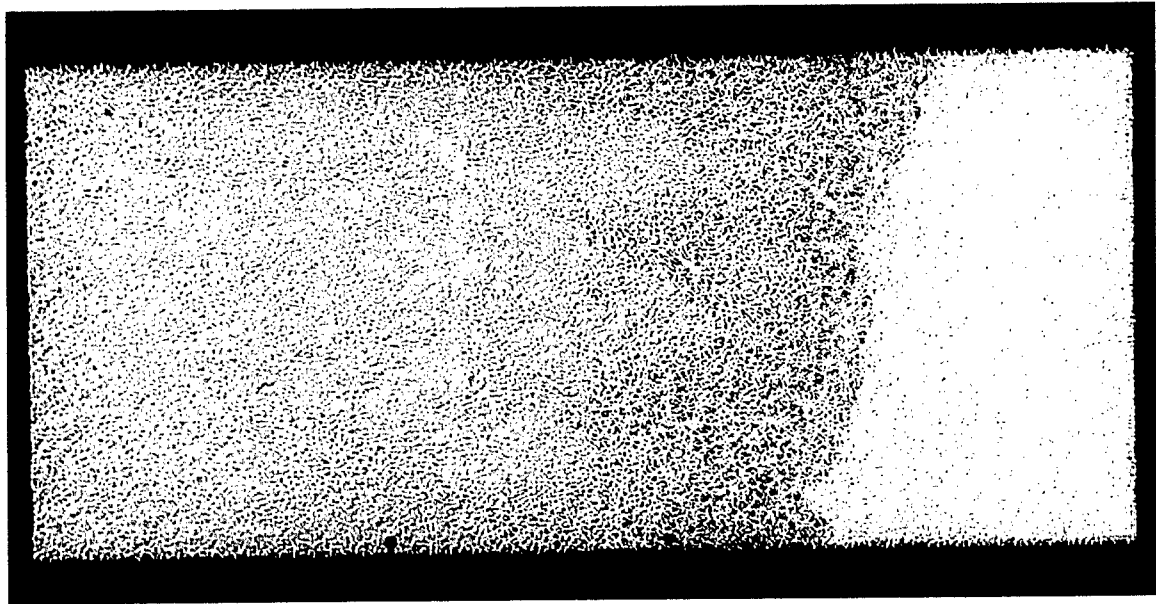


Figure 53 Influence of the reflected shock on the turbulent flowfield at $t = 300 \mu\text{s}$ (Test 15283/11).

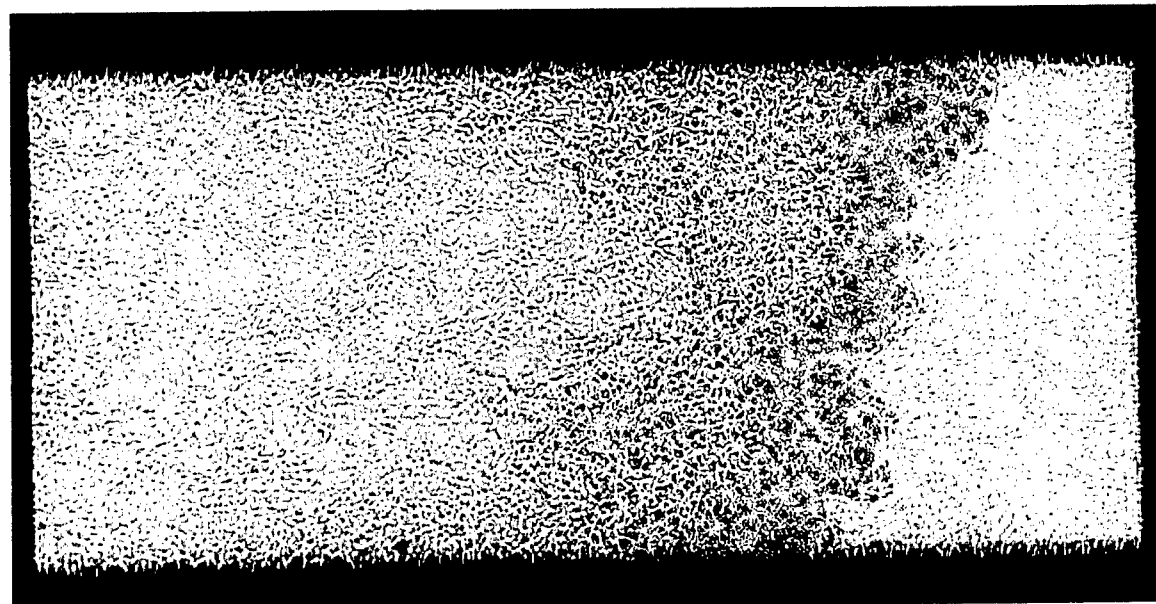


Figure 54 Influence of the reflected shock on the turbulent flowfield at $t = 600 \mu\text{s}$ (Test 15283/7).

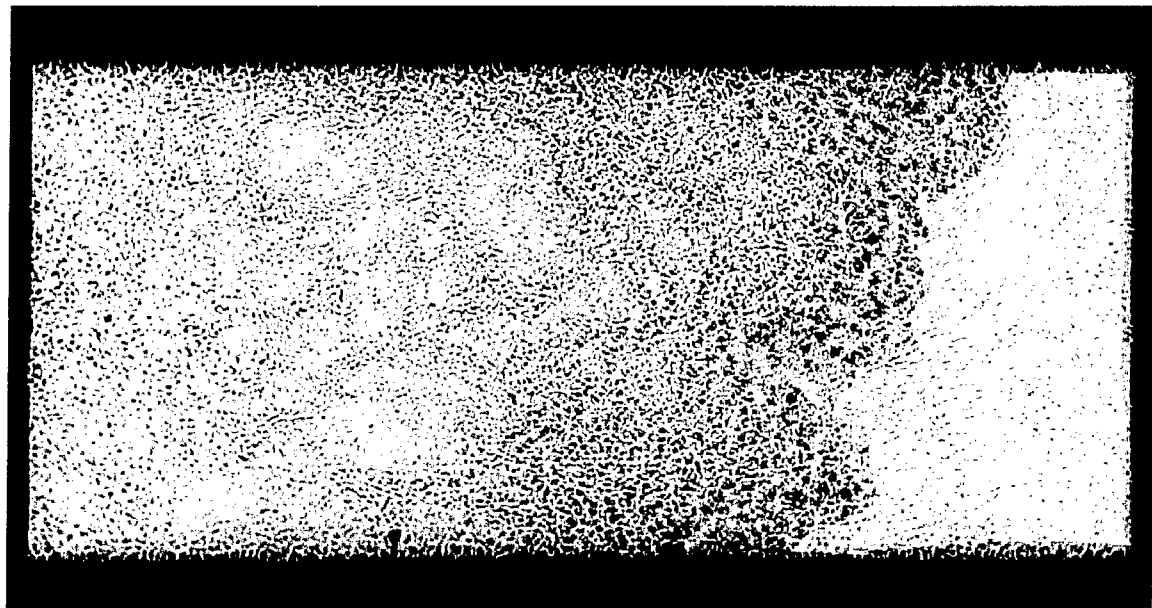


Figure 55 Influence of the reflected shock on the turbulent flowfield at $t = 800 \mu s$ (Test 15283/18).

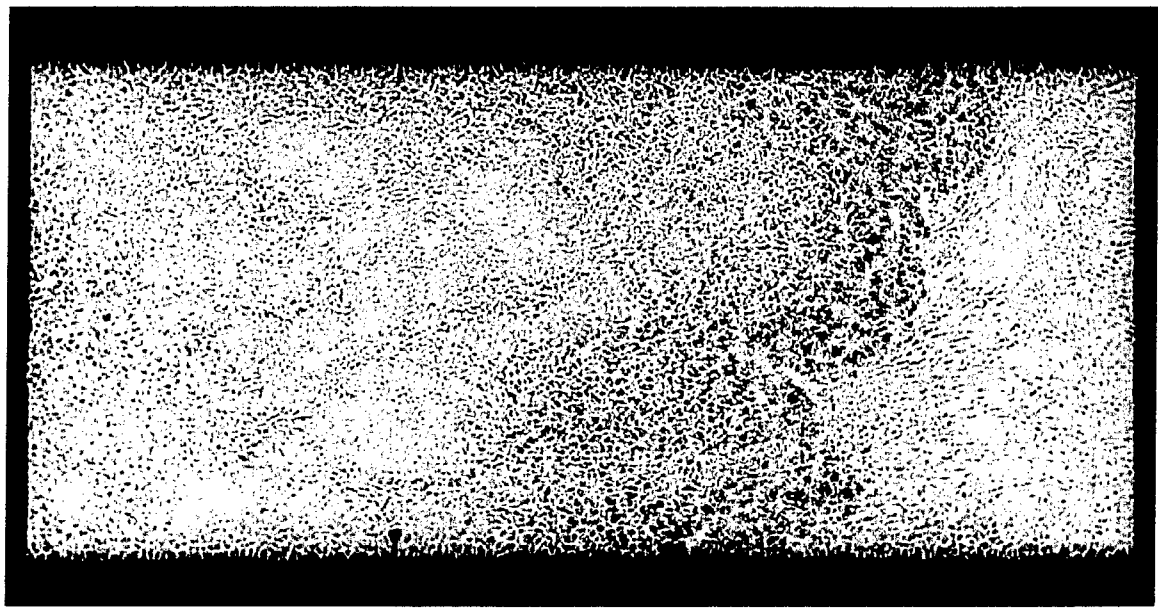


Figure 56 Unprocessed version of Figure 55 in comparison.

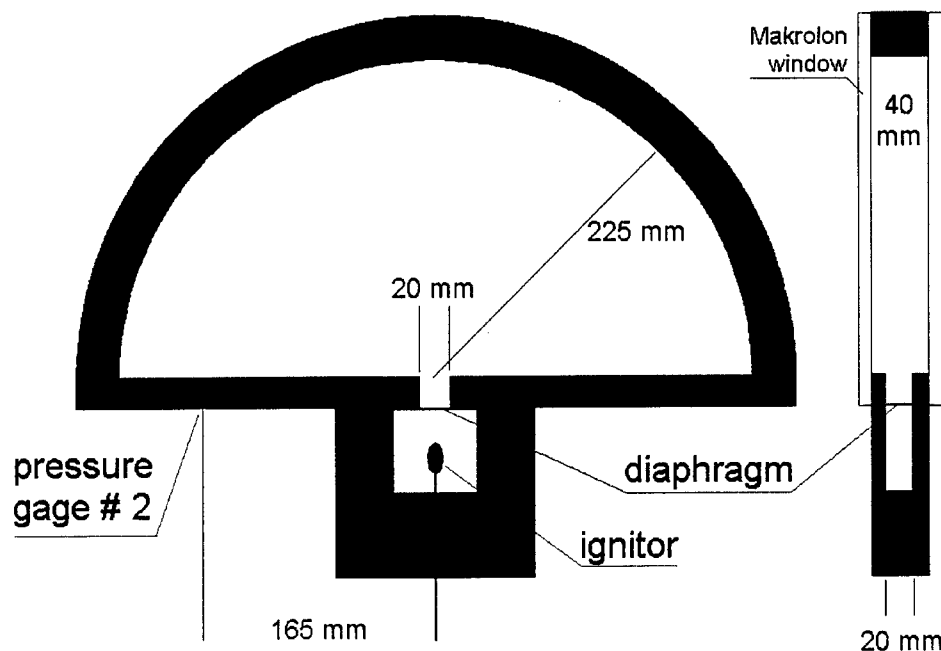
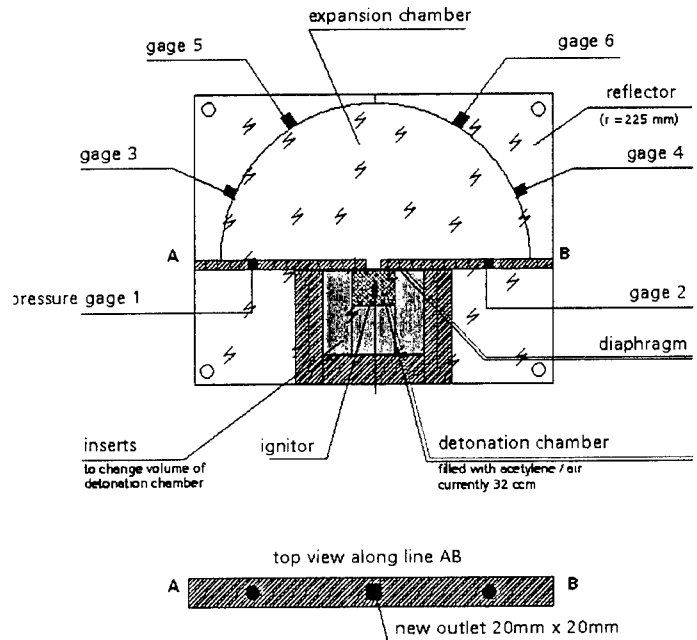


Figure 57 Schematic of the test chamber for experiments on combustion in turbulent jets. Upper picture the initial modifications to the setup Section 5, lower picture the final reconstruction of the setup with steel frame.

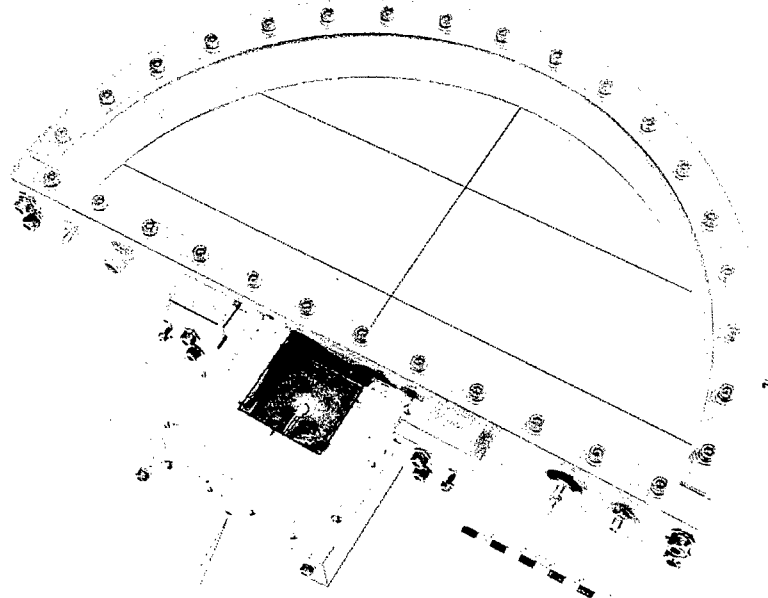


Figure 58 Photograph of the test setup. Front cover of detonation chamber removed.

Table 2 Summary of setup variations.

Version	Detonation Chamber		Outlet dimension [mm]	Expansion Chamber	
	dimension [mm]	volume [cm ³]		radius [mm]	volume [cm ³]
1	40x40x20	32	20x20	225	3181
2	60x60x20	72	20x20	225	3181
3	60x60x20	72	10x20 (insert)	225	3181
4	60x60x20	72	05x20 (insert)	225	3181
5	60x60x20	72	10x20 (knifes)	225	3181
6	60x60x20	72	05x20 (knifes)	225	3181

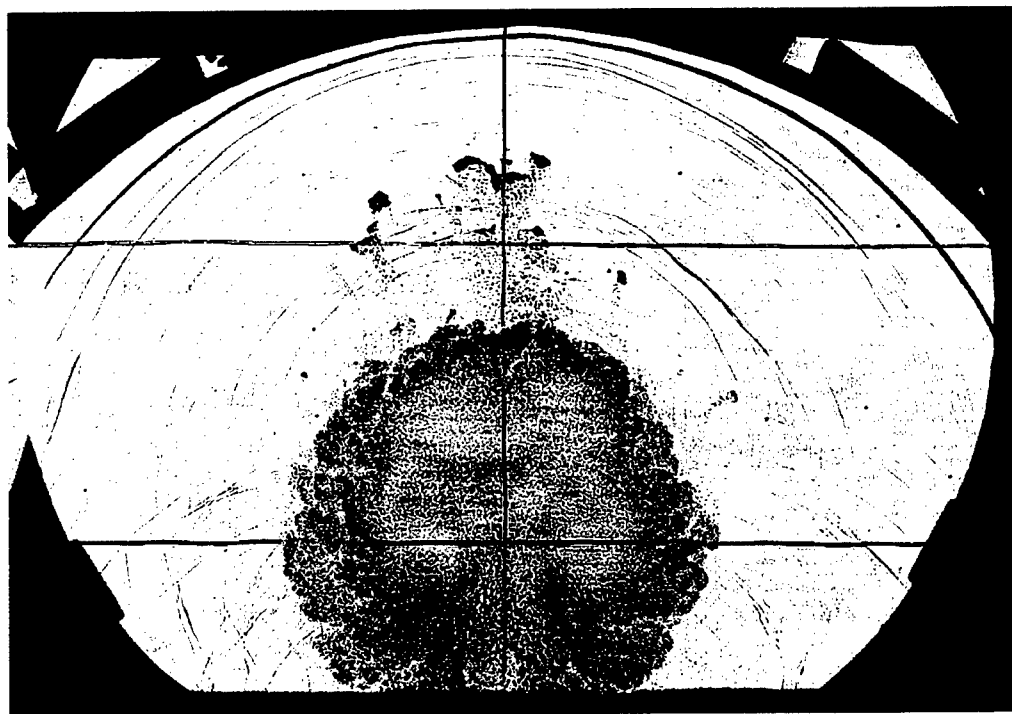


Figure 59 Shadow photograph from the reference test 006/15336 at $t = 0.515$ ms.

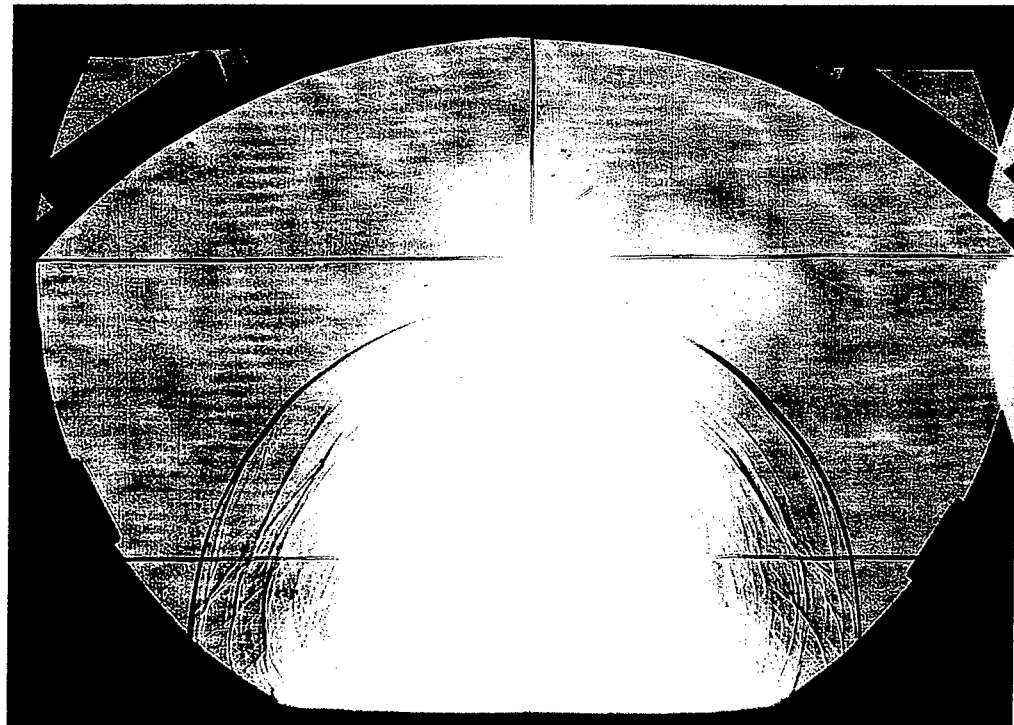


Figure 60 Shadow photograph from Test 0020/15350 at $t = 0.32$ ms

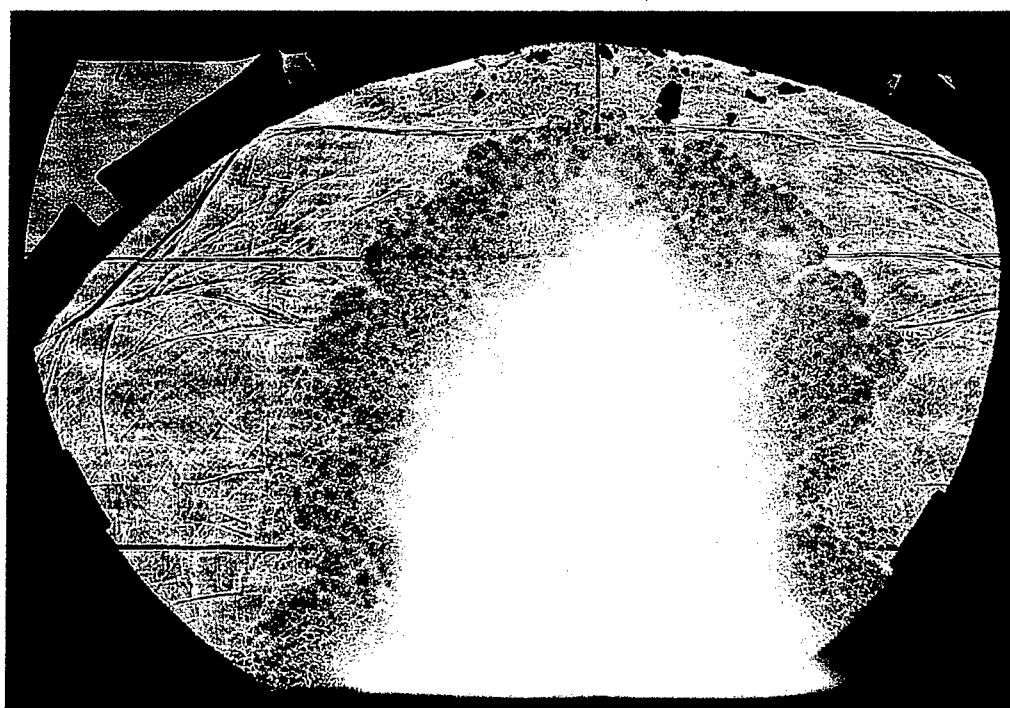


Figure 61 Shadow photograph from Test 0020/15350 at $t = 2$ ms.

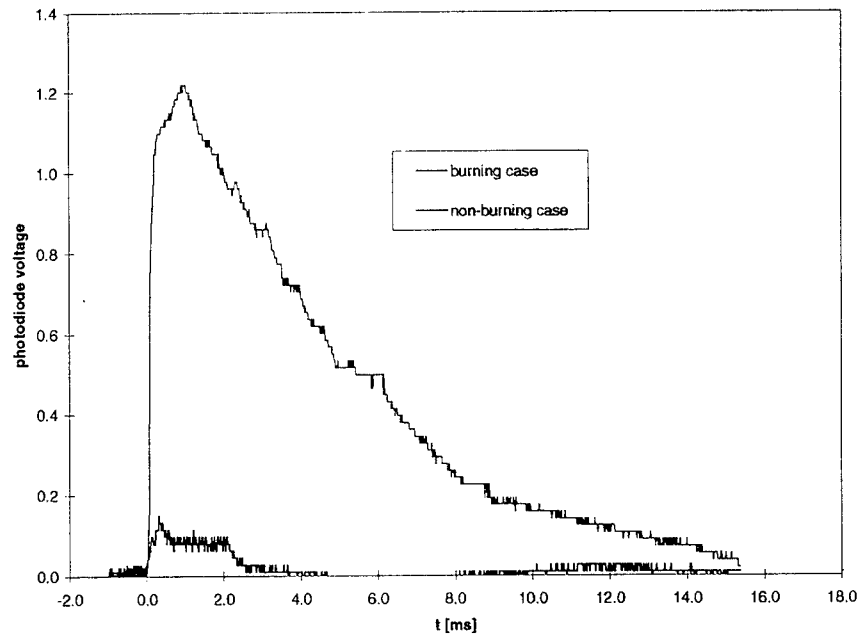


Figure 62 Output of the photodiode monitoring the expansion chamber.
Charge detonates at $t = 0$.

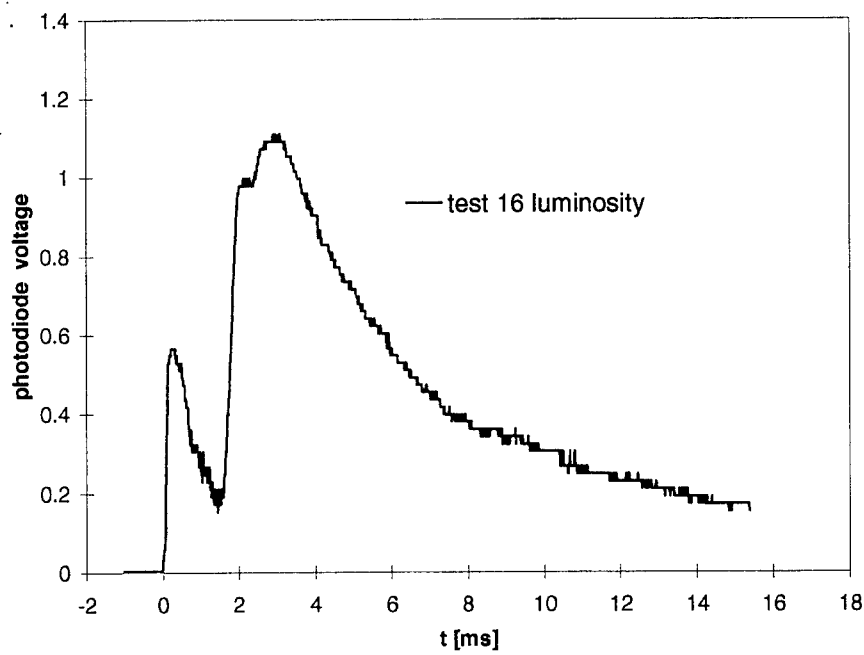


Figure 63 Output of the photodiode for a test with retarded reaction (Test 016).

Table 3 Data of acetylene, C₂H₂

molecular weight M	26 g/mole
heat of combustion ΔH _c	1300.5 kJ/mole
detonability lower limit	4.2 %Vol
upper limit	50 %Vol
inflammability lower limit	2.5 %Vol
upper limit	80 %Vol
stochiometric combustion with air C ₂ H ₂ + 12.5 (0.2 O ₂ + 0.8 N ₂) → 2 CO ₂ + H ₂ O + 10 N ₂	7.4 %Vol
stochiometric combustion with oxygen C ₂ H ₂ + 2.5 O ₂ → 2 CO ₂ + H ₂ O	28.6 %Vol

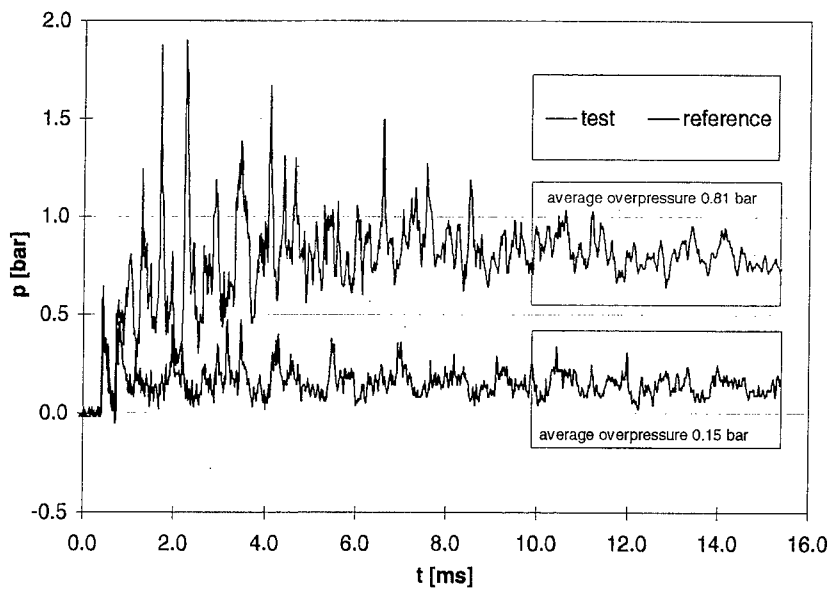
Table 4 Data of methane, CH₄.

molecular weight M	16 g/mole
heat of combustion ΔH _c	890.7 kJ/mole
detonability lower limit	
upper limit	
inflammability lower limit	5.3 %Vol
upper limit	15 %Vol
stochiometric combustion with air CH ₄ + 10 (0.2 O ₂ + 0.8 N ₂) → CO ₂ + 2 H ₂ O + 8 N ₂	9 %Vol
stochiometric combustion with oxygen CH ₄ + 2 O ₂ → CO ₂ + 2 H ₂ O	33 %Vol

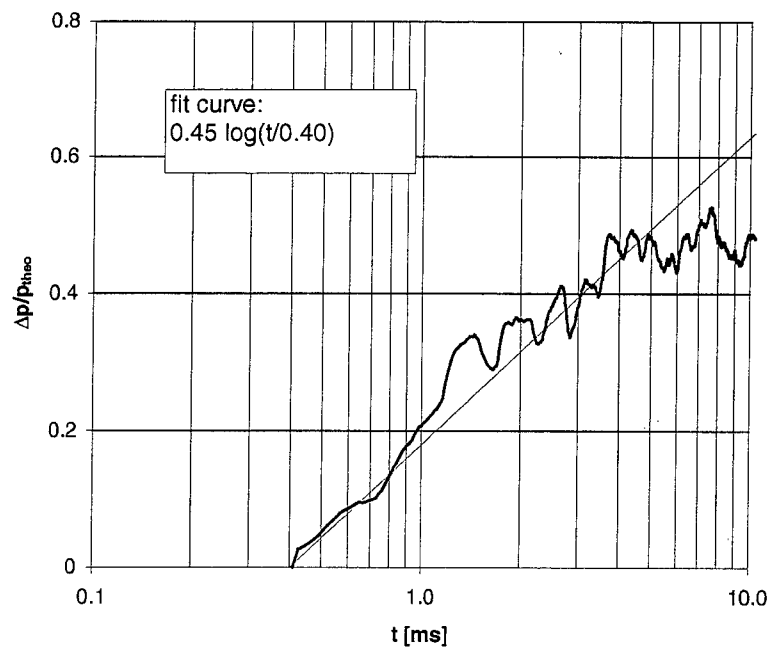
Table 5 Summary of the measurements with acetylene
in the 32 cm³ detonation chamber

In all experiments (see Figures 64 to 74) the expansion chamber was filled with air at ambient pressure and the acetylene in the detonation chamber was mixed with air.

test	comments	C ₂ H ₂	O ₂	N ₂	π_c (theo)	p _{end}	fit curve	burning rate
		[mbar]	[mbar]	[mbar]	[bar]	[bar]	[t in ms]	
05	reference	0	200	800				
06	reference	0	200	800				
07		900	20	80	1.47	0.81	0.45 log ₁₀ (t/0.40)	-0.20 / t
08	no reaction	970	6	24				
09	no reaction	1000	0	0				
10	no reaction	970	6	24				
11		900	20	80	1.47	0.89	0.48 log ₁₀ (t/0.30)	-0.21 / t
12	no reaction	900	20	80				
13		900	20	80	1.47	0.80	0.45 log ₁₀ (t/0.30)	-0.20 / t
14		840	32	128	1.37	0.85	0.48 log ₁₀ (t/0.25)	-0.21 / t
15	no reaction	840	32	128				
16	retarded	800	40	160	1.31	0.88	0.48 log ₁₀ (t/0.30)	-0.21 / t
17	retarded	815	37	148	1.33	0.96	0.50 log ₁₀ (t/0.25)	-0.22 / t
18	no reaction	800	40	160				
19	no reaction	790	42	168				
20		500	100	400	0.82	0.54	0.48 log ₁₀ (t/0.25)	-0.21 / t
21		500	100	400	0.82	0.55	0.50 log ₁₀ (t/0.25)	-0.22 / t
22	no reaction	640	72	288				
23	no reaction	650	70	280				
24	no reaction	600	80	320				
25	no reaction	600	80	320				
26		505	99	396	0.82	0.54	0.50 log ₁₀ (t/0.25)	-0.22 / t
27		500	100	400	0.82	0.53	0.48 log ₁₀ (t/0.25)	-0.21 / t
28		500	100	400	0.82	0.56	0.50 log ₁₀ (t/0.20)	-0.22 / t

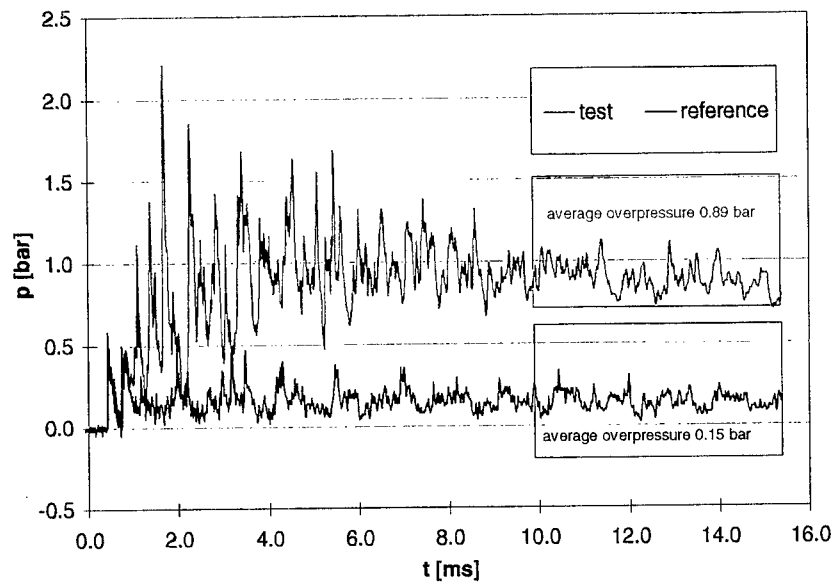


(a) Comparison of the pressure records at gage 2 to the non-reactive reference test.

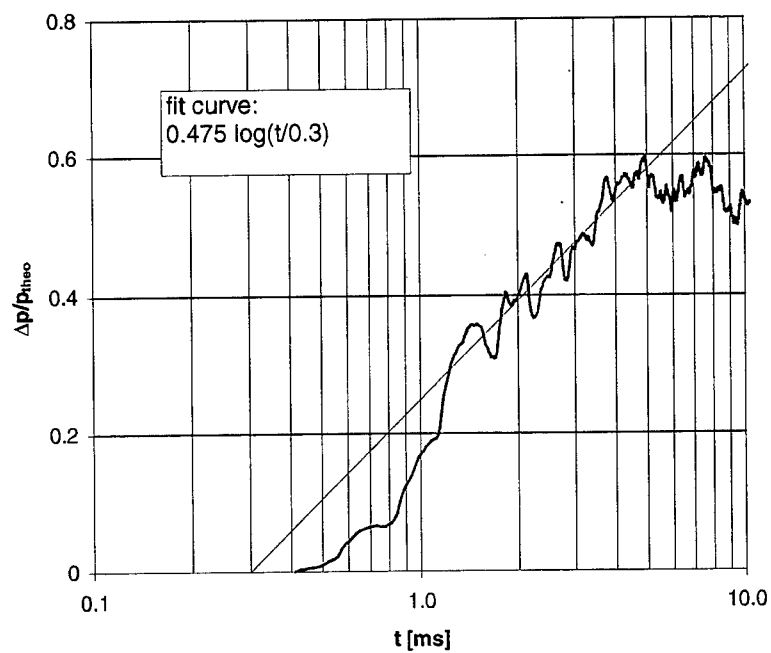


(b) Semi-logarithmic plot of the pressure gain, normalized by π_c .

Figure 64 Test 7: 900 mbar C_2H_2

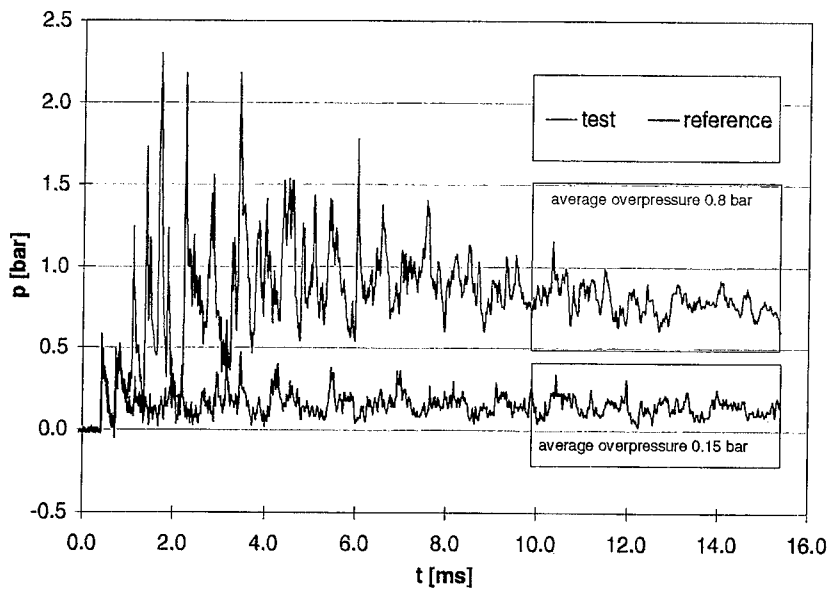


(a) Comparison of the pressure records at gage 2 to the non-reactive reference test.

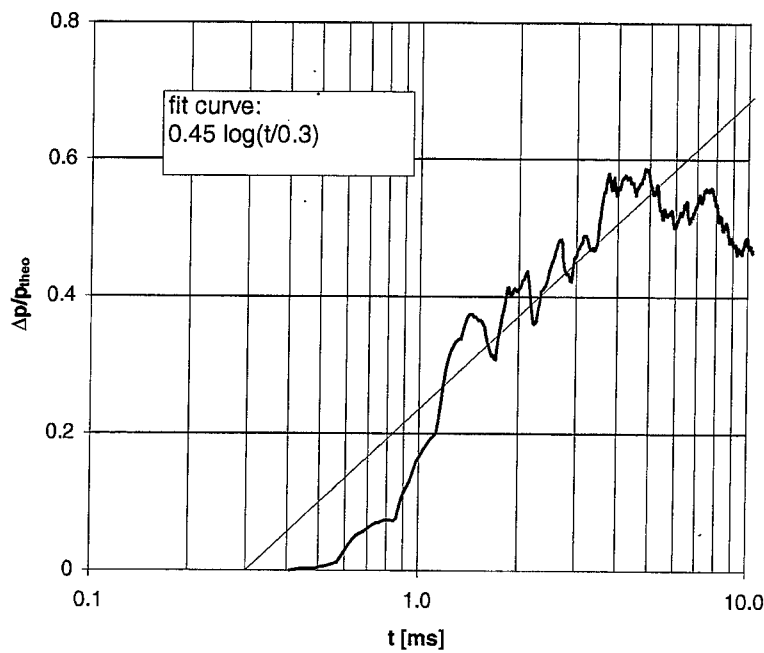


(b) Semi-logarithmic plot of the pressure gain, normalized by π_c .

Figure 65 Test 11: 900 mbar C_2H_2

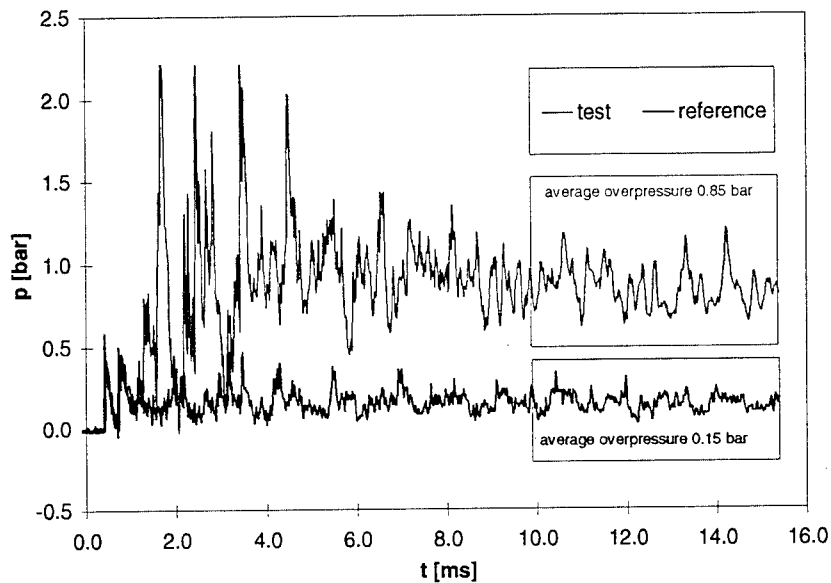


(a) Comparison of the pressure records at gage 2 to the non-reactive reference test.

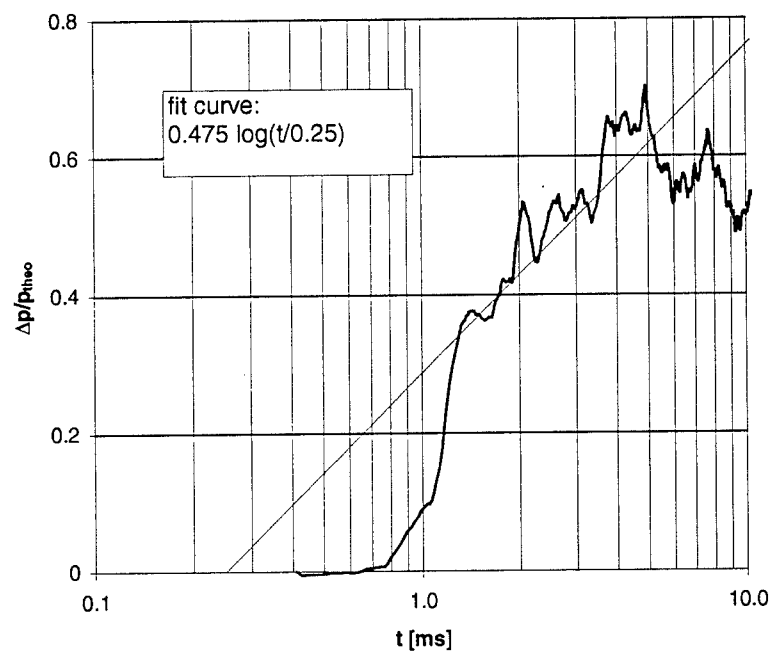


(b) Semi-logarithmic plot of the pressure gain, normalized by π_c .

Figure 66 Test 13: 900 mbar C_2H_2

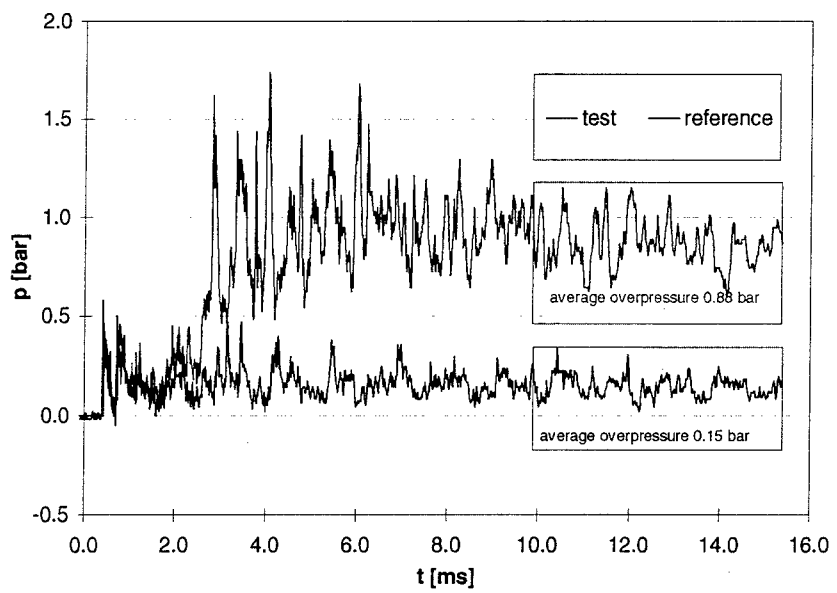


(a) Comparison of the pressure records at gage 2 to the non-reactive reference test.

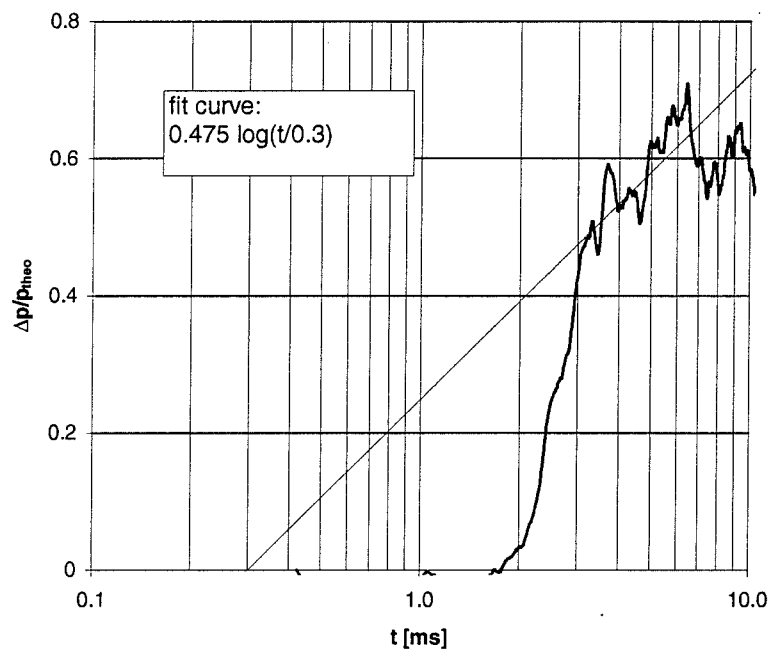


(b) Semi-logarithmic plot of the pressure gain, normalized by π_c .

Figure 67 Test 14: 840 mbar C₂H₂

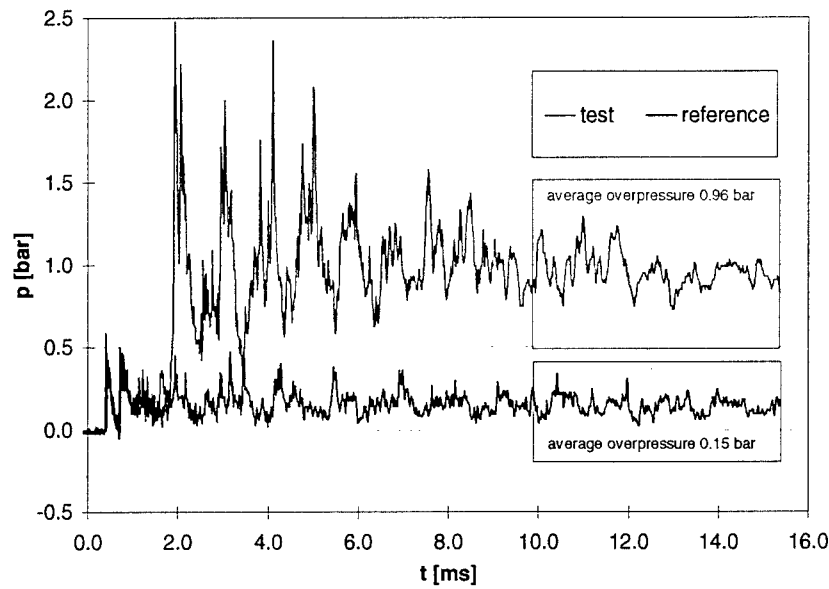


(a) Comparison of the pressure records at gage 2 to the non-reactive reference test.

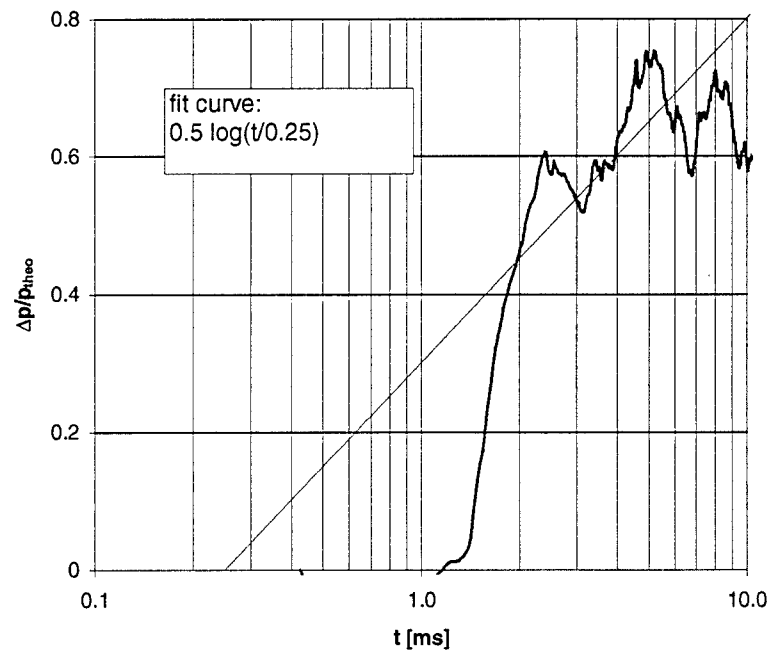


(b) Semi-logarithmic plot of the pressure gain, normalized by π_c .

Figure 68 Test 16: 800 mbar C₂H₂

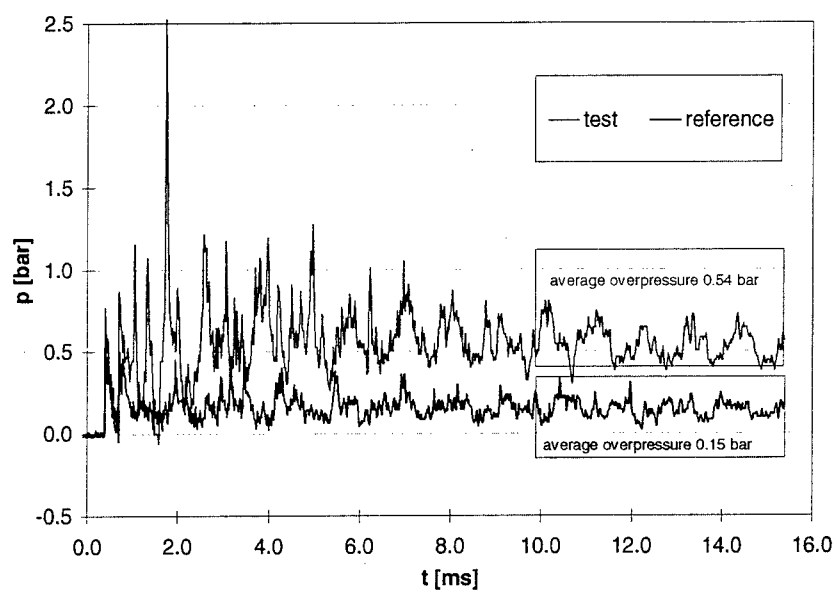


(a) Comparison of the pressure records at gage 2 to the non-reactive reference test.

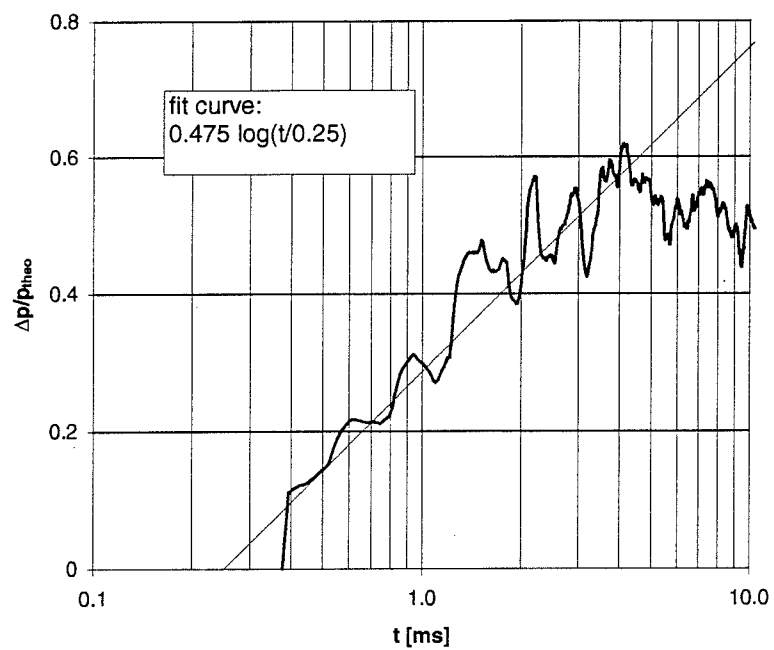


(b) Semi-logarithmic plot of the pressure gain, normalized by π_c .

Figure 69 Test 17: 815 mbar C_2H_2

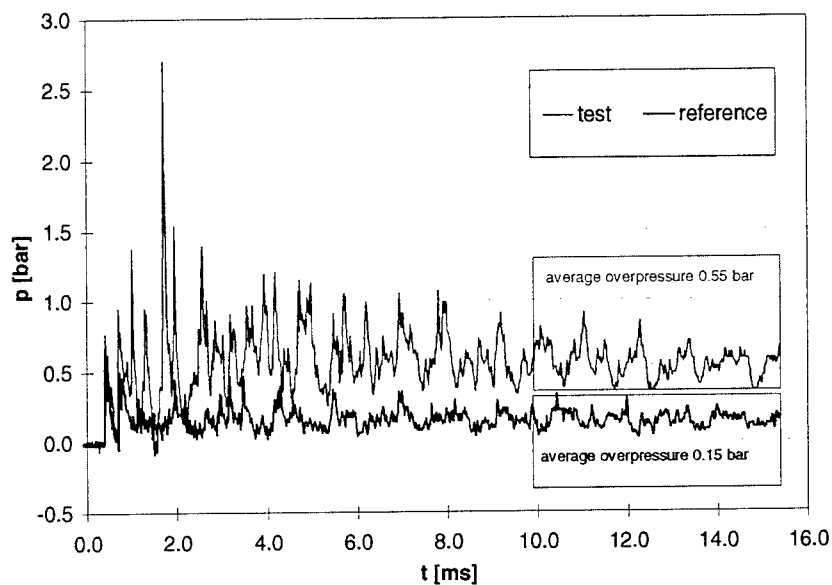


(a) Comparison of the pressure records at gage 2 to the non-reactive reference test.

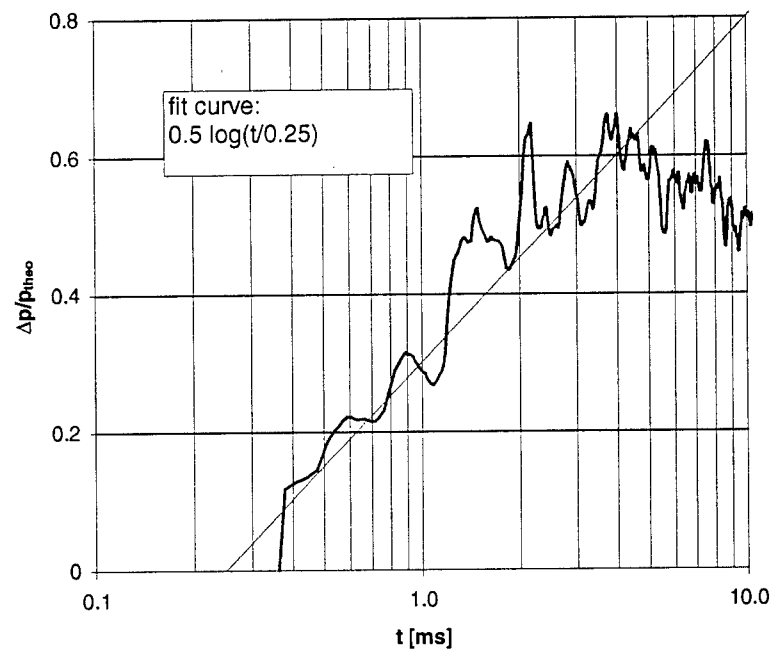


(b) Semi-logarithmic plot of the pressure gain, normalized by π_c .

Figure 70 Test 20: 500 mbar C_2H_2

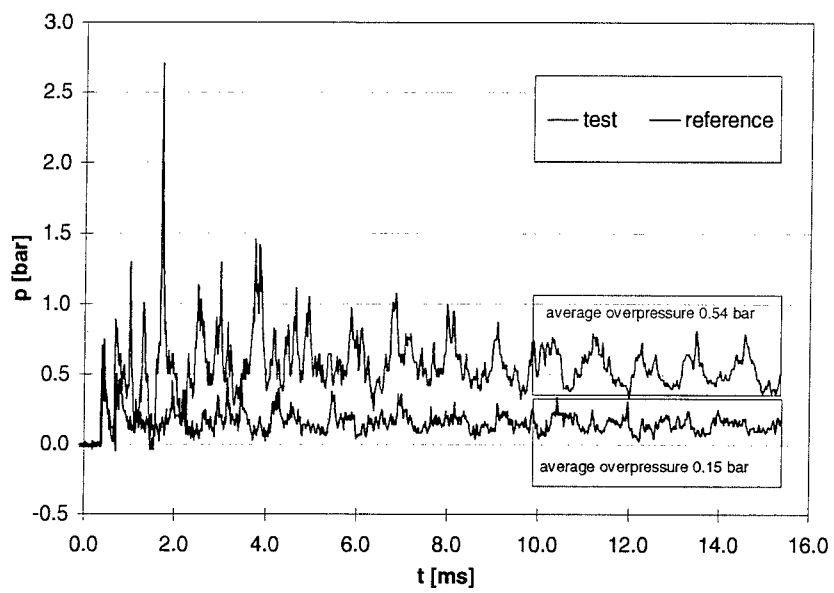


(a) Comparison of the pressure records at gage 2 to the non-reactive reference test.

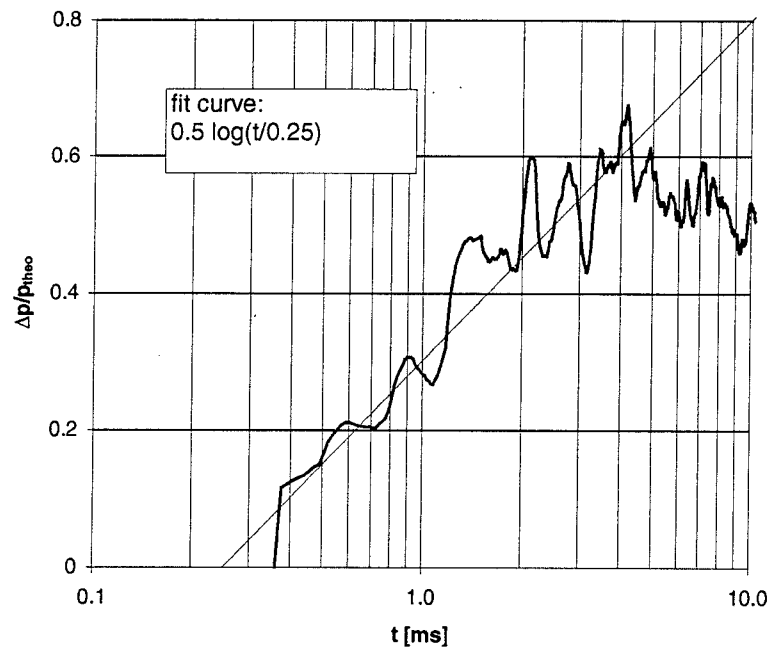


(b) Semi-logarithmic plot of the pressure gain, normalized by π_c .

Figure 71 Test 21: 500 mbar C_2H_2

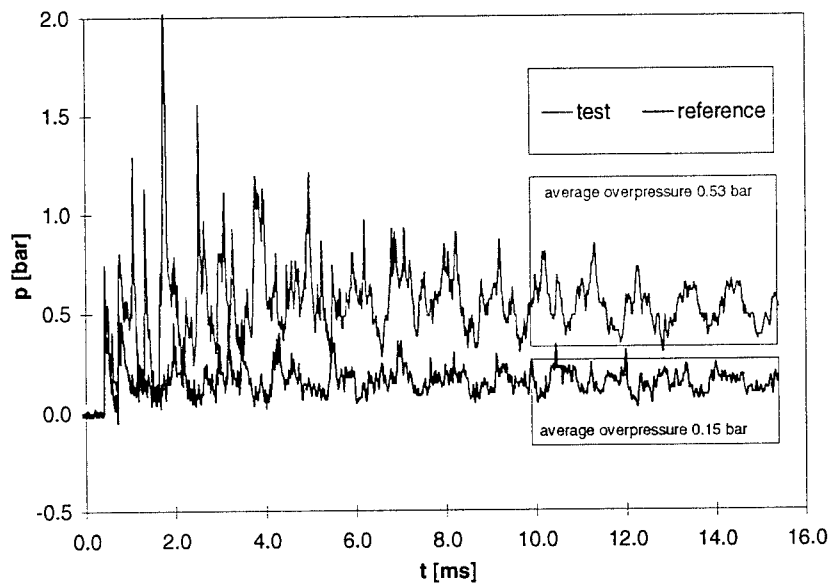


(a) Comparison of the pressure records at gage 2 to the non-reactive reference test.

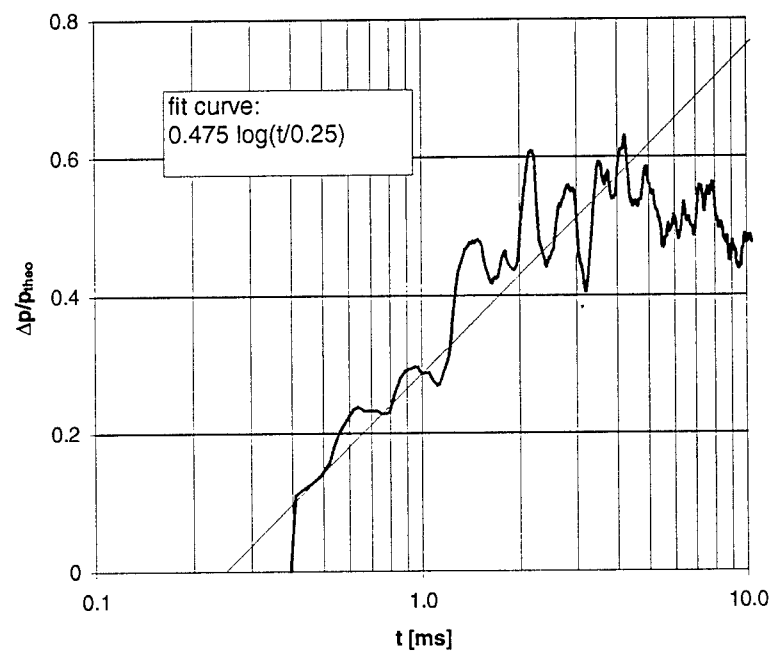


(b) Semi-logarithmic plot of the pressure gain, normalized by π_c .

Figure 72 Test 26: 500 mbar C₂H₂

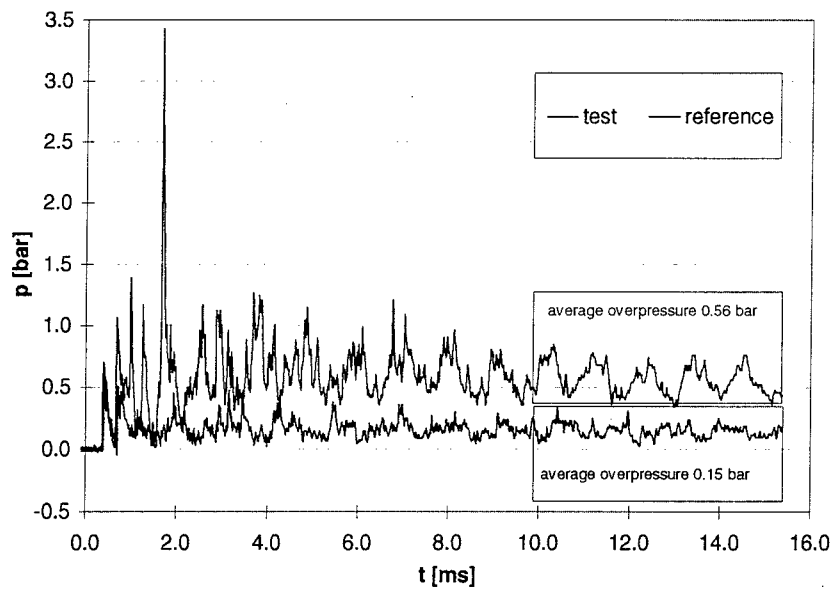


(a) Comparison of the pressure records at gage 2 to the non-reactive reference test.

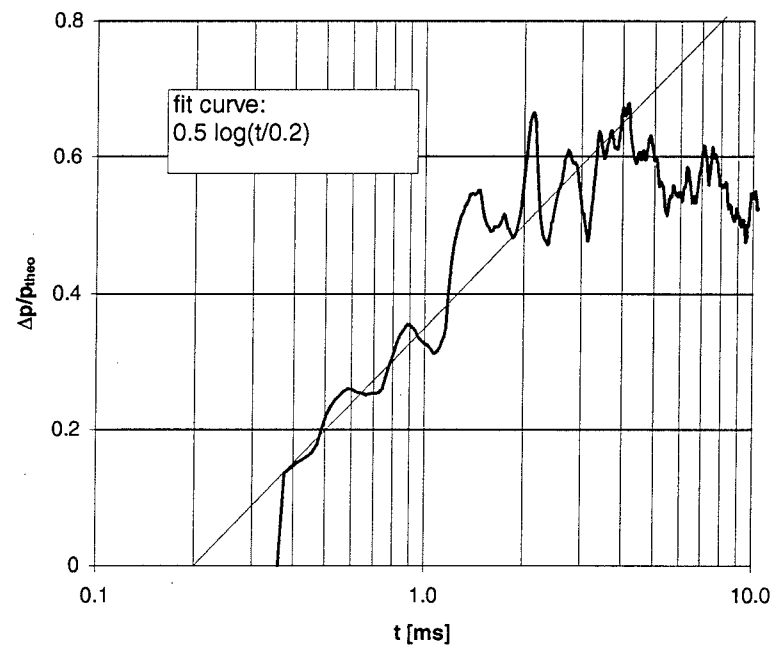


(b) Semi-logarithmic plot of the pressure gain, normalized by π_c .

Figure 73 Test 27: 500 mbar C₂H₂



(a) Comparison of the pressure records at gage 2 to the non-reactive reference test.



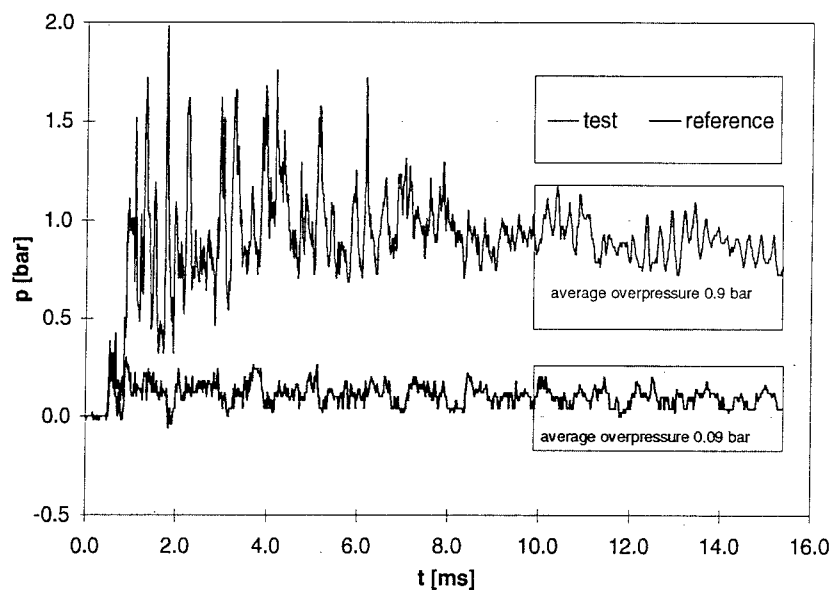
(b) Semi-logarithmic plot of the pressure gain, normalized by π_c .

Figure 74 Test 28: 500 mbar C_2H_2

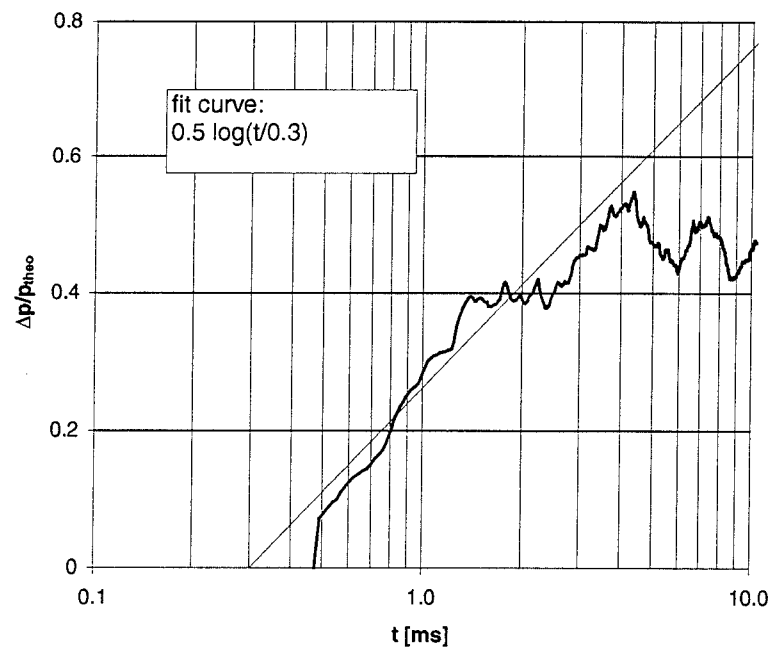
Table 6 Summary of the experiments with acetylene
in the 72 cm³ detonation chamber

In all following tests (see Figures 75 to 89) the expansion chamber was filled with air at ambient pressure and the detonation chamber with various mixtures of acetylene, air and oxygen.

test	comments	C ₂ H ₂	O ₂	N ₂	π_c (theo)	p _{end}	fit curve	burning rate
		version	[mbar]	[mbar]	[mbar]	[bar]	[bar]	{t in ms}
29	2		500	100	400	1.84	0.90	0.50 log ₁₀ (t/0.30) -0.22 / t
30	2	no reaction	500	100	400			
31	2	no reaction	500	100	400			
32	2	reference	0	200	800		0.09	
33	2		400	120	480	1.47	0.77	0.50 log ₁₀ (t/0.25) -0.22 / t
34	2		400	120	480	1.47	0.70	0.45 log ₁₀ (t/0.25) -0.20 / t
35	2		400	120	480	1.47	0.77	0.45 log ₁₀ (t/0.20) -0.20 / t
36	2		400	120	480	1.47	0.78	0.45 log ₁₀ (t/0.20) -0.20 / t
37	2		600	133	267	2.20	0.90	0.38 log ₁₀ (t/0.25) -0.22 / t
38	2		600	133	267	2.20	0.95	0.38 log ₁₀ (t/0.23) -0.22 / t
39	2	no reaction	800	67	133			
40	2		700	100	200	2.57	0.99	0.38 log ₁₀ (t/0.30) -0.22 / t
41	2		700	100	200	2.57	1.01	0.38 log ₁₀ (t/0.30) -0.22 / t
42	2	no reaction	800	100	100			
43	2		700	150	150	2.57	1.05	0.38 log ₁₀ (t/0.25) -0.17 / t
44	2	retarded (?)	700	150	150	2.57	1.02	0.45 log ₁₀ (t/0.40) -0.20 / t
45	3		700	150	150	2.57	0.98	0.38 log ₁₀ (t/0.30) -0.17 / t
46	4		700	150	150	2.57	0.91	0.38 log ₁₀ (t/0.43) -0.17 / t
47	6		700	150	150	2.57	0.94	0.38 log ₁₀ (t/0.43) -0.17 / t
48	5	retarded	700	150	150	2.57	1.14	0.43 log ₁₀ (t/0.45) -0.19 / t

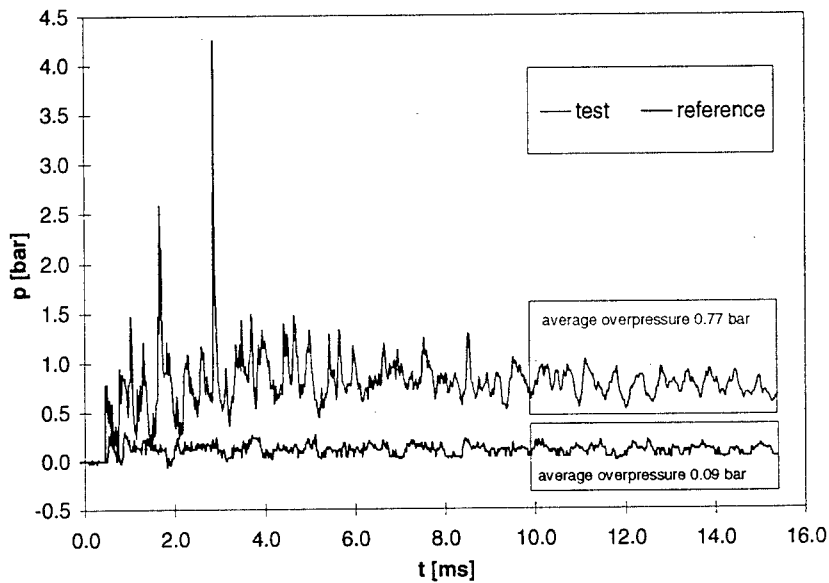


(a) Comparison of the pressure records at gage 2 to the non-reactive reference test.

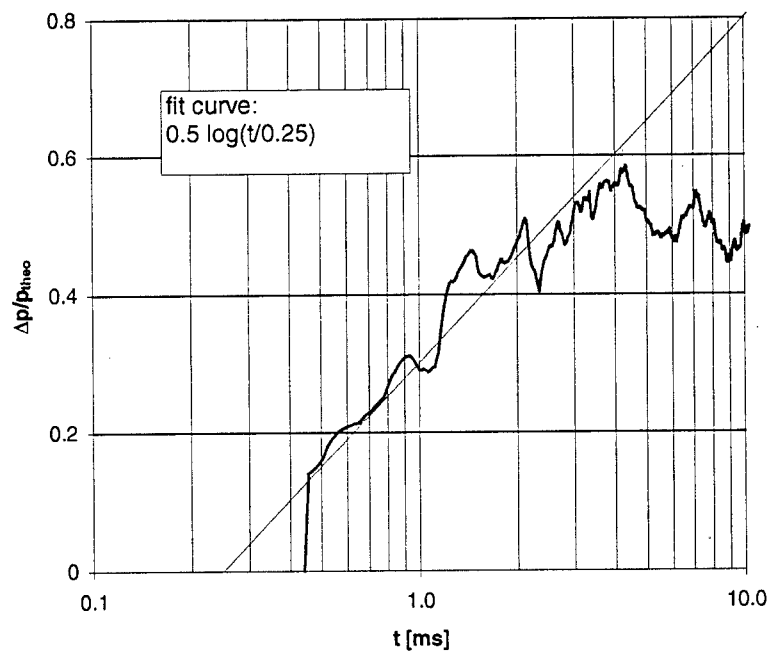


(b) Semi-logarithmic plot of the pressure gain, normalized by π_c .

Figure 75 Test 29: 500 mbar C_2H_2

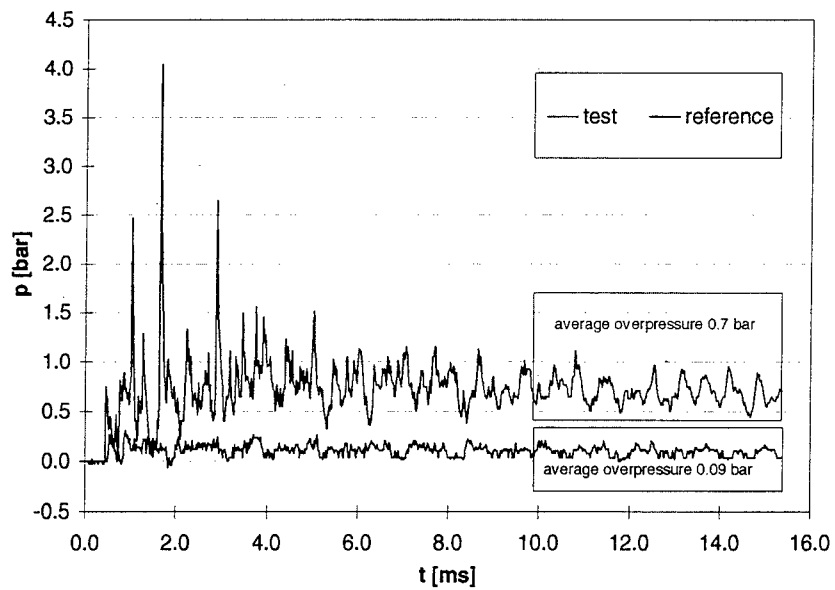


(a) Comparison of the pressure records at gage 2 to the non-reactive reference test.

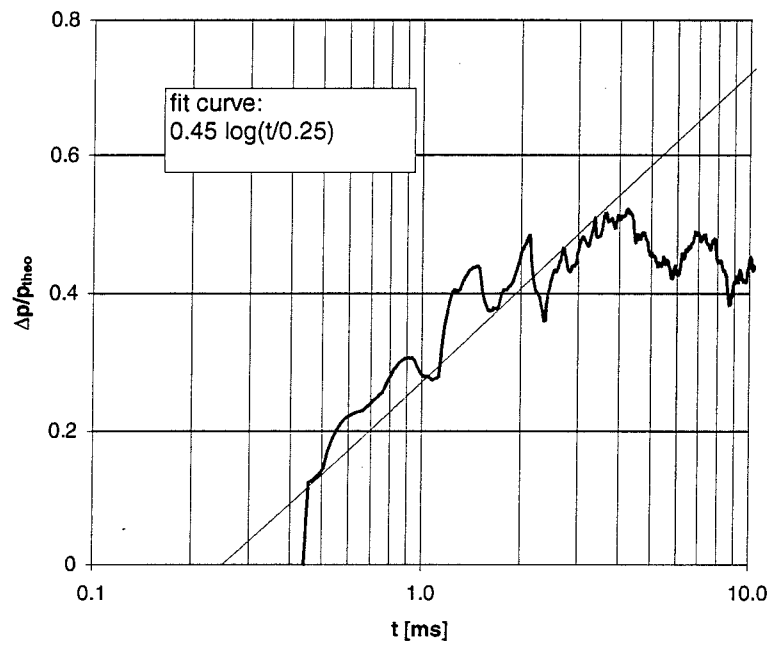


(b) Semi-logarithmic plot of the pressure gain, normalized by π_c .

Figure 76 Test 33: 400 mbar C₂H₂

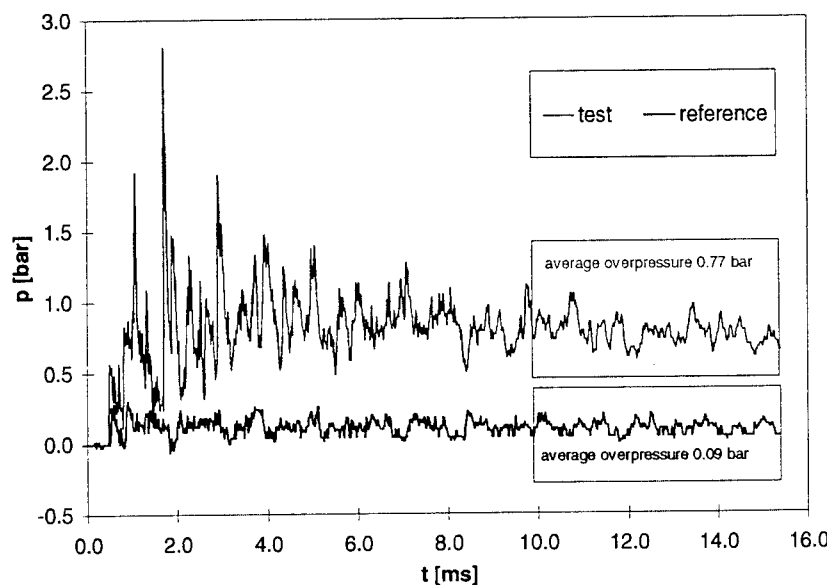


(a) Comparison of the pressure records at gage 2 to the non-reactive reference test.

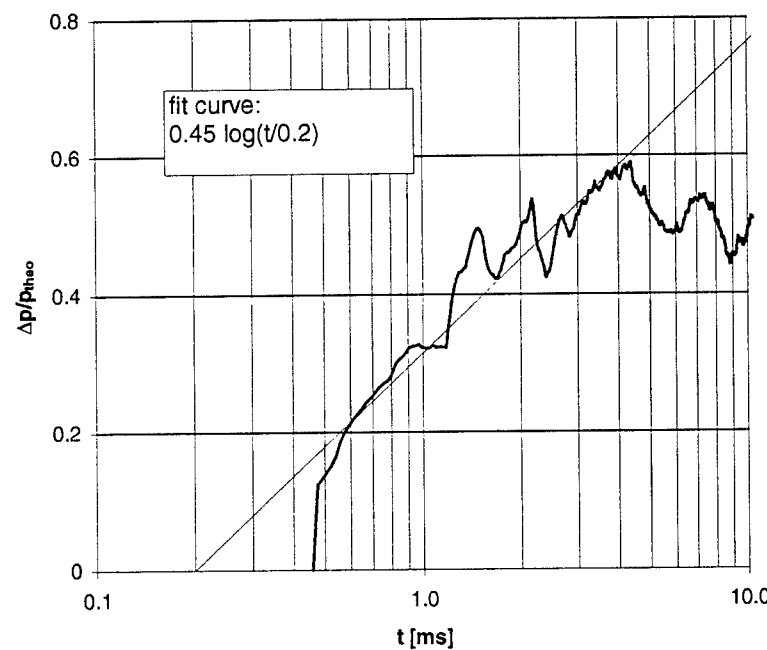


(b) Semi-logarithmic plot of the pressure gain, normalized by π_c .

Figure 77 Test 34: 400 mbar C₂H₂

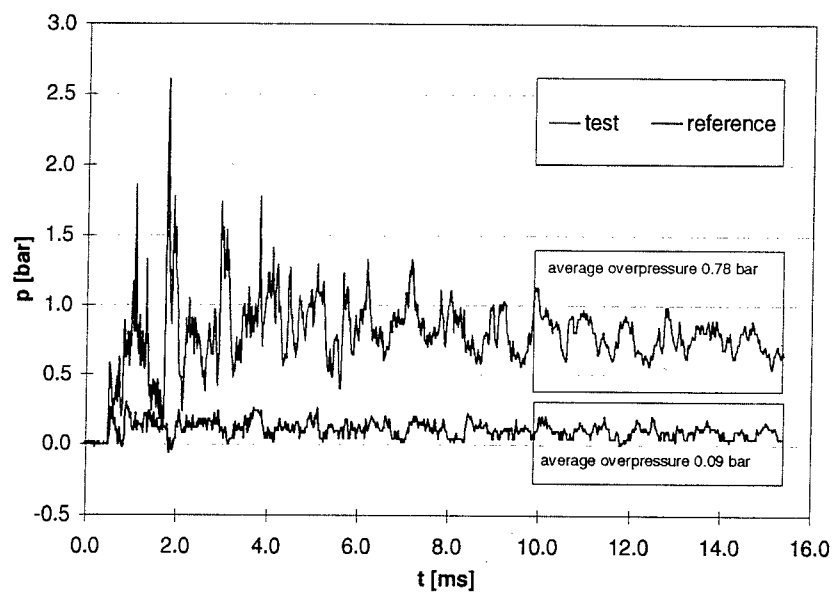


(a) Comparison of the pressure records at gage 2 to the non-reactive reference test.

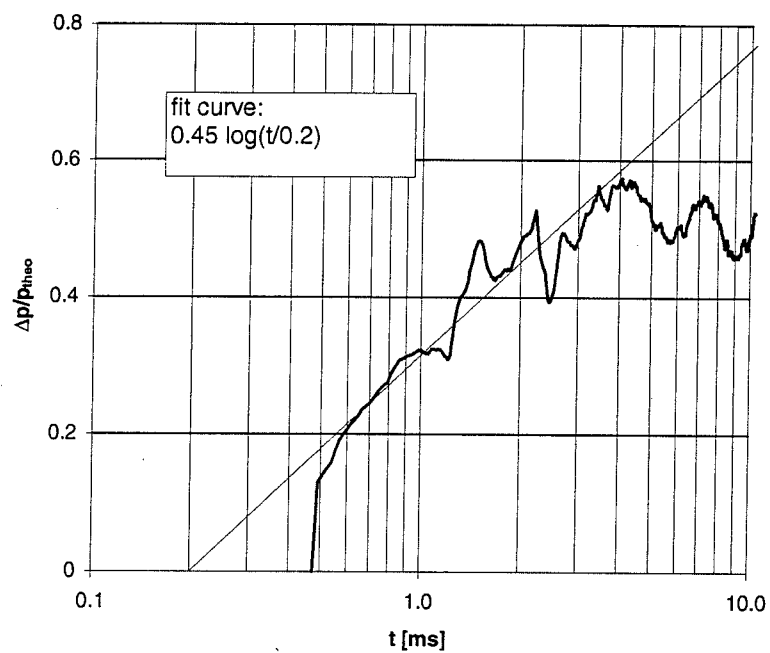


(b) Semi-logarithmic plot of the pressure gain, normalized by π_c .

Figure 78 Test 35: 400 mbar C_2H_2

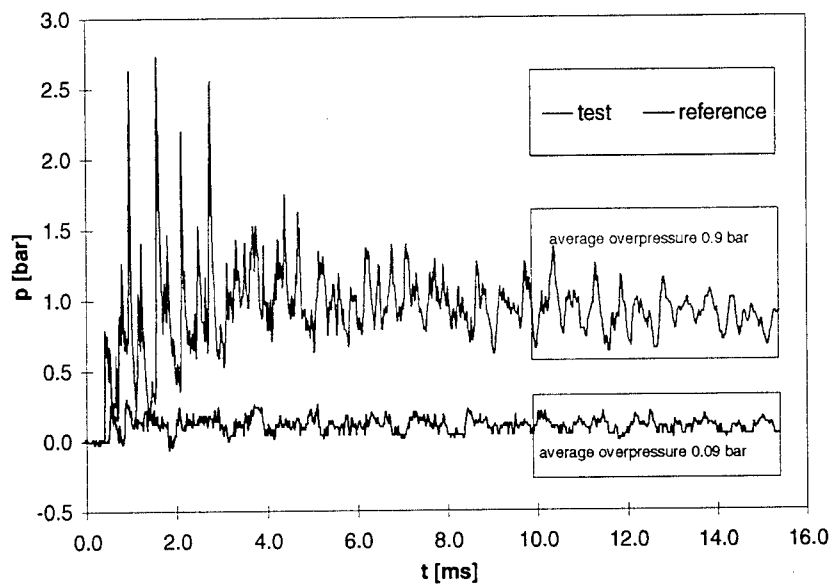


(a) Comparison of the pressure records at gage 2 to the non-reactive reference test.

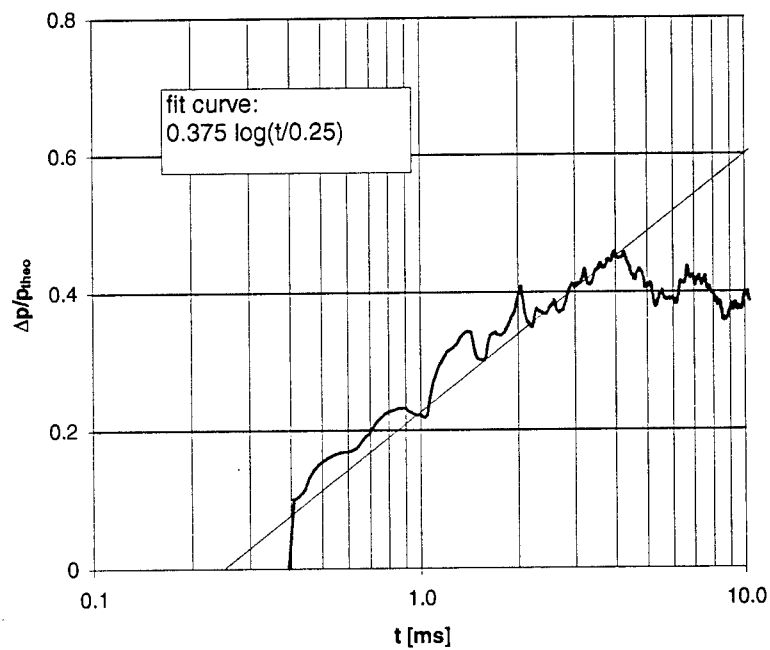


(b) Semi-logarithmic plot of the pressure gain, normalized by π_c .

Figure 79 Test 36: 400 mbar C_2H_2

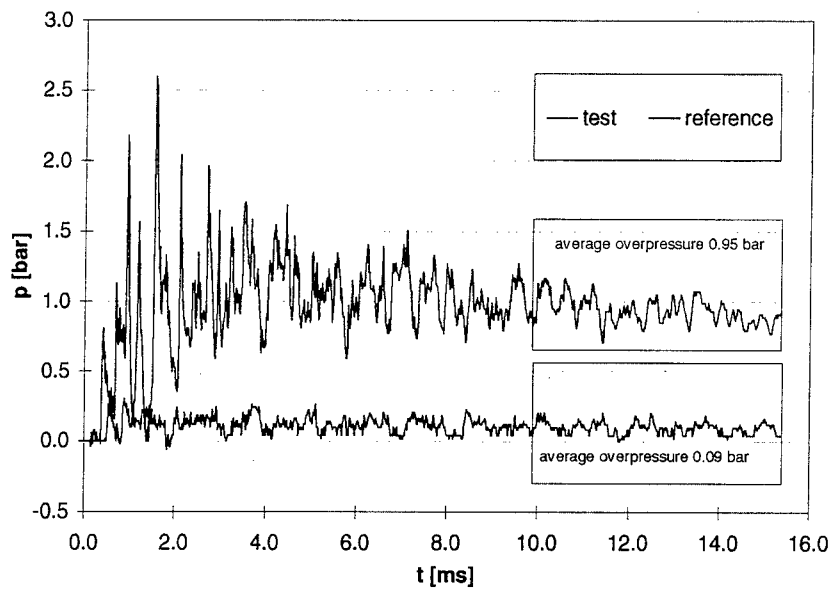


(a) Comparison of the pressure records at gage 2 to the non-reactive reference test.

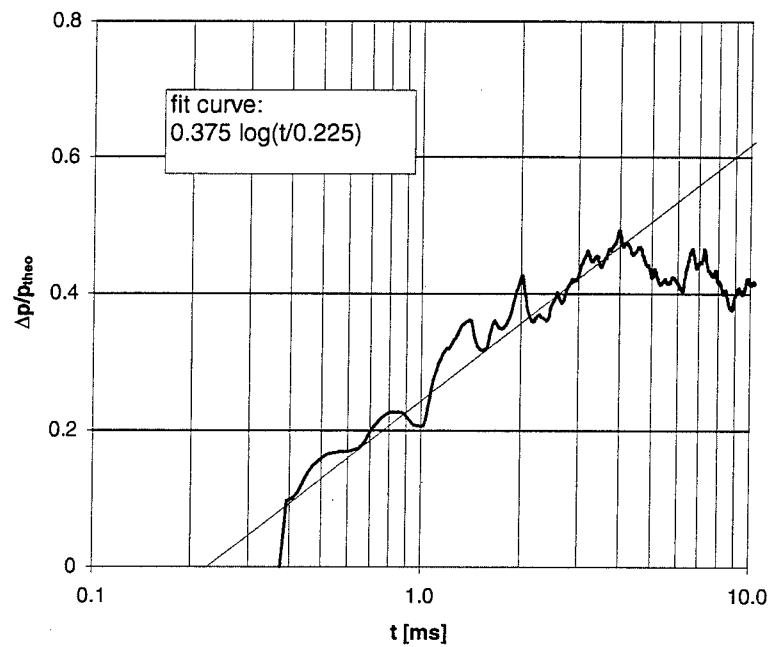


(b) Semi-logarithmic plot of the pressure gain, normalized by π_c .

Figure 80 Test 37: 600 mbar $C_2H_2 + (1O_2 + 2N_2)$

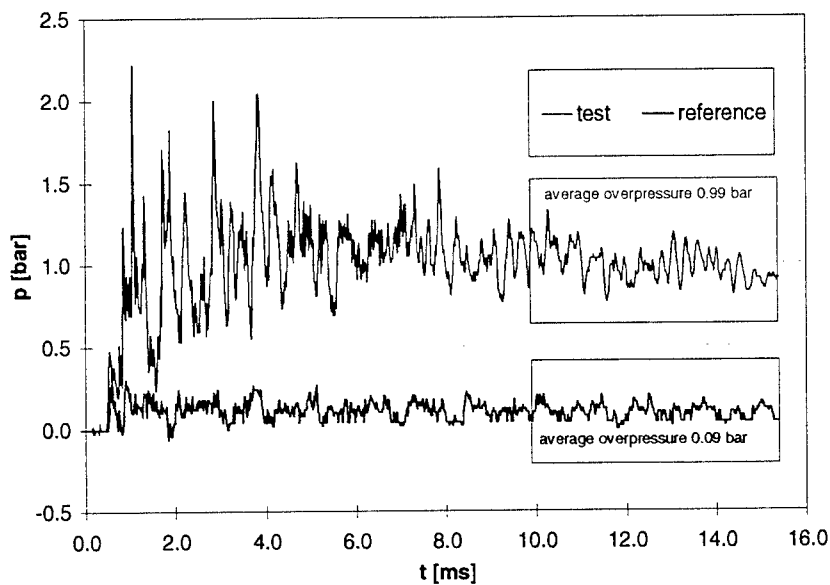


(a) Comparison of the pressure records at gage 2 to the non-reactive reference test.

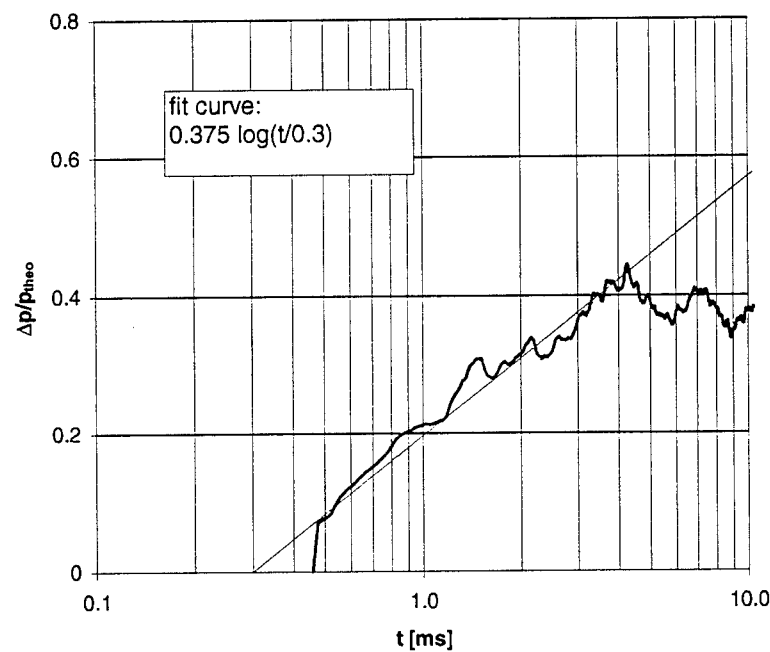


(b) Semi-logarithmic plot of the pressure gain, normalized by π_c .

Figure 81 Test 38: 600 mbar $C_2H_2 + (1O_2 + 2N_2)$

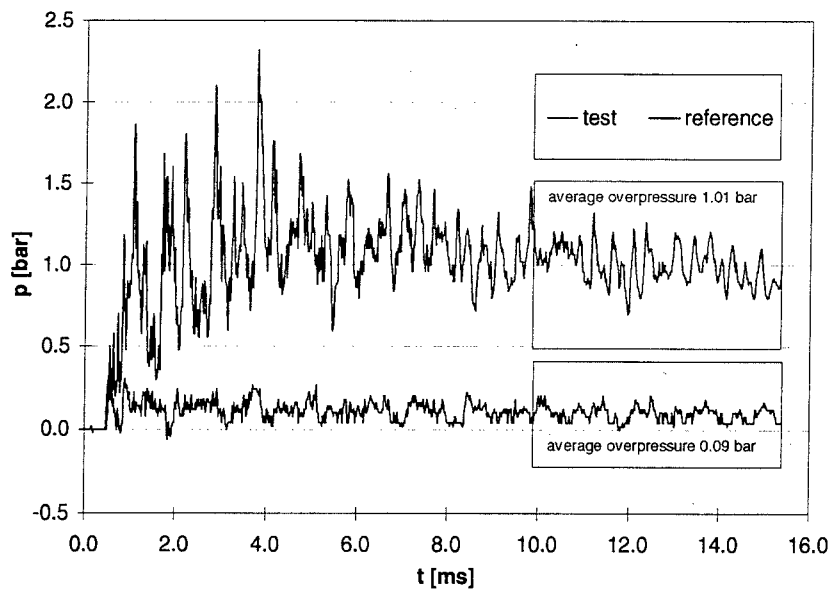


(a) Comparison of the pressure records at gage 2 to the non-reactive reference test.

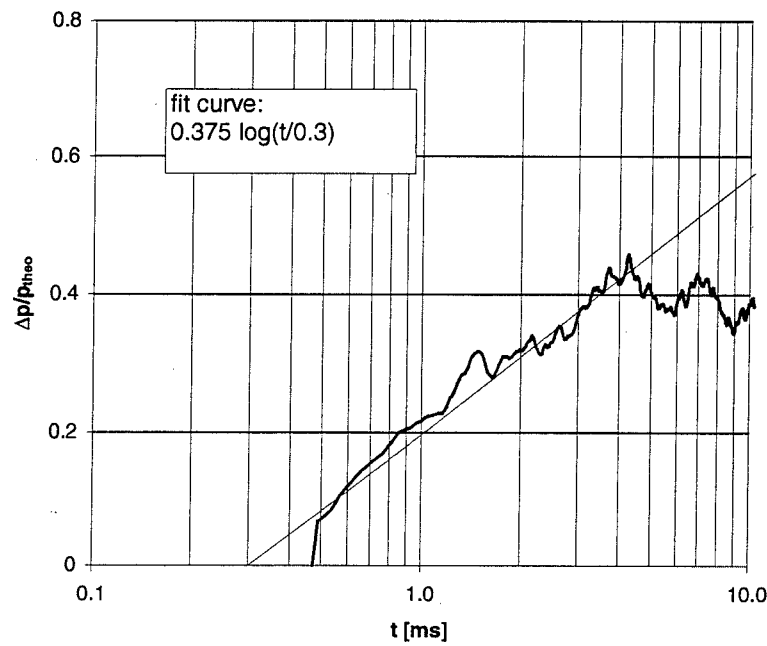


(b) Semi-logarithmic plot of the pressure gain, normalized by π_c .

Figure 82 Test 40: 700 mbar $C_2H_2 + (1O_2 + 2N_2)$

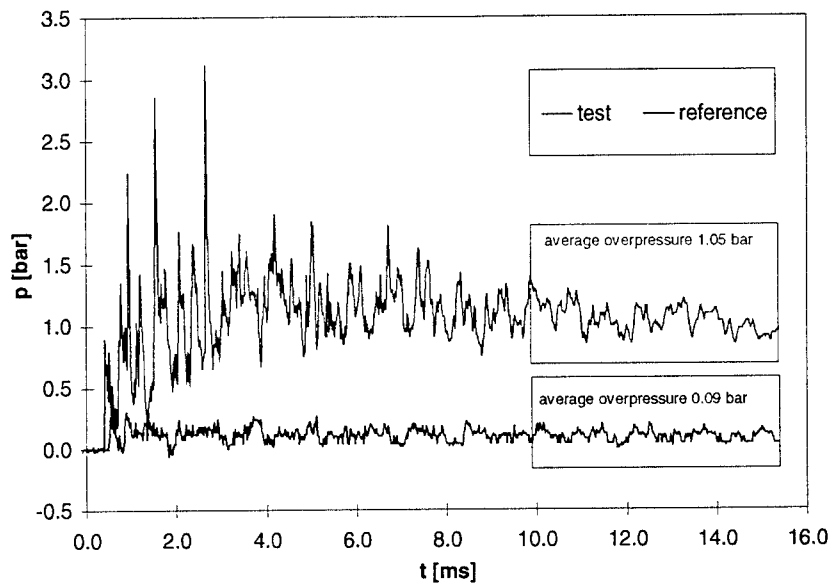


(a) Comparison of the pressure records at gage 2 to the non-reactive reference test.

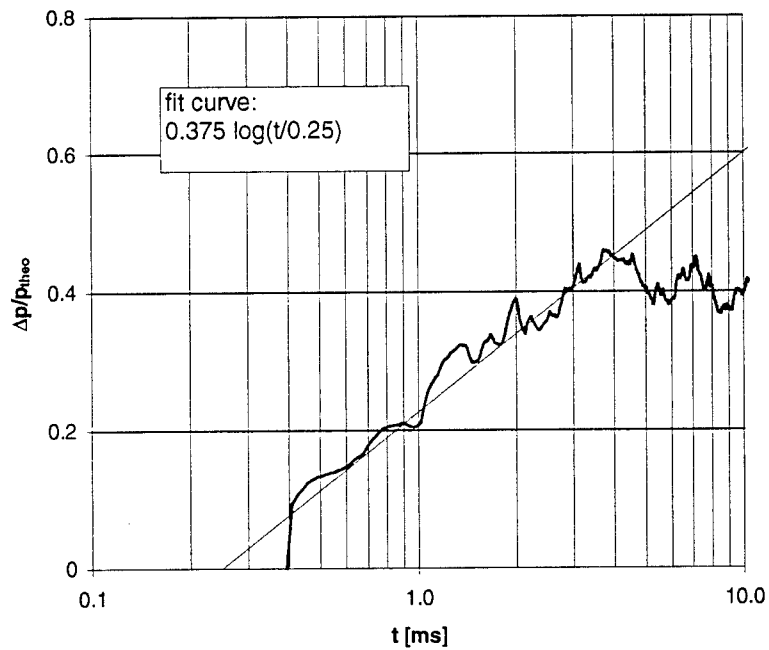


(b) Semi-logarithmic plot of the pressure gain, normalized by π_c .

Figure 83 Test 41: 700 mbar $C_2H_2 + (1O_2 + 2N_2)$

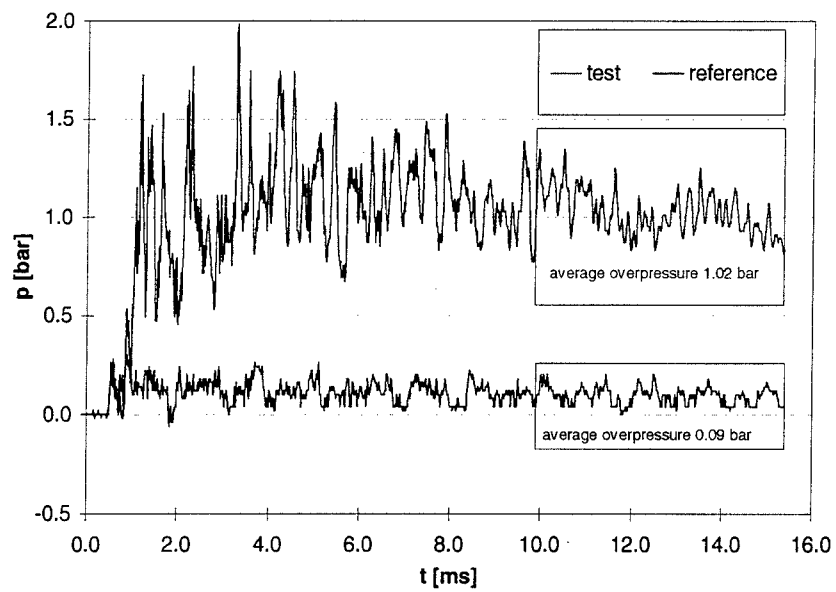


(a) Comparison of the pressure records at gage 2 to the non-reactive reference test.

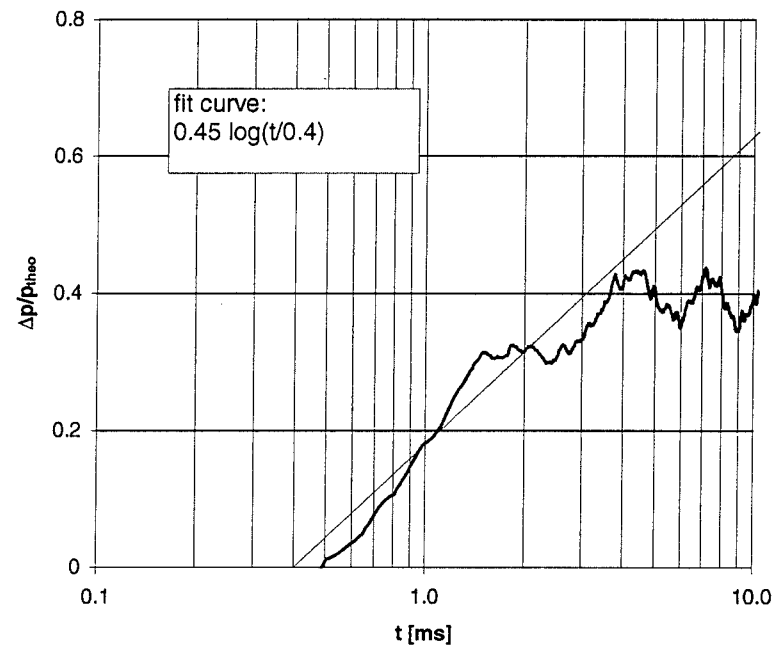


(b) Semi-logarithmic plot of the pressure gain, normalized by π_c .

Figure 84 Test 43: 700 mbar $C_2H_2 + (1O_2 + 1N_2)$

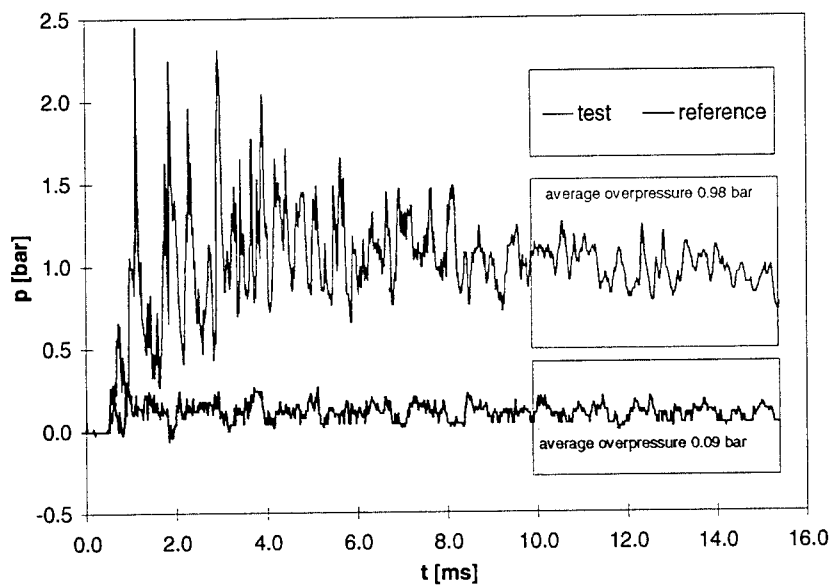


(a) Comparison of the pressure records at gage 2 to the non-reactive reference test.

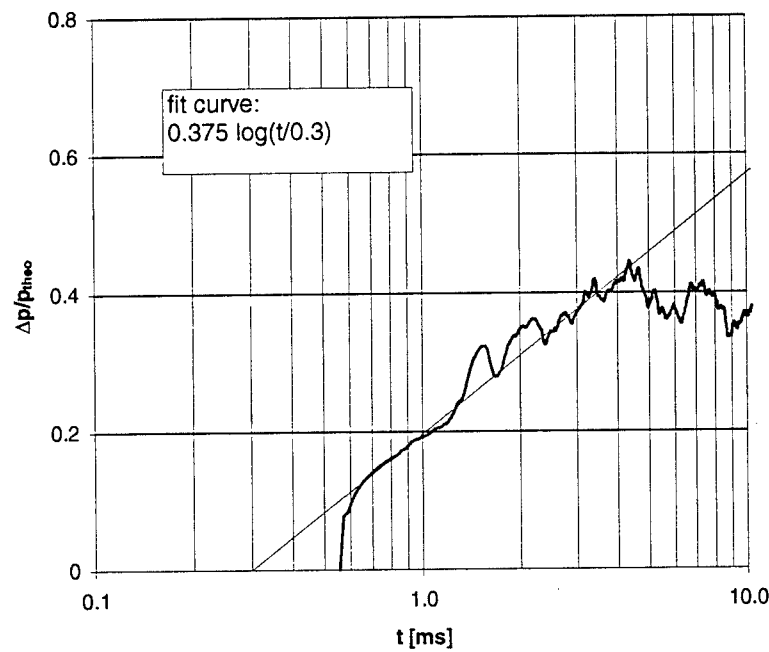


(b) Semi-logarithmic plot of the pressure gain, normalized by π_c .

Figure 85 Test 44: 700 mbar $C_2H_2 + (1O_2 + 1N_2)$

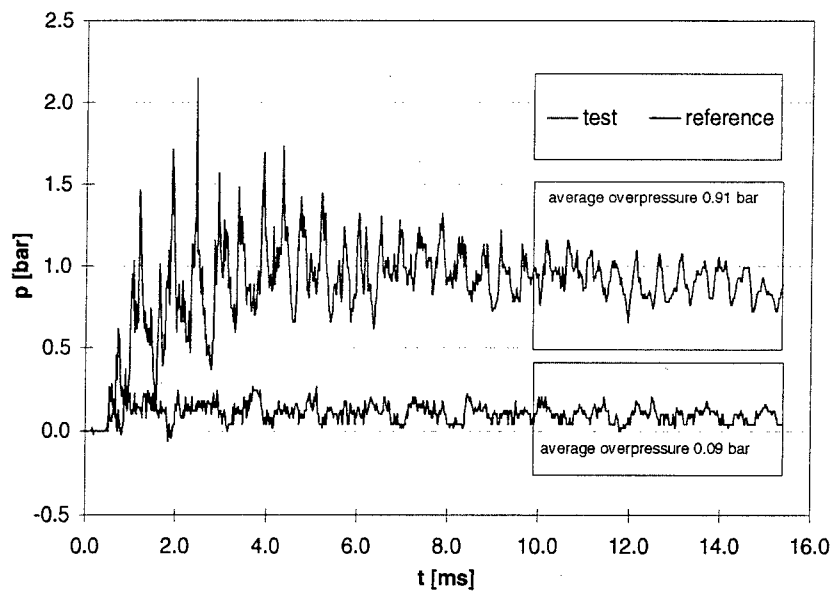


(a) Comparison of the pressure records at gage 2 to the non-reactive reference test.

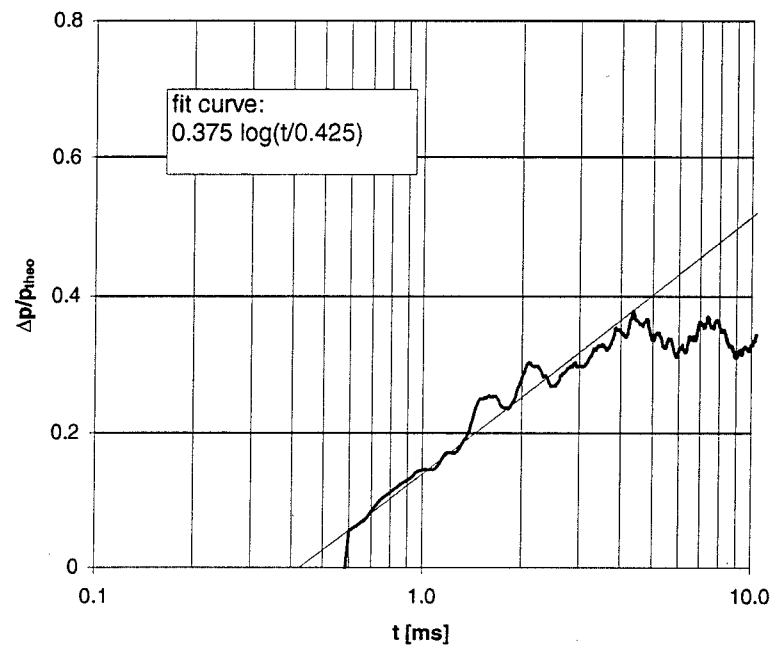


(b) Semi-logarithmic plot of the pressure gain, normalized by π_c .

Figure 86 Test 45: 700 mbar $C_2H_2 + (1O_2 + 1N_2)$

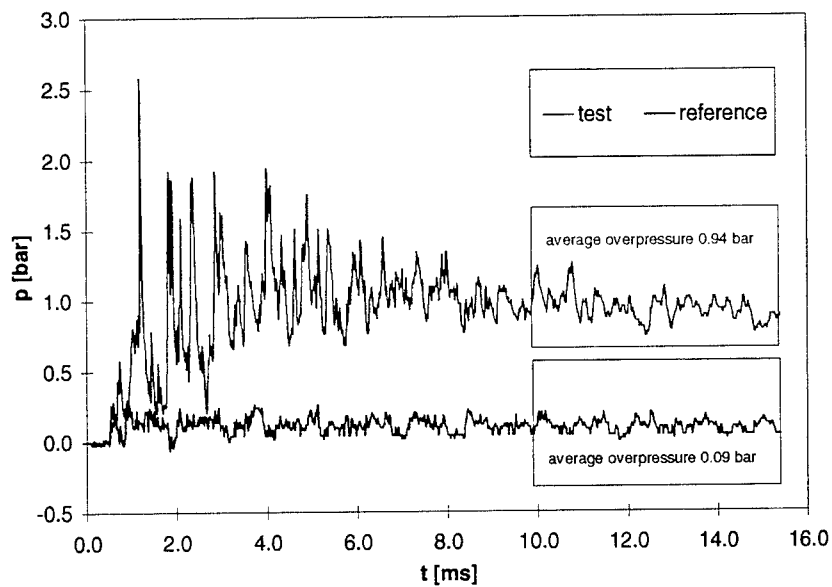


(a) Comparison of the pressure records at gage 2 to the non-reactive reference test.

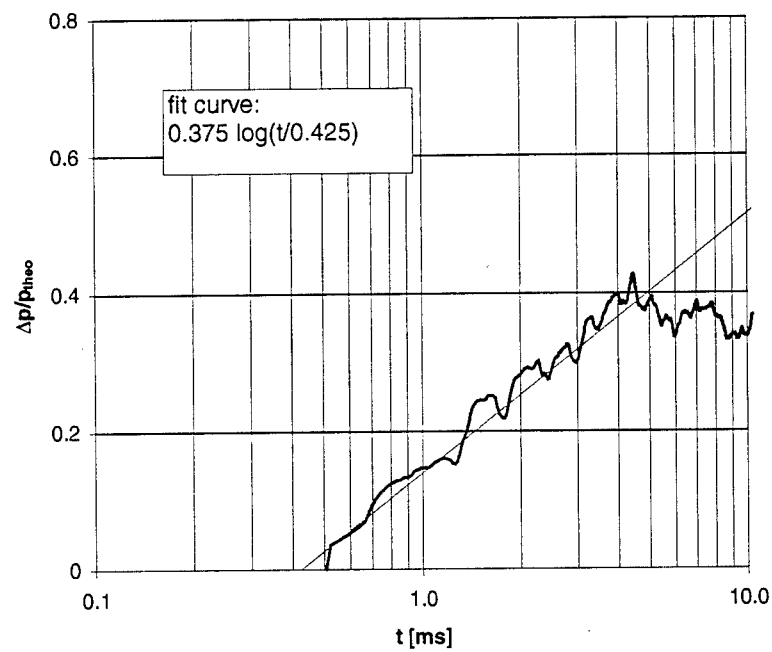


(b) Semi-logarithmic plot of the pressure gain, normalized by π_c .

Figure 87 Test 46: 700 mbar $C_2H_2 + (1O_2 + 1N_2)$

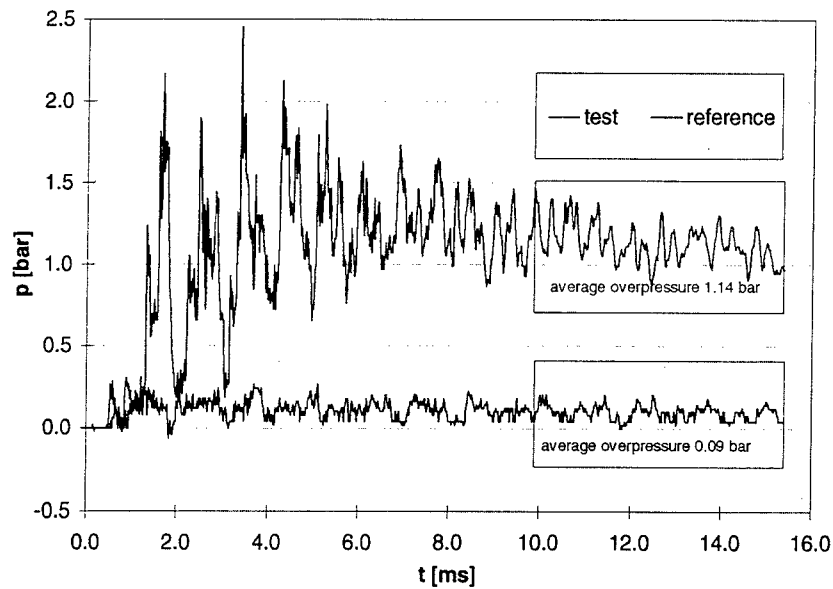


(a) Comparison of the pressure records at gage 2 to the non-reactive reference test.

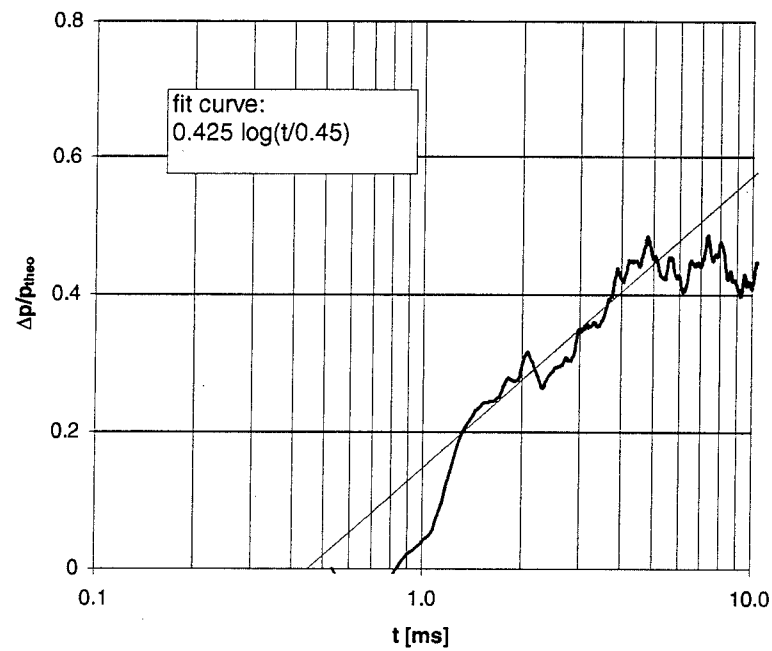


(b) Semi-logarithmic plot of the pressure gain, normalized by π_c .

Figure 88 Test 47: 700 mbar $C_2H_2 + (1O_2 + 1N_2)$



(a) Comparison of the pressure records at gage 2 to the non-reactive reference test.



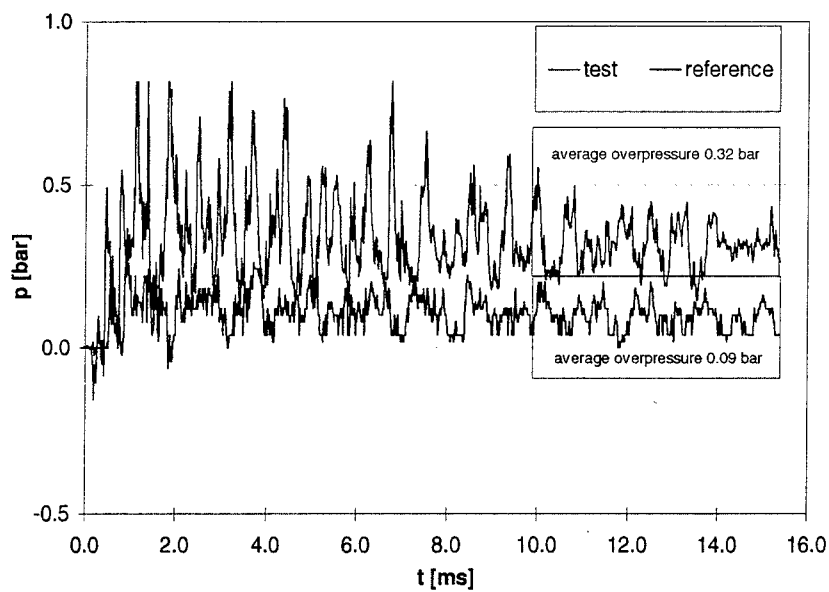
(b) Semi-logarithmic plot of the pressure gain, normalized by π_c .

Figure 89 Test 48: 700 mbar $C_2H_2 + (1O_2 + 1N_2)$

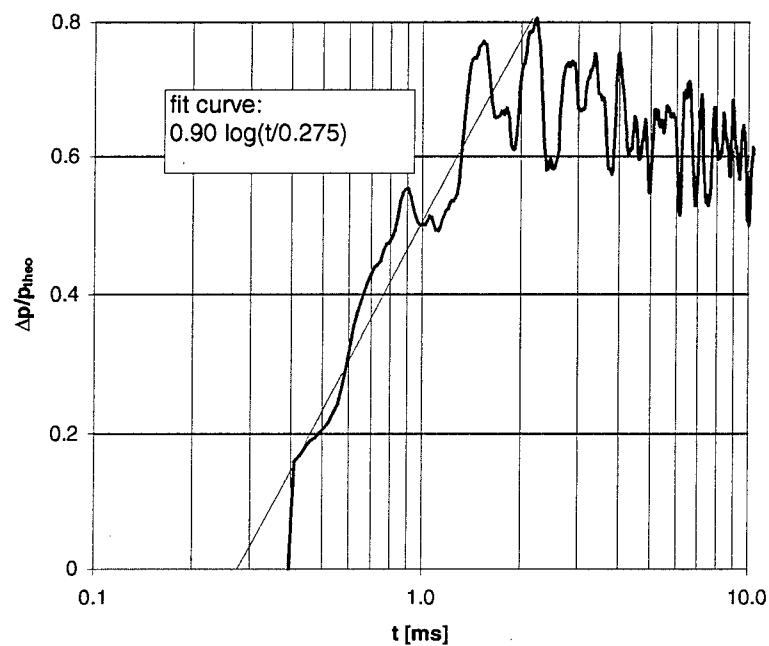
Table 7 Summary of the experiments with methane in the 72 cm³ detonation chamber.

For the following tests (see Figures 90 to 96) the content of oxygen in the expansion chamber was varied, the methane methane in the detonation chamber was mixed with a 1:1 mixture of nitrogen and oxygen.

test	version	comments	CH ₄ [mbar]	O ₂ [mbar]	N ₂ [mbar]	Expansion chamber	π_c (theo) [bar]	P _{end} [bar]	fit curve	burning rate
71	5	no reaction	500	250	250	air				
72	5		150	425	425	air	0.38	0.32	0.90 log ₁₀ (t/0.28)	- 0.39 / t
73	5		250	380	380	air	0.63	0.44	0.90 log ₁₀ (t/0.28)	- 0.39 / t
74	5	retarded	375	315	315	air	0.94	0.66	0.45 log ₁₀ (t/0.30)	- 0.20 / t
75	5	no reaction	380	315	315	air				
77	5	no reaction	375	312	312	air				
78	5	no reaction	375	312	313	air				
79	5	no reaction	375	312	313	air				
80	5		380	310	310	O ₂	0.96	0.58	0.45 log ₁₀ (t/0.35)	- 0.20 / t
81	5	no reaction	375	315	315	O ₂ +N ₂ 1:1				
82	5	no reaction	365	317	318	O ₂ +N ₂ 1:1				
83	5	no reaction	365	317	318	O ₂ +N ₂ 1:1				
84	5	no reaction	365	317	318	O ₂ +N ₂ 1:1				
85	5		250	375	375	O ₂ +N ₂ 1:1	0.94	0.52	0.80 log ₁₀ (t/0.20)	- 0.35 / t
86	5		250	375	375	O ₂ +N ₂ 1:1	0.94	0.49	0.80 log ₁₀ (t/0.23)	- 0.35 / t
87	5		250	375	375	O ₂ +N ₂ 1:1	0.94	0.50	0.80 log ₁₀ (t/0.23)	- 0.35 / t

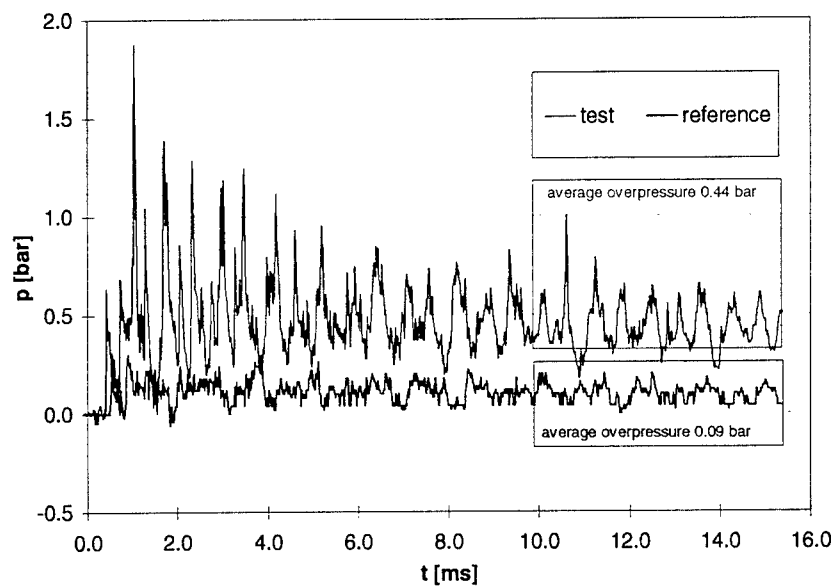


(a) Comparison of the pressure records at gage 2 to the non-reactive reference test.

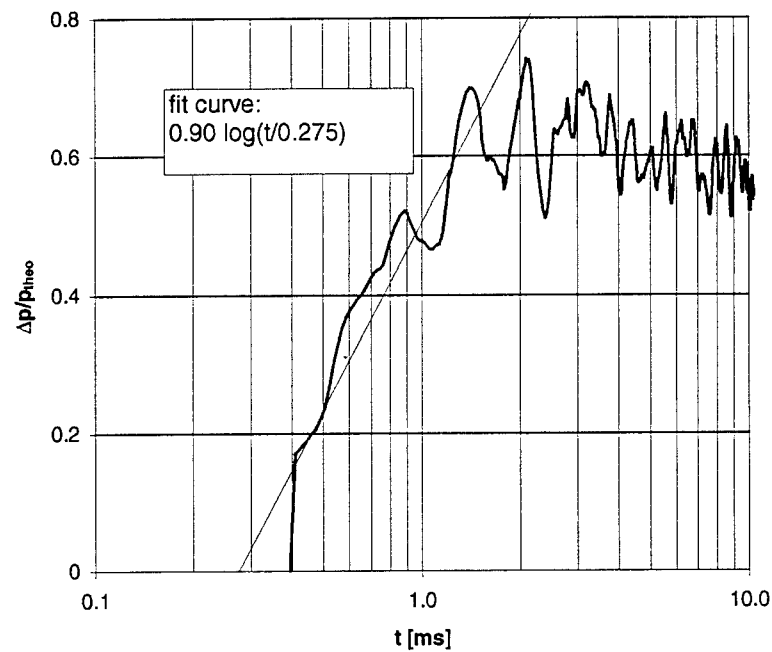


(b) Semi-logarithmic plot of the pressure gain, normalized by π_c .

Figure 90 Test 72: 150 mbar CH₄

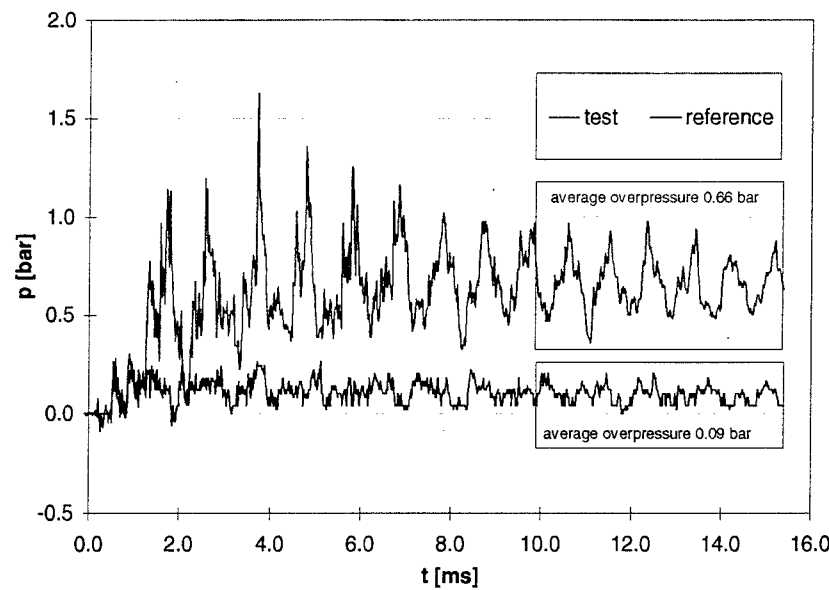


(a) Comparison of the pressure records at gage 2 to the non-reactive reference test.

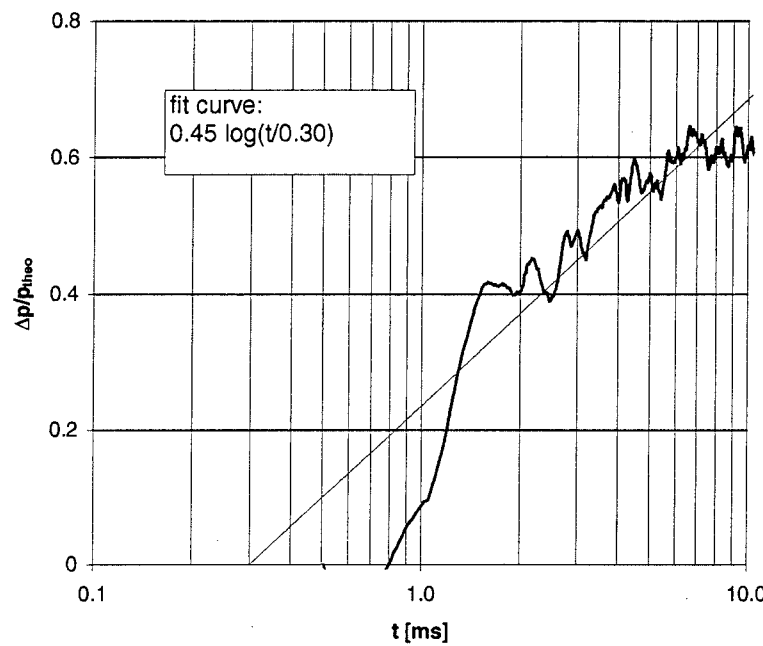


(b) Semi-logarithmic plot of the pressure gain, normalized by π_c .

Figure 91 Test 73: 250 mbar CH₄

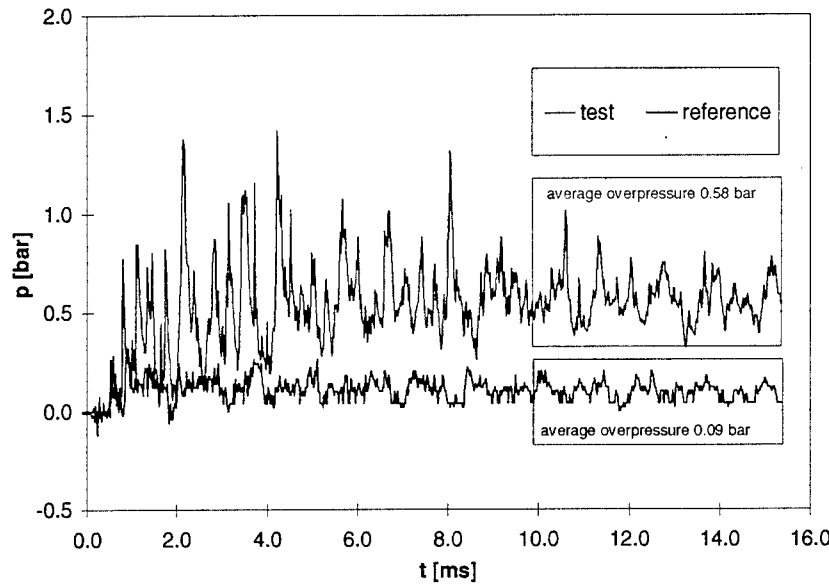


(a) Comparison of the pressure records at gage 2 to the non-reactive reference test.

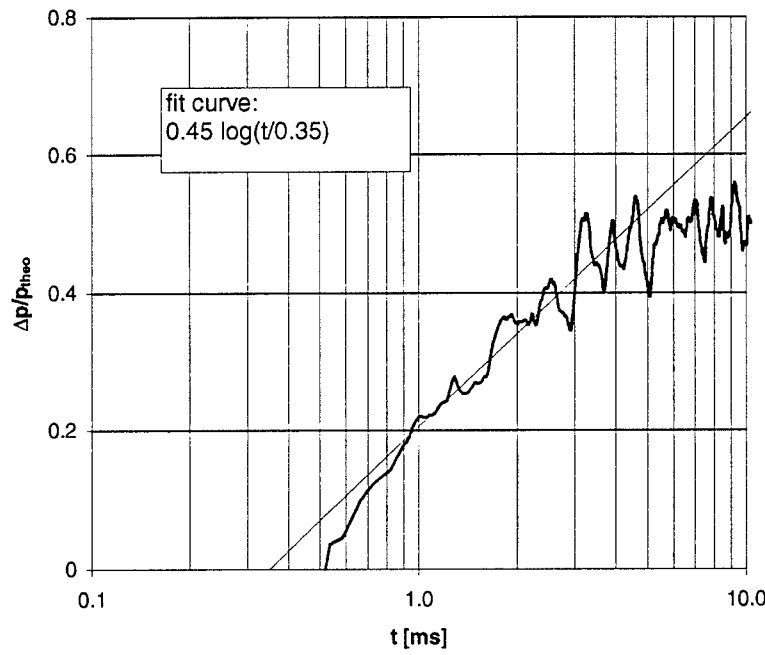


(b) Semi-logarithmic plot of the pressure gain, normalized by π_c .

Figure 92 Test 74: 375 mbar CH₄

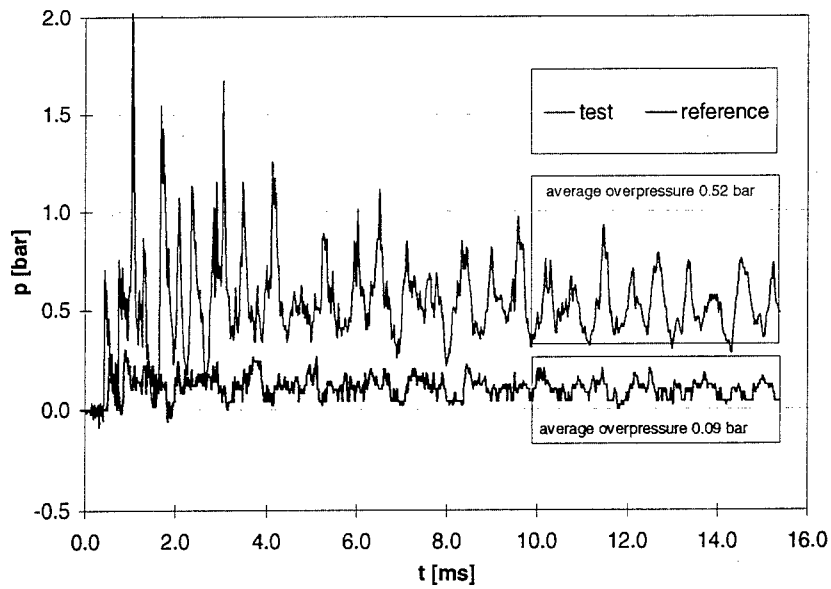


(a) Comparison of the pressure records at gage 2 to the non-reactive reference test.

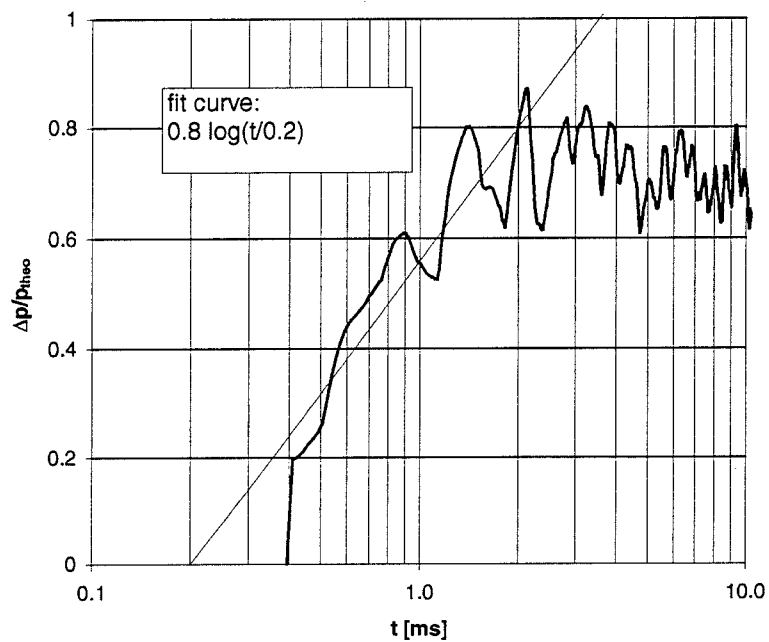


(b) Semi-logarithmic plot of the pressure gain, normalized by π_c .

Figure 93 Test 80: 380 mbar CH₄

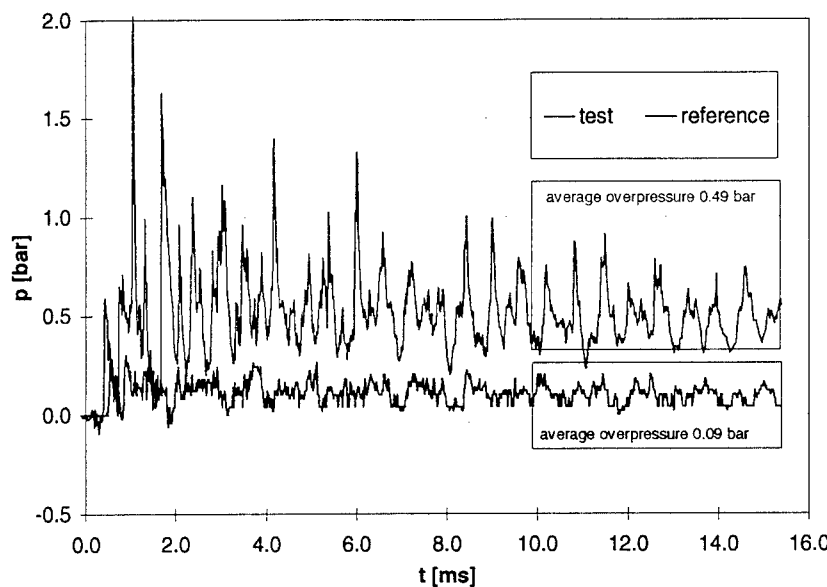


(a) Comparison of the pressure records at gage 2 to the non-reactive reference test.

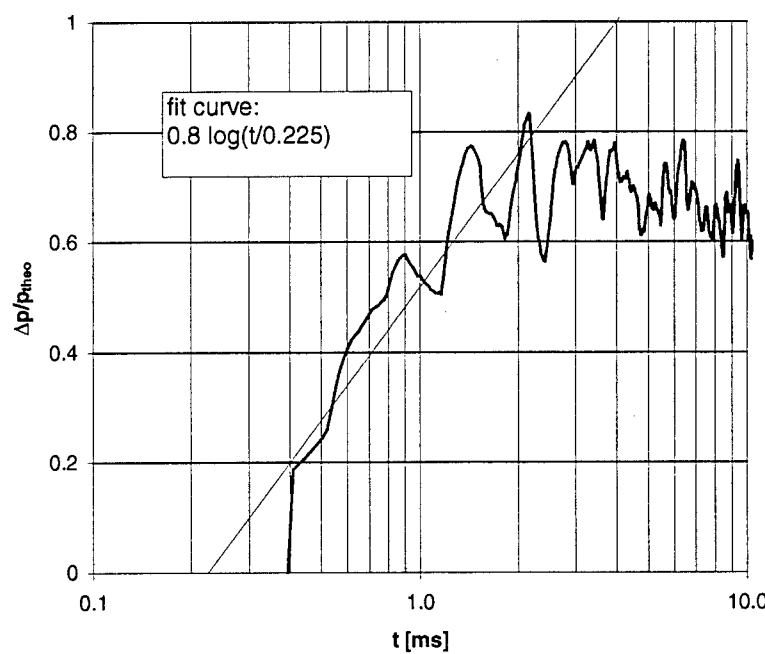


(b) Semi-logarithmic plot of the pressure gain, normalized by π_c .

Figure 94 Test 85: 250 mbar CH₄

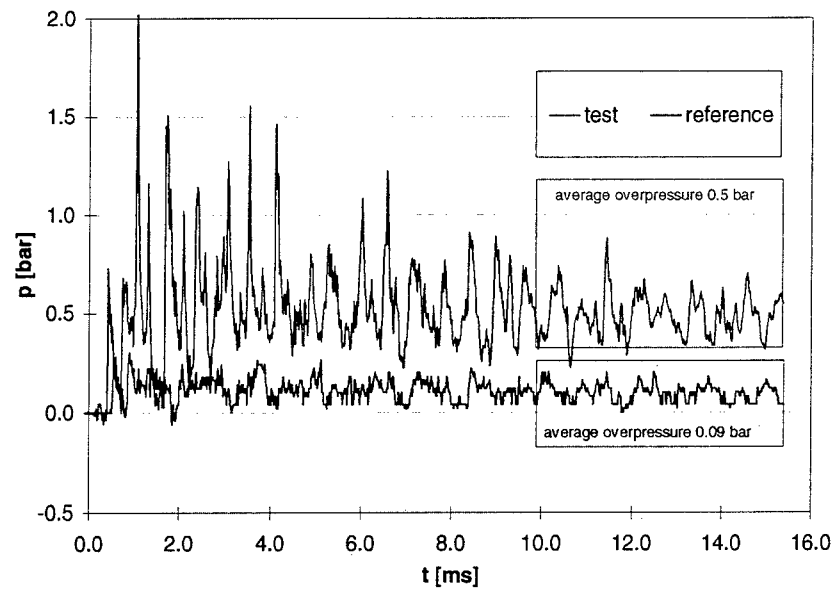


(a) Comparison of the pressure records at gage 2 to the non-reactive reference test.

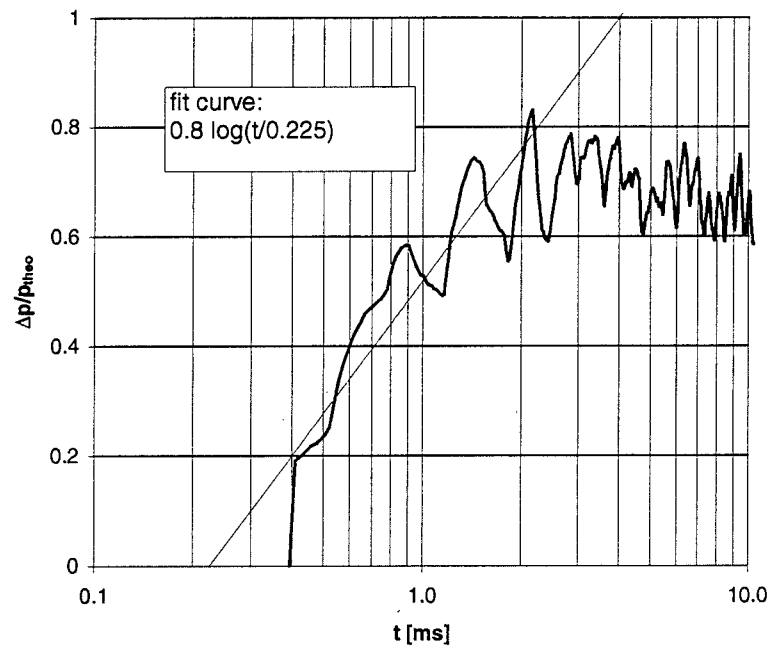


(b) Semi-logarithmic plot of the pressure gain, normalized by π_c .

Figure 95 Test 86: 250 mbar CH₄



(a) Comparison of the pressure records at gage 2 to the non-reactive reference test.



(b) Semi-logarithmic plot of the pressure gain, normalized by π_c .

Figure 96 Test 87: 250 mbar CH₄

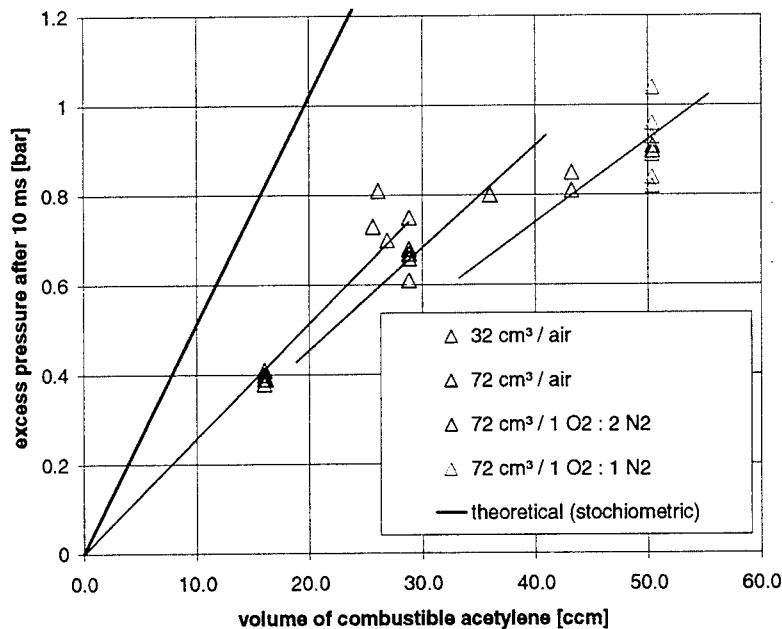


Figure 97 Experimentally obtained excess pressure values for the acetylene experiments.

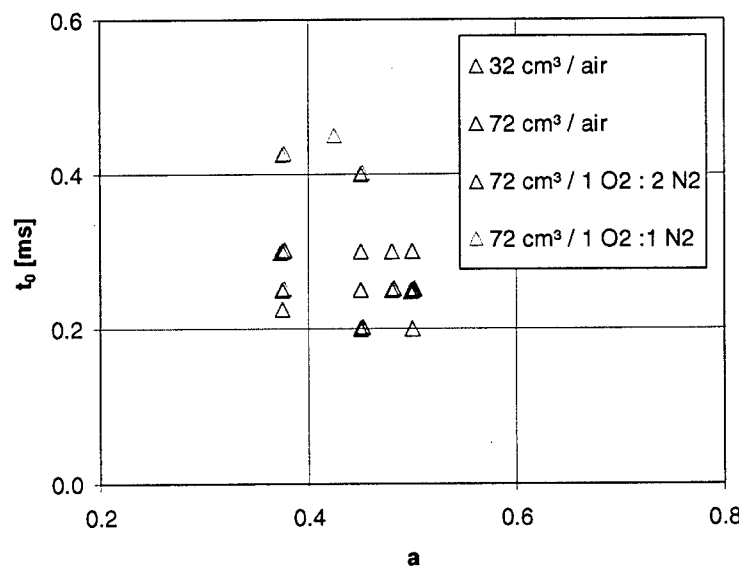


Figure 98 Fit parameters [$a \log t/t_0$] for the acetylene experiments.

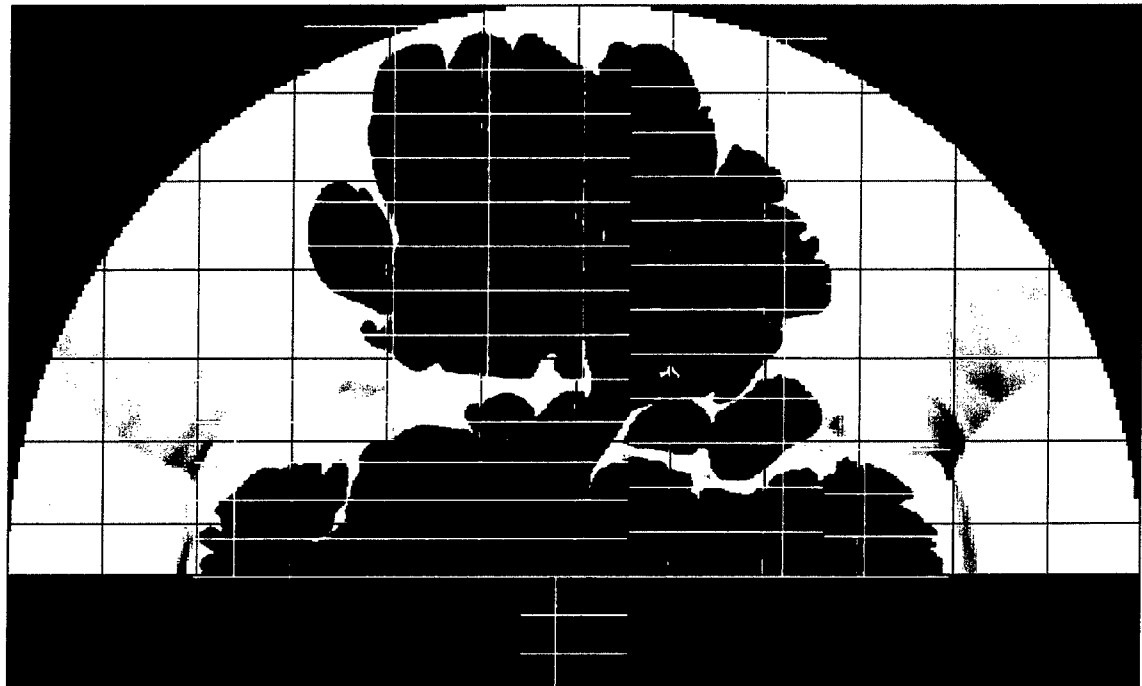


Figure 99 Result of a preliminary Cartesian-Grid AMR simulation of XY combustion jet; visualization of the oxidizer region at $t=1.5$ ms (courtesy Allen Kuhl).

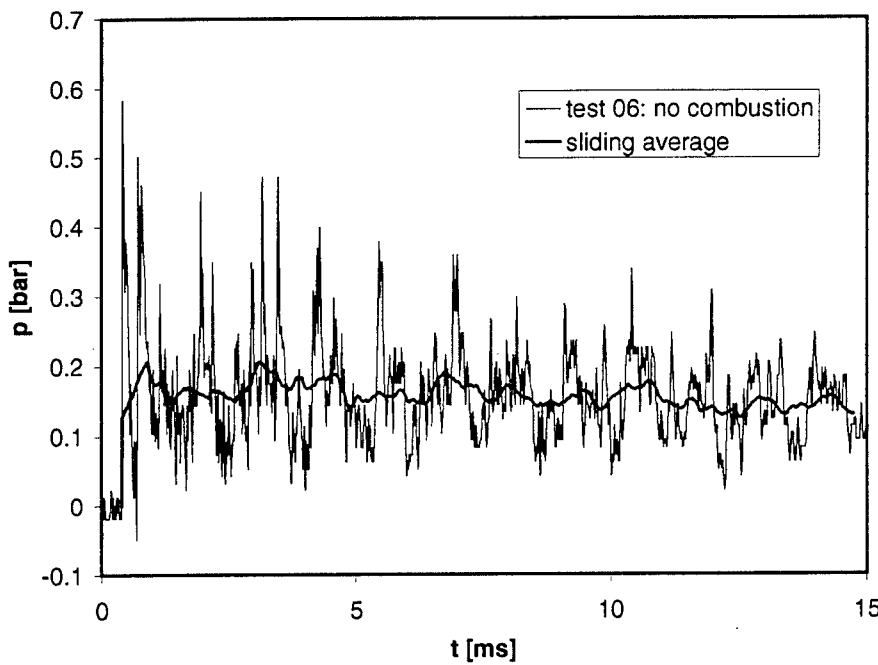


Figure 100 Original pressure-time history of the reference test and sliding average

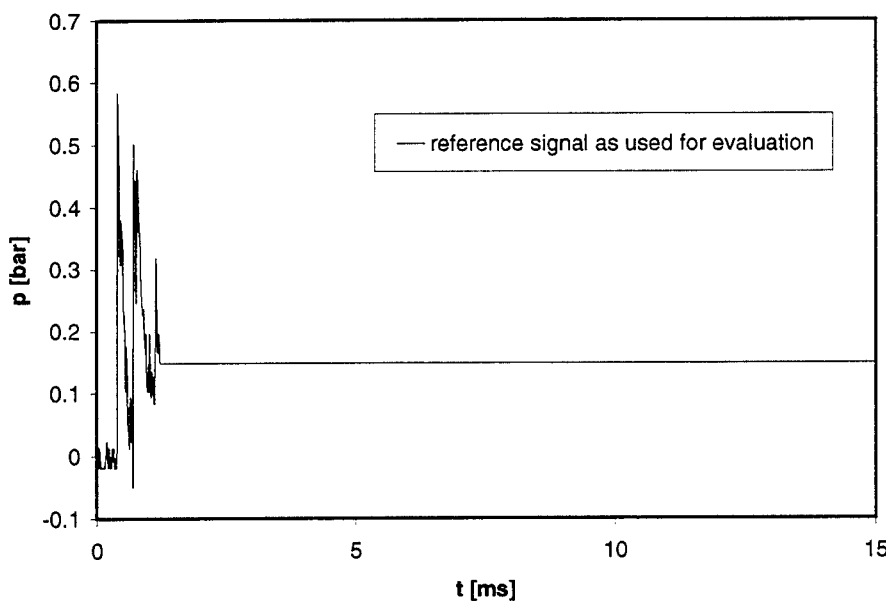


Figure 101 Reference signal used for the modified evaluation modus.

$$y = 0.1301x^6 + 0.2796x^5 - 0.4402x^4 - 0.9475x^3 + 0.4509x^2 + 1.0491x + 0.2582$$

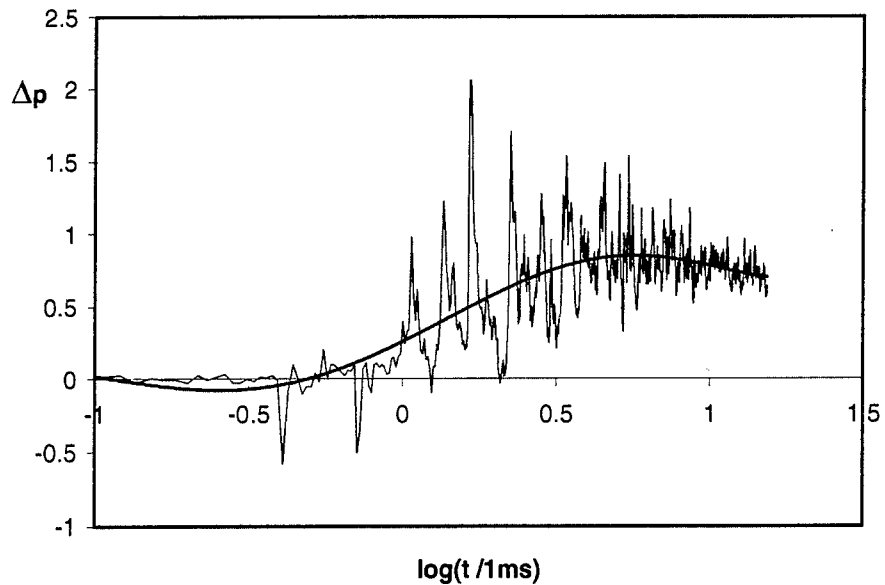


Figure 102 Test 11 (900 mbar acetylene in 32 cm³ prechamber): pressure difference and fit curve.

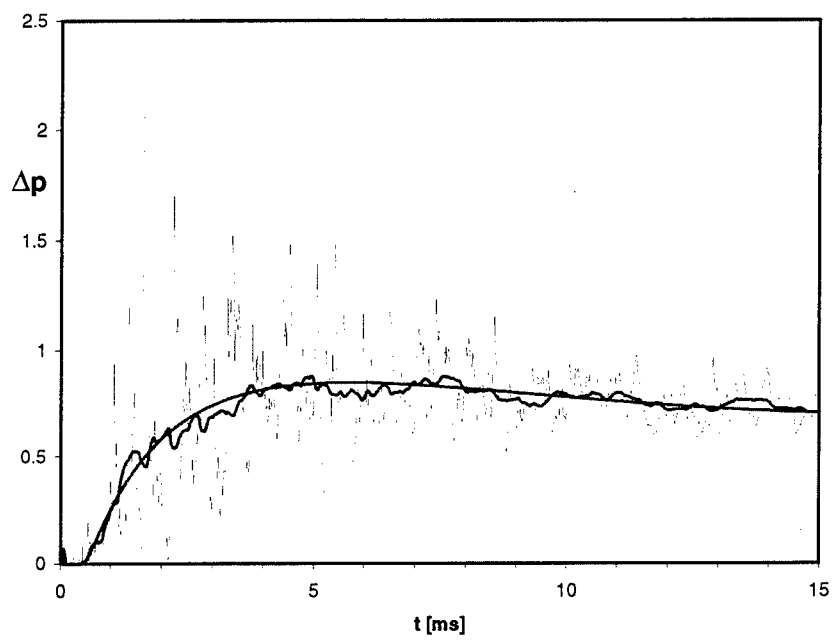


Figure 103 Test 11: grey: original pressure difference, blue: result of sliding average, red: result of power series fit.

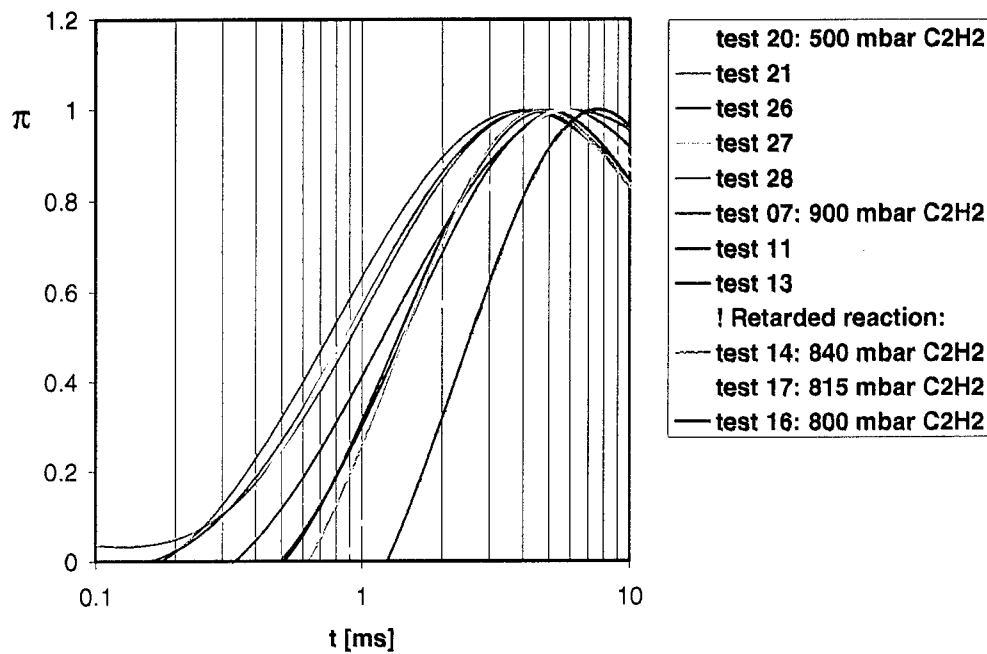


Figure 104 Summary of the results for the experiments acetylene in the 32 cm³ prechamber.

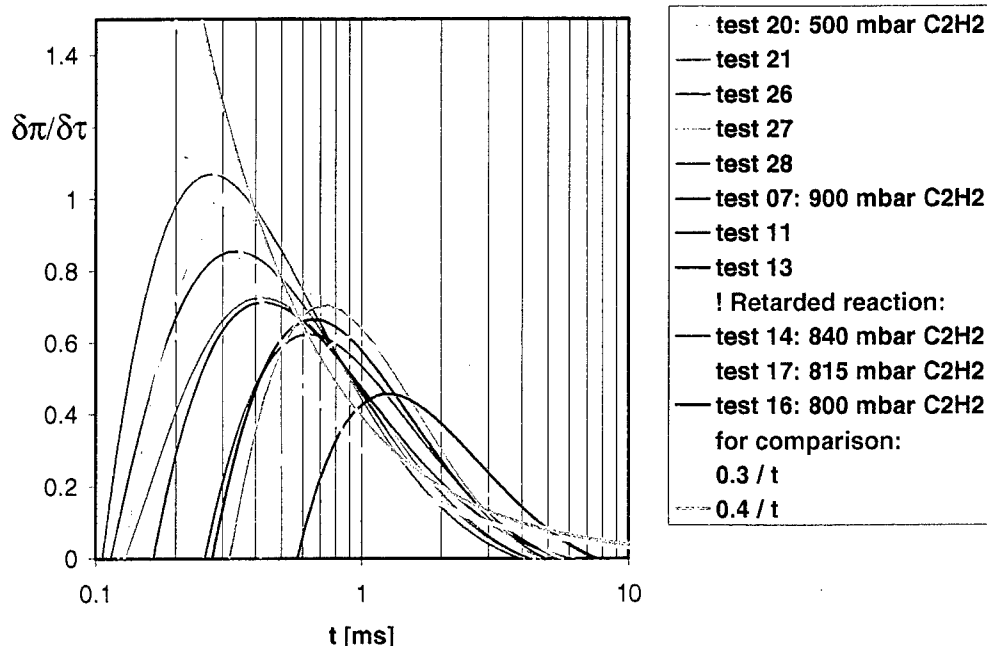


Figure 105 Time derivative of the above tests.

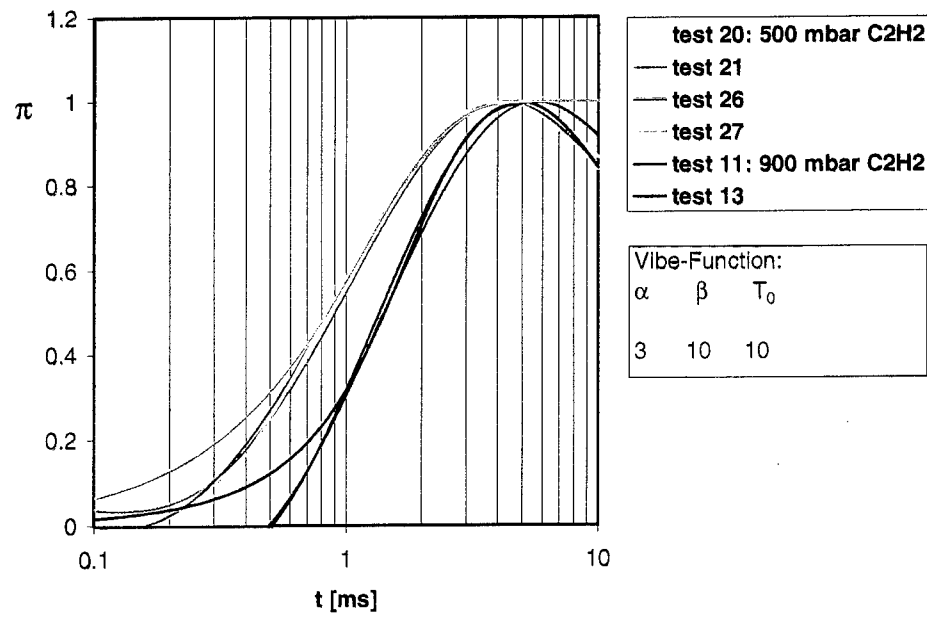


Figure 106 Comparison to an approximation with Vibe-functions.

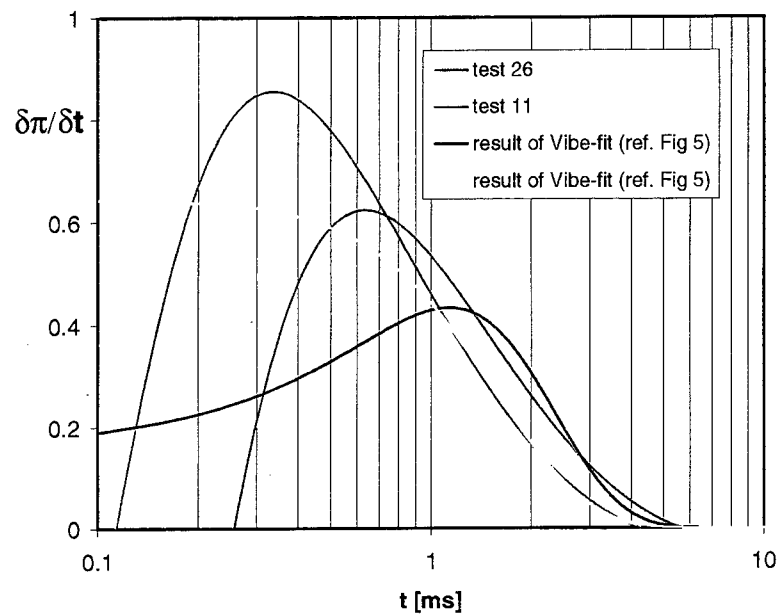


Figure 107 Corresponding comparison for the time derivatives.

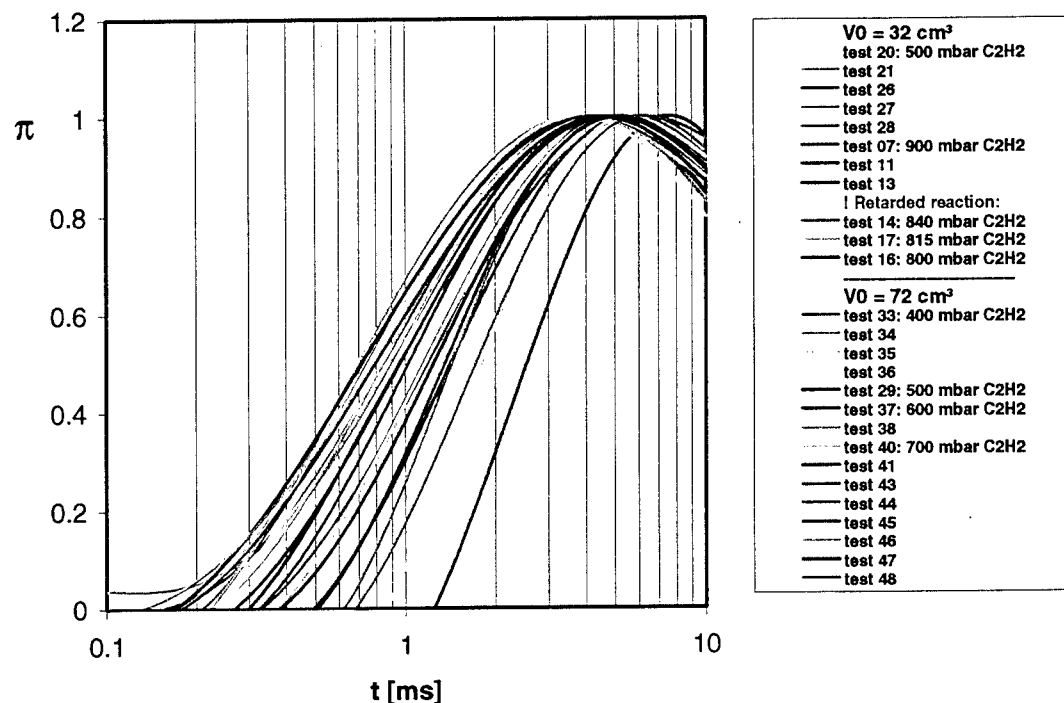


Figure 108 Summarizing the result for the acetylene tests.

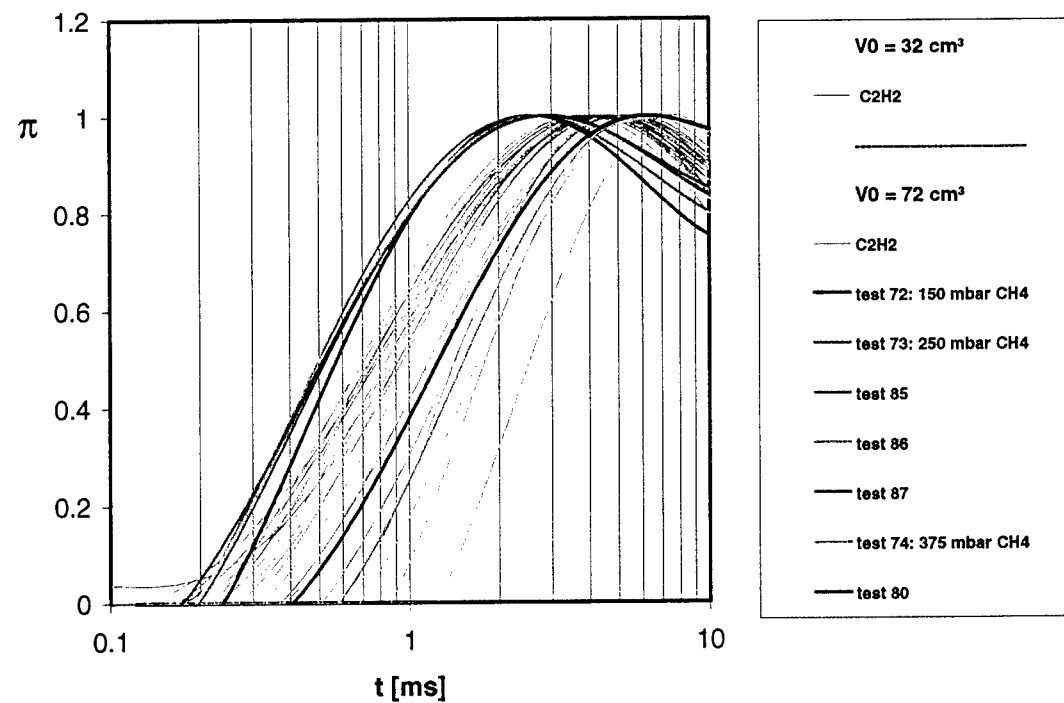


Figure 109 Summarizing the results for the methane tests.

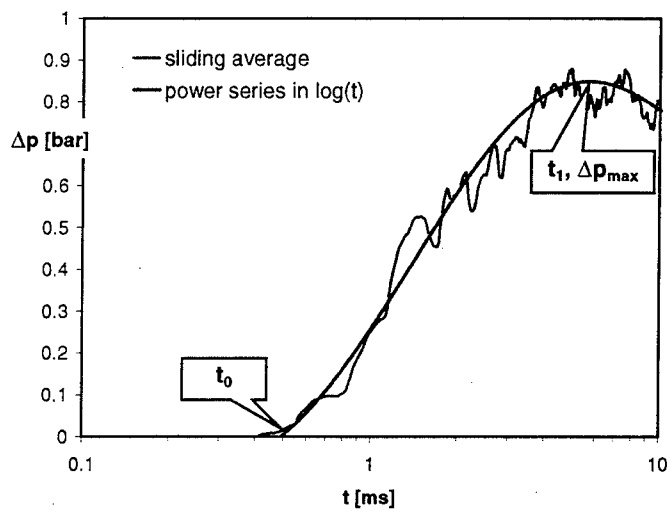


Figure 110 Definition of the parameters t_0 , t_1 and Δp_{\max} .

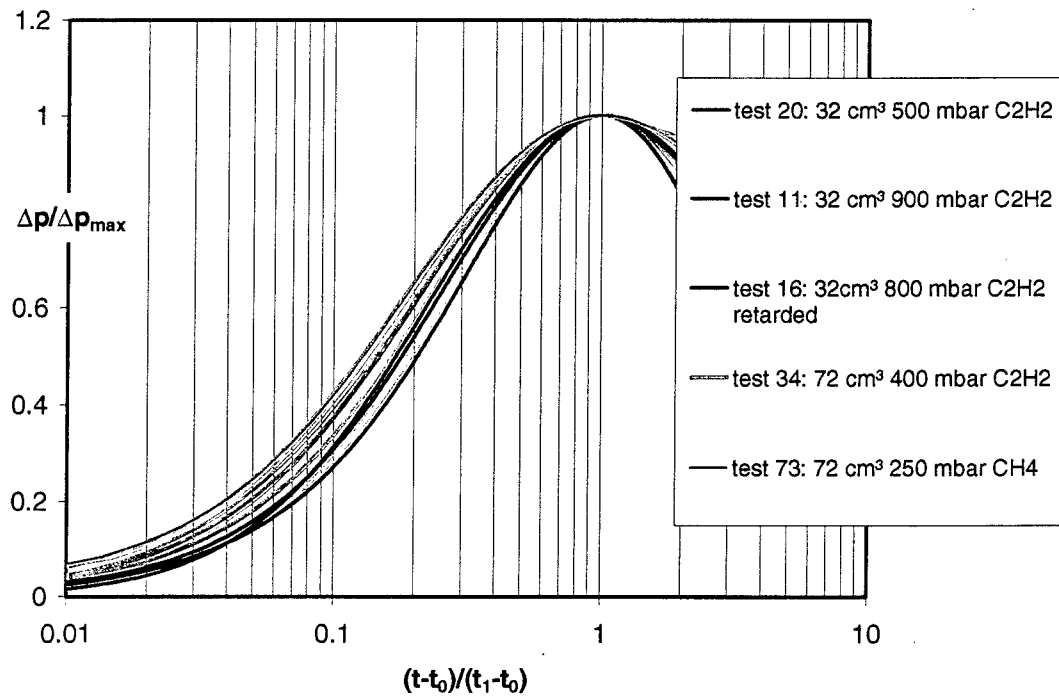


Figure 111 Non-dimensional plots of the pressurization for all tests.

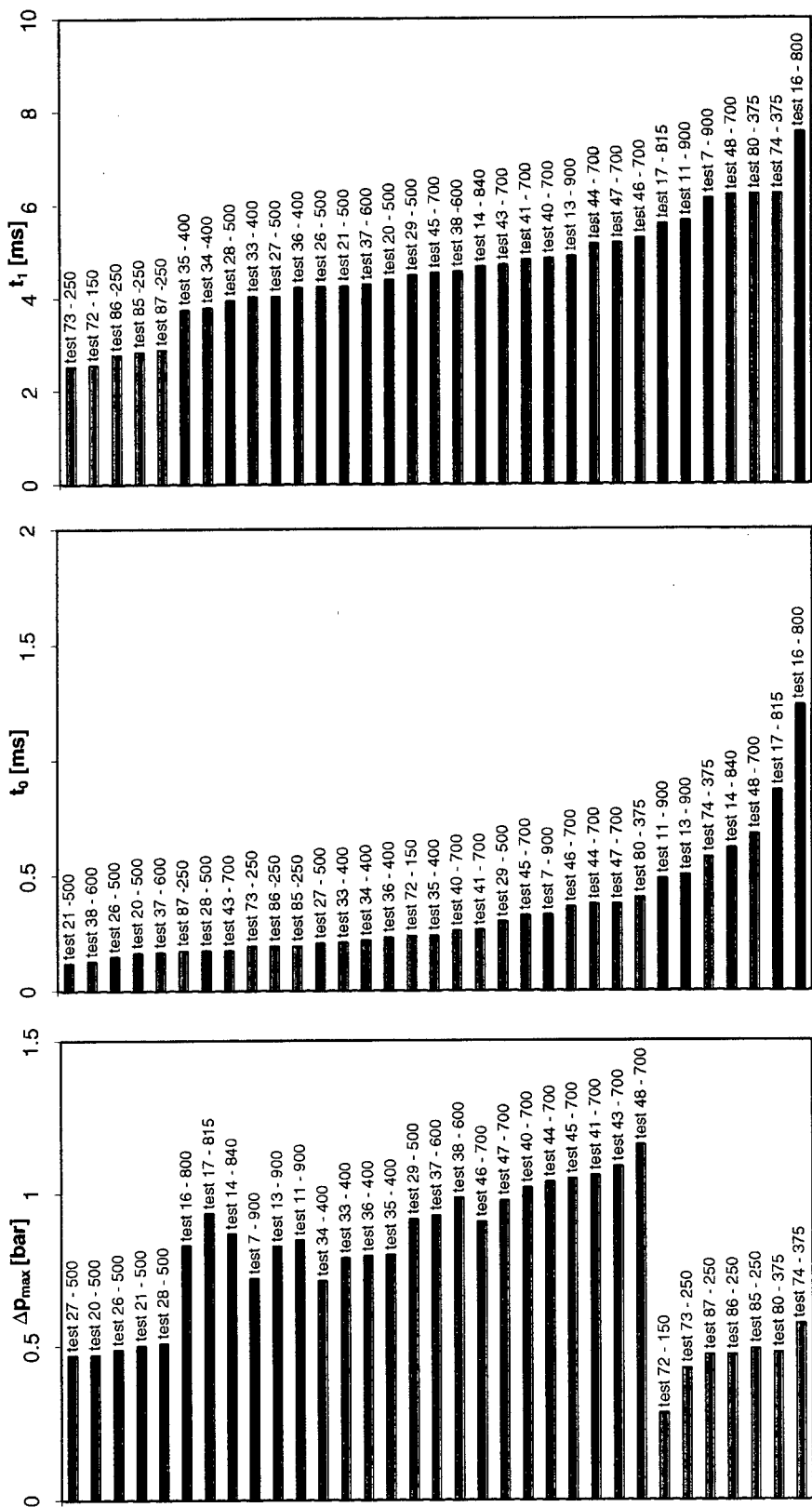


Figure 112 Summary of parameters t_0 , t_1 and Δp_{\max} .

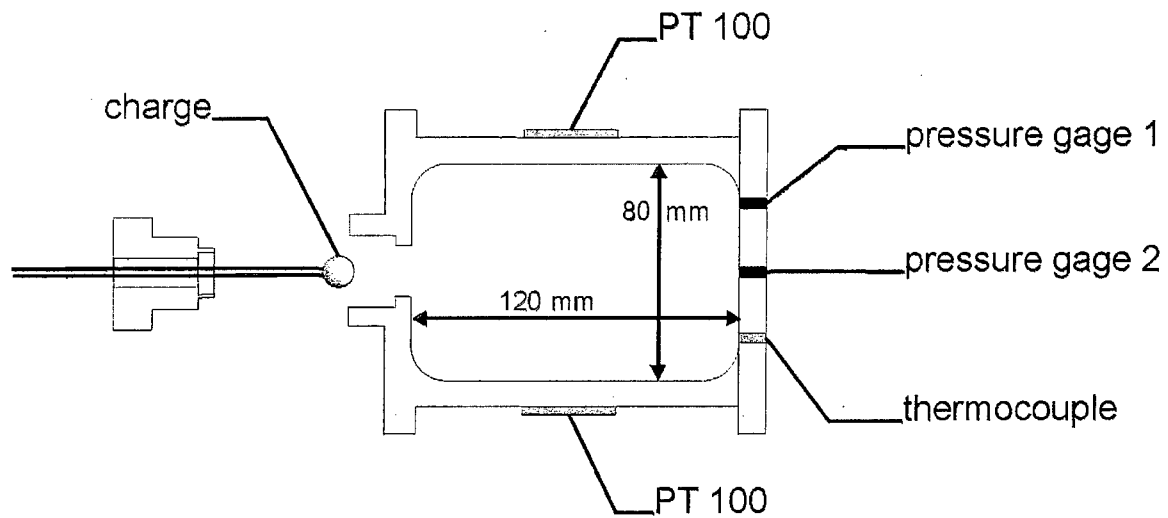


Figure 113 Schematic of the custom-designed small bomb calorimeter.

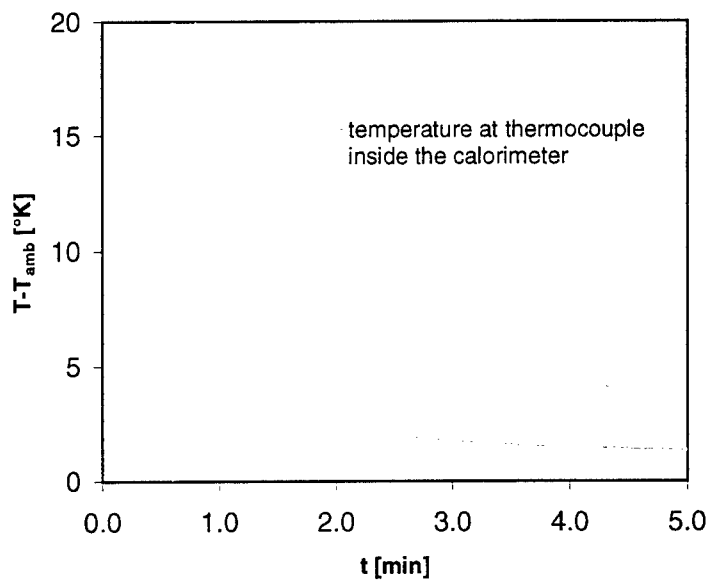


Figure 114 Decrease of overtemperature in the calorimeter for Test 06 (0.25 g NP in air).

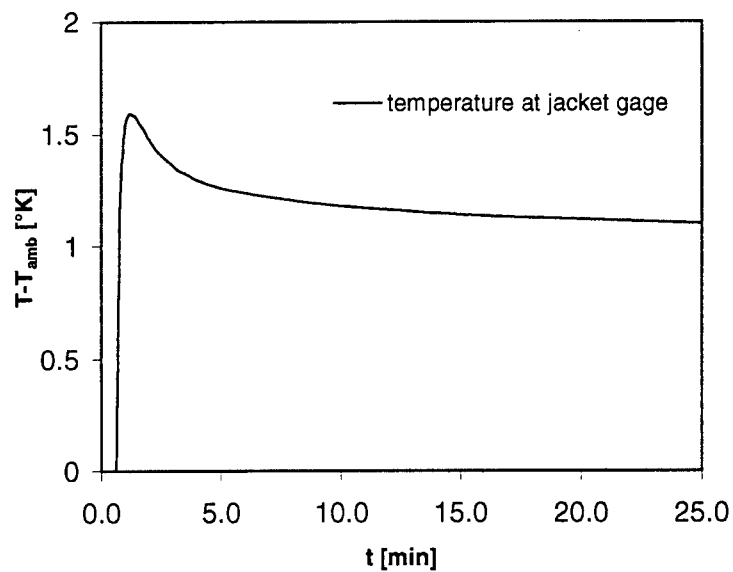


Figure 115 Overtemperature at the outside of the calorimeter jacket. Test 06 (0.25 g NP in air).

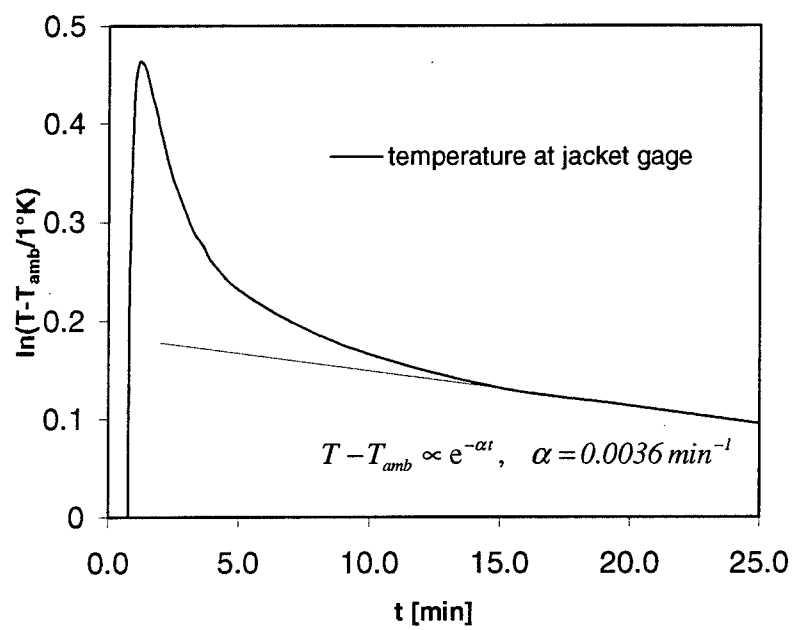


Figure 116 Semilogarithmic plot of the difference of the jacket temperature to the ambient temperature.

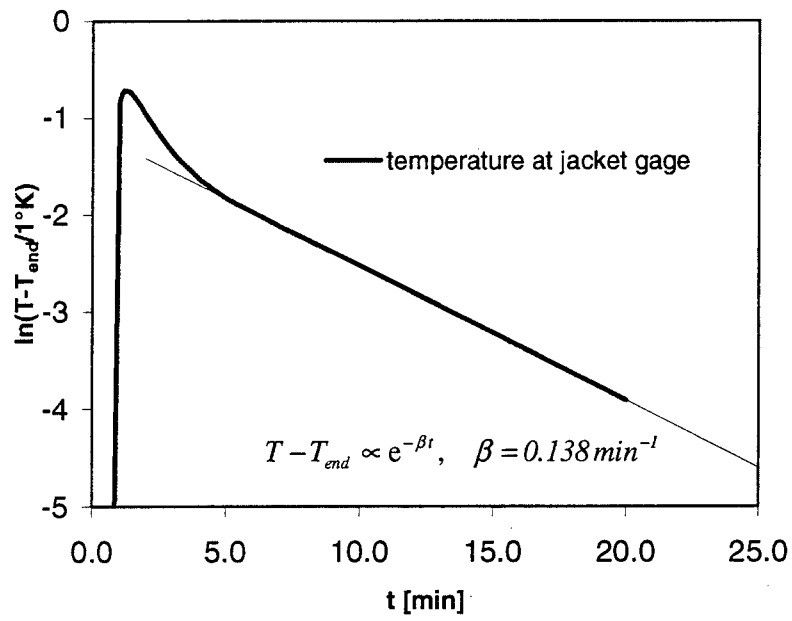


Figure 117 Semilogarithmic plot of the difference of the jacket temperature to the final temperature.

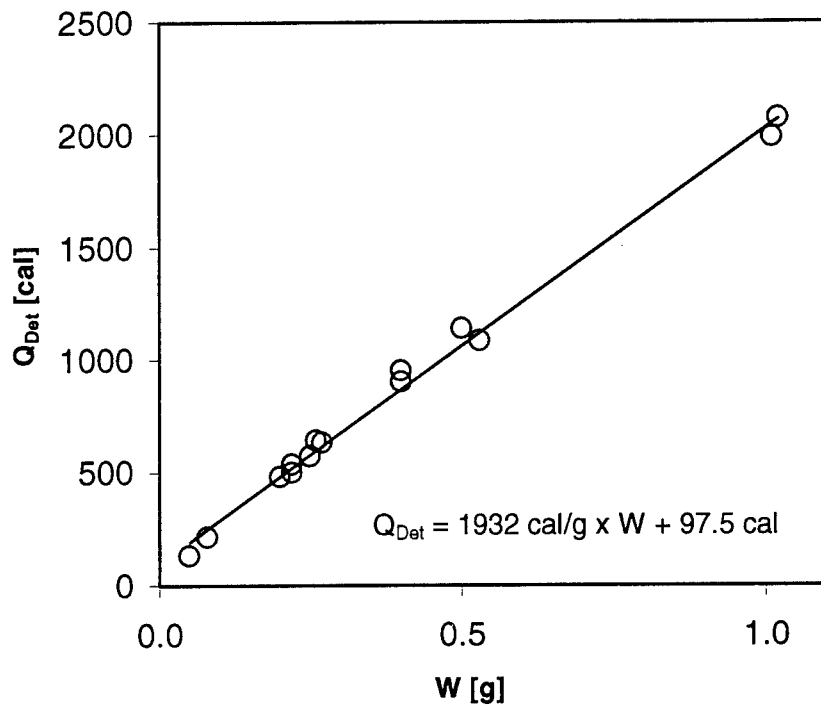


Figure 118 Energy released by the detonation of Nitropenta charges in air.
(test setup: single chamber, Tests 04.KM – 17.KM).

Section 9 References

- [1] Kuhl, A. L., *Spherical mixing layers in explosions*, in "Dynamics of Exothermicity", J.R. Bowen Editor, Gordon and Breach Publishers, Longhorn, PA, (1996), pp. 292 - 320. (UNCLASSIFIED)
- [2] AIRBLAST Version 2.3, experimentally based PC- program by Dewey, McMillan & Associates LTD, Victoria, B.C., Canada. (UNCLASSIFIED)
- [3] Reichenbach, H., Neuwald, P., *Fluid-Dynamics of Explosions in Multi-Chamber Systems – Phenomenology Test Program*, DSWA Report, Contract DNA 001-94-C-0078, (to be published). (UNCLASSIFIED)
- [4] Barton, J. E., Lee, A. T., Oppenheim, A. K. and Kuhl, A. L., *Thermodynamic properties of components in a combustion system produced by explosion*, preprint (private communication A. L. Kuhl). (UNCLASSIFIED)
- [5] Kuhl, A. L.; Ferguson, R. E.; Reichenbach, H.; Neuwald, P.; Oppenheim, A. K. *Fluid Mechanics of a Planar Exothermic Jet*, Centennial Symposium on Fluid Mechanics, Japanese Society of Mechanical Engineers, Tokyo, Japan, 13.07 – 16.07.1997, to be published in *JSME International Journal Series B*, Vol. **41**, No. 2, 1998. (UNCLASSIFIED)
- [6] Kuhl, A. L.; Ferguson, R. E.; Reichenbach, H.; Neuwald, P.; Oppenheim, A. K. *Dynamics of A Turbulent Jet in an Enclosure* Proc. 16th International Colloquium on the Dynamics of Explosions and Reactive Systems, University of Mining and Metallurgy, AGH, Cracow, Poland, 03. – 08.08.1997. (UNCLASSIFIED)
- [7] Neuwald, P.; Reichenbach, H.; Kuhl, A. L.; Oppenheim, A. K. *Self-Similar Combustion of Turbulent Fuel Jets in Air* Proc. 16th International Colloquium on the Dynamics of Explosions and Reactive Systems, University of Mining and Metallurgy, AGH, Cracow, Poland, 03. – 08.08.1997. (UNCLASSIFIED)
- [8] Reichenbach, H., Neuwald, P., *Turbulent Mixing in Explosions*. (UNCLASSIFIED)

Quarterly Letter Report No. 1	26. Sep	1994
Quarterly Letter Report No. 2	10. Jan	1995
Quarterly Letter Report No. 3	5. April	1995
Quarterly Letter Report No. 4	17. July	1995
Quarterly Letter Report No. 5	10. Oct	1995
Quarterly Letter Report No. 6	31. Jan	1996
Quarterly Letter Report No. 7	19. Mar	1996
Quarterly Letter Report No. 8	17. July	1996
Quarterly Letter Report No. 9	17. Oct	1996
Quarterly Letter Report No. 10	27. Jan	1997
Quarterly Letter Report No. 11	16. May	1997
Quarterly Letter Report No. 12	28. July	1997
Quarterly Letter Report No. 13	20. Oct	1997

DISTRIBUTION LIST

DSWA-TR-98-53

DEPARTMENT OF DEFENSE

DEFENSE TECHNICAL INFORMATION
CENTER
8725 JOHN J KINGMAN RD., SUITE 0944
FORT BELVOIR, VA 22060-6218
ATTN: DTIC/OCP

DEFENSE THREAT REDUCTION AGENCY
6801 TELEGRAPH ROAD
ALEXANDRIA, VA 22310-3398
ATTN: CP, D MYERS
ATTN: CP, MAY AMY EHMANN
ATTN: CPW, MAJ T SMITH
ATTN: CPWCT
ATTN: CPWE, MAJ WELLS
ATTN: CPWT
ATTN: CPWT, L WITTLWER
ATTN: CPWT, W ZIMMERS
ATTN: OST, DR C GALLAWAY

DEFENSE THREAT REDUCTION AGENCY
ALBUQUERQUE OPERATIONS
1680 TEXAS ST. SE
KIRTLAND AFB, NM 87117-5669
ATTN: CPT-D G BALADI
ATTN: CPTO

JOINT CHIEFS OF STAFF
DIRECTOR FOR FORCE STRUCTURE,
RESOURCES & ASSESSMENT (J-8)
8000 DEFENSE PENTAGON
WASHINGTON, DC 20318-8000
ATTN: J8 WAR FIGHTING DIV

**DEPARTMENT OF DEFENSE
CONTRACTORS**

APPLIED RESEARCH ASSOCIATES, INC.
4300 SAN MATEO BLVD, NE
SUITE A220
ALBUQUERQUE, NM 87110-1260
ATTN: R NEWELL

APTEK, INC.
1257 LAKE PLAZA DRIVE
COLORADO SPRINGS, CO 80906-3578
ATTN: T MEAGHER

CARPENTER RESEARCH CORP.
P O BOX 2490
(FOR CLASSIFIED MAIL)
ROLLING HILLS ESTATES, CA 90274
ATTN: H J CARPENTER

ERNST-MACH INSTITUT
ECKER STRASSE 4
79104 FREIBURG I. BR.
REPUBLIC OF GERMANY
ATTN: H REICHENBACH
ATTN: P NEUWALD

GENERAL ATOMICS, INC
P O BOX 85608
SAN DIEGO, CA 92138
ATTN: CHARLES CHARMAN

H & H CONSULTANTS, INC
P. O. BOX 2219, STATION A
CHAMPAIGN, IL 61820-2219
ATTN: W HALL

ITT INDUSTRIES
ITT SYSTEMS CORPORATION
ATTN: AODTRA/DASIAC
1680 TEXAS ST SE
KIRTLAND AFB, NM 87117-5669
ATTN: DASIAC
ATTN: DASIAC/DARE

ITT SYSTEMS CORP
2560 HUNTINGTON AVENUE
ALEXANDRIA, VA 22303
ATTN: D MOFFETT

JAYCOR
1410 SPRING HILL ROAD
SUITE 300
MCLEAN, VA 22102
ATTN: DR CYRUS P KNOWLES

LACHEL AND ASSOCIATES, INC
P O BOX 10652
MCLEAN, VA 22102-9652
ATTN: J BECK

LOGICON ADVANCED TECHNOLOGY
6053 WEST CENTURY BOULEVARD
LOS ANGELES, CA 90045-6430
ATTN: LIBRARY

LOGICON RDA
6940 S KINGS HWY
SUITE 202
ALEXANDRIA, VA 22310
ATTN: B WEBSTER
ATTN: R POPE
ATTN: T MAZOLLA

DSWA-TR-98-53 (DL CONTINUED)

LOGICON RDA
P O BOX 9377
ALBUQUERQUE, NM 87119-9377
ATTN: G GANONG

MAXWELL TECHNOLOGIES INC
FEDERAL DIVISION
8888 BALBOA AVENUE
SAN DIEGO, CA 92123-1506
ATTN: J BARTHEL
ATTN: T PIERCE

PACIFIC-SIERRA RESEARCH CORP.
2901 28TH STREET
SANTA MONICA, CA 90405-2938
ATTN: H BRODE

SCIENCE APPLICATIONS INTL CORP
10260 CAMPUS POINT DRIVE
SAN DIEGO, CA 92121-1578
ATTN: J STODDARD

SRI INTERNATIONAL
333 RAVENSWOOD AVENUE
MENLO PARK, CA 94025-3434
ATTN: J GRAN

TECH REPS, INC.
5000 MARBLE AVENUE, NE
SUITE 222
PATIO PLAZA OFFICE BLDG
ALBUQUERQUE, NM 87110-6390
ATTN: F McMULLAN

TITAN CORPORATION (THE)
TITAN RESEARCH & TECHNOLOGY DIVSN
9410 TOPANGO CANYON BLVD
SUITE 104
CHATSWORTH, CA 91311-5771
ATTN: R ENGLAND

TRW S. I. G.
STRATEGIC SYSTEMS DIVISION
P O BOX 1310
SAN BERNARDINO, CA 92402-1310
ATTN: NORMAN LIPNER

WEIDLINGER ASSOC, INC.
4410 EL CAMINO REAL, SUITE 110
LOS ALTOS, CA 94022-1049
ATTN: D TENNANT
ATTN: H LEVINE

WEIDLINGER ASSOCIATES, INC.
375 HUDSON ST., 12TH FLOOR
NEW YORK, NY 10014-3656
ATTN: RAYMOND P DADDARIO

DEPARTMENT OF ENERGY

UNIVERSITY OF CALIFORNIA
LAWRENCE LIVERMORE NATIONAL LAB
P O BOX 808
LIVERMORE, CA 94551-9900
ATTN: L-030 ALLEN KUHL

LOS ALAMOS NATIONAL LABORATORY
P O BOX 1663
LOS ALAMOS, NM 87545
ATTN: MS J514/A S MASON
ATTN: MS670 J NORMAN
ATTN: R W WHITAKER/ESS-5,MS/F665
ATTN: WX-1/B SHAFER

DEPARTMENT OF THE ARMY

US ARMY RESEARCH LAB
AMSRL-SL-CS E3331
5101 HOADLEY RD
ABERDEEN PROVING GROUND, MD 21010-
5423
ATTN: SLCBR-SS-T (TECH LIB)

US ARMY RESEARCH LABORATORIES
2800 POWDER MILL ROAD
ADELPHI, MD 20783-1197
ATTN: AMSRL-SL-CE

US ARMY RESEARCH & DEVELOPMENT
CENTER
WATERWAYS EXPERIMENT STATION
3909 HALLS FERRY RD.
VICKSBURG, MS 39180-6199
ATTN: CEWES-SS-R F DALLRIVA
ATTN: SD-R E JACKSON
ATTN: SD-R WELCH
ATTN: SE-R D RICKMAN

DEPARTMENT OF THE NAVY

NAVAL RESEARCH LABORATORY
4555 OVERLOOK AVE, SW
WASHINGTON, DC 20375-5000
ATTN: CODE 5227 RESEARCH REPORT